Studies of near-critical density laser plasma interactions for ion acceleration

Oliver C. Ettlinger

January 12, 2018

Supervised by Professor Zulfikar Najmudin

Submitted in partial fulfilment of the requirements for the degree of
Doctor of Philosophy of Imperial College London

Department of Physics
Imperial College London
Prince Consort Road
London SW7 2BZ

Declaration

I hereby certify that the material contained within this thesis, which I submit for the award of Doctor of Philosophy, is entirely my own work except where otherwise cited or acknowledged within the body of text.

Oliver Ettlinger
September 2017

Copyright

The copyright of this thesis rests with the author and is made available under a Creative Commons Attribution Non-Commercial No Derivatives licence. Researchers are free to copy, distribute or transmit the thesis on the condition that they attribute it, that they do not use it for commercial purposes and that they do not alter, transform or build upon it. For any reuse or redistribution, researchers must make clear to others the licence terms of this work

Abstract

This thesis presents experimental research, complemented by numerical particle-in-cell simulations, studying the interaction of a high power CO_2 laser with near-critical density plasmas. The experiments all occurred around relativistic intensities, $a_0 \simeq 1$, where radiation pressure effects are important.

Experiments with a high intensity, 3.5 ps beam with peak intensities $I_L > 10^{16}\,\mathrm{Wcm^{-2}}$, focussed on to a shaped, over-critical density hydrogen gas target were studied. The accelerated proton beams showed spectral peaking, indicative of radiation pressure or collisionless shock driven acceleration. Higher than previously observed proton energies for this laser system were observed, with peak energies $> 1.8\,\mathrm{MeV}$, and energy spreads as low as $\sim 5\%$. The peak proton energy showed good agreement with the predicted energy scaling for hole-boring RPA, with $E_p \propto I_L/n_i$.

Experiments were also conducted at lower intensities, with a 5 ps beam of peak intensity $I_L \sim 10^{15}\,\mathrm{Wcm^{-2}}$ again focussed on to a shaped hydrogen gas target. Here, the unique laser and target conditions lead to a plasma grating structure being formed in the density ramp preceding the critical surface, from which radiation pressure driven acceleration could occur. The limited mass of these grating structures, along with the suppressed background density, results in enhanced acceleration when compared to that at the unmodified critical surface. Experimentally, a dependence on the peak proton energy compared with the scale length of the plasma preceding the critical surface was observed, attributed to an optimal density profile for the grating formation.

Finally, using the same experimental conditions, an alternative method for producing thin gas targets was explored, through two colliding blast waves. Proton acceleration was studied for relative levels of separation between the shock fronts, with the optimal case being at the point of collision. Numerical simulations suggest that acceleration was again enhanced by the creation of grating structures in the sharpened density profile.

Role of the Author

The nature of high power laser-plasma experiments, with the time and skills required to develop and maintain the laser systems, and the time constraints on conducting experiments at these facilities, make experiments a collaborative effort. Conducting them by oneself would be near-impossible.

Chapter 4 details a collaborative experiment between Imperial College London and the Accelerator Test Facility at Brookhaven National Laboratory. The author was charged with leading the planning, set-up and running of the experiment. The ion spectrometer diagnostic and optical probes were maintained by the author and Emma-Jane Ditter. The CO_2 laser diagnostics were maintained by Mikhail Polyanskiy from the Accelerator Test Facility. All analysis presented in this chapter was performed by the author.

The experiments in Chapters 5 and 6 were a collaborative effort between Imperial College London, the United States Naval Research Laboratory and the Accelerator Test Facility. The author was involved in the planning, set-up and running of the experiment. The optical probes and proton spectrometer were maintained by the author, Nicholas Dover and Yu-Hsin Chen. All analysis presented was again performed by the author.

The numerical particle-in-cell simulations that were performed and analysed by the author in the thesis were run using the EPOCH code. The EPOCH code was developed by the Extendible PIC Open Collaboration project. This aimed to develop a UK community advanced, relativistic EM PIC code.

Acknowledgements

Firstly I would like to thank my supervisor, Zulfikar Najmudin, for all his help and support throughout the past four years, for answering all my stupid questions, and reading through about 200 pages of my "waffle". I must also extend my gratitude to my second supervisor, Bucker Dangor, for all his help and guidance. I am also extremely grateful to my unofficial supervisor Stuart Mangles. Hopefully over the course of me writing this thesis the balance has shifted somewhat more towards discussing interesting physics problems and not just me asking you to sign my expense claims!

I have been extremely fortunate to spend time with so many different people over the course of the last four years, both on experiment and here at college. Special thanks goes to GPan and EJ, the other two members of "team proton". You both have made BNL/RAL experiments immeasurably more enjoyable than they otherwise would have been (except for *that* bongos incident...). GPan, thank you for somehow always saying or doing something that makes me laugh, even in the middle of the night stuck on Gemini. And for teaching me the answer to the complicated problem of 4×4. It's 8, right?! EJ, thank you for always pushing for "one more shot" even when things were not going to plan, for providing perspective while I was stressed on experiments, and for your forcing me to go to higher densities at BNL in May. Perhaps you should be in charge from now on! Finally, thanks for coming on our trip to Bermuda. It will remain with me for a long time, even if it is only because I had to share a bed with G. Secondly, while he is no longer at Imperial, I need to thank Nick for all his help and advice during the first two years of my PhD. I will always be grateful for your patience in listening to my ill-formed ideas, and your patient explaining of even the most basic concepts to me. Most importantly you showed me the ropes on my first BNL experiments way back when; hopefully it was worthwhile, with some of the results making it into this thesis.

From Imperial, special thanks first goes to the so-called "732 crew"; Gpan, Steve, Stos, Martin, Jason, D-Bob, Gibbo and, to all intents and purposes, Spenny. You have all made my time in the office much more fun and enjoyable that it perhaps should have been. That said, I fear I may have been the initiator of a large percentage of the "extra-curricular" activities we partook in when we should have working. But looking at the positives, we are all much better at Crash Bash now than when we started. A special mention has to go to GPan and Gibbo; drunken crib has to be one of the highlights of the last four years. On the subject of Gibbo, my metaphorical "partner in crime" and

the other member of team tall, thank you for so many laughs over the years, and for introducing me to bouldering, cryptic crosswords and Curb. It is not going to be the same when you leave. As such, I feel it only fair to finally admit I might have been at fault for breaking that light...

I should also thank my current crop of office mates; Sav, Elias, EJ and Gibbo. Sharing an office with you all has been a lot of fun, and I can only apologise for you having to put up with such a grumpy and stressed office-mate over the last couple of months. I also need to thank Aakash for all the useful physics chats over the last couple of years.

Beyond Imperial, I am sincerely grateful for all the help from Misha and Igor at BNL; you have both worked so hard to give us the best laser possible, and have always been willing to shoot late into the night, even when we couldn't find any protons... I am sorry we burnt so many amplifier windows! I also need to thank Chaya Kelly for making all my 3D drawings. And last, but by no means least, thank you Sally for feeding Joe and me so well over the last couple of months!

Finally, I want to thank my family for all their help, each in their own unique way. Having your unwavering support means the world, and I owe you all more than I know how to put into words.

Contents

1 Introduction **3**

1.1 Context . . . 3
1.2 Applications . . . 5
1.2.1 Fast Ignition . . . 5
1.2.2 Hadron Therapy . . . 6
1.2.3 Radiography . . . 10
1.2.4 Isotope Production . . . 10
1.3 Conclusions . . . 12
1.4 Thesis Summary . . . 12

2 Theory **15**

2.1 Plasmas . . . 15
2.1.1 The Debye Length . . . 15
2.1.2 Plasma Frequency . . . 17
2.1.3 The Dispersion Relation . . . 18
2.1.4 The plasma skin depth . . . 20
2.1.5 Electromagnetic wave propagation up a density ramp . . . 21
2.2 Acoustic and Collisionless Electrostatic Ion Waves . . . 22
2.2.1 Ion acoustic waves . . . 22
2.2.2 Solitons . . . 23
2.2.3 Collisionless electrostatic shocks . . . 27
2.3 Laser-Matter Interactions . . . 30
2.3.1 Single Particle Motion . . . 30
2.3.2 Ionisation Processes . . . 31
2.3.3 Absorption Mechanisms . . . 33
2.3.4 Ponderomotive Acceleration . . . 36
2.3.5 Laser Self Focussing . . . 38
2.4 Ion Acceleration . . . 39
2.4.1 Sheath Acceleration . . . 39
2.4.2 Radiation Pressure Acceleration . . . 44

3 Experimental Methods **55**

3.1 High Power $\mathbf{CO_2}$ Lasers . . . 55
3.2 Gas Targetry . . . 60
3.2.1 Target Shaping . . . 61

3.3 Optical Diagnostics . . . 68
3.3.1 Shadowgraphy . . . 68
3.3.2 Interferometry . . . 70
3.4 Ion Diagnostics . . . 74
3.4.1 Magnetic Spectrometer . . . 75
3.5 Experimental Layout . . . 79
3.6 Particle in Cell Modelling . . . 80

4 Radiation pressure acceleration of protons at near critical densities using a CO_2 laser 83
4.1 Experimental Overview . . . 84
4.1.1 Laser Parameters . . . 84
4.1.2 Targetry . . . 85
4.1.3 Diagnostics . . . 86
4.2 Experimental Results . . . 87
4.2.1 Spectral Characterisation . . . 87
4.2.2 Comparison to theoretical scaling . . . 95
4.2.3 Proton Beam Filamentation . . . 97
4.2.4 Comparison to previous work . . . 99
4.3 Simulations . . . 101
4.3.1 Results and Discussion . . . 102
4.4 Conclusions . . . 113

5 Enhanced ion acceleration from an induced grating structure in a near-critical density plasma ramp 115
5.1 Experimental Overview . . . 115
5.1.1 Laser Parameters . . . 115
5.1.2 Targetry . . . 117
5.1.3 Diagnostics . . . 118
5.2 Experimental Results . . . 118
5.2.1 Multiple ion bunches . . . 118
5.2.2 Proton energy vs. scale length . . . 122
5.2.3 Summary of experimental results . . . 130
5.3 Particle-in-cell Simulations . . . 130
5.3.1 Standing wave induced plasma grating structure . . . 132
5.3.2 Comparison to experiment . . . 142
5.4 Conclusions . . . 147

6 Proton acceleration from shaped gas targets produced through colliding blast waves 149
6.1 Context . . . 149
6.2 Experimental Overview . . . 150
6.2.1 Laser Parameters . . . 150

6.2.2 Targetry . . . 151
6.2.3 Diagnostics . . . 152
6.3 Experimental Results . . . 153
6.3.1 The point of collision . . . 156
6.3.2 Proton acceleration results . . . 160
6.4 Particle in cell simulations . . . 166
6.4.1 Effect of the laser train . . . 167
6.4.2 Experimental comparison . . . 168
6.4.3 Proton acceleration from thin gas targets . . . 171
6.5 Conclusions . . . 178

7 Conclusions and Future Avenues 181
7.1 Proton acceleration from pre-pulse shaped gas targets . . . 181
7.2 Proton acceleration off a plasma grating structure . . . 184
7.2.1 Limitations of the acceleration scheme . . . 185
7.3 Colliding blast waves to produce thin gas targets . . . 188
7.3.1 Effect of a rear surface density ramp . . . 189
7.4 Concluding remarks . . . 191

A The Debye Length 193

B Normalised Vector Potential and Laser Intensity 195

C Single Particle Motion 197

List of Tables

2.1 Typical values of the Debye length. 17

3.1 Magnetic ion spectrometer parameters for experiments conducted at the ATF. 79

4.1 CO_2 laser parameters for the results presented in Chapter 4 84
4.2 Comparison of previously observed peak enegies, energy spreads, $\Delta E/E$, and peak signal levels for mono-energetic spectral features observed in a number of laser-driven ion acceleration experiments. 100
4.3 Particle-in-cell simulation parameters used for studies of radiation pressure acceleration of protons from shaped gas targets. 102

5.1 CO_2 laser parameters for the results presented in Chapter 5 116
5.2 The particle-in-cell simulations used for studies into the effect of a scale length preceding the critical surface and subsequent studies into the observed density bunching phenomenon. 131

6.1 CO_2 laser parameters for the results presented in Chapter 6 150
6.2 The particle-in-cell simulation parameters used for the simulation results presented in Chapter 6. 167

List of Figures

1.1 The total number of patients treated to date for all current treatment methodologies combined, protons and carbon ions. 7

1.2 Energy deposition profiles for 6 MeV electrons, 300 MeV protons and 400 MeV/u carbon ions, plotted using TRIM. Electrons deposit their energy along their entire track with the peak intensity close to the patients skin. Protons and carbon ions deposit most of their energy at the end of their track, in the characteristic Bragg peak form. 8

1.3 A photograph of the first PET single plane imaging device, otherwise known as the "head-shrinker". 11

2.1 The electric potential profile around a test charge in a plasma centred at $r = 0$. The field of the test charge is surrounded by oppositely charged plasma particles over the characteristic length scale, the Debye length. . 16

2.2 The phase and group velocities for a laser within a plasma. 20

2.3 The electric field profile in a linear density ramp. The profile is the form of a standing wave exhibiting wavelength swelling preceding the critical surface. Behind the critical surface, the wave decays exponentially. . . . 22

2.4 (a) the potential profile of a soliton moving through a plasma from right to left and (b) the pseudo-potential, known as the "Sagdeev Potential", for a soliton with Mach number 1.3. 23

2.5 The Sagdeev potential for three different Mach numbers, highlighting that soliton solutions can only exist for $1 < M < 1.6$. For $M < 1$ no potential well is formed, while for $M > 1.6$ no particle can be trapped and the potential rises indefinitely. 26

2.6 The potential profile of a collisionless shock. The potential rises to a maximum value, ϕ_m, before oscillating in the downstream region between ϕ_m and ϕ_1. Particle reflection off the shock will result in ions propagating with the opposite velocity to the incident upstream plasma, $-u_0$, in the shock frame. 27

2.7 The Sagdeev potential for a collisionless shock. The two curves demonstrate the different potentials for particles before and after χ_m. A particle initially follows the classical trajectory for a soliton to χ_m, before then oscillating between this value and χ_1. 29

2.8 Plot of the electron motion in a laser field for linear and circular polarisations in (a) the static x-z plane and (b) the average electron drift frame. 30

2.9 Illustration of the field ionisation by barrier suppression. The dashed black line shows the unperturbed atomic potential, the red line is the laser potential and the green line the suppressed atomic potential. (a) shows partial suppression of the barrier, allowing ionisation through multi-photon absorption. (b) shows electron tunnelling through the barrier, made energetically favourable through the barrier suppression; $\gamma_{\mathrm{K}} \simeq 1$. (c) shows full suppression and the electron can escape without tunnelling; $\gamma_{\mathrm{K}} \ll 1$. 32

2.10 Illustration of the ponderomotive force experienced by an electron in a spatially variant intensity profile. 37

2.11 Plot to help illustrate self-focussing. (a) the critical power, P_c, which defines the self-focussing regime. (b) the distance over which a 228 GW beam would collapse to zero radius, z_c, given by equation 2.65. 38

2.12 Figure depicting the process of sheath acceleration, through the interaction of an intense laser pulse with a solid density foil target. 40

2.13 The relation between the vector potential and plasma density when the radiation pressure and plasma thermal pressure are balanced. An interaction sitting well above this line is dominated by hole-boring, while an interaction well below this line is dominated by collisionless shock acceleration 46

2.14 Profiles of the electron density, n_e, ion density, n_i and induced electrostatic field, E_x for the HB front formation (a) at early times when ion motion is fixed and (b) later times during the co-propagation of the electron and ion fronts. 47

2.15 Left, dependence of the hole-boring velocity on the ion density in a Hydrogen plasma and right, the predicted ion energy as a function of density for reflected ions off the critical surface 50

3.1 The three vibrational degrees of freedom of the CO_2 molecule. 56

3.2 The vibrational and rotational energy levels of the CO_2 molecule. Excitation occurs into the (0,0,1) state, before decay into the (1,0,0) or (0,2,0) states. Decay into the excited He and then ground states can then occur (not pictured). 57

3.3 CO_2 gain spectra for the ATF regenerative amplifier, created using the co2amp code. Top, gain spectrum for a $1:1:8$ ratio of CO_2, N_2 and He at 4 bar pressure. Bottom, the gain spectrum for the same gas mixture at 10 bar. 58

3.4 Left: Rendered image of a 1 mm gas nozzle made for experiments at the ATF. Right: Schematic of the gas nozzle, with the three important parameters that determine the gas profile illustrated. 60

3.5 Density lineouts for the 1 mm nozzle used on experiments at BNL for 4, 5 and 6 bar backing pressures at a height of 700 µm from the exit. . . . 61

3.6 (a) The normalised density profile of a blast wave as a function of radius for $\gamma = 1.4$ and $j = 1$, 2 and 3. (b) Normalised scale length as a function of expansion time. 66

3.7 (a) Two-dimensional image of a blast wave in a gas jet, produced using the hydro-code FLASH. (b) Longitudinal density lineouts for the same shock, demonstrating the target shaping and increased, steeper density profile. 67

3.8 Schematic of refraction effect through a cylindrically symmetric, gaussian plasma. Refraction leads to regions of high and low intensity at the detector plane. 69

3.9 Schematic of a Mach-Zehnder interferometer. A laser is split into two arms, a reference arm which passes unperturbed, and a signal arm, which traverses the medium to be probed. These are recombined, with the relative phase difference between the two arms allowing information about the medium to be inferred. Figure by Chaya Kelly. 70

3.10 (a) Raw interferometry image of a collisional shock wave, (b) The three Fourier components of the interferometry image, (c) the retrieved phase profile and (d) the retrieved density profile. The on-axis feature is not real and an artefact of the Abel inversion. 72

3.11 A schematic of the magnetic ion spectrometer used for experiments at the ATF. The magnet is depicted in blue, while the electric field plates are in red. An image of a raw proton trace image is displayed at the scintillator plane. Figure by Chaya Kelly. 77

3.12 The proton energy as a function of dispersion displacement for the magnetic ion spectrometer used on experiments at the ATF. 78

3.13 Diagram of the basic experimental setup for the experiments presented in this thesis. Figure by Chaya Kelly. 79

3.14 Schematic of the feedback loop followed by a PIC code such as EPOCH, proceeding in the clockwise direction, starting from the top of the diagram. 80

4.1 An example CO_2 temporal profile spanning 200 ns, showing the presence of parasitic pre-pulses at ~ 27.5 ns intervals before the main laser pulse. 85

4.2 An example interferogram of a pre-pulse driven blast wave, 10 ps before the arrival of the main CO_2 pulse. 86

4.3 Example magnetic spectrometer proton energy traces which demonstrate the mono-energetic peaked spectra. For the three shots presented, the peak bunch energies are 1.84, 0.83 and 0.55 MeV for (a), (b) and (c), respectively. 88
4.4 Example proton energy spectra for the three shots presented in figure 4.3. Peak energies of 1.84 MeV, 0.83 MeV and 0.55 MeV were observed for the top, middle and bottom profiles, equivalent to shots (a), (b) and (c) in figure 4.3, respectively. 88
4.5 Integrated lineout of the raw spectrum shown in figure 4.3(a), compared to the instrument function of the spectrometer. This was taken to be the integrated lineout of a zero point, also in the direction of magnetic dispersion. 89
4.6 Left: The peak height of the spectral feature as a function of iteration step for the supposed "true" signal obtained by the Richardson-Lucy method. Right: The FWHM of the spectral feature as a function of iteration step. 90
4.7 The retrieved true spectral profile as a function of spatial position after 100 iterations for the shot presented in 4.3(a). 91
4.8 The true and unconvolved energy spectra for the experimental data presented in figure 4.3(a). The true signal demonstrates a peak energy of 1.84 MeV, peak flux of 3.55×10^{11} protons/MeV/sr and an rms energy spread of 12.2%. 93
4.9 The rms energy spread of each shot demonstrating spectral peaking, as a function of the assumed density at the critical surface. 94
4.10 Proton bunch charge estimates compared with the predicted proton energy, assuming a beam divergence of $\sim 3.75°$, as indicated from simulations. 94
4.11 The measured proton energy compared with the predicted proton energy scaling for HB-RPA, $E = 4I/n_i c$. Also plotted a linear fit through the data and the line of equivalent scaling for reference. 95
4.12 An example interferogram of a pre-pulse driven blast wave used for target shaping of the gas density profile for optimal ion acceleration. Inset: The density profile for the presented interferogram along the laser axis (marked by the red line), demonstrating a scale length of 18.6 ± 5.3 µm. 96
4.13 Images of the laser near-field profile for, from left to right, the cases of zero, partial and large damage to the main amplifier input window. The resultant imprint on the spatial profile of the laser near-field is suggested to cause modulation of the proton beam due to laser filamentation in the low density plasma preceding the critical surface. 98
4.14 Magnetic spectrometer proton trace demonstrating the observation of strong spatial modulation of the proton beam in the non-dispersed direction. This is thought to be due to inhomogeneity of the laser near-field caused by non-uniform amplification of the pulse. 98

4.15 On-axis electron density lineouts and 2D density plots for the interaction of a CO_2 laser pulse with $a_0 = 1.25$, incident on a step profile plasma with density $n_e = 1.5n_c$, focussed to a spot size of 35 µm. The dynamics are shown at 0 ps, 1.1 ps, 1.8 ps and 5 ps. These demonstrate the initial conditions, density accumulation and the formation of a hole-boring front, the profile at the peak of the laser pulse and the profile around peak acceleration, respectively. 104

4.16 The proton x-p_x phase space plots for 1.1 ps, 1.8 ps and 3.1 ps for the equivalent temporal outputs from figure 4.15. At early times the protons at the critical surface are observed to be accelerated, before at 3.1 ps upstream protons are reflected off the shock potential to twice the velocity of the critical surface. 105

4.17 Simulation outputs at 5 ps for a CO_2 laser pulse with $a_0 = 1.25$, incident on a step profile plasma with density $n_e = 1.5n_c$. These demonstrate the formation of a collisionless shock structure. The subplots are (a) the on-axis proton density lineout, (b) the full 2D proton density profile. (c) the longitudinal electric field and (d) the x-p_x proton phase space. . . . 106

4.18 The on-axis electron density lineouts and 2D density plots for the interaction of a CO_2 laser pulse with $a_0 = 1.25$, incident on a plasma with peak density $n_e = 1.5n_c$ and 20 µm preceding density ramp. The dynamics are shown at 0 ps, 0.7 ps and 2.3 ps. These demonstrate the initial conditions, the perturbation of the density ramp preceding the initial critical surface and the profile around peak acceleration, respectively. 108

4.19 The proton x-p_x phase space plots for 0.7 ps and 2.3 ps for the equivalent temporal outputs from figure 4.18. 109

4.20 (a) The two-dimensional density profile at 6 ps for the late time collisionless shock formed in simulations with a 20 µm density ramp preceding a $1.5\,n_c$ plasma slab. The incident laser has $a_0 = 1.25$. (b) The phase space plot for the same simulation, showing a bunch of protons previously accelerated by HB-RPA and a broad energy component accelerated off the collisionless shock potential. 109

4.21 (a) The proton energy spectra at 3.8 ps and 5.2 ps for a step density profile. (b) The proton energy spectra at 3.4 ps and 5.2 ps for a 20 µm exponential density profile preceding the plasma slab. In both cases the early time energy peaking is not observed to be maintained at later times. 110

4.22 Peak proton energies observed in simulations, for $a_0 = 1.25$, $a_0 = 1.50$ and $a_0 = 1.75$, for densities over the range 1.5-3 n_c. 111

4.23 Proton energy spectra at two times from 2D PIC simulations, for both circularly and linearly polarised laser pulses with $a_0 = 1.25$ at a density of $1.5\,n_c$. 113

5.1 An example CO_2 temporal profile. Modulation of the gain spectrum results in temporal modulation and a laser train. The given example contains 7 %, 28 % and ∼ 65 % energy in the first, second and third pulses, respectively. 116

5.2 An example interferogram from the experiment, showing a blast wave launched into the gas jet 30 ns before the main CO_2 pulse. The clip, which is shot with a seperate Nd:YAG laser to heat the clip and generate the shock is clearly visible protruding into the gas flow. This laser is incident from above and to the side of the gas jet, with variable energy and timing. 117

5.3 Experimental magnetic ion spectrometer traces illustrating the effect of high energy proton energy bunches, with a lower energy, thermal tail. The peak observed bunch energies were 0.77 ± 0.04 MeV, 1.47 ± 0.11 MeV and 0.88 ± 0.05 MeV for shots (a), (b) and (c), respectively. 119

5.4 Experimental data demonstrating the observation of multiple proton bunches. (a) raw proton energy image from the magnetic ion spectrometer, with three proton energy bunches, (b) raw proton energy image with two energy bunches, (c) and (d) proton energy spectra as a function of counts per MeV per steradian for (a) and (b), respectively. 121

5.5 Experimental proton energy scaling as a function of relative blast wave timing; analogous to scaling versus the scale length. Also plotted is the predicted proton energy from HB-RPA ($E_p = 4I/n_i c$), using the estimated peak density from the shock front location. 123

5.6 Experimental proton energy scaling as a function of the nozzle position along the axis of laser focus. Proton energies are not observed to appreciably decrease over two Rayleigh lengths. Also plotted is the predicted proton energy from HB-RPA ($E_p = 4I/n_i c$). A mean laser energy of 1.1 J was used. The shock expansion was fixed in this case, with the estimated peak density calculated from the average shock front location across all shots. 124

5.7 Left: Experimental density scale lengths obtained using interferometry ∼ 30 ps before the main CO_2 pulse. Right: An example density lineout for the case of 50 ns expansion. 126

5.8 (a) The experimental shock radius, along with the analytical prediction obtained from equation 3.7. (b) The mean experimental blast wave expansion velocity for the temporal scan, demonstrating the shock continues to propagate in the strong shock limit up to the end of the temporal window. Also plotted is the predicted shock velocity from equation 3.8. (c) The theoretical scale length for a spherically expanding shock, assuming the expansion radius from a point source at the clip, using the radius measured in figure (a). For comparison the experimental results are also plotted. All analytical solutions use the YAG energy of $E = 80\,\mathrm{mJ}$ and a density of $5.6 \times 10^{18}\,\mathrm{cm}^{-3}$, which represents the mean unperturbed gas density across all shock locations. 128

5.9 (a) A cartoon of the forces due to a standing wave on the plasma electrons, inducing density bunching at the standing wave nodes. (b) The ponderomotive force for the depicted standing wave. 132

5.10 Simulation output at 2.7 ps showing the 2D density electron profile for a 25 µm scale length exponential density ramp preceding the critical surface. Also shown are 1D lineouts of the on-axis transverse component of the laser field, the electron and ion densities. A 10 µm, 5 ps CO_2 laser pulse with $a_0 = 0.62$ is incident on the plasma. A standing wave is formed between the incident and reflected pulse components, producing a grating structure in the electron and ion densities. 133

5.11 Simulation output at 2.3 ps showing the 2D density electron profile for a 5 µm scale length exponential density ramp preceding the critical surface. Also shown are 1D lineouts of the on-axis transverse component of the laser field, the electron and ion densities. A 5 ps CO_2 laser pulse with $a_0 = 0.62$ is incident on the plasma. 134

5.12 Simulation output at 3.3 ps showing the 2D density electron profile for a long, 75 µm scale length exponential density ramp preceding the critical surface. Also shown are 1D lineouts of the on-axis transverse component of the laser field, the electron and ion densities. A 5 ps CO_2 laser pulse with $a_0 = 0.62$ is incident on the plasma. 135

5.13 Simulation outputs showing the temporal evolution of bunch formation from the initial conditions through to the time of maximum density in the structure closest to the critical surface. 1D lineouts of the on-axis transverse laser field, ion and electron densities at 0, 1.7, 2.4 and 3 ps are shown. A 10 µm, 5 ps CO_2 laser pulse with $a_0 = 0.62$ is incident on the plasma, as in figure 5.10. 137

5.14 The 2D density profile for the grating structure formation, for equivalent temporal snapshots from the same simulation as shown in figure 5.13. The temporal evolution of the grating structure is depicted, with formation up to 2.4 ps, before the structure begins to collapse at 3 ps. Note the colour scale is saturated to highlight the effect. 138

5.15 (a) The number of over-critical density bunches formed for a given exponential density scale length. (b) The peak density for the highest density grating structure. (c) The corresponding time of the peak density value shown in (b) relative to the scale length. The time of peak laser intensity is shown as the dashed black line for comparison. (d) The density of the highest density structure at the peak of the laser pulse. 139

5.16 Proton energy scaling vs. scale length from 2D PIC simulations for exponential density ramps with $a_0 = 0.62$ and $a_0 = 1.45$. The $a_0 = 0.62$ case shows a peaked dependence on the scale length, as for the experimental results, albeit for shorter scale lengths. 140

5.17 Top: the on-axis electron and proton densities, plus the transverse electric field profile at 2.4 ps for a 20 µm density ramp with a 10 µm, 5 ps CO_2 laser pulse of $a_0 = 0.62$ incident on the plasma. Bottom: the proton phase space for the equivalent time. 144

5.18 Top: the on-axis electron and proton densities, plus the transverse electric field profile at 3 ps for a 20 µm density ramp with a 10 µm, 5 ps CO_2 laser pulse of $a_0 = 0.62$ incident on the plasma. Bottom: the proton phase space for the equivalent time. 145

5.19 Top: the on-axis electron and proton densities, plus the transverse electric field profile at 5.2 ps for a 20 µm density ramp with a 10 µm, 5 ps CO_2 laser pulse of $a_0 = 0.62$ incident on the plasma. Bottom: the proton phase space for the equivalent time. 146

5.20 (a) The proton energy spectrum for a 25 µm exponential ramp, showing a peaked spectrum at 0.48 MeV (b) Integrated proton energy spectrum for a 20 µm exponential ramp, demonstrating multiple ion energy bunches. 147

6.1 An example CO_2 temporal profile for the experimental conditions in Chapter 6. Pulse trains typically consisted of 3 pulses, separated by ~ 25 ps. The given example contains 10 ± 6 %, 30 ± 12 % and $\sim 60 \pm 17$ % of the total energy in the first, second and third pulses, respectively. . . 151

6.2 An example interferogram from the experiment, demonstrating two colliding blast waves. Two clips were shot with an Nd:YAG laser, with ~ 40 mJ each, to generate the shocks. 152

6.3 Top: shadowgraphy optical probe images of the shock expansion for three increasing expansion times, showing evolution up to the point of collision. Bottom: the equivalent interferometry images corresponding to the shadowgraphy images above. Shots were taken at 4.5 bar backing pressures, corresponding to peak gas densities of $7.4 \times 10^{18}\,\mathrm{cm}^{-3}$, or $\sim 0.65\,n_c$. . . 153

6.4 Left: two dimensional density profiles for three different shock expansion radii. Right: lineouts of the density profile in the direction of laser propagation for the same density profiles. The profiles are for the raw interferometry images given in figure 6.3 and demonstrate increased convergence of the shocks until they collide. 154

6.5 Left: the experimentally obtained shock radii as a function of expansion time, along with the theoretical scaling as predicted by Sedov (equation 3.7), showing good agreement when the finite explosion centre size is accounted for. Right: the experimentally obtained density scale length and predicted scale lengths from the Sedov scaling. 156

6.6 The retrieved density profile for the case of two colliding blast waves, along with a fitted function of the form $n_e/n_c \propto n_{max}\, e^{-|r|}$, fitted to match the resolvable, low density portion of the interferogram and set to a peak density of $5.8\, n_c$ 158

6.7 (a) & (b): example raw proton energies traces observed with the magnetic ion spectrometer. (c) & (d): the corresponding proton energy spectra for (a) and (b), with peak bunch proton energies of 0.46 MeV and 0.74 MeV, respectively. 161

6.8 The deconvolved proton energy spectra for the equivalently labelled shots in figure 6.7. RMS energy spreads of 17.4% and 16.8% were found for each shot, respectively. 161

6.9 The experimentally obtained peak proton energy versus the expansion radius for colliding shocks in the case of spectral peaking of the proton energy. 162

6.10 The experimentally obtained proton bunch rms energy spread values for the shots presented in figure 6.9, demonstrating a decrease in the rms energy spread with increasing target density. 163

6.11 (a) & (b): example raw proton energies traces observed with the magnetic ion spectrometer. (c) & (d): the corresponding proton energy spectra for (a) and (b), with maximum observed proton energies of 0.49 ± 0.03 MeV and 0.97 ± 0.05 MeV, respectively. 164

6.12 The experimentally obtained maximum proton energy versus the expansion radius for colliding shocks in the case of no observed spectral peaking. Instead, broadband energy spread beams are observed. 165

6.13 The steepened density profile of a target with a peak density of $4\, n_c$ and scale length of 70 µm at the arrival of the main CO_2 pulse. This was induced by a pre-pulse with 30% of the total integrated laser energy, 25 ps before the main pulse. A new density profile emerges, with scale length of 7 µm. 168

6.14 The full 2D and on-axis electron density lineouts for the interaction of a CO_2 laser pulse with intensity $I = 7.5 \times 10^{15}\,\mathrm{Wcm}^{-2}$, incident on a target with peak density $n_e = 5.8\,n_c$ with a front surface exponential density gradient with a scale length of 7 µm. The dynamics are shown at 2 ps and 4 ps, along with the initial density profile. These demonstrate the formation of a single density structure due to a standing wave, which is subsequently accelerated. Note the 2D density images are on a saturated colour scale to better illustrate the interaction 169

6.15 The x-p_x proton phase space for at 2 ps and 4 ps for the interaction conditions given in figure 6.14. 170

6.16 Example target conditions at 2.3 ps, for the interaction of a CO_2 laser pulse of peak intensity $I = 7.5 \times 10^{15}\,\mathrm{Wcm}^{-2}$, incident on a 5 µm plasma slab of density $5.8\,n_c$. (a) The full 2D electron density of the target, illustrating density steepening at the front surface, (b) the on-axis electron density, (c) the longitudinal electric field, demonstrating the formation of a sheath field at the rear of the target due to expansion, (d) the x-p_x proton phase space for the temporal snapshot. This illustrates that the protons gain energy from two mechanisms, at the critical surface due to the radiation pressure, and more significantly, at the target rear due to the sheath formation. 172

6.17 The proton energy spectrum for a 2 µm slab target with density of $5.8\,n_c$. The incident laser had a peak intensity of $I = 3 \times 10^{16}\,\mathrm{Wcm}^{-2}$. A thermal energy spectrum is observed due to the expansion of the heated target, while also present is a narrow energy spread feature due to radiation pressure acceleration at the front surface of the target. 173

6.18 The on-axis electron density lineouts and on-axis longitudinal electric field for the interaction of a CO_2 laser pulse with intensity $I = 3 \times 10^{16}\,\mathrm{Wcm}^{-2}$, incident on a 2 µm thick plasma with peak density $n_e = 5.8\,n_c$. The dynamics are shown at 1 ps, 3 ps and 3.5 ps. These demonstrate the initial density steepening, the point the target expands to the critical density and later subcritical phase, where bulk electron heating due to relativistic transparency is possible. 175

6.19 The maximum proton energy versus target thickness for the case of slab targets. Results are given for two intensities, $I = 7.5 \times 10^{15}\,\mathrm{Wcm}^{-2}$ and $I = 3 \times 10^{16}\,\mathrm{Wcm}^{-2}$, equivalent to the estimated experimental parameters and an intensity with 4 times higher energy, roughly equivalent to the currently available intensities. 176

6.20 The proton energy spectra for the case of an idealised thin slab target at a peak density of $n_i = 5.9\, n_c$ and peak intensity of $I = 7.5 \times 10^{15}\,\mathrm{Wcm}^{-2}$. Energy spectra for both linear and circular polarisations are presented at a time of 5.6 ps, equivalent to the energy at time of the end of the laser pulse. Also presented is the energy spectrum at the peak of the laser pulse, 2.8 ps, corresponding to the peak of the laser pulse. This demonstrates a radiation pressure driven component to the interaction. 177

7.1 The predicted maximum proton energy scaling versus laser intensity for the CO_2 laser at the ATF for a critical density interaction. Experimental results from chapters 4, 5 and 6 are also given. The points correspond to the mean measured proton energy and on target intensity. The errorbars define the range over which these values varied. Important historic and future laser development milestones are also given. 182

7.2 Example shaped temporal pulse structure for the ATF CO_2 beam to optimise the formation of a plasma grating structure for subsequent ion acceleration. 187

1 Introduction

1.1 Context

The idea of accelerating charged particles is not new; mankind has been doing so for over a century. The first so called "cathode ray tube" was developed by Braun in 1897 [1], though the so called "cathode rays" had been discovered some 30 years earlier. It was in fact not until the same year, 1897, that Thomson managed to demonstrate that these cathode rays were in fact negatively charged particles, which would later become known as the electron; a discovery which would form part of the basis for his award of the Nobel Prize in Physics in 1906. One of the first linear accelerator systems was proposed by Ising in 1924, using a a system of sequentially triggered drift tubes between which acceleration could occur. In 1928, Winderøe took this idea further and demonstrated the first experiments using such drift tubes and a resonating radio-frequency, creating an alternating electric field; it was realised that charged particles co-moving in phase with an oscillating electric field could obtain energy and are accelerated. This work formed the basis for Lawrence developing the first cyclotron[1] in 1929. Around the same time Cockroft and Walton were working on their own accelerator, producing protons approaching 1MeV, used to perform "Nuclear disintegration experiments" [2] [3]. Sloan, along with Lawrence, further improved Winderøe's linear accelerator design in 1931, although it was not until the end of the second world war that development of such linear accelerators really gathered pace [4]. This has ultimately paved the way for the varied range of accelerators used today, from large scale research machines such as the Large Hadron Collider (LHC) and Stanford Linear Accelerator (SLAC), to the cyclotrons used at medical facilities for isotope production and radiotherapy.

Since these early experiments there has been an ever present desire for higher and higher particle energies. While this has traditionally been achieved using ever larger machines over immense scales, traditional methods are limited. The LHC produces $\sim 7\,\mathrm{TeV}$ proton beams, but requires a $27\,\mathrm{km}$ circumference ring to achieve this. Furthermore, the proposed VLHC upgrade is required to have a ring circumference of $100\,\mathrm{km}$ and twice the magnet strength of the present LHC, delivering $\sim 100\,\mathrm{TeV}$ beams. The expansive nature of these machines is in part due to the breakdown that occurs at the metal walls of the accelerating cavity; this limits the maximum practical accelerating gradient

[1] another feat which resulted in the award of a Nobel Prize to Lawrence in 1939 for "the invention and development of the cyclotron and for results obtained with it, especially with regard to artificial radioactive elements"

to $\sim 30\,\mathrm{MVm}^{-1}$. This effect is the critical factor limiting the energy gain for linear accelerators and the reason for their large size. These accelerators typically consist of a series of joined cavities, with adjacent cavities exhibiting alternating field polarity. In such cases that the field polarity can be switched in phase with a particle bunch as it moves between successive gaps, a continual accelerating force is experienced and the bunch can reach high energies. However, the aforementioned limited acceleration gradients mean large numbers of successive cavities are required to achieve high particle energies. While multipass, circular cyclotron/synchrotron designs somewhat overcome these difficulties, they are similarly not without limitations. Synchrotron radiation losses for electron/positron colliders, and the escalating requirements on the bending dipole magnet strength necessary to keep ions confined to the ring strongly limit these geometries. Alternative methods, such as dielectric laser acceleration (DLA) [5], can achieve $> 100\,\mathrm{MVm}^{-1}$ acceleration gradients. In this scheme, dielectric structures are machined such that when a laser is passed over the top, a field is induced above the structure, within which charged particles can be accelerated. Careful design of the machined dielectric structure allows tailoring of the accelerating fields. However, this scheme has a number of drawbacks, most notably the localised nature of these fields; the field strength drops away exponentially from the surface, limiting the characteristics of the bunch that can be accelerated.

Fortunately, alternative solutions to the problem exist. Plasmas are able to support significantly higher fields than the environment in conventional machines like the LHC; these plasma based fields can exceed $100\,\mathrm{GVm}^{-1}$. A plasma, by its very nature has already undergone "breakdown"; the limitations of conventional accelerators therefore do not apply. The seminal paper by Tajima and Dawson [6] proposed the use of a laser-plasma based acceleration scheme for electrons, indicating the possibility of these previously unachievable high acceleration gradients by driving electron plasma waves. These plasma waves act as an accelerating structure for injected electrons from the upstream bulk. Since then, various work has used this idea and attempted to produce the highest possible energy electron beams over the shortest distances. Research was given a significant boost with the invention of chirped pulse amplification (CPA) [7], which allowed for major increases in the available driving laser intensity; intensities have been increased from $\sim 10^{15}\,\mathrm{Wcm}^{-2}$ to $> 10^{21}\,\mathrm{Wcm}^{-2}$. This in fact led to a remarkable rise into research in this area.

The increase in laser intensity provided the opportunity for rapid advances in plasma research, with, Modena et al. experimentally able to demonstrate 44 MeV electrons and accelerating gradients of the order $\sim 100\,\mathrm{GeVm}^{-1}$ [8]. Subsequently, electrons have been accelerated to ever higher energies ($> 1\,\mathrm{GeV}$) over centimetre scales [9] [10] [11] [12] [13].

Ion acceleration is also of interest. However reaching these energies is significantly more challenging for ions. The ions' increased mass results in much higher injection velocity

requirements, else the ions cannot stay in phase with the driven plasma waves which travel at close to the speed of light. As such, proton driven wakes, while theoretically possible [14] have not been experimentally realised. While wake accelerated proton beams have not yet been realised, ion beam production through laser-solid interactions have been demonstrated for over 30 years. Initially the energies were relatively modest [15] [16] [17] [18], but again CPA allowed for significant advances [19] [20] [21] [22] [23] [24]. Today, ion beams are multi-energetic, high flux and at significantly higher energies at up to $\sim 90\,\mathrm{MeV}$ [25].

Laser accelerated ions possess many beneficial properties when compared to their conventionally accelerated counterparts [26]. The higher acceleration gradients allow for more compact sources, while co-propagating ion and electron bunches accelerated in the interactions make the beams charge neutral, permitting higher beam charges. With this, the bunch length of the particles is extremely short, at least over low propagation distances. For large energy spread beams, the multitude of energies results in the beam current degrading with distance. As will be discussed later in this thesis, the beams are often comprised of a range of energies (often termed "thermal"), which is desirable for a number of applications. Finally, the beams possess low transverse and longitudinal emittance, a measure of a particle beams' momentum spread as a function of spatial position. These are up to a factor of ~ 100 better than conventional sources [26].

1.2 Applications

There are numerous potential applications for laser-accelerated ion beams. Their unique properties outlined above make them particularly interesting in areas such as radiography and fast ignition inertial confinement fusion (ICF). Other applications include isotope production for use in medical imaging, proton beam machining and hadron therapy.

1.2.1 Fast Ignition

Since the industrial revolution began around 260 years ago, mankind has been consuming ever more energy; the rate of this growth has been exponential. This has meant the necessary adoption of new energy sources. While pre 1820's mankind consumed power through wood and other bio-fuels, we have since as a species transitioned to coal, oil and gas. With these resources ever depleting, their price has also grown near exponentially. Couple this with the way in which mankind is irreparably altering the Earth's climate through our energy use and the idea of fusion energy becomes extremely attractive.
Most current efforts focus on the fusion of a deuterium-tritium (DT) fuel mix. A DT scheme is favourable due to the relatively high fusion cross-section at modest, laboratory achievable temperatures of the order $10\,\mathrm{keV}$. These temperatures allow the

Coulomb barrier to be overcome and fusion to occur. A single DT fusion reaction releases 17.6 MeV of energy in the form of an alpha particle and a neutron.

$$^{2}_{1}\mathrm{D} + ^{3}_{1}\mathrm{T} \rightarrow ^{4}_{2}\mathrm{He}\,(3.5\,\mathrm{MeV}) + ^{1}_{0}\mathrm{n}\,(14.1\,\mathrm{MeV}) \tag{1.1}$$

For comparison, a rough estimate can be made for the equivalent amount of DT fuel needed compared to a barrel of oil. The amount of energy that can be extracted from a barrel of oil is $\sim 6.1\,\mathrm{GJ}$ (converting to J from BTU) [27]. A barrel of oil ($\sim 150\,\mathrm{kg}$) is therefore equivalent to a mere 18 mg of DT fuel.

Deuterium and tritium are relatively easy to source; deuterium in particular is readily available and can be extracted from seawater. Furthermore, the process produces no long-lived, harmful radioactive waste, assuming the reactor walls are formed of a low-Z material.

There are two main approaches to producing sustainable fusion energy. First is magnetic confinement fusion, which involves magnetically confining a plasma in a torus producing a sustained reaction [28] [29]. The second method, inertial confinement fusion [30], involves the compression of a DT fuel pellet until it ignites, releasing energy in the form of neutrons which are captured in a lithium blanket surrounding the interaction. So called indirect drive uses lasers to generate soft x-ray beams from the heated walls of a hohlraum. These x-rays heat the DT fuel pellet, causing it to compress and driving a shock wave which, under the correct conditions upon convergence, can cause ignition [31]. A second scheme, fast ignition, separates the compression and burn phases. Compression is initiated, and ignition then induced by energy deposition at the edge of the fuel core from ion [32] [33] or electron beams [34] [35]. Fast ignition reduces the required driver energy and also reduces the symmetry requirements of direct drive methods [36]. There is also the potential for higher energy efficiencies; the fuel compression conditions are less strict, and for a targeted particle beam a large fraction of the energy can be deposited in the target hotspot. Indirect drive suffers from relatively poor conversion efficiency due to losses in laser energy conversion to x-rays and the subsequent coupling to the fuel pellet. Laser-accelerated ion beams have high fluxes, which make them particularly suited to fast ignition applications. The potential to possibly produce arbitrary energy with a given spread based on the acceleration mechanism might also one day be feasible.

1.2.2 Hadron Therapy

One of the most commonly cited potential applications for laser-driven ion beams is in the field of hadron therapy; the treatment of cancer through ion beams. First postulated by Wilson in 1946 [37], hadron therapy is already used across the globe in a number of facilities to treat various cancers. The use of hadron therapy has been steadily increasing

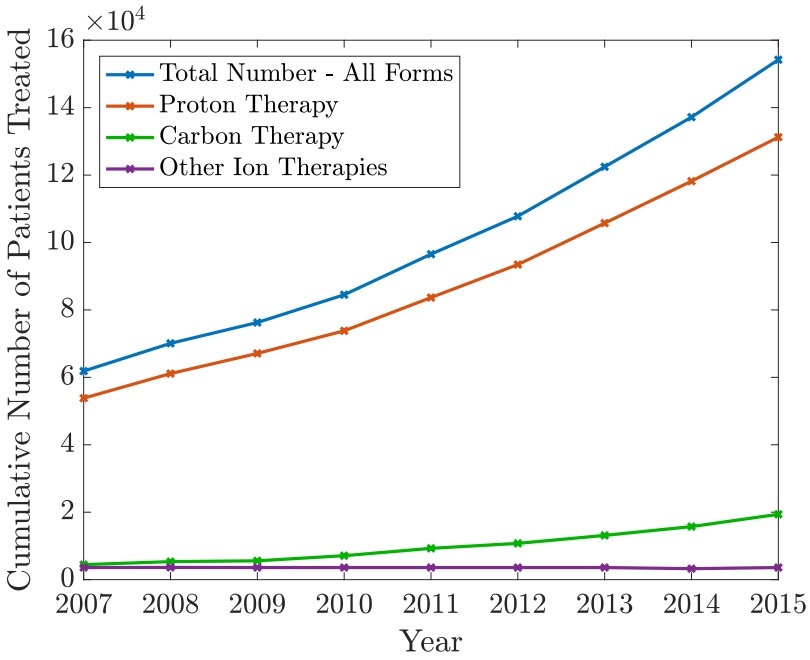


Figure 1.1: The total number of patients treated to date for all current treatment methodologies combined, protons and carbon ions. Data collated from [42].

since the first treatment centres opened in 1954, as shown in figure 1.1. As of December 2015, 62 treatment centres were operational worldwide where 154,203 patients had been treated with hadron therapy of some form, the majority (85%) of which was via protons [38]. It is suggested that more than 50% of all cancer patients have radiotherapy of some form and 20% would benefit from ion beam therapy [39]. Given it is predicted that 1 in 2 people born in the UK after 1960 will contract cancer in some form [40], a vast number of patients would benefit from safe, affordable hadron therapy. This is supported by the global market being worth $4 billion and growing at some 5 % annually [41].

Current systems use conventional RF accelerators, which are well understood and characterised. However, while they offer a number of advantages, their size and associated infrastructure costs have historically made their installation and operation extremely expensive. Consider the recent capital investment committed by the UK government to two proton therapy treatment centres, one in London and the other in Manchester, of the order £250m. Further examples of these extreme costs exist, for example the $370m spent on two treatment centres in Arizona and Minnesota in the USA [43]. This total is not purely for the accelerator and gantry system. However, the gantries in particular, used for beam delivery to the patient, constitute much of the cost. Given the requirement for highly targeted dose delivery, the patient is held in a fixed position and the gantry rotated around the patient. This, along with the need for flexible ion energies and the associated increased complexities of the magnet system for steering and focussing the beam, has resulted in these large footprints and costs. That said, re-

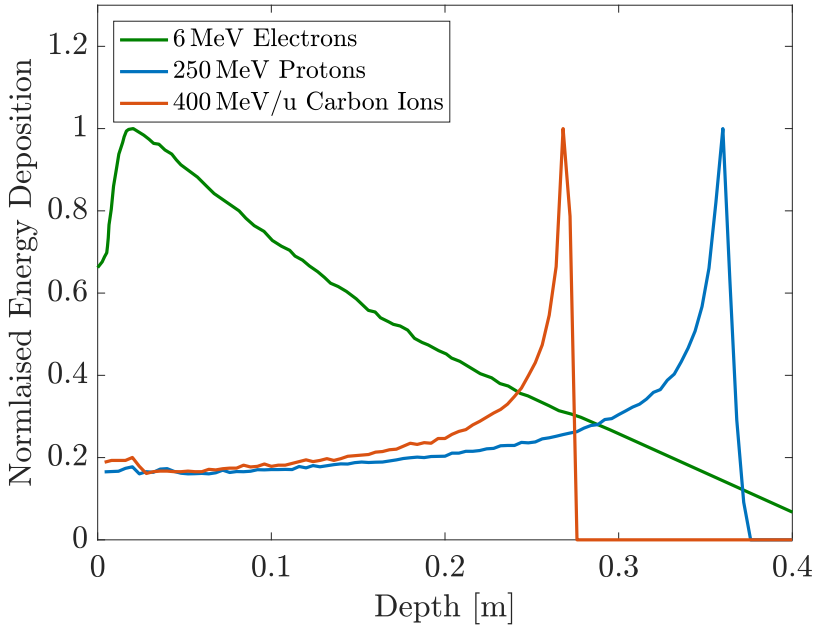


Figure 1.2: Energy deposition profiles for 6 MeV electrons, adapted from [45], 300 MeV protons and 400 MeV/u carbon ions, plotted using TRIM [46]. Electrons deposit their energy along their entire track with the peak intensity close to the patients skin. Protons and carbon ions deposit most of their energy at the end of their track, in the characteristic Bragg peak form.

cent technological developments in the field, spurred on by the adoption of the scheme by industry, has resulted in a remarkable decrease in both of these aspects; full treatment machines now occupy footprints of the same size as a magnetic resonance imaging machine [44].

One might ask why hadron therapy is being adopted as an alternative to traditional radiotherapy methods? This is in the large part because of the unique energy deposition profile of protons and heavier ions. Ions deposit their energy in the form of a Bragg peak, described by the Bethe formula, given as

$$-\frac{dE}{dr} = \frac{4\pi n Z^2}{m_e v^2} . \left(\frac{e^2}{4\pi\epsilon_0}\right)^2 . \ln\left[\frac{2m_e v^2}{I}\right] \tag{1.2}$$

This energy deposition, as shown in figure 1.2, is unique in that almost all the ion energy is deposited in a narrow region at the end of the particle track. This is in stark contrast to the energy deposition profiles of electrons and the traditional radiotherapy delivery method, photons. Unlike ions, electrons and photons deliver a relatively steady energy profile, with the most intense deposition at the start of their track, just under a patients skin. This can lead to significant issues when irradiating patients, since not only the cancerous tissue, but also the healthy surrounding parts are dosed; secondary cancers and damage to the growth of young patients are the result.

The highly targeted nature of hadron therapy is desirable given it presents the possibility to reduce side effects, while at the same time allowing higher, targeted doses to be delivered; ions also suffer much less lateral scattering. Hadron therapy has been shown to be advantageous in the treatment of some specific paediatric patients [47], although other studies have found its use and the reduction in side effects less easy to diagnose [48].

An obvious next question is 'Why are laser accelerated ion sources of interest when conventional sources already exist and are well characterised?'. There has been much recent interest in the development and suitability of laser accelerated ion sources for use in hadron therapy [49] [50] [51] [52] [53]. Laser based sources offer superior flexibility in terms of the ion species and energies that can be delivered [54]; assuming targets can be made and the laser parameters tuned there are a near infinite number of options. This flexibility would be extremely useful, given that by nature, no two people or tumours are the same. As such each person requires different treatment parameters. Furthermore, the ability to easily switch between various ion species, for example between protons and carbon ions, depending on any given treatment requirement, would be a unique feature of laser based sources.

One of the most significant current obstacles are the energy requirements for clinical applications. Energies of $\sim 300\,\mathrm{MeV}$ and $\sim 400\,\mathrm{MeV/u}$ are required for protons and heavier ions, respectively. These are currently not attainable, with a number of varying schemes proposed to reach these energies, making the path to achieving this unclear. Furthermore, given the targeted nature of therapy, narrow energy spread beams are desirable to minimise unwanted damage to healthy surrounding tissue. Whether this will be achieved through the acceleration mechanism itself or a latter energy selection stage is a matter of debate. The high flux nature of laser produced beams also presents a challenge given the current methodology. Current treatment plans typically irradiate tumours over the course of hundreds of consecutive shots, using a narrow energy spread pencil beam to raster across the tumour. Laser accelerated ion beams provide the possibility to deliver greatly enhanced fractions of the total required dose, possibly even the whole dose, in a single shot. This would require a significant shift in the current treatment thinking, with obvious concerns for patient welfare in the case of inaccurate dose delivery. However, if these concerns could be overcome, this could prove an interesting benefit of laser driven sources. In fact, so called ultra high dose rates may offer a number of benefits over the current treatment methodology.

Therefore, while laser-produced ions are an interesting source for future hadron therapy schemes, there are still a number of challenges to solve before their implementation can be put into practice.

1.2.3 Radiography

The probing of plasmas is an interesting application of ion beams. Optical diagnostics allow the investigation of density gradients through the diffraction of light rays as they traverse a change in refractive index. Probing plasmas to look at their field structure is not such an easy task. The proposition of ions as a diagnostic for probing matter is not a new idea [55] [56]. Laser produced ion beams have a number of properties which make them ideal for observing these field structures, as well as the density isotropy/homogeneity of the plasma [57]. Their small source size, high flux and divergence properties, and particularly broadband energy profile coupled with a short formation time make these beams ideal for probing plasmas.

Experiments where two high intensity laser beams are available use one target to produce ions which can then in turn be used to image a second interaction [58]. Ions are emitted from one target and then pass through the plasma created at the front and/or back of the second target, where they are deflected dependant on the electric and magnetic field structure. These beams can then be imaged. Interestingly, laser accelerated beams are often thermal in nature; they are formed of a range of energies. For appropriate distances between the ion source and probed target these ions are spatially separated owing to their different velocities, facilitating temporal information about the probed target to be retrieved.

A number of authors have successfully used ion radiography techniques for probing. Romagnani et al. were able to temporally resolve the sheath field expansion from the rear surface of a foil target [59]. The same author also used proton probing to resolve an electrostatic collisionless shock wave [60]. Willingale et al. [61] used proton radiography to observe channel formation in a near-critical density plasma, while authors have used the technique to observe magnetic field generation in laser-solid interactions [62][63][64].

1.2.4 Isotope Production

Positron emission spectroscopy (PET) is a medical imaging technique by which gamma-photon pairs are detected. The patient is injected with a choice of radioactive isotopes, most commonly fluorine-18 and oxygen-15 for oncology and neuroimaging applications, respectively. Isotopes are attached to molecules which imitate those found in the body, often in the form of sugars which gravitate towards regions of high metabolic rate, for example cancerous tumours. The short lived, unstable isotopes decay via positron emission which annihilate with electrons within the patient, producing a pair of gamma photons which are emitted in opposite directions from the point of view of their centre of mass frame. These photons can be observed by scintillator detectors which surround the patient, with the temporal separation allowing the location of electron-positron annihilation to be determined [65]. With this a picture of the area of interest can be

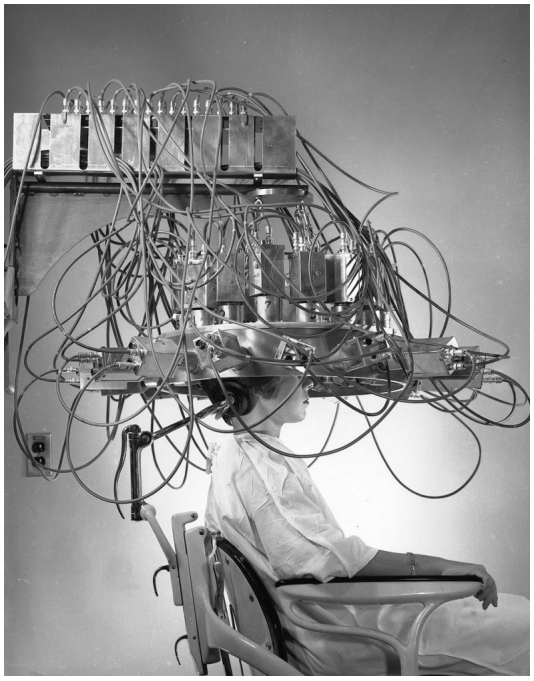


Figure 1.3: A photograph of the first PET single plane imaging device, otherwise known as the "head-shrinker" [70].

constructed [66].

The first demonstration of annihilation radiation being used for medical imaging came in 1953 [67], with PET being posited in the late 1950′s. The first single plane PET scanner was developed at Brookhaven National Laboratory in 1961, which was given the rather ominous nickname of the "head-shrinker" (see figure 1.3) [68]. Research has since continued with ever more sophisticated scanners being developed and PET has gone on to become an important medical imaging technique used for a number of applications [69].

Again, one of the major limiting factors in the use of PET as an imaging technique lies with the short-lived nature of the radioisotopes used. With half-lives typically ranging from 2 minutes to 2 hours, they must be produced and quickly administered to the patient, allowing the molecules to move around the body to the site of interest before imaging. Production is currently through cyclotrons situated at the hospital. It is hoped that laser-driven ion sources could provide a viable alternative for producing these medical isotopes. As such, a number of authors have attempted to demonstrate the production of these isotopes from laser driven ions [71] [72] [73] [74]. Unfortunately, current work has not been able to produce high enough activity levels of these isotopes to make them viable for clinical use. However, it is hoped with further advances in ion acceleration research it could be possible to demonstrate a laser source as a viable isotope production mechanism.

1.3 Conclusions

The previous pages have put forward convincing arguments that the rewards for producing high energy, high flux ion beams through laser acceleration are significant. Much progress has been made in the last couple of decades, although there is still a long way to go to achieve beams suitable for many applications. While it may be argued that the push to higher ion energies will require the generation of new, higher intensity laser systems that are currently proposed [75] [76] or under construction [77], there is still significant progress to be made in better understanding the ion acceleration mechanisms in the current regime. This also does not preclude further incremental optimisation of conditions to drive higher energy, higher flux beams with narrow energy spreads.

1.4 Thesis Summary

This thesis contains results from experiments studying proton acceleration at near critical densities using the mid-IR ($\sim$10 µm) CO_2 laser at the Accelerator Test Facility (ATF) at Brookhaven National Laboratory. These wavelengths are of interest due to a number of beneficial scalings related to the critical plasma density (section 2.1.3) and normalised vector potential (section 2.3.1). These quantities and benefits will be outlined in detail in future sections. At this point, it is sufficient to state that with a mid-IR laser the densities required for an overcritical, reflective plasma, and the intensities needed for relativistic electron motion in a laser field are each decreased by a factor of 100. This allows the use of gas targets for studies into proton acceleration mechanisms which would not otherwise be possible with a near-IR laser; it is currently challenging to make gas systems which can deliver the required pressures to achieve over-critical densities for near-IR lasers.

Chapter 2 outlines the theoretical background of plasmas and some of their characteristics. The theory of laser plasma interactions is then presented, along with the relevant mechanisms which can result in ion acceleration from such events.

Chapter 3 describes the experimental parameters relevant to results presented in this thesis. The concepts behind the design and operation of a high power CO_2 laser are given. Gas targets are described, with emphasis on the shaping of their density profile with a collisional shock wave. Optical and ion diagnostic collection and analysis techniques are also outlined.

Chapter 4 presents proton acceleration results in a near-critical density plasma, demonstrating superior peak proton energies over those previously achieved at the ATF. A very good agreement with the theoretical energy scaling laws was also observed, strongly indicating hole-boring radiation pressure acceleration is the source of these peaked proton beams.

Chapter 5 again details proton acceleration from near-critical density plasmas, although at lower intensities and for longer laser pulse durations. The results demonstrated higher than expected proton energies. This is explained using particle-in-cell simulations which demonstrate the formation of a plasma grating structure and subsequent acceleration off these structures.

Chapter 6 concerns results from experiments aimed at creating thin gas targets from colliding shocks. Results showed a dependence on the maximum observed proton energy with the expansion radius, with optimal conditions found for the case of these colliding shocks.

Chapter 7 summarises the work in this thesis, then gives an outlook to future avenues relevant to the results presented.

2 Theory

2.1 Plasmas

A plasma is a medium composed of an electron and ion fluid. A formal definition is given in Chen [78] as:

> "... a quasi-neutral gas of charged and neutral particles which exhibits collective behavior."

Here, collective behaviour describes the way a change in plasma properties in a given region will affect the plasma as a whole [79]. Consider a plasma in which a group of particles is displaced by a force. This displacement will be felt by the whole plasma through the transfer of energy mediated by collisions. Concurrently, the particles are charged and as such, a net movement of ions or electrons leads to a charge imbalance; any net charge difference between two regions results in an electric field. The movement of charged particles also gives rise to current flow in the plasma and induces magnetic fields. These electric and magnetic fields affect the motion of charged particles within the plasma; this characteristic length scale is given by the Debye length, the distance over which fields are effectively screened (see equation 2.2). Hence, collective behaviour depends not only on local plasma conditions but on the whole system.

In the case of laser plasma interactions, a plasma is formed via induced ionisation of a material. At the front surface of the target, this is caused either through collisions or by the associated electric field of the leading edge of the laser pulse, while in the bulk of the target there are more complex mechanisms at work (see section 2.3.2). The plasma will have electron and ion densities, n_e, and n_i, respectively, where $n_e \approx Zn_i$. The electrons within the plasma have a much lower mass than the ions and as such, respond much faster. This leads to the assumption that the electrons are the dominant species to be accounted for when considering the interaction between a laser pulse and a plasma.

2.1.1 The Debye Length

For a more rigorous description of a plasma. To do this, it is pertinent to consider the various involved length, time and velocity scales. Consider the characteristic length scale, called the Debye length.

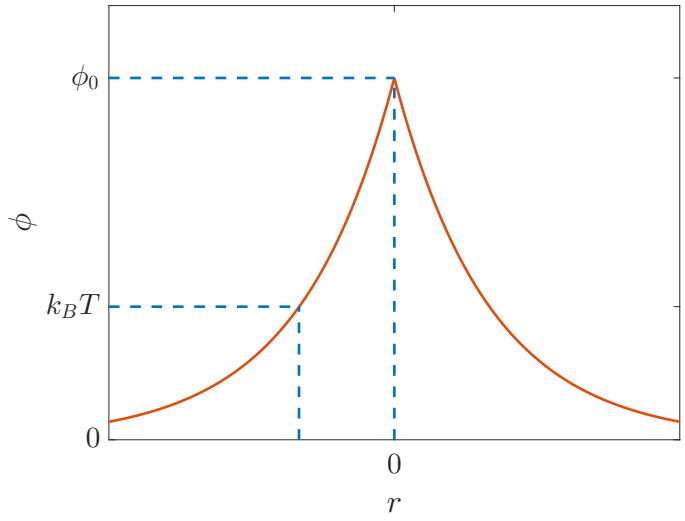


Figure 2.1: The electric potential profile around a test charge in a plasma centred at $r = 0$. The field of the test charge is surrounded by oppositely charged plasma particles over the characteristic length scale, the Debye length.

The Debye length describes the response of a plasma to an external charge placed in it. If a test charge is placed into the plasma, oppositely charged particles from the plasma would move to form a volume around the charge to minimise the potential energy of the system. For a cold plasma the shielding would be perfect and no field would exist beyond the edge of the volume formed by the responding charges.

For a finite temperature plasma, the responding particles have a thermal energy that allows those at the edge of the volume to escape the potential of the test charge. The point at which a responding particle's kinetic energy is equal to the potential experienced from the test charge is known as the Debye length. It is the distance over which the electric field from a source is shielded to $1/e$ of its original value through 'Debye Shielding' and an example of collective behaviour in a plasma.

The potential of the volume occupied by the shielding particles around a test charge can be expressed as

$$\phi = \phi_0 e^{-\frac{r}{\lambda_D}} \tag{2.1}$$

where λ_D is the Debye length, given as

$$\lambda_D = \left(\frac{\epsilon_0 k_B T_e}{n_0 e^2} \right)^{\frac{1}{2}} \tag{2.2}$$

A full derivation of the Debye length is given in appendix A, with typical values given in table 2.1. Associated with the Debye length is a parameter called the Debye Number, N_D. This is defined as the number of electrons in a Debye Sphere (a sphere of radius

Plasma	Density [m^{-3}]	Temperature [eV]	Debye Length [m]
Interstellar Medium	10^5	1	10
Solar Core	10^{32}	1000	10^{-11}
Solid Target Experiment, $a_0 = 10$	10^{29}	10^6	10^{-8}
Gas Target Experiment, $a_0 = 1$	10^{25}	10^5	10^{-7}

Table 2.1: Typical values of the Debye length.

equal to the Debye Length).

$$N_D = \frac{4\pi}{3}{\lambda_D}^3 n_e \tag{2.3}$$

The Debye Number suggests whether Debye Shielding occurs, with $N_D \gg 1$ signifying a plasma. This is because a significant number of particles are required for effective shielding. Similarly, a large Debye Number is a condition of quasi-neutrality, since the larger the number of particles, the less significant small local perturbations become.

2.1.2 Plasma Frequency

The previous section considered the relatively localised displacement of electrons due to a test charge being placed in the plasma. The next step is to consider a much larger scale displacement. Consider the displacement of a single electron within the plasma. When displaced, the electron will experience a restoring force due to space-charge fields being created by the breaking of the quasi-neutrality. This restoring force will cause the electron to return to its original position and, due to the conservation of momentum, overshoot; the particle oscillates about its initial position. The frequency of these oscillations is called the plasma frequency, ω_p.

The electron plasma frequency provides a measure of the response of plasma electrons to an external stimulus and is given by

$$\omega_{p_e} = \left(\frac{n_e e^2}{m_e \epsilon_0}\right)^{\frac{1}{2}} \tag{2.4}$$

The Plasma Frequency and Debye Length

The plasma frequency is similar to the Debye length in that it describes the quasi-neutrality in the plasma. The difference is that the plasma frequency considers time scales, while the Debye length is concerned with length scales. As such, it can be said that for length scales, l, and time scales, τ, with $l \gg \lambda_D$ and $\tau \gg \frac{1}{\omega_p}$, the plasma is quasi-neutral. For $l \ll \lambda_D$ and $\tau \ll \frac{1}{\omega_p}$ charge imbalances can occur.

Given the two parameters represent time and length scales, they can be used to obtain a characteristic velocity scale. This is termed the thermal velocity of the electrons, v_{th},

the distance an electron travels in one plasma period.

$$\omega_p \lambda_D = v_{th} = \left(\frac{k_B T_e}{m_e} \right)^{\frac{1}{2}} \tag{2.5}$$

2.1.3 The Dispersion Relation

Maxwell's equations for time varying electric and magnetic fields are given by Faraday's and Ampère's laws

$$\vec{\nabla} \times \vec{E} = -\frac{\partial \vec{B}}{\partial t} \tag{2.6a}$$

$$\vec{\nabla} \times \vec{B} = \mu_0 \vec{j} + \mu_0 \epsilon_0 \frac{\partial \vec{E}}{\partial t} \tag{2.6b}$$

For a propagating electromagnetic wave, assuming the ion motion is negligible relative to that of the electrons, for a collisionless plasma $\vec{j} = e n_e \vec{v_e}$ is the displacement current and $\vec{v_e}$ is the electron velocity. Taking the time derivative of equation 2.6b and through substitution one obtains

$$\vec{\nabla}(\vec{\nabla} \cdot \vec{E}) - \nabla^2 \vec{E} = -\frac{\omega^2}{c^2} \epsilon \vec{E} \tag{2.7}$$

Assuming $\vec{\nabla} \cdot \vec{E} = 0$, or, in other words, the plasma reacts sufficiently fast to remain quasi-neutral, one obtains the dispersion relation for a plasma

$$\omega^2 = c^2 k^2 + \omega_p^2 \tag{2.8}$$

where k is the wavenumber, i.e.

$$k = \frac{\omega}{c} \left(1 - \frac{\omega_{p_e}^2}{\omega^2} \right)^{\frac{1}{2}} \tag{2.9}$$

The dispersion relation describes the electromagnetic modes which can be supported within the plasma. It can be readily modified to consider more complex plasmas, for example with $T_e \neq 0$, $B \neq 0$, etc. For the case of $\omega > \omega_{p_e}$, an electromagnetic wave can propagate the plasma. Conversely, in the limit $\omega \ll \omega_{p_e}$, the plasma electrons respond sufficiently fast and their number is great enough to prevent the propagation of an electromagnetic wave. In this case, the plasma is termed over-critical.

When $\omega = \omega_{p_e}$, the critical density is reached, the point at which the an electromagnetic wave cannot propagate. Rearranging 2.4, one then obtains the critical density

$$n_c = \frac{\epsilon_0 m_e \omega^2}{e^2} \tag{2.10}$$

The critical density is a measure of the plasma opacity i.e. whether it is over or underdense to an incident laser pulse. When overdense, the plasma is opaque to the incident laser pulse. When underdense, the laser can propagate through the plasma. Therefore, the density of the plasma relative to the critical density determines the interaction of the incident laser with the plasma. This can be extended to the relativistic case, for $a_0 \gg 1$, giving[1]

$$n_c = \langle\gamma\rangle \frac{\epsilon_0 m_e \omega^2}{e^2} \tag{2.11}$$

where $\langle\gamma\rangle$ is given as,

$$\langle\gamma\rangle = \left(1 + \frac{j a_0^2}{2}\right)^{\frac{1}{2}} \tag{2.12}$$

with $j = 1$ and $j = 2$ for linear and circular polarisation, respectively.

The Group and Phase Velocities

Consider the dispersion relation from equation 2.8. Rearranging for the refractive index, η

$$\eta = \frac{ck}{\omega} = \left(1 - \frac{\omega_{p_e}^2}{\omega^2}\right)^{\frac{1}{2}}$$

And so the phase velocity, $v_\phi = \frac{\omega}{k}$, is given by

$$v_\phi = \frac{c}{\eta} = c\left(1 - \frac{\omega_{p_e}^2}{\omega^2}\right)^{-\frac{1}{2}} \tag{2.13}$$

Similarly, the group velocity, the rate at which energy is transferred by the plasma wave is given by $v_g = \frac{d\omega}{dk}$. Therefore, the group velocity is

$$v_g = \frac{c^2 k}{\omega} = c\eta = c\left(1 - \frac{\omega_{p_e}^2}{\omega^2}\right)^{\frac{1}{2}} \tag{2.14}$$

Since $\omega_{p_e} < \omega$, the refractive index of the plasma is less than one (i.e. $\eta < 1$). This means that the group velocity is always less than the speed of light, $v_g < c$.

[1] a_0 is the normalised vector potential, see 2.3.1 later for more information

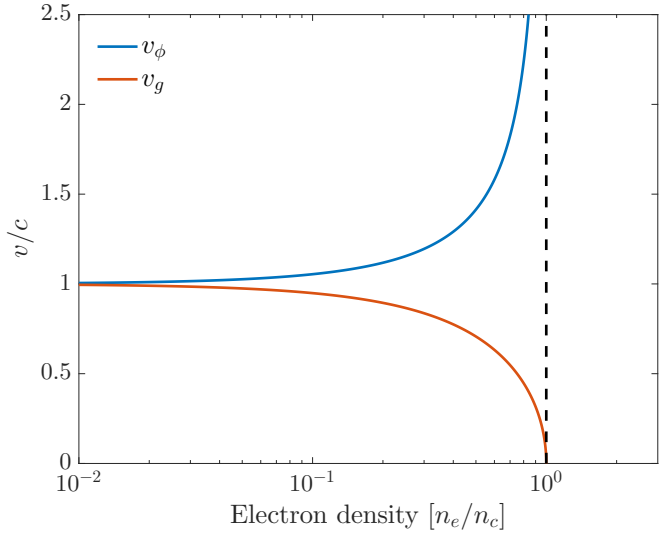


Figure 2.2: The phase and group velocities for a laser within a plasma.

2.1.4 The plasma skin depth

For the case of an incident electromagnetic wave on a plasma-vacuum interface with a step-like density profile, the wave equation can be solved either side of the density step [80]. For an arbitrary incidence angle, θ, the electric field component in the direction of laser propagation, E_z, in the vacuum region takes the form

$$E_z = 2E_0 \sin(kx\cos\theta + \phi) \tag{2.15}$$

In the plasma region, the field profile takes the form of an evanescently decaying wave, with an electric field profile of the form

$$E_z = 2E_0 \frac{\omega}{\omega_{p_e}} \cos\theta \exp\left(-x\frac{\omega_{p_e}}{c}\left[1 - \frac{\omega^2}{\omega_{p_e}^2}\cos^2\theta\right]^{\frac{1}{2}}\right) \tag{2.16}$$

where δ can be defined as the plasma skin depth, which takes the form

$$\delta = \frac{c}{\omega_{p_e}}\left(1 - \frac{\omega^2}{\omega_{p_e}^2}\cos^2\theta\right)^{-\frac{1}{2}} \tag{2.17}$$

In the limit where $n_e \gg n_c$, i.e. $\omega_{\mathrm{p_e}} \gg \omega$, for normal incidence, equation 2.17 reduces to

$$\delta = \frac{c}{\omega_{p_e}} \tag{2.18}$$

The skin depth represents the distance over which a drop of 1/e in the electric field

amplitude is observed. For an overcritical density plasma, the effects of an external electric field are effectively screened beyond the skin depth.

2.1.5 Electromagnetic wave propagation up a density ramp

Consider a plane wave normally incident on an inhomogeneous plasma, propagating in the z-direction. The wave equation for the electric field takes the form

$$\frac{d^2E}{dz^2} + \frac{\omega^2}{c^2}\epsilon\left(\omega, z\right)E = 0 \tag{2.19}$$

For a linear density ramp, the density can be given in the form $n = n_c z/L$, where n_c is the relativistically correct critical density (see equation 2.11) and L the position of the critical surface. The wave equation can then be represented in the form

$$\frac{d^2E}{dz^2} + \frac{\omega^2}{c^2}\left(1 - \frac{z}{L}\right)E = 0 \tag{2.20}$$

Through a change in variables to $\zeta = (\omega^2/c^2L)^{1/3}(z - L)$, the wave equation reduces to [81]

$$\frac{d^2E}{d\zeta^2} - \zeta E = 0 \tag{2.21}$$

Second order differential equations of this type have a general solution of the form

$$E(\zeta) = \alpha A_i(\zeta) + \beta B_i(\zeta) \tag{2.22}$$

where $A_i(\zeta)$ and $B_i(\zeta)$ are the Airy functions of the first and second kind, while α and β are constants dependent on the boundary conditions of the solution. From physical intuition the solution for E can be expected to take the form of a standing wave for $\zeta < 0$ in the linear ramp preceding the point where $n = \gamma n_c$, the critical surface. This arises given reflection of the incident wave can be expected off the critical surface; the incident and reflected components can be expected to interfere with each other, forming a standing wave. Such intuition justifies why the standing wave equation is used.

The solution is an exponentially decaying function for $\zeta < 0$. Since $B_i(\zeta) \to \infty$ as $\zeta \to \infty$, it is possible to choose $\beta = 0$ [82]. The solution therefore takes the form shown in figure 2.3.

Wavelength swelling is observed as the electromagnetic wave propagates up the density ramp. As the wave propagates up the density ramp, $k \to 0$, so the electric field amplitude must increase and so must the wavelength of the electromagnetic wave.

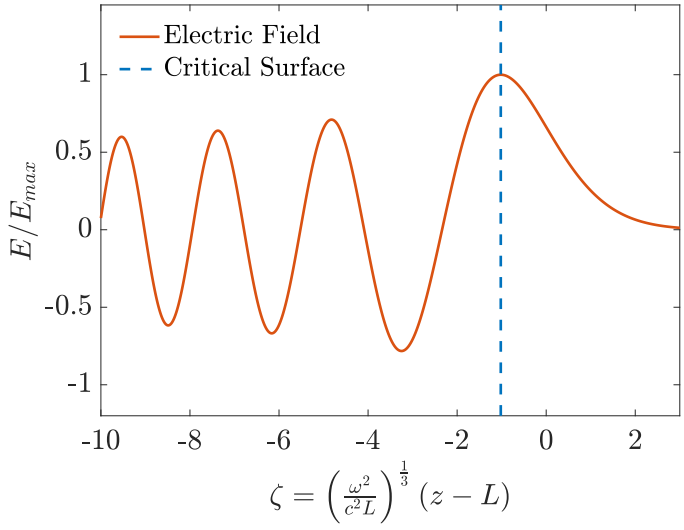


Figure 2.3: The electric field profile in a linear density ramp. The profile is the form of a standing wave exhibiting wavelength swelling preceding the critical surface. Behind the critical surface, the wave decays exponentially.

2.2 Acoustic and Collisionless Electrostatic Ion Waves

2.2.1 Ion acoustic waves

One of the most basic waves that can propagate in a plasma is an ion acoustic wave. The dispersion relation for an ion acoustic wave is given as

$$\omega^2 = k^2 \left(\frac{Z k_B T_e}{m_i} \frac{1}{1 + k^2 {\lambda_D}^2} + \frac{\gamma k_B T_i}{m_i} \right) \tag{2.23}$$

For $k\lambda_D \ll 1$, the ion acoustic wave wavelength is much longer than the Debye length, and the $1/(1 + k^2{\lambda_D}^2)$ term can be ignored. At high wavenumbers, the term dominates; it is a measure of whether the plasma can be considered quasi-neutral. In this case the dispersion relation becomes $\omega_{p_i}^2 = (Z^2 n_{i_0} e^2)/(\epsilon_0 m_i)$, and the ion plasma frequency can be expressed as

$$\omega_{p_i} = \left(\frac{Z^2 n_{i_0} e^2}{\epsilon_0 m_i} \right)^{\frac{1}{2}} \tag{2.24}$$

For the limit of $T_e \gg T_i$ and $k\lambda_D \ll 1$, the phase velocity of the wave, also known as the plasma sound speed, c_s, is given as

$$v_\phi = c_s = \left(\frac{Z k_B T_e}{m_i} \right)^{\frac{1}{2}} \tag{2.25}$$

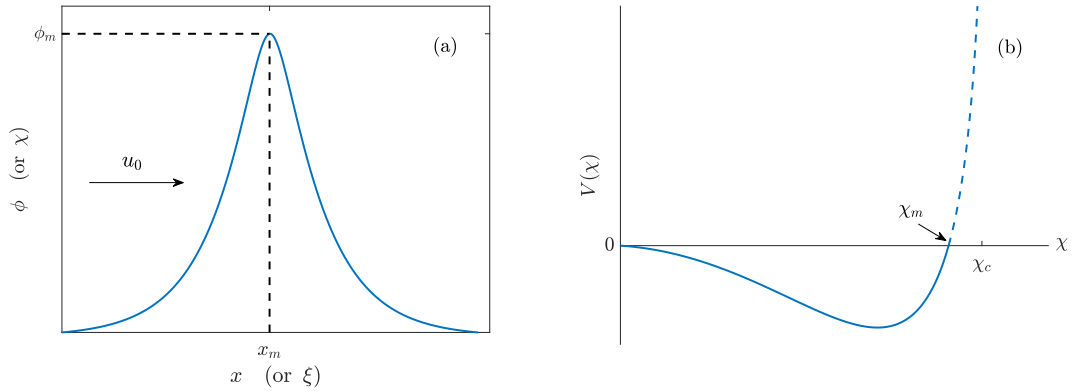


Figure 2.4: (a) the potential profile of a soliton moving through a plasma from right to left and (b) the pseudo-potential, known as the "Sagdeev Potential", for a soliton with Mach number 1.3.

2.2.2 Solitons

Consider the continuity equation for an electron-ion plasma as given by

$$\frac{\partial n_j}{\partial t} + \vec{\nabla} \cdot (n_j \vec{u_j}) = 0 \tag{2.26}$$

where j denotes the particle species, $n_j(\vec{r}, t)$ is the charge density and $u_j(\vec{r}, t)$ the fluid velocity. Also recall the fluid equation of motion

$$\rho_j \frac{d\vec{u_j}}{dt} = -\vec{\nabla} \cdot \underline{\underline{P_j}} + n_j q_j \left(\vec{E} + \left[\vec{u_j} \times \vec{B} \right] \right) + \mu \tag{2.27}$$

where all symbols have the same meaning, with $\underline{\underline{P_j}}$ the pressure tensor and μ the friction term. For simplicity, these can be simplified to a one-dimensional form. Make the assumptions that there is no viscosity in 1D so that all off elements in the pressure tensor go to zero and $\vec{\nabla} \cdot \underline{\underline{P_j}} = \vec{\nabla} p_j$, there is no friction and no magnetic fields. This gives

$$\frac{\partial n_j}{\partial t} + \frac{\partial}{\partial x} (n_j \vec{u_j}) = 0 \tag{2.28}$$

$$\frac{\partial \vec{u_j}}{\partial t} + \vec{u_j} \cdot \frac{\partial \vec{u_j}}{\partial x} = -\frac{1}{m_j n_j} \frac{\partial \vec{p_j}}{\partial x} + \frac{q_i}{m_j} \vec{E_x} \tag{2.29}$$

Finally, let us assume the electrons within the plasma are Maxwellian, resulting in their density, assuming a Boltzmann distribution, taking the form

$$n_e = n_{e_0} e^{\frac{e\phi}{k_B T_e}} \tag{2.30}$$

Consider the potential profile in figure 2.4(a). The wave is travelling from right to left at a velocity $-u_0$. In the wave's frame of reference, the potential appears stationary with plasma streaming towards it with velocity u_0. We assume a cold ion plasma, $T_i = 0$ and that all ions are incident with the same velocity. Furthermore, if the shock moves at a velocity much slower than thermal velocity of the electrons, the shock contribution (centre shift) to the Maxwellian velocity distribution can be ignored. These conditions result in a solution for a stationary shock. In the isothermal limit equation 2.29 becomes

$$u_j \cdot \frac{\partial u_j}{\partial x} = -\frac{q_i}{m_j} E_x = \frac{m_j}{2} \frac{\partial u_j}{\partial x} \tag{2.31}$$

Through integration one obtains the ion velocity within the shock as a function of the upstream velocity.

$$u = \left({u_0}^2 - \frac{2e\phi}{m_i} \right)^{\frac{1}{2}} \tag{2.32}$$

This is just energy conservation of the up and downstream kinetic energies and potential of the shock, i.e. $\frac{\mathrm{m_i u^2}}{2} = \frac{\mathrm{m_i {u_0}^2}}{2} - \mathrm{e}\phi$.

Similarly, for $Z = 1$ such that $n_{i_0} = n_{e_0} = n_0$ the continuity equation, 2.28, in the wave frame becomes

$$\frac{\partial}{\partial x} \left(n_i v_i \right) = 0 \tag{2.33}$$

This yields $n_i u_i = n_{i_0} u_{i_0}$. Finally, through substitution with equation 2.32, the density of ions within the wave can be expressed in terms of the upstream quantities as

$$n_i = \frac{n_0 u_0}{u_i} = n_0 \left(1 - \frac{2e\phi}{m_i {u_0}^2} \right)^{-\frac{1}{2}} \tag{2.34}$$

Poisson's equation then yields

$$\frac{\partial^2 \phi}{\partial x^2} = \frac{e}{\epsilon_0} \left(n_e - n_i \right) \tag{2.35a}$$

$$= \frac{e n_0}{\epsilon_0} \left[e^{\frac{e\phi}{k_B T_e}} - \left(1 - \frac{2e\phi}{m_i {u_0}^2} \right)^{-\frac{1}{2}} \right] \tag{2.35b}$$

Now let us introduce the dimensionless variables

$$\chi \equiv \frac{e\phi}{k_B T_e} \tag{2.36a}$$

$$\xi \equiv \frac{x}{\lambda_D} = x\left(\frac{n_0 e^2}{\epsilon_0 k_B T_e}\right)^{\frac{1}{2}} \tag{2.36b}$$

$$M \equiv \frac{u_0}{(k_B T_e/m_i)^{\frac{1}{2}}} = \frac{u_0}{c_s} \tag{2.36c}$$

where c_s is the plasma sound speed. It is possible to re-express equation 2.35b in terms of these dimensionless quantities, yielding

$$\frac{d^2\chi}{d\xi^2} = e^{\chi} - \left(1 - \frac{2\chi}{M^2}\right)^{-\frac{1}{2}} \equiv -\frac{dV(\chi)}{d\chi} \tag{2.37}$$

The benefit of expressing Poisson's equation in terms of these dimensionless parameters was recognised by Sagdeev [83]. Equation 2.37 takes a form analogous to that of an oscillator in a potential well, i.e. the displacement, x, of an oscillator subjected to a force $-\mathrm{d}V(x)/\mathrm{d}x$ is given by $\mathrm{d}^2x/\mathrm{d}t^2 = -\mathrm{d}V/\mathrm{d}x$. Sagdeev realised by equating the right hand side of equation 2.37 to $\mathrm{d}V/\mathrm{d}\chi$, the analogy applies with the potential, χ, playing the role of x and $\mathrm{d}/\mathrm{d}\xi$ replacing $\mathrm{d}/\mathrm{d}t$. $V(\chi)$ is the quasi-potential termed the "Sagdeev Potential", obtained through integration of equation 2.37 with the boundary condition $V(\chi) = 0$ at $\chi = 0$

$$V(\chi) = 1 - e^{\chi} + M^2\left[1 - \left[1 - \frac{2\chi}{M^2}\right]^{\frac{1}{2}}\right] \tag{2.38}$$

which can be plotted as shown in figure 2.4(b) for a given Mach number. Assuming no dissipation, a quasi-particle will move from $\chi = 0$ to positive χ before returning to its initial potential. This is the behaviour of a soliton [84], a potential and density perturbation as depicted in figure 2.4. After the passing of the soliton, the medium is restored to its initial state.

These soliton-like solutions can only exist for a range of Mach numbers, imposed by restrictions to the possible values that can be assumed by the Sagdeev Potential. Three cases are shown in figure 2.5. The lower limit arises due to the condition of a potential well. This requires $\chi \ll 1$, or equivalently $e\phi >> k_B T_e$. This yields the lower limit

$$M > 1 \tag{2.39}$$

The upper limit comes from recognising that V(χ) must cross the χ axis for $\chi > 0$, otherwise a particle cannot be trapped and the potential would rise indefinitely. One

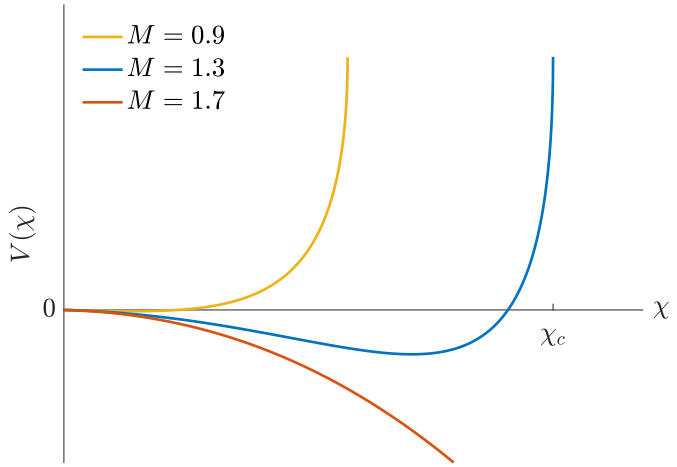


Figure 2.5: The Sagdeev potential for three different Mach numbers, highlighting that soliton solutions can only exist for $1 < M < 1.6$. For $M < 1$ no potential well is formed, while for $M > 1.6$ no particle can be trapped and the potential rises indefinitely.

can rewrite the Sagdeev Potential as

$$e^{\chi} - 1 < M^2 \left[1 - \left[1 - \frac{2\chi}{M^2} \right]^{\frac{1}{2}} \right] \tag{2.40}$$

Here, the left hand side of the equality represents the electron density integral from $0 \rightarrow \chi$ and the right hand side the equivalent ion density integral. The electron density will initially be greater than the ion density before they slowly equilibrate towards the limit $\chi = M^2/2$. This limit is imposed by the root within equation 2.38, which for χ values above this limit becomes imaginary. Physically, this implies $e\phi > m_i {u_0}^2/2$ or, qualitatively speaking, above this limit ions would be excluded from the downstream region and reflected off the soliton. Inserting this limit for χ into the Sagdeev Potential gives the upper limit,

$$M < 1.6 \tag{2.41}$$

Hence, for a cold ion plasma the critical Mach number can take any value within $1 < M < 1.6$. With the condition that for the potential $e\phi < m_i {u_0}^2/2$ ion reflection cannot occur, this allows us to define the critical potential, ϕ_c, above which ion reflection can occur. The critical potential is found to be

$$\phi_c = \frac{m_i {u_0}^2}{2e} \tag{2.42}$$

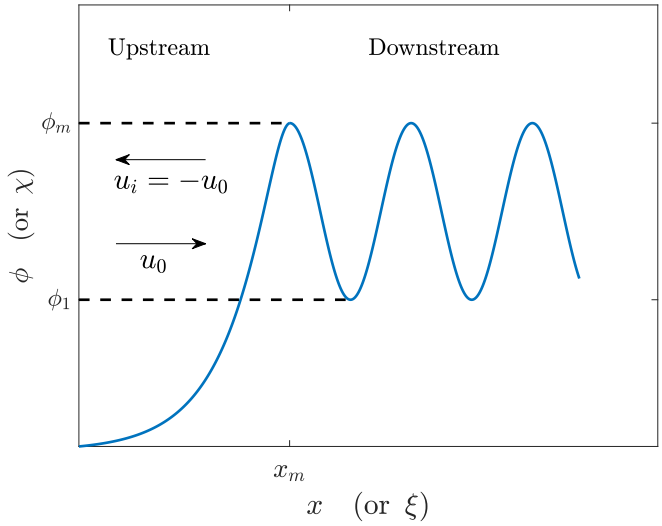


Figure 2.6: The potential profile of a collisionless shock. The potential rises to a maximum value, ϕ_m, before oscillating in the downstream region between ϕ_m and ϕ_1. Particle reflection off the shock will result in ions propagating with the opposite velocity to the incident upstream plasma, $-u_0$, in the shock frame.

2.2.3 Collisionless electrostatic shocks

The previous section considered the case where particles experience no loss of energy as the shock propagates. Let us return to the analogy of an oscillator in a potential well but now consider the case where the particle loses energy. In this case, the particle will not return to $x = 0$ but instead oscillate around some positive value of x. This also applies to a particle within the shock; if energy is lost, particles can become trapped within the shock structure, oscillating between two, non-zero values of $V(\chi)$. In this case, the shock takes on the form as shown in figure 2.6.

This phenomenon occurs due to symmetry breaking introduced by the inclusion of particle trapping within the shock. Alternatively, particle reflection off the shock front breaks the symmetry through modification of the upstream plasma conditions, leading to a wavetrain solution as shown in figure 2.6.

Now assume the ions have a small but finite, non-zero temperature distribution so that $T_i \neq 0$; $T_i << T_e$. It is now conceivable to have a situation of partial reflection of ions off the shock front. This can be used to give a modified upstream ion density profile which, when combined with Poisson's equation, can be used to find a new, modified Sagdeev Potential for a collisionless shock as demonstrated by Moiseev and Sagdeev [85]. Through the introduction of a parameter, $F(\phi)$, which quantifies the fraction of ions reflected off the shock front as a function of the shock potential, the modified upstream ion density, ${n_{i_0}}'(\phi)$, can be written as

$$n_{i_0}{}'(\phi) = (1 - F(\phi))n_{i_0} + 2n_{i_0}F(\phi) \tag{2.43}$$

It is then possible to modify equation 2.35b with two terms

$$-\frac{en_0F(\phi)}{\epsilon_0\left(1-\frac{2e\phi}{m_i{u_0}^2}\right)^{\frac{1}{2}}} \tag{2.44a}$$

$$\frac{en_0}{\epsilon_0}F(\phi) \tag{2.44b}$$

where equation 2.44a corrects for the subtracted reflected ion component from the total number of transmitted particles behind the shock, while 2.44b adds the contribution of the reflected ions to the upstream region. One then obtains the modified Poisson's equation for the upstream region

$$\frac{\partial^2\phi}{\partial x^2} = \frac{en_0}{\epsilon_0}\left[(1+F(\phi))e^{\frac{e\phi}{k_BT_e}} - 2F(\phi) - \frac{(1-F(\phi))}{\left(1-\frac{2e\phi}{m_i{u_0}^2}\right)^{\frac{1}{2}}}\right] \tag{2.45}$$

Similarly, the downstream region can be formulated by adjusting the local electron density to match the ion density, giving

$$\frac{\partial^2\phi}{\partial x^2} = \frac{en_0}{\epsilon_0}\left[(1+F(\phi))e^{\frac{e\phi}{k_BT_e}} - \frac{(1-F(\phi))}{\left(1-\frac{2e\phi}{m_i{u_0}^2}\right)^{\frac{1}{2}}}\right] \tag{2.46}$$

For the solution to be valid these solutions must be continuous in ϕ and $\partial\phi/\partial x = V(\chi)$ at x_c, the spatial position of the critical potential.

The solution can be simplified by assuming the reflection coefficient behaves as a step-like function of the form

$$F(\phi) = 0 \quad \text{for} \quad \phi < \phi_c \tag{2.47a}$$

$$F(\phi) = F_{max} \quad \text{for} \quad \phi \geqslant \phi_c \tag{2.47b}$$

It is then possible to form two equations which can be solved independently, as demonstrated in figure 2.7. A particle will initially move from $\phi = 0$ ($\chi = 0$) to $\phi = \phi_m$ ($\chi = \chi_m$). Unlike in the soliton example, energy is lost by the particle and it returns to a new potential, $\phi = \phi_1$. The particle becomes trapped behind the shock, oscillating between ϕ and ϕ_1, giving the wavetrain solution as shown previously in figure

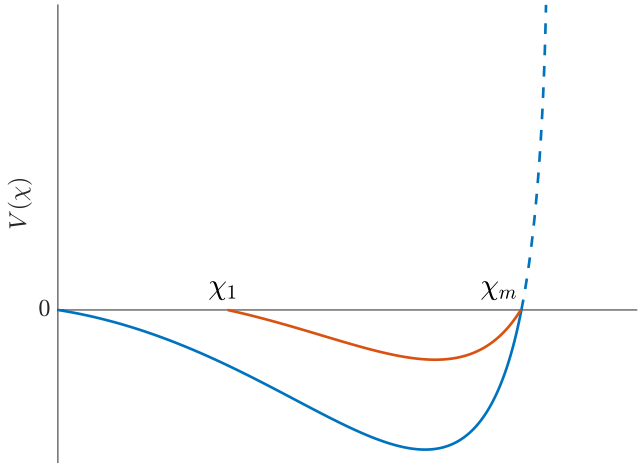


Figure 2.7: The Sagdeev potential for a collisionless shock. The two curves demonstrate the different potentials for particles before and after χ_m. A particle initially follows the classical trajectory for a soliton to χ_m, before then oscillating between this value and χ_1.

2.6. This describes a so-called collisionless shock, a name given since the size of the shock is less than the collisional mean free path of the particles that comprise it. The potential profile is equivalent to that of a soliton up to ϕ_m, before forming a wavetrain solution.

While the previous discussion is useful in describing the difference between shocks and solitons, the assumptions made in the soliton model are not strictly required for shocks. The assumption is made that no consideration for electron reflection off the potential associated with the shock is required. It is reasonable to assume that there exists a regime in which $e\phi \gg k_B T_e$. Physically this means it is possible for electrons to become trapped behind the shock, modifying the electron pressure in the shock. Forslund and Shonk [86] made the assumption of maximum electron trapping behind the shock to modify the electron pressure, resulting in an increased critical Mach number $M \approx 3.1$. This was extended further by Forslund and Freiberg [87] to a critical Mach number of $M = 6.5$. The model developed by Sorasio et al. [88] showed the Mach number increases with the ratio of the upstream to downstream electron temperatures, Θ and densities, γ, with no absolute upper limit.

$$M_{max} \simeq \frac{3\,(\gamma+1)}{\gamma}\sqrt{\frac{\pi\Theta}{8}} \tag{2.48}$$

However, they conclude that for their double layer shock solution to exist the electron pressure must exceed the ion pressure along the shock, while both must be equivalent at the layer boundary. The result of higher critical Mach numbers is in fact intuitive. Decreasing downstream electron temperature decreases the number of trapped electrons,

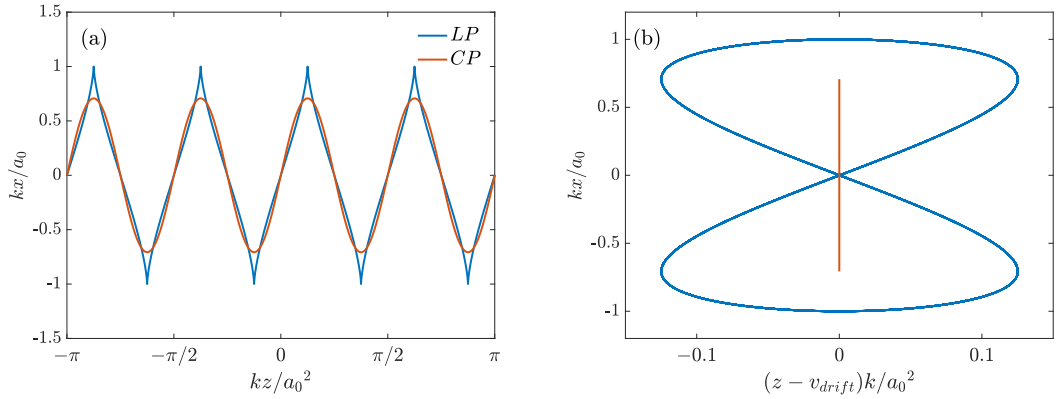


Figure 2.8: Plot of the electron motion in a laser field for linear and circular polarisations in (a) the static x-z plane and (b) the average electron drift frame.

lowering the electron pressure behind the shock; the maximum electrostatic potential increases and high Mach numbers can be supported.

2.3 Laser-Matter Interactions

For laser-plasma based ion acceleration, the interaction of a laser with materials and the directly or otherwise laser induced motion of electrons and ions within the plasma must be considered.

2.3.1 Single Particle Motion

For an incident laser, the electrons within a plasma will respond to the electromagnetic fields which gives particle motion. On the same timescales, ions are unable to respond to these fields due to their increased mass; energy transfer from the laser is typically through electron-ion interactions. Therefore, to understand the mechanisms behind laser-plasma energy absorption and ion acceleration, it is to important to understand electron motion in a laser field. A full treatment of a single particle in an electromagnetic field is given in Appendix C. The components of the electron motion can be shown to be

$$\begin{aligned} x &= \frac{a_0 c}{\omega}(1 - \cos(kz - \omega t)) \\ y &= 0 \\ z &= (\frac{a_0^2 c}{4})t - (\frac{a_0^2 c}{8\omega})\sin 2(kz - \omega t) \end{aligned} \tag{2.49}$$

This result describes the particle motion. The motion of the particle in the x-z plane for linear and circular polarisation is plotted in figure 2.8(a). The particle motion in the

drift frame of the particle is shown in figure 2.8(b). For linear polarisation this takes the form of a figure of eight pattern.

2.3.2 Ionisation Processes

When an intense laser is incident on a material, the initial process of interest is ionisation of the target, predominantly through one of two mechanisms. Both are related to the interaction of the laser's electric field with the atomic electrons.

Multi-photon Ionisation

The first process is multi-photon ionisation. Here, as the name suggests, multiple photons lose their energy to atomic electrons on the front surface of the target, pushing these electrons to higher and higher energy levels until they can escape the atomic potential; the minimum number of photons required is given by the relation $n\hbar\omega_L > \epsilon_i$, where ϵ_i is the ionisation potential. As successive photons are absorbed, the atomic electrons transition through successive short-lived virtual states until they gain sufficient energy to become ionised.

For the case of overdense targets, these so called seed electrons can then be accelerated by the laser field into the target, causing further ionisation. This process occurs through inelastic collisions between electrons. If the scattering is strong enough, or a sufficient number of scattering events occur, the energy required to liberate atomic electrons can be overcome.

A requirement for high density targets comes from the dependence of the collisional cross-section on target density and the inverse dependence on electron temperature. A general relationship for the number of collisionally ionised electrons can be estimated to be of the form $N_{col} = \frac{<k_B T_e>}{\epsilon_i} n_i n_e < v_e \sigma_s >$, where σ_s is the collisional cross section. Other authors have developed methods for estimating the rate of collisional ionisation, most notably Lotz [89]. Lotz developed an expression for the rate of collisional ionisation as

$$\sigma_{coll} = \sum_{i=1}^{N} a_i q_i \frac{\ln\left(E_e/\epsilon_i\right)}{E_e \epsilon_i} \left\{1 - b_i . e.^{-c_i(E_e/\epsilon_i - 1)}\right\} \tag{2.50}$$

where E_e is the energy of the scattering electron, q_i is the number of electrons in the outer shell and a_i, b_i and c_i are constants given by Lotz. This can be similarly represented in the form [90]

$$\sigma_{coll} = n_e \frac{a_i q_i}{\epsilon_i (k_B T_e)^{\frac{1}{2}}} \int_{\epsilon_i/k_B T_e}^{\infty} \frac{e^{-x}}{x} dx \tag{2.51}$$

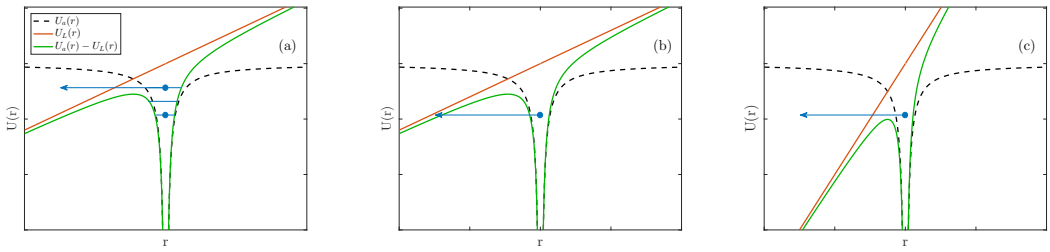


Figure 2.9: Illustration of the field ionisation by barrier suppression. The dashed black line shows the unperturbed atomic potential, the red line is the laser potential and the green line the suppressed atomic potential. (a) shows partial suppression of the barrier, allowing ionisation through multi-photon absorption. (b) shows electron tunnelling through the barrier, made energetically favourable through the barrier suppression; $\gamma_{\mathrm{K}} \simeq 1$. (c) shows full suppression and the electron can escape without tunnelling; $\gamma_{\mathrm{K}} \ll 1$.

Barrier Suppression Ionisation

The second process is called field ionisation by barrier suppression (FIBS) or tunnelling ionisation. It is the result of electrons tunnelling through the Coulomb barrier which is made probabilistically significant through the barrier suppression. This can occur in the intense electric fields of the laser at the front surface of a target, or from a Debye sheath at the target rear. The suppression makes it energetically favourable for tunnelling to occur. Furthermore, if the magnitude of the laser field exceeds that of the Coulomb barrier, it is suppressed to such an extent that the electrons can escape without the need for tunnelling. This process has been modelled by various authors. The ionisation rate for hydrogen like ions, where only a single 1s electron remains, was determined by Keldysh [91] who used a quantum mechanical approach to determine the probability of tunnelling. A more general solution for many-electron ion systems was developed by Ammosov, Delone and Krainov [92], which is given by the so-called ADK ionisation rate, which depends on the configurational quantum numbers of the ion. Experimentally measured ionisation rates for a number of the inert gases at intensities in the range 10^{13}-$10^{18}\,\mathrm{Wcm}^{-2}$ have been compared with the ADK model [93] [94], demonstrating reasonable agreement. However, some deviation from the ADK model occurs for heavier elements at higher charge states.

To characterise the regime in which ionisation occurs, the Keldysh parameter, γ_K, [95] can be used

$$\gamma_K = \left(\frac{\epsilon_i}{2U_p}\right)^{\frac{1}{2}} \tag{2.52}$$

Here, ϵ_i is again the ionisation potential and $U_p = (\sqrt{1+{a_0}^2} - 1)m_e c^2$, the ponderomotive potential. Effectively, the Keldysh parameter is a measure of the ionisation energy compared to the potential energy gained by an unbound electron in the laser electric

field. Put another way, it is the ratio of the electron tunnelling time to the laser period i.e. the time required for a bound atomic electron to tunnel through the Coulomb barrier relative to one laser period. For the condition $\gamma_{\mathrm{K}} \gg 1$, the ionisation potential is much larger than the potential energy that an electron gains within the laser field. Ionisation occurs through a multi-photon absorption process, with successive photons being absorbed. Atomic electrons are excited to ever higher energy states until their energy exceeds that of the bounding potential and ionisation occurs.

For $\gamma_{\mathrm{K}} \ll 1$, it is energetically favourable for electrons to exist in an unbound state, although this is prevented by the atomic potential. The electric field becomes strong enough to at least partially suppress the Coulomb barrier, resulting in an increased probability of electron tunnelling; the tunnelling time of the electron decreases with the suppressed Coulomb potential, allowing tunnelling to occur within a laser period. Barrier suppression ionisation occurs. The ionisation in this case is described by the ADK ionisation rate.

2.3.3 Absorption Mechanisms

Once the target is ionised, the next consideration concerns how laser energy is coupled to the plasma. This is an important area of the interaction physics, since many applications require efficient coupling of the laser energy to the accelerated ions and electrons.

The transfer of energy from an incident laser to a plasma is determined by the intensity, density profile of the plasma, the laser wavelength and the angle of incidence. There are four main mechanisms for energy coupling in near and above critical density plasmas ($n_e \geq n_c$); inverse bremsstrahlung, resonance absorption, vacuum heating and $\vec{J} \times \vec{B}$ heating. Parametric instabilities, or non-linear wave-wave interactions can also occur in a plasma, which provide further mechanisms for energy absorption [78]. Examples include two plasmon decay [82] and stimulated Raman scattering [96] [97]. The four mechanisms can be divided into two subgroups, those at high intensities, above $10^{18}\,\mathrm{Wcm}^{-2}$ and those below this intensity, respectively. At moderate intensities, inverse bremsstrahlung and resonance absorption are dominant. At high intensities, the main energy transfer occurs via vacuum heating and $\vec{J} \times \vec{B}$ heating.

Inverse Bremsstrahlung

Inverse bremsstrahlung is similar to the ionisation mechanism mentioned earlier (see 2.3.2). However, the energy deposited instead heats the plasma. Electrons are accelerated by the oscillating laser electric field, before losing their energy through collisions with the plasma ions. The electron-ion collision frequency is given by [98]

$$\nu_{ei} = \frac{1}{3(2\pi)^{3/2}} \frac{n_e Z e^4 \ln\Lambda}{{\epsilon_0}^2 {m_e}^{1/2} (k_B T_e\,[\mathrm{K}])^{3/2}} \approx \frac{2.9 \times 10^{-12} Z n_e\,[\mathrm{m}^{-3}]}{(T_e\,[\mathrm{eV}])^{3/2}}, \tag{2.53}$$

where n_e is the plasma electron density, T_e is the electron temperature, k_B is the Boltzmann constant, Z is the atomic number and $\ln\Lambda$ is the Coulomb logarithm. Inverse bremsstrahlung is efficient in long density scale lengths and at low temperatures. The energy and density requirements therefore limit the intensity range at which the mechanism is relevant to intensities of the order $10^{12}\,\mathrm{Wcm^{-2}} \rightarrow 10^{15}\,\mathrm{Wcm^{-2}}$.

Resonance Absorption

Resonance absorption is the second relevant mechanism at moderate intensities. Unlike inverse bremsstrahlung, it occurs solely at the critical surface. In this case, the energy in the laser is coupled into plasma waves. Unlike inverse bremsstrahlung, it is a collisionless mechanism [80]. Consider the case of a plane p-polarised laser incident on an overdense plasma at an angle $\phi \neq 0$. Here, a component of the electric field of the laser acts in the direction normal to the target. The exponential decay of the electric field has a finite distance, the skin depth (see equation 2.18). Since there exists a component of the electric field which causes electron oscillations in the direction of the target normal, $\vec{E} \cdot \vec{\nabla} n_e \neq 0$; charge density fluctuations are induced. The density perturbations can become resonant in the plasma at the critical surface with the condition $\omega_p = \omega_L$. The induced plasma wave can grow over a number of laser periods and deposit energy in the bulk of the plasma through collisions or, at high intensities via wave breaking [82]. The energy deposition creates hot electrons; these are electrons with a higher energy than the bulk temperature. The electron temperature for resonance absorption has been shown to scale as $T_e \propto I^{\frac{1}{3}} t^{\frac{1}{6}}$ [99], giving electron temperatures of $100'\mathrm{s\,eV}$ at the critical surface after only 10 fs for an intensity of $\mathrm{I} = 10^{15}\,\mathrm{Wcm^{-2}}$. Note that in the plane wave approximation, s-polarised light incident on the plasma cannot create a density perturbation (plasma wave) at the critical surface and there is no resonance.

The requirement of a component of the laser field pointing into the target leads to an angular dependence. It has been shown that enhanced absorption is possible for deformed target surfaces [100] [101]. Denisov [102] showed a self-similar dependence of the absorption on the angle for targets with long density scale lengths. The mechanism in fact cannot be supported for very sharp density scales [80]. Consider the field amplitude of a resonantly driven plasma wave at the critical surface for a slab. There will be little field swelling due to the propagation of the laser in a density gradient (see section 2.1.5) and the amplitude of the plasma wave will be of the order of the laser field amplitude, $x_p \simeq eE_L/m_e\omega_L^2 = v_{os}/\omega_L$. Since the resonance cannot be sustained if the amplitude becomes greater than the density scale length (which tends to zero for a step density gradient) the mechanism cannot occur.

Vacuum Heating

In the relativistic intensity regime ($a_0 > 1$), heating can occur through Vacuum or Brunel heating [103]. First, consider a relativistic ($\mathrm{I} > 10^{18}\,\mathrm{Wcm}^{-2}$) p-polarised laser pulse incident at an angle ϕ on a plasma. For an overcritical plasma slab the laser cannot penetrate beyond its skin depth ($\sim c/\omega_p$). However, as electrons reach the target edge they will directly experience the laser field. Assuming their arrival coincides with the correct period of the laser cycle, the electron is accelerated from the target into the vacuum beyond the thermal Debye sheath, $\lambda_D = v_{th}/\omega_p$. As the field polarity reverses the electron is accelerated back towards the target. For relativistic intensities, the field strength is such that the electron can penetrate the target to a distance exceeding the skin depth; the laser field is completely screened and the electron experiences only half the laser cycle. With no decelerating force from the laser, the electron is free to ballistically traverse the target. Since the laser pulse repeats this process every cycle, the effect is that bunches of electrons are accelerated into the target at the frequency of the incident laser pulse, ω_L.

A variation on vacuum heating comes in the form of the anomalous skin effect. Here, as in vacuum heating, electrons within the skin depth oscillate with the laser field, depositing energy and thermalising through collisions. For the case of the anomalous skin effect, the electrons gain sufficient energy within the field that their mean free path exceeds the skin depth, i.e. $\lambda_{mfp} > l_s = v_{th}/\omega$. As such, the laser heats an increased volume of the target, with an effective skin depth, l_α given as [104]

$$l_\alpha \simeq \left(\frac{c^2 v_{th}}{\omega_L {\omega_{p_e}}^2}\right)^{\frac{1}{3}} \tag{2.54}$$

$\vec{J} \times \vec{B}$ Heating

At high intensities, electron motion becomes relativistic and the $\vec{v} \times \vec{B}$ component of the Lorentz force becomes comparable with the electric field contribution to the electron motion. The oscillating laser field accelerates electrons at the target surface into the overdense bulk plasma. The mechanism is physically similar to vacuum heating given electrons are directly accelerated by the laser field. Consider the Lorentz force equation

$$\vec{F}_L = e(\vec{E} + [\vec{v} \times \vec{B}]) \tag{2.55}$$

The primary driving force is the $\vec{v} \times \vec{B}$ component, which causes the electrons to oscillate at twice the laser frequency, i.e. $\omega = 2\omega_\mathrm{L}$ [105]. This allows some of the electrons to gain enough kinetic energy to escape the laser field and propagate into the overdense plasma along the laser axis.

$\vec{J} \times \vec{B}$ heating becomes significant at relativistic electron quiver velocities with the absorption fraction increasing with laser intensity [106]. Hence, $\vec{J} \times \vec{B}$ absorption has been shown to be a highly efficient method of energy conversion for intensities above $10^{18}\,\mathrm{Wcm}^{-2}$. For example, it was shown that for intensities of $10^{20}\,\mathrm{Wcm}^{-2}$ at 6° incidence, 60% laser absorption can be achieved [107].

The dominant mechanism at high intensities is dependent on both the magnitude of the $\vec{v} \times \vec{B}$ term compared with the laser electric field normal to the target surface and the plasma scale length on the target front surface. As such, $\vec{J} \times \vec{B}$ heating is the dominant mechanism at (near) normal incidence. However, it can be suppressed by using circularly polarised laser light.

2.3.4 Ponderomotive Acceleration

Traditional methods for deriving the non-relativistic ponderomotive force make the assumption that the electron quiver motion in an applied electric field is much less than the speed of light. For more information on this see for example [78] or [80]. This gives the result

$$\vec{f_p} = -\frac{e^2}{2m_e\omega^2}\vec{\nabla}\vec{E}^2 \tag{2.56}$$

However, in the relativistic regime ($a_0 > 1$), one must consider the case when the quiver velocity approaches the speed of light. With this in mind, consider the electron-fluid momentum equation as shown in [108]

$$(\frac{\partial}{\partial t} + \vec{v}\cdot\vec{\nabla})(\gamma\vec{v}) = -(\vec{E} + [\vec{v} \times \vec{B}]) \tag{2.57}$$

where γ is the Lorentz factor. Applying the Coulomb gauge, $\vec{\nabla}\cdot\vec{A} = 0$ [109], the magnetic vector potential can be related to the electric and magnetic fields by

$$\begin{aligned} \vec{E} &= -\frac{\partial\vec{A}}{\partial t} - \vec{\nabla}\phi \\ \vec{B} &= \vec{\nabla} \times \vec{A} \end{aligned} \tag{2.58}$$

Only the electric field relation is changed, with the electric potential going to zero. This can be rationalised if one considers the case of a single electron in a laser field experiencing the ponderomotive force. By applying the Coulomb gauge, one is essentially imposing the condition that the particle is in a vacuum; for a single electron no potential term can exist. Now, consider the vector identity

$$(\vec{v}\cdot\vec{\nabla})(\gamma\vec{v}) = \vec{\nabla}\gamma - \vec{v} \times [\vec{\nabla}(\gamma\vec{v})] \tag{2.59}$$

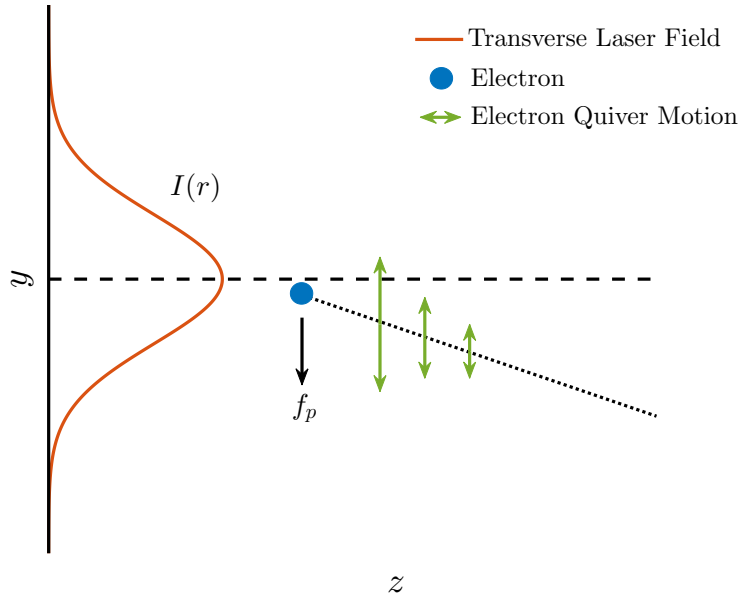


Figure 2.10: Illustration of the ponderomotive force experienced by an electron in a spatially variant intensity profile.

Therefore, the momentum equation (2.57) can be rewritten as

$$\frac{\partial}{\partial t}(\gamma\vec{v} - \vec{A}) = \vec{v} \times [\vec{\nabla} \times (\gamma\vec{v} - \vec{A})] - \vec{\nabla}\gamma \tag{2.60}$$

From this, the relativistic vorticity equation can be expressed as

$$\frac{\partial}{\partial t}[\vec{\nabla} \times (\gamma\vec{v} - \vec{A})] = \vec{\nabla} \times \{\vec{v} \times [\vec{\nabla} \times (\gamma\vec{v} - \vec{A})] - \vec{\nabla}\gamma\} \tag{2.61}$$

For a plasma initially at rest it can be said $[\vec{\nabla} \times (\gamma\vec{v} - \vec{A})] = 0$. The vorticity equation ensures this holds for all time, since the laser itself cannot generate vortices. Therefore, the final momentum equation can be written

$$\frac{\partial}{\partial t}(\gamma\vec{v} - \vec{A}) = -\vec{\nabla}\gamma \tag{2.62}$$

The ponderomotive term on the right hand side of 2.62 is valid for any intensity. The term on the left hand side of equation 2.62 is the canonical momentum. Therefore the interaction of a laser pulse with an electron fluid can be analysed if the continuity equation and Maxwell's equations are used. In the non-relativistic limit, by recognising that as $v \ll c$, a Taylor expansion can be applied to the right hand side of equation 2.62, giving $-\vec{\nabla}\gamma \backsimeq -\vec{\nabla}(1 + \frac{1}{2}\frac{v^2}{c^2} + 0v^4) = -\vec{\nabla}\frac{v^2}{2c^2}$. Recalling $a_0 = \frac{v}{c} = eE_0/m_e\omega_L c$ and substituting, the non-relativistic relation given in equation 2.56 is recovered.

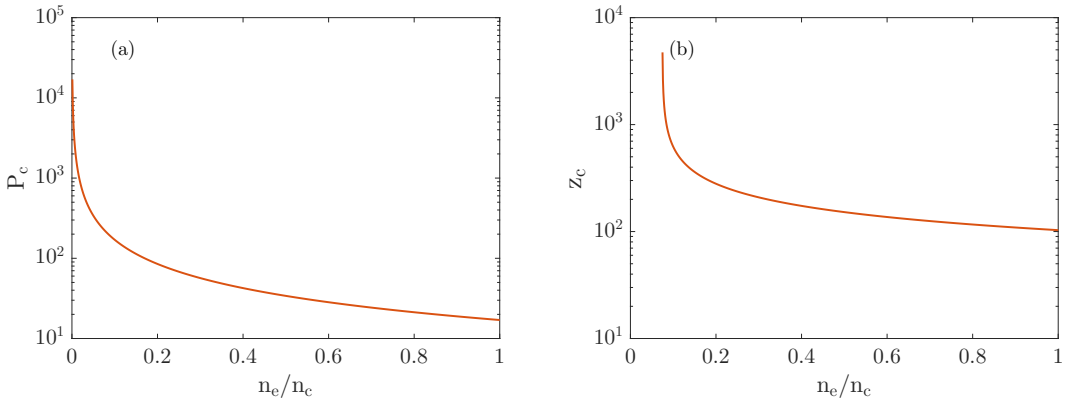


Figure 2.11: Plot to help illustrate self-focussing. (a) the critical power, P_c, which defines the self-focussing regime. (b) the distance over which a 228 GW beam would collapse to zero radius, z_c, given by equation 2.65.

The effect is illustrated in figure 2.10. Electrons oscillate during the laser cycle; the amplitude of this quiver motion is dependent on the laser intensity. The spatially varying field intensity profile results in an asymmetry in the force experienced by the electron, with the restoring force in the second half of the laser cycle reduced. There is a net force away from regions of high intensity, the ponderomotive force.

2.3.5 Laser Self Focussing

Self focussing is the process of an induced change in the local plasma refractive index by a propagating laser pulse. Electrons motion induces a spatial variation of the refractive index, forming an effective "plasma lens" which acts to focus the beam. Self focussing can occur in three manners; through thermal, ponderomotive (see section 2.3.4) or relativistic effects. Thermal and ponderomotive effects result in the expulsion of electrons from regions of high intensity, creating local spatial variations in the refractive index [110]. Relativistic self focussing arises due to a change in the refractive index caused by a reduction in plasma frequency from induced relativistic electron motion in the laser field. This is a third order non-linear process known as the optical Kerr effect, with the refractive index change scaling as E^2 (or equivalently, I_L) [111]. Again, this occurs most strongly on axis, resulting in a focussing effect.

Self-focussing can be characterised by the critical power, P_c, the laser power at which diffraction effects are equivalent to those of self-focussing [80]. This can be expressed as

$$P_c = \frac{4\pi\epsilon_0 m_e^2 c^5 \omega_L^2}{e^2 {\omega_{p_e}}^2} \simeq 17 \left(\frac{\omega_L^2}{\omega_{p_e}^2}\right) [\mathrm{GW}] \tag{2.63}$$

Above this threshold, self focussing effects exceed diffraction effects and the beam radius spatially decreases. This threshold level is represented graphically in figure 2.11(a).

Further, the beam radius, $\langle r^2 \rangle$, can be expressed as a function of the Rayleigh length, z_R, and associated beam waist, σ_0,

$$\langle r^2 \rangle = \sigma_0^2 \left[1 + \frac{z^2}{z_R^2} \left(1 - \frac{P_L}{P_c} \right) \right] \tag{2.64}$$

In the limiting case $P_L > P_c$, an expression can be derived for the distance over which the beam would collapse to zero radius, z_c, in the idealised case of no opposing forces. This is given by

$$z_c = \frac{z_R}{P_L/P_c - 1} \tag{2.65}$$

The relation is plotted in figure 2.11(b). Here a laser with power of 228 GW is used to illustrate equation 2.65. This value is chosen as it equates to the mean laser power of results presented in Chapter 5.

2.4 Ion Acceleration

2.4.1 Sheath Acceleration

For thick targets at intensities $\leqslant 10^{21}\,\mathrm{Wcm^{-2}}$, laser-plasma induced ion acceleration is typically dominated by sheath acceleration, commonly called target normal sheath acceleration [TNSA][2]. The basic interaction process is shown in figure 2.12. The process starts with a high intensity laser pulse interacting with the front surface of the target, near-instantaneously ionising and transferring energy to the electrons as described in sections 2.3.2 and 2.3.3. Hot electrons are generated at the front surface and accelerated into the bulk of the target, causing further ionisation. If sufficiently energetic, these electrons can escape the rear of the target into the vacuum. As the number of electrons leaving the target accumulates, the rear surface of the target becomes positively charged. The electrostatic sheath field can accelerate ions from the surface of the target into the vacuum. The energy and charge of the accelerated ion bunch depends on the sheath profile created by the hot electrons. These electrostatic fields can arise at both the front and rear surface of the target and as such, ion acceleration is possible in both the forward and backwards directions. The fields present can reach of the order $10^{12}\,\mathrm{Vm^{-1}}$ [22] [112].

The question of where the accelerated ions exiting the rear of the target originate has generated much debate. Clark et al. [20] measured protons with peak energies of 18 MeV, emitted from the rear side of the target. The observation of an annular ring structure to the proton beam lead to the suggestion of large magnetic fields induced in

[2] Although this is not strictly metonymically correct

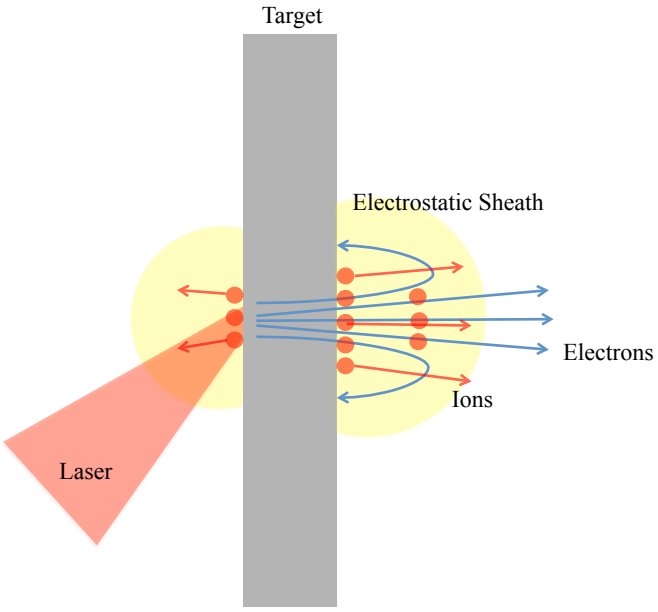


Figure 2.12: Figure depicting the process of sheath acceleration, through the interaction of an intense laser pulse with a solid density foil target.

the target by laser generated fast electrons from the front surface. They argued that this suggests the observed protons were generated at the front surface [113] [114]. Clark et al. [20] also demonstrated ions being emitted backwards from the front surface of the target. They observed proton energies up to 30 MeV. There has been considerable other work by other authors, for example Snavely et al. [21], who have attempted to resolve this issue, but it seems apparent that there is a contribution from both surfaces of the target, as concluded by Zepf et al. [113].

If an electron is not sufficiently energetic to escape the sheath field, it will return to the target; if it has the required kinetic energy it can still escape. Electrons which return to the target can recirculate; becoming trapped between sheath fields formed at the front and rear target surfaces. This acts to increase the hot electron temperature, boosting the sheath fields. The phenomenon is particularly effective in thin targets, where the relatively short transition time across the target facilitates multiple passes. The increased electron temperatures form a stronger sheath, increasing the maximum ion energy [115].

Various authors have attempted to come up with models to describe this acceleration. Mora [116] uses a collisionless model for ions and attempts to predict quantities such as the position and velocity of the ion front. It assumes half the considered space is an electron-ion plasma, with the other half vacuum; the initial density assumes the shape of a step-function. The electron distribution is assumed to be Boltzmann-like. Mora [116] finds an expression for the field at the ion front, which is true at all times, takes the form

$$E_{\text{front}} \backsimeq \frac{2E_0}{\sqrt{2e + \omega_{p_i}^2 t^2}} \tag{2.66}$$

This result also allows for expressions for the velocity and position of the ion front as a function of time to be deduced

$$v_{\text{front}} \backsimeq 2c_s \ln\left(\tau + \sqrt{\tau^2 + 1}\right) \tag{2.67}$$

$$x_{\text{front}} \backsimeq 2\sqrt{2e}\lambda_{D_0}[\tau \ln\left(\tau + \sqrt{\tau^2 + 1}\right) - \sqrt{\tau^2 + 1} + 1] \tag{2.68}$$

where $\tau = \frac{\omega_{p_i} t}{\sqrt{2e}}$. By taking equation 2.67 in the limit $\omega_{p_i} \gg 1$, the cut-off energy of the ion spectrum, the maximum ion energy, can be obtained

$$E_{\text{max}} \backsimeq 2Zk_B T_e[\ln\left(\tau + \sqrt{\tau^2 + 1}\right)]^2 \tag{2.69}$$

Mora went a step further and further expanded the model with an adiabatic expansion which resulted in an analogous scaling law which depends on the target thickness [117].

While this model demonstrated some agreement with experimental and simulation results, it is limited in practicality due to the assumptions made. Firstly, the model takes the ion density to be $n_i = n_e/q_i$ at the rear surface of the target. Whether this is a valid assumption needs to be considered, since the density is determined by the hot electron distribution and this in turn is predicated on the interaction at the front surface of the target.

The second limitation concerns the way the cut-off energy is calculated. This maximum energy is related to a time parameter which describes how long the sheath is under the influence of the laser accelerated electrons; any evolution post-laser pulse cannot be accounted for. It has been suggested that the Mora model overestimates the cut-off energy [118] [119]. The model was shown to inadequately predict the change in E_{max} as a function of increasing pulse length. However, a second, more complete two phase model was introduced by Mora that better estimated the latter time evolution process [117]. Finally, the model requires knowledge of the generated hot electron temperature, T_e.

This final limitation of the Mora model is particularly problematic since the hot electron temperature itself is not readily determined. Various authors have attempted to provide scaling laws for multiple intensity regimes, but the relation between the various ionisation and absorption mechanisms, themselves dependant on intensity as discussed previously, makes these difficult to determine. Work by Beg et al. [120] suggested

that for $a_0 \lesssim 1$, the hot electron temperature scales as $T_e \propto (I\lambda^2)^{\frac{1}{3}}$; this matches the resonance absorption scaling. For $a_0 > 1$, Wilks et al. [105] found the hot electron temperature scales with the ponderomotive potential, such that for circular polarisation,

$$T_e = (\sqrt{1 + {a_0}^2} - 1)m_e c^2 \tag{2.70}$$

which simplifies to $T_e = a_0 m_e c^2$ for $a_0 \gg 1$. Therefore, $T_e \propto (I\lambda^2)^{\frac{1}{2}}$. Gibbon also suggested a transition regime [121], around $a_0 \simeq 1$, where the scaling goes as $T_e \propto (I\lambda^2)^{\frac{1}{2}\rightarrow\frac{1}{3}}$, up to $10^{19}\mathrm{Wcm}^{-2}$, as the absorption and electron acceleration mechanisms change.

More recently, Kluge et al. [122] studied the hot electron scaling with intensity using two dimensional particle in cell simulations. For $a_0 \ll 1$, the hot electron temperature was shown to scale as $T_e = {a_0}^2 = I\lambda$, while for $a_0 \gg 1$, the scaling goes as

$$T_e = \left(\frac{\pi a_0}{2\ln 16 + 2\ln a_0} - 1 \right) m_e c^2 \tag{2.71}$$

These results were shown to be in good agreement with experimental results, especially for $a_0 > 1$.

A number of authors other than Mora have attempted to develop models to examine sheath acceleration scaling. These include Schreiber et al. [123], Passoni and Lontano [124], Albright et al. [125] and Robinson et al. [126]. A review by Perego et al. [119] of all these and the Mora model compared the predicted ion energies with experimental results. Remarkable agreement was seen with some of the models. The model by Passoni et al [124] performed particularly well when compared to experimental results over an intensity range $10^{18} \rightarrow 10^{21}\mathrm{Wcm}^{-2}$.

Ion Beam Characteristics

Much of the attraction of sheath accelerated ion beams are their unique properties. The sheath acceleration mechanism produces thermal ion spectra [21] [127] useful for many applications. The nature of the sheath field profile at the rear of the target generates this spectrum. The sheath is dependent on the fast electron profile at the rear surface. Typically, the front surface electron beam is divergent from its interaction with the laser, the highest energy electrons being in the target normal direction. The sheath field and hence highest ion energies are also typically strongest in this direction, with lower energies at larger angles. This leads to the sheath field at the rear of the target taking a quasi-gaussian profile parallel to the surface [59], while falling away exponentially perpendicular to the target. Since the accelerating field is normal to the sheath the ion beam is divergent and has a thermal profile (typical half angles are $\sim 20^\circ$

[59], although this clearly depends on the sheath field profile, which is susceptible to perturbation from instabilities in the hot electron propagation and target deformation [128]).

While no spectral energy peaking typically exists, a number of authors have attempted to achieve such features through careful target manipulation. Schwoerer et al. [129] demonstrated a 1.2 MeV proton beam with $\sim 25\%$ energy spread through the use of proton rich dots placed on the rear surface of a titanium foil. Hegelich et al. demonstrated 3 MeV $^{5+}$C ions, with an energy spread of $\sim 17\%$ from palladium targets with a thin carbon surface layer.

The typical thermal ion spectrum is of interest for certain applications, for example proton radiography. Since a thermal spectrum comprises multiple energies, there is also a multitude of ion velocities. With adequate separation between the source and the object to be imaged, time resolved images can be achieved. Furthermore, these ion beams have been shown to have an extremely small effective source size $< 15\,\mu$m with very low transverse emittance [26] [130], again important for proton radiography.

Limitations and Conclusions

Sheath acceleration is now a relatively well understood mechanism for ion acceleration capable of consistently producing proton or ion beams, although the properties of these beams themselves are not necessarily consistent. This, along with the ion source properties continues to drive research motivated by applications. Many applications require not only good shot to shot reproducibility, but also monoenergetic features. This is clearly challenging as discussed previously, but various authors have attempted to solve the solution through target and laser manipulation. Some authors have attempted to produce low energy spread beams with some success. The process usually involves careful target control to reduce unwanted impurities and the addition of artificial contaminants on the rear surface which act to allow energy selection in the sheath at the cost of energy conversion efficiency. The reader is directed to any of the following for more information [129] [131] [132].

There exist a second modus operandi to produce these beams through post acceleration energy selection techniques. Hadron therapy is a good example. Various authors have suggested and applied the use of post accelerating structures, for example quadrupoles [133] or a Gabor Lens [134] [135]. These structures work by discarding the unwanted energies, through focussing of the ion beam and then passing the beam through an aperture. The problem with these designs is that they are very energy inefficient; for a small energy spread most of the ions are discarded, meaning most of the coupled laser energy is also lost. Use of these devices therefore exacerbates the already low coupling efficiencies. A secondary issue is the limited maximum energy of the ions that can currently be produced. The maximum proton energies produced to date are of the

order of 85-90 MeV [25], while hadron therapy requires protons up to 250 MeV, rising to 300 MeV for radiography. Substantial progress is needed to achieve the ion energies required. One of the great challenges is the energy scaling as one goes to relativistic intensities ($T_e \propto (I\lambda^2)^{\frac{1}{2}}$). This makes the intensity requirements excessively prohibitive. Add to this the low repetition rate of the world's leading high intensity lasers and the task becomes even more daunting.

Considering the above, one clearly has two avenues of pursuit in the drive for higher energy (perhaps monoenergetic) ions. First, one can drive for higher intensity lasers capable of higher repetition rates, thus allowing for sheath accelerated beams to be used. A second, perhaps more interesting solution is the use of a different acceleration scheme to produce the desired beam characteristics. With this in mind, the next section will consider two different accelerating mechanisms based on ion acceleration driven by the radiation pressure exerted by a laser incident on a plasma.

2.4.2 Radiation Pressure Acceleration

Radiation pressure acceleration (RPA) is the method by which ions are accelerated through the pressure exerted upon a plasma by a laser. For an overdense plasma, if the laser exerted pressure exceeds the electron thermal pressure, the plasma can be accelerated in the direction of laser propagation. This is not actually a new idea; Marx [136] proposed a terrestrial laser could be used as a propulsion system for an interstellar spacecraft by using the pressure exerted by the laser photons on a 'light sail'. The pressure exerted on a plasma by a laser is proportional to the intensity, $P_R \propto I_L$. This means that current laser systems can exert pressures in excess of 100 GBar, albeit only for a fraction of a second. Even so, it was theorised ions could be accelerated to high energies using this technique [105] [137] [138]. Initially, it was predicted that for linearly polarised lasers, intensities of the order $10^{23}\,\mathrm{Wcm}^{-2}$ would be required [137] for radiation pressure dominated acceleration; a currently unattainable level. It was soon realised that by using circular polarisation, this requirement could be brought down by a factor of 100, attributed to the suppression of hot electron generation via $\vec{J} \times \vec{B}$ forces with a circularly polarised pulse [139] [140]. Further work by Palmer et al. [141] showed that these intensity requirements could be reduced even further by using a mid-IR ($\lambda \simeq 10\,\mu\mathrm{m}$) CO_2 laser like the one found at the Brookhaven National Laboratory. These experiments exploited the favourable wavelength scaling of the vector potential (equation C.2).

There are two manifestations of RPA; hole-boring and light sail acceleration. They are distinguished by the type of plasma with which they interact. Hole-boring RPA (HB-RPA, or just HB) is concerned with plasmas which can be assumed infinitely thick during the acceleration phase, while light sail (LS) considers the acceleration of an entire, thin plasma slab. They are of interest due to their common defining features, namely favourable peak ion energy scaling with intensity and the monoenergetic ion

bunches they can generate.

Collisionless shocks (see section 2.2.3) are also of interest as a mechanism for ion acceleration. Hole-boring and collisionless shock acceleration share many common features; the most important being both propagate the plasma with an associated potential which acts to "sweep up" upstream ions. Assuming $k_B T_i < e\phi_{shock}$, ions can be reflected off the potential to velocities twice that of the shock. Whether acceleration is due to HB or collisionless shock acceleration depends on the balance between the radiation pressure of the laser and thermal pressure of the plasma. Assuming ponderomotive scaling[3] for the electron temperature, the plasma thermal pressure can be taken as

$$P_{th} = n_e k_B T_e = n_e m_e c^2 \left[\sqrt{1 + \frac{{a_0}^2}{2}} - 1 \right] \tag{2.72}$$

while the radiation pressure is of the form given in equation 2.78 which can be re-expressed as

$$P_{rad} = n_c m_e c^2 {a_0}^2 \tag{2.73}$$

For the case that $P_{rad} > P_{th}$ it can then be said that for radiation pressure to dominate

$$a_0 > \sqrt{\frac{{n_e}^2}{2{n_c}^2} - \frac{2n_e}{n_c}} \tag{2.74}$$

This result is shown in figure 2.13.

For the case of radiation pressure domination, the critical surface is spatially driven into the target (a hole is "bored"). As the critical surface moves into the plasma ions can be swept up and accelerated to high energies. For the case where the thermal pressure dominates, the laser cannot drive the critical surface spatially, but electron heating means it is possible to form a collisionless shock.

Both mechanisms comprise of the formation of a shock with subsequent reflection of upstream ions from the potential associated with this structure. The formation mechanism is the characteristic feature. For hole-boring, the ponderomotive force forms the shock, while for collisionless shock acceleration, temperature or density gradients are the cause.

[3] linear polarisation is assumed as this is most relevant to the work in this thesis.

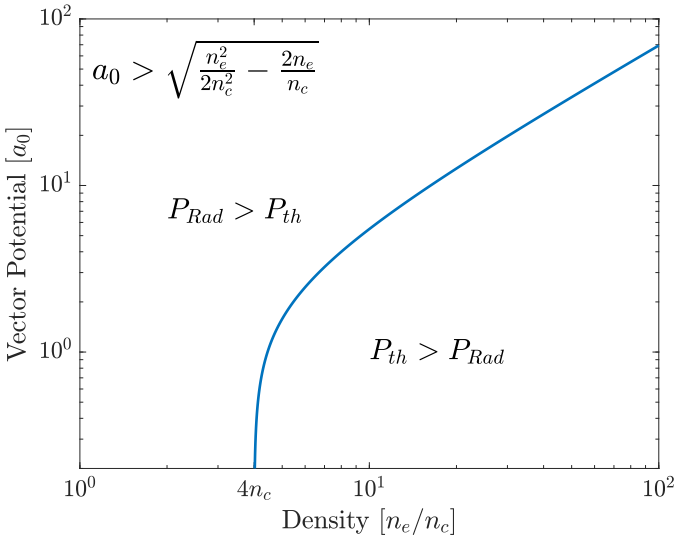


Figure 2.13: The relation between the vector potential and plasma density when the radiation pressure and plasma thermal pressure are balanced. An interaction sitting well above this line is dominated by hole-boring, while an interaction well below this line is dominated by collisionless shock acceleration

Hole-Boring

First consider a plasma slab with electron and ion densities, n_e and n_i, respectively. An incident laser pulse ponderomotively accelerates electrons at the front surface of the plasma, causing charge separation and forming electron depletion ($0 < x < x_1$) and electron compression ($x_1 < x < x_2$) regions (see figure 2.14(a)). The size of the compression region is defined by the penetration distance of the ponderomotive force into the target, $l_s = c/2\omega_p$. The ponderomotively accelerated electrons continue to pile up until the induced charge separation field, E_x, balances the ponderomotive force.

Macchi et al. [142] use a Lagrangian scheme to describe the ion motion within the charge separation layer. In one-dimension, the equation of motion is given as

$$m_i \frac{d^2 x_i(t)}{dt^2} = ZeE_{x_0} = ZeE_0 \left(1 - \frac{x_i(0) - x_1}{l_s}\right) \tag{2.75}$$

where $x_i(0)$ is the initial position for a given ion and E_{x_0} is the field at the initial ion position. It is possible to solve the equation of motion to find the position of any given ion as a function of time, given as

$$x_i(t) = x_i(0) + \left[\frac{Ze}{2m_i} E_0 \left(1 - \frac{x_i(0) - x_1}{l_s}\right)\right] t^2 \tag{2.76}$$

This result indicates the field and density profiles are self-similar in the compression region and all ions will arrive at the same time, $t_b = (2l_s m_i / ZeE_0)^{1/2}$. The model

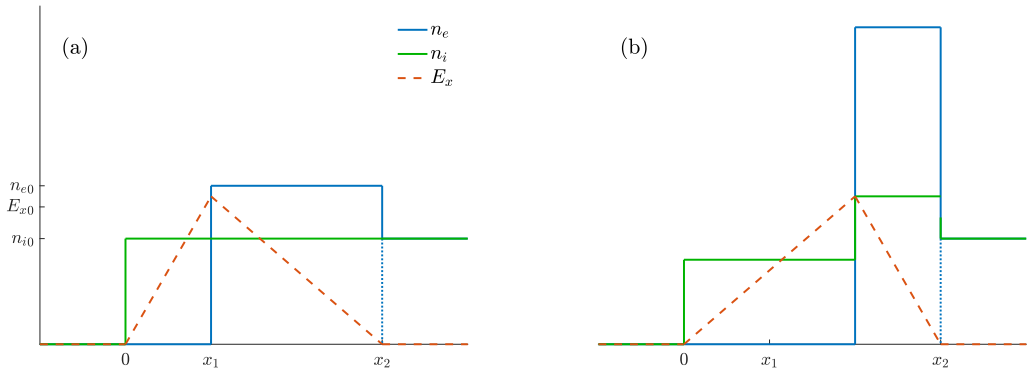


Figure 2.14: Profiles of the electron density, n_e, ion density, n_i and induced electrostatic field, E_x for the HB front formation (a) at early times when ion motion is fixed and (b) later times during the co-propagation of the electron and ion fronts.

further predicts that at time t_b a singularity forms in the density. Obviously in practice this does not occur; either equilibrium is reached before this, or wave-breaking occurs and the density structure collapses.

Simultaneously, the radiation pressure drives the critical surface spatially into the plasma. For steady conditions within the charge separation layer, the velocity of the critical front can be simply calculated hydrodynamically by first recalling the continuity and force balance equation for a simple plasma,

$$\begin{aligned} \frac{\partial \rho}{\partial t} + \frac{\partial}{\partial x}(\rho u) &= 0 \\ \frac{\partial}{\partial t}(\rho u) - \frac{\partial}{\partial x}(\rho u^2) + \frac{\partial}{\partial x}(ZP_e + P_L) &= 0 \end{aligned} \tag{2.77}$$

In the reference frame of the HB front, the front itself is stationary and so the time derivatives will go to zero. In the stationary frame, the continuity equation becomes $\frac{\partial}{\partial x}(\rho u) = 0$ and for the force balance, $P_L \gg ZP_e$, giving the result

$$\begin{aligned} \rho u &= constant \\ \rho u^2 &= P_L = \frac{2I}{c} \end{aligned} \tag{2.78}$$

resulting in a velocity

$$u = \sqrt{\frac{2I}{\rho c}} \tag{2.79}$$

Similarly, the HB velocity can be obtained by a 1D quantum mechanical consideration of the change in photon momentum, $\delta p_{photons}$, in a time δt. This is done through the

balancing of the photon and mass momentum flows. In the frame of the moving shock, the ion density can be given as $n_i\gamma_{hb}$, where γ_{hb} is the Lorentz factor due to the length contraction in the shock frame. For simplicity assume total reflection of N photons with momentum $\hbar\omega$ in a bunch duration τ; the intensity is then $I = N\hbar\omega/\tau$. Since the number of photons is invariant in reflection, N must be conserved. The reflected photons are Doppler red shifted in the shock frame owing to the moving critical surface. The frequency of the reflected photons, ω_r with respect to their initial frequency, $\omega^{'}$ is given by

$$\omega_r = \omega^{'}\left(\frac{1-\beta}{1+\beta}\right)^{\frac{1}{2}} = \omega\left(\frac{1-\beta}{1+\beta}\right) \tag{2.80}$$

where $\omega^{'} = \omega\left[(1-\beta)/(1+\beta)\right]^{\frac{1}{2}}$. $\omega_r/\omega = I^{'}/I = (1-\beta)/(1+\beta)$ is the ratio of the intensities in the shock to lab frame. Here, $(1-\beta)/(1+\beta)$ represents the reflection coefficient, R, of the incident pulse off the critical surface [143]. In the lab frame, this occurs in a time $\tau = \tau^{'}/(1-\beta)$. The resultant radiation pressure is, as previously expressed, given as the change in photon momentum for a given period of time, $P_{rad} = \delta p_{photons}/\delta t$, which can be expressed as

$$P_{rad} = \frac{N\hbar}{c}\frac{(\omega+\omega_r)}{\tau} = \frac{2I}{c}\frac{1-\beta}{1+\beta} \tag{2.81}$$

Note the radiation pressure here is just the frame corrected non-relativistic result found in equation 2.78. In the shock frame the upstream plasma ions travel towards the laser-plasma interface with velocity $-v_{hb}$. The momentum of n_i ions is therefore assumed to be $-\gamma_{hb}n_i m_i v_{hb}$.

Through momentum conservation, assuming total ion reflection through elastic collisions in an incompressible plasma, the total reflected ion momentum is $\gamma_{hb}n_i m_i v_{hb}$. However, to equate this with the radiation pressure, we need the change in momentum to be in terms of a unit area (i.e. it needs to also be a pressure). This is done by multiplying by the rate at which ions arrive at the interface, which is v_{hb}. Therefore, an expression for the total change in momentum is given by

$$\delta p_{ions} = n_i\gamma_{hb}\left(2m_i\gamma_{hb}v_{hb}\right)v_{hb}\delta t \tag{2.82}$$

where $n_i\gamma_{hb}v_{hb}\delta t$ is the total number of reflected ions within δt. The factor of 2 arises since the reflected ions arrive and leave with velocities of equivalent magnitude but opposite sign. Balancing the mass and photon momentum flows leads to

$$2m_i{v_{hb}}^2 n_i\gamma_{hb} = \frac{2I}{c}\frac{(1-\beta)}{(1+\beta)} \tag{2.83}$$

From here, the solution for the hole-boring velocity can be found purely algebraically. Let

$$\Gamma = \frac{I_L}{n_i m_i c^3} = \alpha \frac{Z}{A} \frac{n_c}{n_e} \frac{m_e}{m_i} {a_0}^2 \tag{2.84}$$

where α is equal to 1 or 1/2 for circular and linear polarisation, respectively. Through substitution

$$(\Gamma - 1)\beta^2 - 2\Gamma\beta + \Gamma = 0 \tag{2.85}$$

The root that then corresponds to the hole-boring velocity is then given as

$$\frac{v_{hb}}{c} = \frac{\Gamma^{\frac{1}{2}}}{1 + \Gamma^{\frac{1}{2}}} \tag{2.86}$$

where Γ represents the dimensionless piston parameter. Note that the other root is unphysical as it would result in $v_{hb} > c$. The energy of the ions in the lab frame, ϵ_i, is given by

$$\epsilon_i = (\gamma_{hb} - 1) m_i c^2 \tag{2.87}$$

To determine the ion energy in the lab frame, one must obtain an expression for γ_{hb}, which is done by a transformation of the shock frame velocity into the lab frame. This is done through the relativistic velocity transformation, $u = \frac{u'v}{1+\frac{u'v}{c^2}}$, giving

$$v_{LF} = \frac{2v_{hb}}{1 + \beta^2} = \frac{2\beta c}{1 + \beta^2} \tag{2.88}$$

Substituting into the expression for γ_{hb}, one obtains $\gamma_{hb} = \frac{1+\beta^2}{1-\beta^2}$, which in turn can be fed into the energy equation, giving

$$\epsilon_i = m_i c^2 \left[\frac{1 + \beta^2}{1 - \beta^2} - 1 \right] = 2 m_i c^2 \left[\frac{\Gamma}{1 + 2\Gamma^{\frac{1}{2}}} \right] \tag{2.89}$$

This result gives the relativistically correct HB velocity as first formulated by Robinson et al. [144]. This and the piston velocity as a function of the density are plotted for Hydrogen in figure 2.15.

The result also holds in the non-relativistic limit, $\Gamma \ll 1$, $v_{hb} \ll c$, with

$$v_{hb} \simeq \Gamma^{\frac{1}{2}} = \sqrt{\frac{I}{m_i n_i c^3}} \tag{2.90}$$

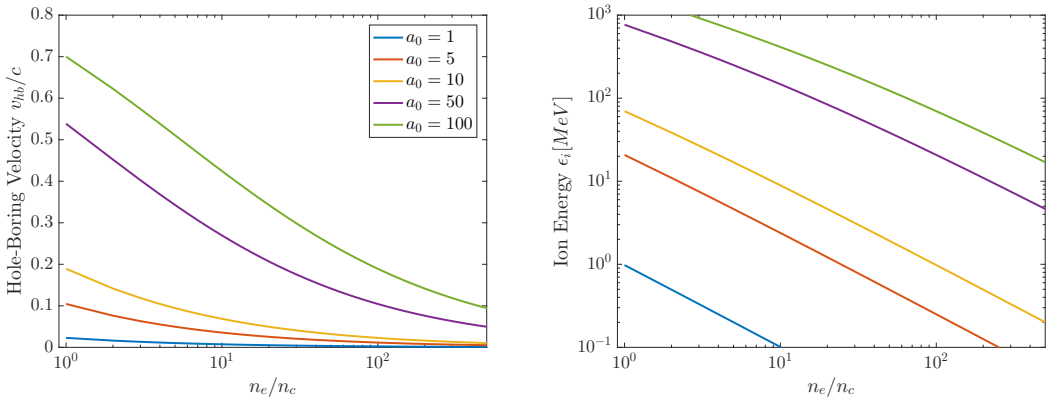


Figure 2.15: Left, dependence of the hole-boring velocity on the ion density in a Hydrogen plasma and right, the predicted ion energy as a function of density for reflected ions off the critical surface

$$\epsilon_i \simeq 2m_i c^2 \Gamma = \frac{2I}{n_i c} \tag{2.91}$$

As shown above, the energy scaling for the HB accelerated ions is better than sheath acceleration, with $E_i \propto I_L$, going to $E_i \propto {I_L}^{\frac{1}{2}}$ in the relativistic intensity regime for a fixed density. However, accounting for the fact $n_c \propto {I_L}^{\frac{1}{2}}$ too, working at the same n_e/n_c gives the equivalent scaling.

The reflected ion beam co-propagates through the target with reflected electrons as a charge neutral bunch. This ensures the transport is ballistic. The stopping power is given by the Bohr formula [98],

$$L_{Bohr} = \ln\left(\frac{m_e {v_p}^3}{Ze^2\omega_p}\right) \tag{2.92}$$

where v_p is the relative velocity of the ions relative to the background electrons. Therefore for thin, low Z targets collisional energy loss should not be significant.

Various authors have studied HB-RPA theoretically [105] [145] [146]. Liseikina and Macchi [147] demonstrated a 13.7% conversion efficiency into ions as well as low divergence and monoenergetic ion features. This conversion efficiency is favourable in comparison to sheath acceleration methods, while monoenergetic features are desirable for many applications, further motivating research. Cattani et al. [148] showed through an analytical model looking at a steady state solution for the electron motion of an overdense plasma that enhancement of the electron density at the surface occurs, i.e. a sharp density gradient above the background is formed through snow ploughing. Robinson et al. [149] showed that hole-boring is possible for densities below the critical density due to this induced density spike. This allows for higher ion energies, since the HB velocity scales with the inverse of the density. Therefore, for lower bulk plasma densities, the front moves faster and the energy gained by snowploughed ions increases. Palmer et al.

[150] demonstrated the effects of linear density gradients on the front edge of the target on the ion beam profile.

Experimentally, observations are more difficult. The scaling of equation 2.89 shows that for solid densities only modest ion energies are expected. Furthermore, target heating inhibits the acceleration process, either through an increase in the thermal plasma pressure or through the formation of strong electrostatic fields at the target rear surface. That said, Palmer et al. [141] observed mono-energetic ions from a near-critical density gas jet whose energies showed agreement with the $\epsilon_i \simeq I/n$ scaling of equation 2.91.

Collisionless Shock Acceleration

Expressions have in the last section been derived for the piston velocity of a shock front being driven into a plasma at the critical surface due to the exerted radiation pressure. This implicitly assumes an essentially cold plasma i.e. $P_{th} < P_{Rad}$. Now consider the case where this is not true and the thermal pressure dominates. For such a plasma the thermal pressure acts to oppose the radiation pressure exerted upon it by an incident laser pulse, slowing the HB-RPA front. For the case $P_{th} \gg P_{Rad}$, the critical surface motion is totally suppressed. However, it is possible to launch a collisionless electrostatic shock. The incident laser can locally heat electrons at the critical surface which propagate and heat the upstream plasma and increase the bulk sound speed, c_s. A density enhancement can be launched into the plasma ahead of the critical surface which, if its velocity falls within the limits $1 < M < 1.6$, can transition to a collisionless shock. Collisionless shock acceleration of ions is of interest as an alternative to laser hole-boring. Some of the important basic physics for these collisionless shocks was outlined in section 2.2.

Rapid heating of the plasma electrons can lead to a shock structure being formed due to induced temperature gradients. Unlike in HB-RPA, when the shock can be driven for as long as the incident laser maintains the induced charge separation, a collisionless shock can be sustained long after the laser pulse has terminated; the collisionless nature of these shocks means heat transfer occurs over relatively long timescales. Dissipation occurs via the population of electrons trapped behind the shock front [151] [152], or for strong shocks due to the reflection of the upstream ions off the front [153] [154].

Much in the same way as hole-boring acceleration, ions can be reflected off the shock front and accelerated to high energies [155][156]. Considering the shock frame, if the ions have a kinetic energy less than the electrostatic potential across the shock front (i.e. $\phi_{crit} = {M_{cr}}^2/2$), they can be reflected and accelerated by the shock, with most joining the shock formation while a few are reflected to twice the shock velocity. It is possible for some ions to gain energy equivalent to twice the shock velocity. To obtain monoenergetic ion features, the shock velocity should be uniform, which relies on the uniform heating

of the upstream plasma electrons relative to the radiation pressure.

Initial work by Denavit [145] used one dimensional particle-in-cell simulations to show the formation of these shocks by relativistic intensity lasers incident on overdense plasmas. Furthermore, he showed the properties of ion acceleration depend on the ratio of bulk up- and down-stream electron temperatures. A scan of the incident laser intensity and target electron density provided evidence for significant variation in the shocks and resultant ion beams. The higher the upstream electron temperature (lower density), the faster a shock can propagate and the higher the reflected ion energy.

Various authors have extended this work. Authors such as Silva et al. [157], Chen et al. [158][159] and Macchi et al. [160], investigated thin targets, the effect of varying the target properties and temperature effects, respectively. Silva et al. showed that for thin targets the formation of high velocity shocks was possible. Simulations demonstrated that electron recirculation could cause uniform, high electron temperatures. For shock formation times longer than the recirculation time of electrons, shock velocities $v_{shock}/c > 0.1$ were possible. Further studies by Fiuza et al. [156] [161] demonstrated that plasma heating and density steepening in near-critical plasmas with a gradually decreasing density ramp can theoretically generate high energy protons up to 200 MeV with a 100 TW laser system. Work has also studied the interaction of shock accelerated ions with a sheath formed at the rear of a target, demonstrating the ability for enhanced ion energies [162] [163] [164].

A number of authors have experimentally investigated ion acceleration. Wei et al. [165] demonstrated transversely accelerated 13 MeV helium ions using the a 0.7 ps, 180 J laser incident on an underdense gas jet. Henig et al. [166] reported shock-accelerated 8 MeV protons from microsphere targets. Haberberger et al. [167] observed narrow energy spread, ~ 20 MeV protons with a CO_2 pulse train incident on a hydrogen plasma.

Collisionless shocks are also of interest due to their presence as astrophysical objects. Theoretically there has been much interest suggesting the benefit of their creation in the laboratory [168] [169] [156] [170] [171] There has been much work to produce these shocks in the laboratory for study. Romagnani et al. [60] observed ion acoustic solitons and collisionless shock waves from solid targets propagating into a surrounding gas. Nilson et al. [172] studied cylindrically driven collisionless shocks undergoing a corrugation instability relevant to high Mach-number ionising astrophysical shocks. Huntington et al. [173] experimentally observed the magnetic fields associated with the Weibel instability [174] which it has been posited leads to collisionless shock formation.

Light-Sail Acceleration

A further radiation pressure induced acceleration mechanism, light-sail (LS), considers thin targets from which the region within the focal spot can be accelerated as a single entity. Unlike in hole-boring, for LS the ions are coupled to the electrons and accelerated

solely through the radiation pressure. This increased acceleration time, τ, results in higher ion energies and favourable energy scaling over not only sheath acceleration but also HB-RPA, with the ion energy scaling as $E_i \propto {I_L}^2$.

LS acceleration was first outlined through three dimensional simulations by Esirkepov et al. [137], with predictions of up to 100 GeV/u ions possible for laser intensities of $> 10^{23}\,\mathrm{Wcm}^{-2}$. This work was further expanded by authors such as Robinson et al. [175], who developed a full one dimensional model to describe the ion acceleration in the light sail regime.

In the non-relativistic limit, the energy gained by a plasma slab of thickness l_d with ion mass, m_i, and ion density, n_i, can be calculated by using a rate of change of momentum. The radiation pressure exerted on a plasma is given by 2.81, so from this the force can be shown to be

$$(1+R)\frac{I_L}{c}A = \frac{dp}{dt} = m_i n_i l_d A \frac{dv}{dt} \tag{2.93}$$

Through integration, it is possible to retrieve the light-sail velocity

$$v_{ls} = \frac{\tau}{m_i n_i l_d}(1+R)\frac{I_L}{c} \tag{2.94}$$

Since electrons and ions co-move ahead together ahead of the laser pulse, this represents the velocity of the accelerated ions. This has also been extended to the relativistic limit by Robinson et al. [175].

An approximation for the optimal thickness of the target can also be made. This is achieved by assuming that maximum ion energies result when the radiation pressure from the laser is exactly balanced by the thermal/electrostatic pressure of the plasma. This can be done by using the analogy of the radiation pressure being the same as the force between two capacitor plates. Again using the radiation pressure and also the force between two parallel capacitor plates ($F_E = \frac{\sigma E}{2}$), where $\sigma = n_i e L$ is the charge on the plates. The electric field can be found using Gauss' law ($E = \frac{\sigma}{\epsilon_0}$). Therefore, $F_E = \frac{\sigma^2}{2\epsilon_0} = \frac{n_i^2 e^2 L^2}{2\epsilon_0}$ and so by equating these forces, one can obtain an expression for the optimal thickness of the target, L,

$$L = \sqrt{\frac{2(1+R)\epsilon_0 I_L}{c n_i^2 e^2}} \tag{2.95}$$

This essentially assumes that there is no transverse ponderomotive acceleration component, which will arise from a spatially varying intensity profile given the ponderomotive force scale as $f_p \propto \vec{\nabla} E^2$. The condition that the electrons and ions must remain coupled to ensure the plasma slab moves together also requires cold electrons. This makes

circular polarisation optimal for this scheme as it suppresses $\vec{J} \times \vec{B}$ heating, ensuring efficient acceleration.

From the result, it can also be seen that if a target is above the optimum thickness there is an increase in the overall mass of the target. This leads to a reduction in the overall acceleration, but more importantly a balance cannot be reached between the radiation pressure and the resultant charge separation, leading to the decoupling of the electrons and ions.

While the model proposed above gives very favourable peak ion energy scaling and the possibility for monoenergetic ion spectrum features, the model is too idealised to be applicable in most experimental situations. The model is based on a one dimensional approximation in which supergaussian intensity profiles are used. This acts to suppress the generation of hot electrons, but in reality these beam profiles are hard to achieve. Consequentially, target deformation and spatially varying intensity profiles lead to suppressed ion acceleration. It has been suggested through simulations that shaped foils with density profiles designed to match the incident laser intensity profile could help mitigate this problem [176], although to design such a target would be challenging. The model also fails because Rayleigh-Taylor like [177] and Weibel-like [178] instabilities are prevalent.

3 Experimental Methods

For any given laser-plasma experiment it is important to be able to characterise the interaction to the fullest extent. An understanding of the laser and target conditions both independently and during an interaction is crucial. This chapter describes the CO_2 laser from Accelerator Test Facility (ATF) at Brookhaven National Laboratory used for experimental work presented in this thesis, along with gas targetry methods employed. A number of optical and ion diagnostic tools are then described along with simulation tools employed in analysis and understanding the work presented.

3.1 High Power CO_2 Lasers

The experimental work in this thesis was carried out at the ATF at Brookhaven National Laboratory. The ATF offers the use of a high power CO_2 laser, either as a standalone experimental tool or in conjunction with a 70 MeV electron beam [179]. A number of previous CO_2 only experiments into ion acceleration [141] [180] [181] [182] and laser wakefield acceleration have been conducted. Furthermore, a large number of CO_2-electron beam experiments have also explored staged electron acceleration [183], non-linear Thomson scattering [184], inverse free electron lasers [185] [186] and inverse Compton scattering [187] [188].

The use of CO_2 as a gain medium for lasers is not particularly novel, with high power CO_2 lasers being used extensively in industry [189] [190]. However, short-pulse, high power lasers are not commonplace. A number of systems have existed, for example, the Neptune laser at UCLA [191], but currently the sole operational short pulse, high power CO_2 laser for research applications is located at the ATF.

CO_2 is attractive for use in a gas laser for a number of reasons. Unlike atomic gases, the upper energy levels are energetically relatively close to the ground state; the lasing transitions have an energy that represents a large fraction of the energy needed to excite the molecule. The efficiency of this molecular laser is therefore quite high. CO_2 is one of the most simple of the triatomic molecules, since it is linear and symmetric with three degrees of rotational freedom (see figure 3.1). These take the form of the symmetric stretch mode, ν_1, the bending mode, ν_2 and the asymmetric stretch mode, ν_3. As such, the vibrational level of a given molecule can be represented in the form (ν_1, ν_2, ν_3). The molecule also possesses rotational modes. The energy of any given

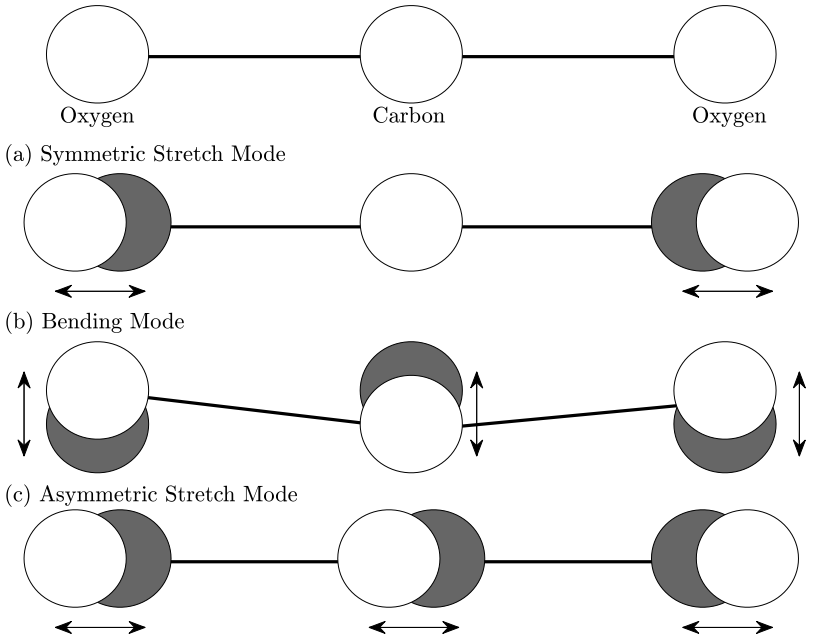


Figure 3.1: The three vibrational degrees of freedom of the CO_2 molecule.

state can be represented as the sum of the energy of the vibrational and rotational modes, $E = E_{rot.} + E_{vibr.} = (n + 1/2)\hbar\omega + J(J + 1)\hbar^2/2\mu L^2$, where n and J are these vibrational and rotational quantum numbers, respectively, μ is the reduced mass and L is the molecular size. The rotational states are typically much lower in energy when compared to the vibrational states, so act to provide the fine structure to a given vibrational state. An example of the energy levels of a CO_2 molecule is shown in figure 3.2.

In an excited molecule, a transition can occur to a lower level through the emission of a photon. For a given transition, from one vibrational state to another, selection rules dictate there must also be a change in the rotational quantum number, J. For a transition such that $\Delta J > 0$, this is denoted the P-branch, while for $\Delta J < 0$ the transition falls in the R-branch. These result in a $+h/2\pi$ and $-h/2\pi$ change in angular momentum, respectively. Since the selection rules prohibit a transition $\Delta J = 0$, this leads to the so-called "centre band" which is a zero point in the gain spectrum and lies between the R- and P-bands, as shown in figure 3.3. The fine modulation of the two bands is the result of the various transitions that are possible between the rotational modes in the two vibrational levels.

At the ATF, matters are complicated somewhat by the addition of a number of other molecules to the CO_2 gain medium; for the regenerative amplifier this consists of a mixture containing CO_2, N_2 and He in a typical $1 : 1 : 8$ ratio [192]. Nitrogen is added to assist in the population inversion of the gain medium. In a pure CO_2 medium, excitation can occur to a number of states aside from the desired $(0, 0, \nu_3)$ mode, reducing efficiency and the power output. The addition of N_2 molecules helps overcome this issue.

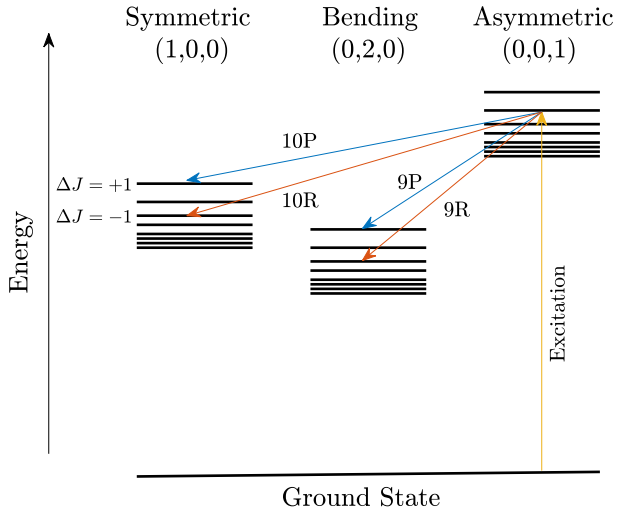


Figure 3.2: The vibrational and rotational energy levels of the CO_2 molecule. Excitation occurs into the (0,0,1) state, before decay into the (1,0,0) or (0,2,0) states. Decay into the excited He and then ground states can then occur (not pictured).

N_2 is a diatomic molecule and so has only one degree of vibrational freedom along its internuclear axis. The lifetime of excitations into these higher vibrational states is relatively long and conveniently the energy of the excited $N_2(\nu = 1)$ is nearly equivalent to the desired $CO_2(0, 0, 1)$ asymmetric stretch mode. As such, efficient energy transfer can occur between the readily excited $N_2(\nu = 1)$ mode and a ground state $CO_2(0, 0, 0)$ molecule via collisions. It is then possible to achieve efficient excitation into the desired $CO_2(0, 0, 1)$ state. The excited asymmetric stretch mode then radiatively decays into one of either the first symmetric stretch mode, $CO_2(1, 0, 0)$, or the second bending mode, $CO_2(0, 2, 0)$; these emit at 10.4 µm and 9.4 µm central wavelengths, respectively. These modes are subsequently depopulated via collisions with the added He molecules on relatively fast timescales, giving the required population inversion between the ground and excited $CO_2(0, 0, 1)$ mode.

While the two primary transitions are centred at 10.4 µm and 9.4 µm, the various rotational sub-levels result in a broader spectrum, modulated by the probability of each of these various modes. The result is the true central wavelength of the R- and P-branches sits at 10.2 µm and 10.6 µm, respectively. The ATF laser operates using the R-branch owing to its superior line density. Since the gain spectrum is constructed of multiple spectra corresponding to the rotational mode transitions whose bandwidth is small, it is not possible to extract a short pulse. This is clear given the temporal full width at half maximum pulse length τ_p that can be extracted from a spectrum with bandwidth $\delta\nu_p$ is given by $\tau_p = \beta/\delta\nu_p$, where $\beta = 2\ln 2/\pi \approx 0.44$ for a gaussian pulse [80]. Brimacombe and Reid [194] demonstrated the bandwidth, $\delta\nu$ (in GHz) of a given transition can be found using the formula

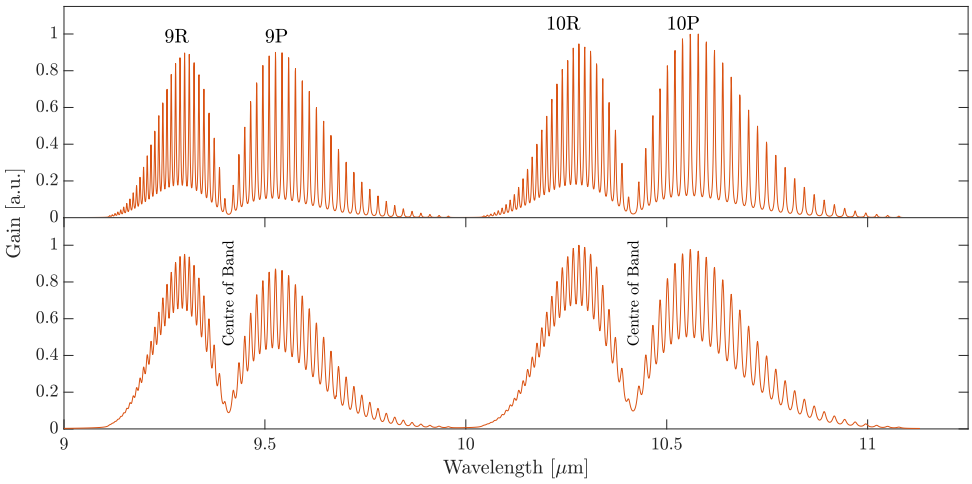


Figure 3.3: CO_2 gain spectra for the ATF regenerative amplifier, created using the co2amp code [193]. Top, gain spectrum for a $1:1:8$ ratio of CO_2, N_2 and He at 4 bar pressure. Bottom, the gain spectrum for the same gas mixture at 10 bar.

$$\delta\nu \approx P \cdot (5.79\psi_{CO_2} + 4.25\psi_{N_2} + 3.55\psi_{He}) \tag{3.1}$$

where P is the pressure in bar and ψ_α is the relative concentration of the given molecule. For the previously stated $CO_2 : N_2 : He = 1:1:8$ ratio of molecules at 1 bar, this results in a frequency of $\delta\mu \approx 3.8$ GHz. This would give a typical minimum pulse length of $\tau_p \approx 120$ ps, although in reality the extracted pulse is closer to 1 ns [195]. Amplification is strongest at the centre of bandwidth spectrum, increasing the ratio between the centre of the pulse and the wings and lengthening the pulse [192]. Furthermore, since any modulation in the frequency domain will translate to a modulation in the temporal domain of the extracted pulse, without smoothing a single, short pulse will not be extracted; instead a pulse train will be produced, the temporal separation of which will be equal to the inverse separation of the rotational spectral lines (25 ps and 18 ps for the R- and P-branches, respectively). For short pulses, it is necessary to remove the modulation caused by the rotational modes in the spectrum to increase the bandwidth.

A smoothing of the gain spectrum can be achieved in a number of ways. Collisional broadening, if strong enough, is one method that can be employed. As the pressure of the gas is increased, the effective lifetime of excited states is reduced since collisions induce radiative transitions on timescales shorter than their mean lifetime. The reduced lifetime increases the energy uncertainty of the emitted photon, broadening the spectrum. Should the broadening become large enough, such that the bandwidth pro-

files from neighbouring rotational transitions overlap, the spectrum is smoothed. From equation 3.1, it can be calculated that pressures of the order 25 bar would be required for full smoothing. Practically however, this is not achievable at the ATF since it is not possible to efficiently arrange the electrical discharge system used in the amplifier and achieve uniform excitation. Pressures are limited to a more modest 10 bar as a result. As such, the bandwidth remains less than the rotational line spacing, although the spectrum is modified to some extent (see figure 3.3). A further method to modify the gain spectrum comes in the form of using a mixture of Oxygen isotopes. By using both ^{16}O and ^{18}O the molecular symmetry is broken, doubling the density of rotational lines. The regenerative amplifier[1] at the ATF uses a combination of isotopes, ^{16}O : ^{12}C : ^{16}O, ^{16}O : ^{12}C : ^{18}O and ^{18}O : ^{12}C : ^{18}O in a 1 : 2 : 1 ratio [196]. A combination of using the superior line density in the R-branch, pressure broadening and isotopic CO_2 allows an ~ 3.5 ps pulse to be extracted.

The seed pulse for the ATF CO_2 laser is based on an optical parametric amplification system (OPA). This uses a frequency doubled erbium oscillator, Ti:sapphire regenerative amplifier and a mid-IR wavelength converter to produce a ~ 350 fs pulse with 12-15 µJ of energy [193]. This is tuned to the desired branch of the CO_2 gain spectrum. The pulse is then positively chirped, longer wavelengths at the start of pulse, using a stretcher, which also acts as a bandpass filter to select the region of the spectrum that matches the desired branch of the gain spectrum[2] i.e. the 10R branch. The pulse energy after the stretcher is 1 µJ. The beam is passed through a CdTe half-wave Pockels cell and polarising splitter which acts as an optical isolator, before being injected into the regenerative amplifier. This is isotopic as earlier described and UV pre-ionised before being excited by a transverse electric discharge. It is multi-pass, with the beam extracted by reflection off a germanium optical switch, which consists of a Ge wafer orientated at Brewster's angle, optically excited by a mode-locked Nd:YAG laser so that it becomes reflective. The energy of the extracted pulse can be tuned by changing the discharge voltage and the number of passes, but is of the order 10 mJ. The beam is then injected into the 8 bar main amplifier which is non-isotopic and contains a $CO_2 : N_2 : He = 2 : 1 : 28$ ratio of molecules. This is x-ray pre-ionised and again transverse electrically discharged. The beam makes multiple passes and can be amplified up to ~ 20 J. The beam is then recompressed before the interaction chamber down to ~ 3.5 ps, with the damage threshold of the gratings effectively limiting the deliverable energy to ~ 3.5 J; the peak laser power is of the order 1 TW. The beam is transported to the target, where it is focussed by an $f/2$ parabola (although the beam diameter is sub-aperture, giving an effective $f/2.5$ focussing geometry) to a measured, best achievable spot size of 33 µm. The peak on shot intensity is nominally 3×10^{16} Wcm^{-2}, $a_0 \sim 1.4$.

[1] The main amplifier does not currently use isotopes due to the $\sim$ \$250k cost, although there are plans to implement this in the near future which would reduce the pulse length to ~ 1.5 ps

[2] This is achieved by carefully selecting the size of the grating to act as your filter

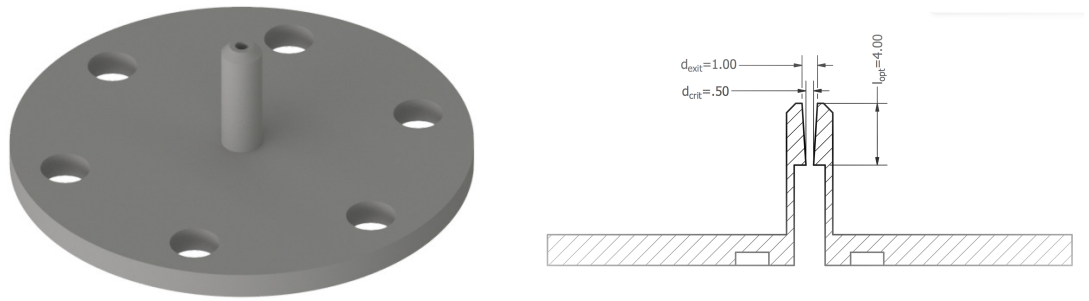


Figure 3.4: Left: Rendered image of a 1 mm gas nozzle made for experiments at the ATF. Right: Schematic of the gas nozzle, with the three important parameters that determine the gas profile illustrated.

3.2 Gas Targetry

For the work presented in this thesis, near- and over-critical density gas jet targets were used. Gas targets offer a number of advantages over more conventional thin foils. Gas targets are flexible in the species of ions to be accelerated and inherently less prone to localised contamination, unlike their foil counterparts. It is also possible to operate gas targets at high repetition rates, an important consideration for potential applications. To this point it has been difficult to produce over-critical density gas jets for conventional Nd:YAG and Ti:Sapp based laser systems; the electron densities required have not been achievable. One significant benefit of going to CO_2 lasers is the ~ 100-fold decrease in the critical density (equation 2.10) owing to the longer emission wavelength. For comparison, the critical density is $\sim 10^{21}\,\mathrm{cm}^{-3}$ and $\sim 10^{19}\,\mathrm{cm}^{-3}$ for 1 µm and 10 µm wavelengths, respectively. It is quite straightforward to achieve over-critical densities for CO_2 wavelengths in gas targets.

Experiments in this thesis use a supersonic gas nozzle attached to a high pressure gas valve. The nozzle design determines the peak achievable pressure and the spatial density profile [197]. The free parameters are the throat and exit diameters, d_{crit} and d_{exit}, respectively, and the length of the nozzle, l_{opt}. This is shown in figure 3.4. These define a basic gas profile, with a change in the reservoir pressure behind the nozzle used to alter the peak density. The minimum aperture diameter should also be d_{crit} to minimise instabilities in the flow.

It was earlier stated the nozzles used in this thesis were supersonic. A nozzle is termed supersonic when the mass flow rate through the throat of the nozzle exceeds the sounds speed of the gas ($M > 1$). Supersonic nozzles can exhibit steep density gradients at the gas-vacuum interface, although it has been shown these gradients become shallower and the peak density decreases with distance from the exit of the nozzle [197].

The specific nozzle used in this thesis, a so called "1 mm" nozzle, has a $\mathrm{d_{crit}} = 0.5\,\mathrm{mm}$,

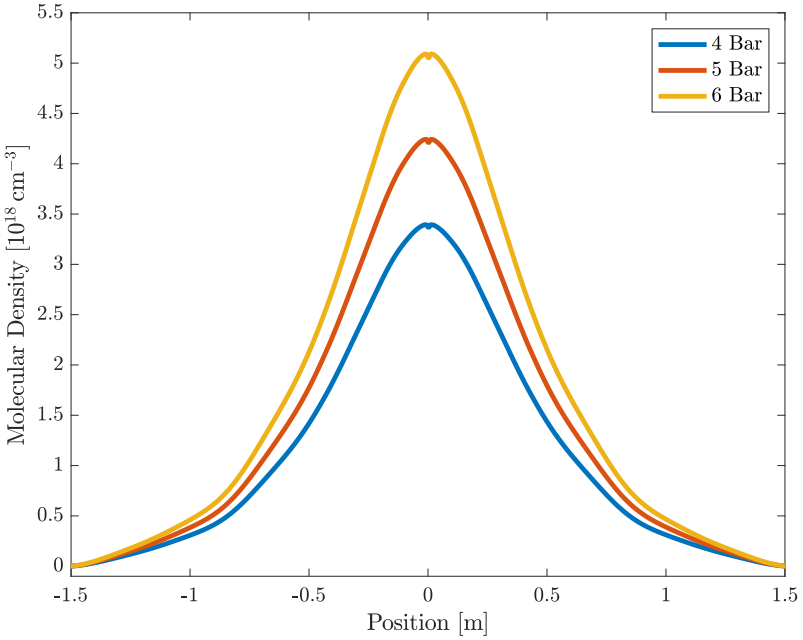


Figure 3.5: Density lineouts for the 1 mm nozzle used on experiments at BNL for 4, 5 and 6 bar backing pressures at a height of 700 µm from the exit.

$d_{exit} = 1\,mm$ and $l_{opt} = 4\,mm$. For a typical experimental scenario the gas is shot at a vertical height of $\sim 0.5 - 1\,mm$. This protects the nozzle from damage due to ablation from the laser, while maintaining a high peak density. Tapering of the top of the nozzle to the cone angle of the laser allows the interaction region to be closer to the nozzle exit. At these heights, it has been shown the longitudinal density profile can be approximated as triangular [180]. Characterisation of the nozzle was conducted at Imperial College using a Mach-Zehnder interferometer setup, as described in section 3.3.2. Density profiles for the nozzle at 4, 5 and 6 bar backing pressures are given in figure 3.5. This comes from a linear extrapolation from characterisation of the nozzle at higher backing pressures; it is not possible to observe sufficient fringe shift at low densities to accurately determine the pressure. This is appropriate since for high pressures where the density can be accurately measured, the peak density as a function of backing pressure is linear and tends to zero.

3.2.1 Target Shaping

As discussed above, gas targets offer a number of benefits over foil targets. However they do possess one significant drawback; their density profile. The long, gradual ramps either side of the peak density at the centre of the jet are not conducive for efficient ion acceleration, especially that driven by the radiation pressure [181]. Some authors have suggested that a density ramp at the target rear side could also benefit ion acceleration, through the suppression of sheath fields which preserves mono-energetic features [22]

[167]. Others have suggested the scale length must be kept to a minimum ($< 0.13\lambda_L\sqrt{a_0}$) to ensure instabilities are not seeded which can detrimentally modulate the proton beam [198].

Perhaps less controversially, most authors agree that for efficient radiation pressure acceleration the front surface scale length must be extremely sharp. This minimises the energy loss in any pre-plasma and maximises the reflection coefficient in the radiation pressure equations. Short scale lengths can be achieved through shaping of the gas profile, which is achieved with the creation of a collisional shock wave, or blast wave (BW) [199]. Blast waves arise in a number of situations, including from nuclear explosions [200] and in the solar wind, induced by solar flares [201].

The theory of a strong, collisional shock wave driven by a point explosion was initially described by von Neumann [202], Taylor [200] and Sedov [203] [204]. Sedov developed a self-similar description of the evolution of a BW in a cold, uniform density gas with an instantaneous explosion at $t = 0$. The idea of self-similarity describes a system in which phenomena differ only in the numerical values of their governing parameters, while the parameters adhere to an equivalent form [205]. Expressed another way, a given function, $f(\alpha)$, is termed self-similar if its general profile can be expressed through only a change in numerical constants for all values of a given dependent variable, α. The equivalent phenomenon in geometry is an affine transformation, which provides an intuitive example of the idea of self-similarity.

The motion of a fluid can be thought of as one-dimensional should all properties depend only on one geometric variable and time. By using the ideal of self-similarity, it is possible to derive expressions for a collisional shock wave in a compressional fluid, as shown by Sedov [206]. First, to simplify the problem, let us make the following assumptions. Consider an ideal gas in which a large amount of energy is deposited in a short time frame; energy deposition can be considered instantaneous. Second, only consider the induced shock for radii much greater than the size of the deposition region such that the energy can be assumed to originate from a point source. For an ideal gas in the adiabatic limit, the equations of motion, continuity and energy take the form

$$\frac{\partial \rho}{\partial t} + u\frac{\partial \rho}{\partial r} + \frac{\rho}{r^{j-1}}\frac{\partial (r^{j-1}u)}{\partial r} = 0 \tag{3.2a}$$

$$\frac{\partial u}{\partial t} + u\frac{\partial u}{\partial r} + \frac{1}{\rho}\frac{\partial p}{\partial r} = 0 \tag{3.2b}$$

$$\frac{\partial}{\partial t}\left(\frac{p}{\rho^\gamma}\right) + u\frac{\partial}{\partial r}\left(\frac{p}{\rho^\gamma}\right) = 0 \tag{3.2c}$$

where ρ is the density, p is the pressure, u is the velocity and j is an integer of 1, 2 or 3 which defines planar, cylindrical and spherical geometries, respectively. These expressions are in themselves not self-similar, but can be made self similar should it be possible to re-express them in terms of dimensional constants.

Solutions for the conditions either side of a strong shock can be obtained (in the shock frame), which take the form

$$\rho_0 (u_0 - \chi) = \rho_1 (u_1 - \chi) \tag{3.3a}$$

$$\rho_0 (u_0 - \chi)^2 + p_0 = \rho_1 (u_1 - \chi)^2 + p_1 \tag{3.3b}$$

$$\frac{1}{2}(u_0 - \chi)^2 + \frac{\gamma}{\gamma - 1}\frac{p_0}{\rho_0} = \frac{1}{2}(u_1 - \chi)^2 + \frac{\gamma}{\gamma - 1}\frac{p_1}{\rho_1} \tag{3.3c}$$

where χ is the shock velocity. Through the assumption of an infinitely strong shock such that the upstream pressure and velocity are zero, these can then be simplified to

$$\rho_1 = \frac{\gamma + 1}{\gamma - 1}\rho_0 \left[1 + \frac{2}{\gamma - 1}\frac{{c_s}^2}{\chi^2}\right]^{-1} \tag{3.4a}$$

$$u_1 = \frac{2}{\gamma + 1}\chi \left[1 - \frac{{c_s}^2}{\chi^2}\right] \tag{3.4b}$$

$$p_1 = \frac{2}{\gamma + 1}\rho_0 \chi^2 \left[1 - \frac{\gamma - 1}{2\gamma}\frac{{c_s}^2}{\chi^2}\right] \tag{3.4c}$$

where c_s denotes the sound speed ahead of the shock. The subscripts 0 and 1 denote quantities in front and behind the shock, respectively. Now we impose the limit, $M = \chi/c_s > 1$,

$$u_1 = \frac{2}{\gamma + 1}\chi \tag{3.5a}$$

$$\rho_1 = \frac{\gamma + 1}{\gamma - 1}\rho_0 \tag{3.5b}$$

$$p_1 = \frac{2}{\gamma + 1}\rho_0 \chi^2 \tag{3.5c}$$

In other words, the shock velocity is a characteristic parameter and these three relations can be used to define the strong shock limit in this case. It can now be said the fluid motion is dependent on two dimensional parameters, the energy of the explosion, E, and the initial density, ρ_0. These parameters are dimensionally independent; $[E] = ML^2T^{-2}$ and $[\rho] = ML^{-3}$. Here, M, L and T represent unit mass, length and time scales, respectively. However, while E and ρ_0 are independent, the unit scales are dependent [207]. A such, the motion can be described as self-similar and will depend on the spatial co-ordinate, r, and the time, t [208]. Sedov demonstrated the only dimensional variable which contains only length and time is the ratio of E to ρ_0. In this case a dimensionless quantity, ξ, can serve as the similarity variable, with

$$\xi = r\left(\frac{\rho_0}{Et^2}\right)^{\frac{1}{2+j}} \tag{3.6}$$

It is then possible to express final results for the radius and velocity of the shock

wave

$$r_1 = \xi_0 \left(\frac{E}{\rho_0}\right)^{\frac{1}{2+j}} t^{\frac{2}{2+j}} \tag{3.7}$$

$$\chi = \frac{\mathrm{d}r_1}{\mathrm{d}t} = \frac{2\xi_0}{2+j} \left(\frac{E}{\rho_0}\right)^{\frac{1}{2+j}} t^{\frac{-j}{2+j}} \tag{3.8}$$

where ξ_0 is a constant of order unity.

Physically this result is rather intuitive. Consider a spherical geometry; at a given time t the shock will expand to evacuate a volume $V = \frac{4}{3}\pi {r_1}^3$ with the mass swept up equal to $m = V\rho_0$. The pressure behind the shock is proportional to the energy per unit volume, $p \sim E/{r_1}^3$, while the shock and gas velocities are also proportional, so from equation 3.5c, $\chi \propto u_1 \sim (p/\rho_0)^{1/2} \sim (E/\rho_0 {r_1}^3)^{1/2}$. Hence through integration the radius can be expressed as $r_1 \sim (E/\rho_0)^{1/5} t^{2/5}$. This result is equivalent to that developed by Sedov, minus the constant ξ_0.

Again using the strong shock relation 3.5c, it is possible to demonstrate the self-similarity of the solution. In spherical geometry, $p_1 \sim \rho_0 \chi^2$ and through substitution of equation 3.8, it can be shown $p_1 \sim E/{r_1}^3$. The pressure behind the shock is fixed for distances and times proportional to $E^{1/3}$; similarity is exhibited for a different energies.

Shell thickness

Similar considerations using equation 3.5b allow the thickness of the shell that forms behind the shock front to be approximated. The mass swept up by the shock is given by

$$m = V\rho_0 = \frac{4}{3}\pi {r_1}^3 \rho_0 \tag{3.9}$$

In the limit of the shell thickness, δr, being much less than the expansion of the shock such that $\delta r \ll r_1$, the mass in the shell is given as

$$m = 4\pi \rho_1 {r_1}^2 \delta r \tag{3.10}$$

Combining these two expressions with 3.5b, one obtains an expression for the shell thickness as a function of radius

$$\delta r = \frac{\rho_0}{3\rho_1} r_1 = \frac{(\gamma - 1)}{3(\gamma + 1)} r_1 \tag{3.11}$$

Shock scale length

A final interesting quantity comes in the form of the scale length of the shock, specifically on the internal side. The scale length is the distance over which the density drops to $1/e$ of its peak value. Sedov also provides means for computing this, although the derivation is rather convoluted. The reader is directed to the book by Sedov [206] for the complete derivation.

The final results are expressed below as a function of the non-dimensional variable, ψ, which can take any value between $2/\gamma(j+2) \leq \psi \leq 4/(\gamma+1)(j+2)$ for $j = 1, 2$ with $\gamma > 1$ and $j = 3$ with $\gamma < 7$. These represent the explosion point and edge of the shock in space, respectively.

$$\frac{r}{r_1} = \left[\frac{(j+2)(\gamma+1)}{4}\psi\right]^{\frac{-2}{2+j}} \left[\frac{\gamma+1}{\gamma-1}\left(\frac{\gamma(j+2)}{2}\psi - 1\right)\right]^{-\alpha_2} \left[\frac{(j+2)(\gamma+1)}{(j+2)(\gamma+1) - 2[2+j(\gamma-1)]}\left(1 - \frac{2+j(\gamma-1)}{2}\psi\right)\right]^{-\alpha_1} \tag{3.12}$$

$$\frac{\rho}{\rho_1} = \left[\frac{\gamma+1}{\gamma-1}\left(1 - \frac{(j+2)}{2}\psi\right)\right]^{\alpha_5} \left[\frac{\gamma+1}{\gamma-1}\left(\frac{\gamma(j+2)}{2}\psi - 1\right)\right]^{\alpha_3} \left[\frac{(j+2)(\gamma+1)}{(j+2)(\gamma+1) - 2[2+j(\gamma-1)]}\left(1 - \frac{2+j(\gamma-1)}{2}\psi\right)\right]^{\alpha_4} \tag{3.13}$$

with the constants

$$\begin{aligned}
\alpha_1 &= \frac{\gamma(j+2)}{2+j(\gamma-1)}\left[\frac{2j(2-\gamma)}{\gamma(j+2)^2} - \alpha_2\right] \\
\alpha_2 &= \frac{1-\gamma}{2(\gamma-1)+j} \\
\alpha_3 &= \frac{j}{2(\gamma-1)+j} \\
\alpha_4 &= \frac{\alpha_1(j+2)}{2-\gamma} \\
\alpha_5 &= \frac{2}{\gamma-2}
\end{aligned} \tag{3.14}$$

The normalised density, ρ/ρ_1, and radius, r/r_1, can be plotted for $\gamma = 1.4$ (equivalent to hydrogen gas) and $j = 1$, 2 and 3, giving the results shown in figure 3.6. This result is important as it indicates the scale length is a function of the shock radius, determined by the energy absorbed and expansion time. For the conditions plotted in figure 3.6(a), the scale length, r_s, is given as $0.125r_1$, $0.076r_1$ and $0.057r_1$ for $j = 1$, 2 and 3, respectively. The scale length is shorter for higher dimension solutions since the amount of areal mass

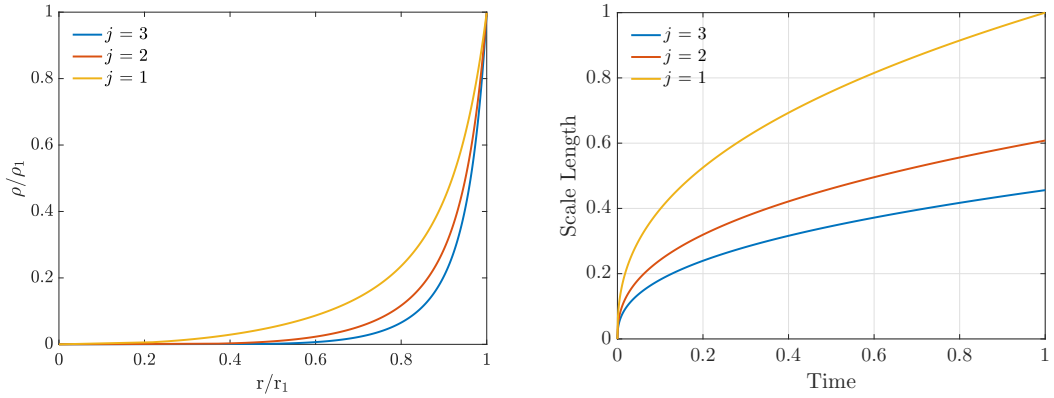


Figure 3.6: (a) The normalised density profile of a blast wave as a function of radius for $\gamma = 1.4$ and $j = 1$, 2 and 3. (b) Normalised scale length as a function of expansion time.

that is swept up by the shock front occupies a larger volume; the peak density condition of the shock (equation 3.5b) results in a longer scale length.

Let us now address some of the limitations of the model. Practically speaking, a number of the assumptions simply do not hold true in the real world. Energy deposition is not instantaneous, nor is the density homogeneous. Furthermore, the expansion is, in reality, not precisely cylindrical or spherical. However, despite this, the model represents a reasonable approximation of reality [209]. In fact Taylor was able to demonstrate remarkable agreement between these solutions and an "atomic explosion" [210]. Let us return to the idea of gas homogeneity. In practice, the density profile of the explosion medium will take an alternate form. Much work has studied alternative density profiles, be it exponential as in the atmosphere [211] [212] or of some other form as possible in astrophysical scenarios [213] [214] [215]. In fact, for reference Sedov also provides a more generalised set of solutions for density profiles that follow a power law of the form $\rho_1 = A/{r_0}^{\omega}$, where ω is a positive or negative constant that defines the density inhomogeneity and A is a positive constant.

Experimentally, shock generation can occur through the deposition of energy within a gas jet by a laser in a small, localised volume or along a narrow channel. The energy parameter, E, in this case is the absorbed laser energy. A number of authors have studied the formation of cylindrical BWs ($j = 2$) in gas cluster targets [217] [218] [219]. Here strong laser absorption by the clustered medium along the laser path creates a hot plasma filament which can drive a cylindrical BW. Nilson et al. [172] showed that at late times a cylindrical collisionless shock formed in an underdense helium gas jet decays into a cylindrical BW which followed the predicted scaling given by equation 3.7.

As earlier stated, BWs can be used to favourably shape the gas profile and provide steeper density gradients, as shown in figure 3.7. Aside from the favourable density scale length, the density increase from equation 3.5b allows for over-critical density targets

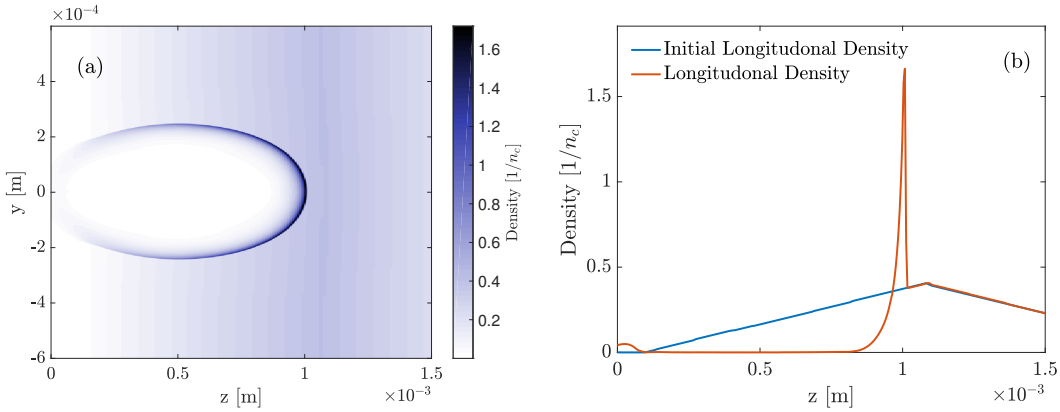


Figure 3.7: (a) Two-dimensional image of a blast wave in a gas jet, produced using the hydro-code FLASH [216]. (b) Longitudinal density lineouts for the same shock, demonstrating the target shaping and increased, steeper density profile.

while minimising the background target density; from equation 2.91, this maximises the ion energy.

Practically, for the work in this thesis, a blast wave is achieved in one of two ways. Firstly, a CO_2 pre-pulse can be used to deposit $\sim 1-10\,\mathrm{mJ}$ of energy in the jet at some time, $\tau \sim 5-25\,\mathrm{ns}$, before the main pulse. Ionisation can result in over-critical plasma formation and impeded propagation of the pre-pulse, leading to more localised heating and a spherical expansion of the BW. This method has been studied theoretically, through simulations and experimentally by Dover et al. [199] and is the basis for a number of previous experiments [141] [181]. The time is dependent on the pre-pulse mechanism used. This is achieved through pulse splitting before the regenerative amplifier or is part of a pulse train inherent to the laser generation process, with the timing variable and fixed at 25 ns, respectively. This method is desirable since it deposits energy on picosecond timescales in an assumed small, localised volume and has both energy and timing flexibility. It also provides variability of the deposition region within the gas in three dimensions. In reality, this method suffers from a number of challenges related to reproducibility. The inherent instability of the laser can result in large energy variations which appreciably affect the BW generation.

The second method involves the use of a stainless steel "clip", positioned on top of the nozzle such that it covers the edge of the gas flow. This has also been used previously for ion acceleration experiments at the ATF [220] [182]. The clip is shot with a secondary YAG laser, focussed with energy $\sim 70\,\mathrm{mJ}$ and pulse length $\tau_{\mathrm{YAG}} = 5\,\mathrm{ns}$. The clip is heated by the laser, ejecting ablated material in to the gas inducing heating and a shock to form. This approach is based on a similar scheme developed in which the nozzle is shot directly [221]. This scheme offers the benefit of superior shot to shot reproducibility of the shock, along with variable timing. However, it suffers the major drawback that the laser pulse length is long, of the order of hydrodynamic

timescales. As such long expansion times are required, giving larger expansion radii and shallower density gradients at the rear of the shock; this is conventionally believed to be undesirable for ion acceleration.

For the purposes of this thesis, both pre-pulse generation mechanisms are used.

3.3 Optical Diagnostics

An important branch of diagnostic tools for characterising a plasma created during laser-matter interactions are optical probes. These beams propagate through a plasma, typically transversely to the drive laser, and through the phase change induced by density gradients allow plasma conditions to be inferred. For this to be possible at near- and above-critical densities, the probe beam is often at a much higher frequency to ensure the beam can propagate. If this were not the case the probe beam would be refracted to such an extent it would not be collected for imaging or, in extreme cases for $n_e > n_c$, it would not propagate at all.

Given this information, probe beams are often frequency doubled (or higher order) sections of the main driver pulse, or better still separate, higher frequency beams. For this thesis a separate, synchronised YAG beam, also employed in the CO_2 laser chain, is used at both its fundamental (1064 nm) and second harmonic (532 nm) wavelengths. Each harmonic is further split by polarisation with all beams independently, temporally tunable to provide up to four-time optical probing of the interactions on any given shot.

3.3.1 Shadowgraphy

Shadowgraphy is the process by which the spatial intensity profile of an optical probe beam is imaged and the modulation of this profile used to infer information about density gradients within the plasma. Typically, the beam traverses the plasma before being imaged at the detector plane at a distance L from the plasma, as shown in figure 3.8.

For a given plasma profile, the phase difference, ϕ, along a given path can be expressed as

$$\phi = \int \frac{\omega}{c} \eta \, \mathrm{d}l \tag{3.15}$$

Hence, in the small angle approximation ($\theta \ll 1$ and $L \gg d$), the angle of deflection of the emerging wavefront, θ, is given as [222]

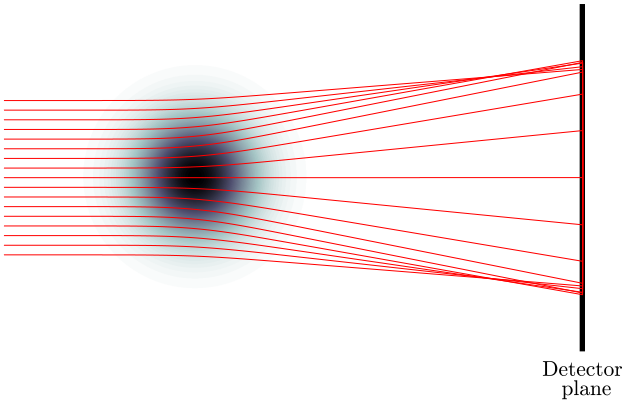


Figure 3.8: Schematic of refraction effect through a cylindrically symmetric, gaussian plasma. Refraction leads to regions of high and low intensity at the detector plane.

$$\theta = \frac{\mathrm{d}\phi}{\mathrm{d}y}\frac{\lambda}{2\pi} = \frac{\mathrm{d}}{\mathrm{d}y}\int \eta \,\mathrm{d}l \tag{3.16}$$

For shadowgraphy, variations in the intensity arise from deviations in the wavefront due to refraction in the probed medium which, when projected to the imaging plane cause regions of relative high and low intensity. For a given light ray, in 1D the beam would be deflected from its initial position, y, to $y' = y + \theta \cdot L$, which can be re-expressed as

$$y' = y + L\frac{\mathrm{d}}{\mathrm{d}y}\int \eta \,\mathrm{d}l \tag{3.17}$$

As such, the deflection in 2D can be given more generally as

$$(x', y') = \left(x + L\frac{\mathrm{d}}{\mathrm{d}x}\int \eta \,\mathrm{d}l \,,\, y + L\frac{\mathrm{d}}{\mathrm{d}y}\int \eta \,\mathrm{d}l\right) \tag{3.18}$$

If the intensity of the incident beam is uniform and since the total amount of light is conserved, the adjusted intensity at the detector plane becomes $I'dx'dy' = Idxdy$ and the change in intensity profile at the imaging plane can be expressed as

$$\frac{I}{I'} = 1 + \left[\frac{\mathrm{d}^2}{\mathrm{d}x^2} + \frac{\mathrm{d}^2}{\mathrm{d}y^2}\right]\int \eta \,\mathrm{d}l \tag{3.19}$$

This expression implies the refraction of the beam is dependent on the second derivative of the refractive index which itself confirms the effect is dependent on the plasma

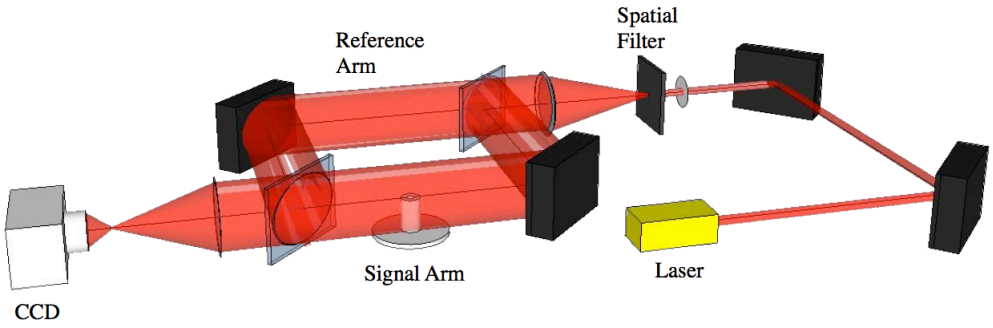


Figure 3.9: Schematic of a Mach-Zehnder interferometer. A laser is split into two arms, a reference arm which passes unperturbed, and a signal arm, which traverses the medium to be probed. These are recombined, with the relative phase difference between the two arms allowing information about the medium to be inferred. Figure by Chaya Kelly.

density.

The intensity profile at the detector will be a combination of bright and dark patches (high and low intensities). Dark regions in the image represent high density gradients. For the experiments in this thesis, the refracted beams are collected by a large numerical aperture imaging lens; this is a requirement to ensure strongly refracted rays can be collected. The beam can then be imaged onto a CCD.

3.3.2 Interferometry

Interferometry describes the method by which two laser beams are interfered with each other in the detection plane. The two beams are incident on the detector with a small angular offset to each other, resulting in a phase difference which gives a periodic fringe (interference) pattern. For experimental purposes, the formed image in this scenario is referred to as the reference image. Should one of the arms pass through a plasma or gas, this induces a further phase shift due to the refractive index gradients, perturbing the periodic fringe structure. Comparison of a reference and perturbed image allows for the density profile of the probed medium to be retrieved.

There exist a number of different methods to achieve interferometry, but for the purposes of this thesis a variation on the Mach-Zehnder is used. Traditionally, the Mach-Zehnder system splits the probe beam in two before the interaction region, with one arm perturbed by the gas or plasma while the other is undisturbed. This is shown in figure 3.9. These are then recombined before being imaged on a CCD. This is the scheme used for gas jet calibration, as outlined in section 3.2. Experimental interferograms in the following chapters use only one beam which is interfered with itself. The beam is larger than the interaction region so that both perturbed and unperturbed regions exist, the beam can be split after the interaction and these two regions can be overlapped at the detector. This has a number of advantages, with the most important being the relative

ease of temporally overlapping the two beams. Since the dynamics in a laser plasma interaction occur on very fast timescales ($< 1\,\mathrm{ps}$), the probe beam is also necessarily temporally very short; this ensures interaction dynamics can be resolved without being smeared out. Strict requirements on the spatial accuracy of the path length in the two arms are imposed. By splitting post interaction and recombining quickly, this minimises the path length and makes temporal alignment significantly more simple.

To deconvolve the plasma density, the phase shift, ϕ, must first be calculated. The recorded intensity profile for the perturbed arm can be expressed in the form

$$I(x,y) = I_b(x,y) + I_f(x,y)\cos\left(ky + \phi(x,y)\right) \tag{3.20}$$

where I_b and I_f describe the intensity profiles of the background and fringes, respectively, and $k = 2\pi/\lambda_f$ with λ_f the fringe spacing. Expansion of the cosine gives

$$I(x,y) = I_b(x,y) + \frac{1}{2}I_f(x,y)e^{i[ky+\phi(x,y)]} + \frac{1}{2}I_f(x,y)e^{-i[ky+\phi(x,y)]} \tag{3.21}$$

Note that this implies a π phase shift in the perturbed image would result in a $\lambda_f/2$ shift in a given fringe relative to the reference image; a fringe maximum would become a minimum. Similarly, for the reference image the intensity profile takes the form

$$I(x,y) = I_b(x,y) + \frac{1}{2}I_f(x,y)e^{iky} + \frac{1}{2}I_f(x,y)e^{-iky} \tag{3.22}$$

A two-dimensional Fourier transform acting upon equation 3.21 yields an expression for the intensity profile in frequency space

$$\widetilde{I}(p,q) = \widetilde{I}_b(p,q) + \Gamma(p,q) + \Gamma(p,-q) \tag{3.23}$$

where $\Gamma(p,q)$ and $\Gamma(p,-q)$ are the Fourier transforms of the second and third terms in equation 3.21, respectively. This results in a profile in Fourier space consisting of three peaks, separated by $\pm k$ from the centre, where the $k = 0$ central peak arises from the $\widetilde{I}_b(p,q)$ signal. Through selection of a region of Fourier space including only one of the outer peaks, a mask can be applied to both the reference and perturbed images. This mask will remove both the contribution of the $\widetilde{I}_b(p,q)$ signal and any high frequency noise, leaving only the contribution from, for example, $\Gamma(p,q)$. The inverse Fourier transform can then be applied to both images which gives 2D images of the phase information contained in the $\frac{1}{2}I_f(x,y)e^{i[ky+\phi(x,y)]}$ term in equation 3.21. The ratio of the perturbed image to the reference can be taken

$$\frac{I'_f(x,y)}{I'_b(x,y)} = \frac{\frac{1}{2}I_f(x,y)e^{i[ky+\phi(x,y)]}}{\frac{1}{2}I_f(x,y)e^{iky}} = e^{i\phi(x,y)} \tag{3.24}$$

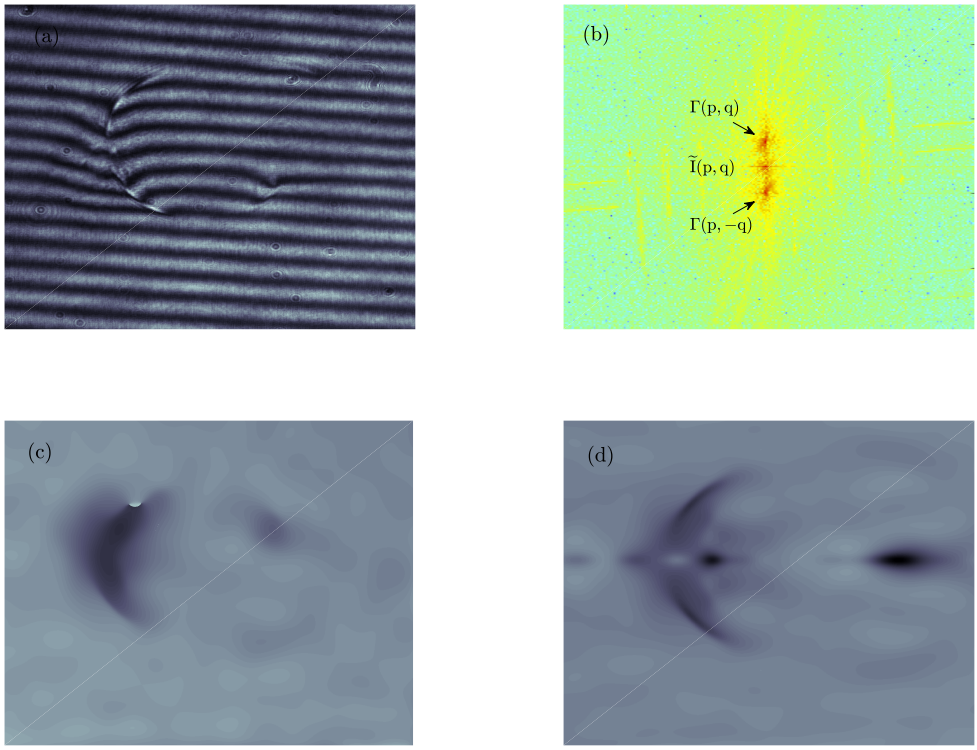


Figure 3.10: (a) Raw interferometry image of a collisional shock wave, (b) The three Fourier components of the interferometry image, (c) the retrieved phase profile and (d) the retrieved density profile. The on-axis feature is not real and an artefact of the Abel inversion.

The relative phase can then be expressed as

$$\phi(x,y) = \arctan\left(\frac{I'_f(x,y)}{I'_b(x,y)}\right) \tag{3.25}$$

where $\phi(x,y)$ can assume any value between $-\pi$ and π. The phase shift can be used to extract the density of the gas through use of an Abel inversion, which in its general form is given as

$$F(y) = 2\int_y^\infty f(r)\frac{r}{\sqrt{r^2-y^2}}dr \tag{3.26}$$

This assumes a radially symmetric density profile. The phase shift and density can be related using

$$\Delta\phi(y,z) = \frac{2\pi}{\lambda_L}\int_{-\infty}^{\infty}(\eta(r,z)-1)\;dx = \frac{4\pi}{\lambda_L}\int_0^\infty(\eta(r,z)-1)\;dx \tag{3.27}$$

The refractive index of a plasma was given previously in equation 2.13 and can be expanded in the limit $\omega_L \gg \omega_p$ to give $\eta \approx 1 - \frac{1}{2}\frac{{\omega_p}^2}{{\omega_L}^2} = 1 - \frac{1}{2}\frac{n_e}{n_c}$, with n_c the critical density of the probe beam. The phase difference can be re-expressed as

$$\Delta\phi(y,z) = -\frac{2\pi}{\lambda_L}\int_0^\infty \frac{n_e(r,z)}{n_c}\,dx \tag{3.28}$$

Transforming into polar co-ordinates using $r = \sqrt{x^2+y^2}$ and changing the integration variables to r gives

$$\Delta\phi(y,z) = -\frac{2\pi}{n_c\lambda_L}\int_y^\infty \frac{r}{\sqrt{r^2-y^2}}\,n_e(r,z)\,dr \tag{3.29}$$

This is now exactly of the form of the Abel inversion (equation 3.26). The inverse Abel inversion can be expressed as

$$f(r) = -\frac{1}{\pi}\int_r^\infty f(r)\frac{\mathrm{d}F(y)}{\mathrm{d}y}\frac{\mathrm{d}x}{\sqrt{y^2-r^2}} \tag{3.30}$$

Therefore, the plasma density can finally be expressed as

$$n_e(r,z) = \frac{n_c\lambda_L}{\pi^2}\int_r^\infty \frac{\mathrm{d}\phi(y,z)}{\mathrm{d}y}\frac{\mathrm{d}x}{\sqrt{y^2-r^2}} \tag{3.31}$$

$\frac{\mathrm{d}\phi(y,z)}{\mathrm{d}y}$ is the gradient of the phase and can be extracted from the phase map retrieved from the interferometry images. By performing an Abel inversion for all values of z in

the image, $n_e(r, z)$ can be obtained.

Interferometry analysis in this thesis is conducted using the Interpret [223] code, written by Jason Cole from the Imperial College plasma physics group, or the Magic code [224] [225], written by George Swadling, formerly of the MAGPIE group at Imperial College. Interpret retrieves the density profile as outlined in this section. A number of alternative phase retrieval methods are offered by the code, but only the method described here was used. The code is particularly useful since it is fully automatable, which is desirable for analysing large volumes of data. However, the code cannot handle interferograms with poor fringe contrast, in which case manual intervention is required.

Magic uses a different approach to the density retrieval. By recognising that the fringe spacing in the interferometric image represents a 2π phase shift, the displacement of each fringe is used to calculate the density. First, the fringes are traced using a combination of automated and manual fringe tracing. Automatic tracing is achieved by following the maximum and minimum values either side of a user set threshold value. Manual fringe tracing is used in regions of the image where this process fails; the fringes are traced by the user with a drawing package such as Adobe photoshop. The automated tracing fails in regions of poor image contrast, and where interferometric information is lost due to very sharp density gradients, causing probe deflection outside the collection angle of the imaging system. Phase maps of the modified and reference images are extracted by interpolating between the fringes using a linear interpolation method, called a Delaunay triangulation algorithm [224]. Subtraction of the background phase map from the modified map gives the phase due to the plasma. The electron density can then be extracted. For a 532 nm probe the areal electron density per fringe shift is $4.2 \times 10^{17}\,\mathrm{cm}^{-2}$. The density is extracted by multipling the phase map by the areal density calibration and then dividing by the size of the plasma structure in the direction of probing. While this tool provides a reliable method for density extraction from the interferograms, the process is often extremely labour intensive; manual fringe tracing of a single image can often take several hours.

The choice of analysis code therefore depends on the quality of the interferograms obtained. For those with good fringe contrast, Interpret is used as this offers the fastest density retrieval. For those interferograms where Interpret fails, manual fringe tracing in combination with Magic is used.

3.4 Ion Diagnostics

Ions can be detected in a number of ways on laser-plasma experiments. Radiochromic film stacks are placed directly into the beam path and utilise the deposition characteristics of ions to create two-dimensional spatial profiles in discretised energy bins [226]. The film undergoes a chemical reaction when exposed to radiation due to damage induced in the molecular bonds, turning blue. The greater the change in colour the higher

the particle flux. Columbia resin 39 (CR-39) [227] [228] [229] works on a similar principle, with damage centres induced within the resin due to the ionising radiation. This is then etched in a heated sodium hydroxide solution with the damage centres preferentially etched away, forming pits. These can be imaged under a microscope, with the size and shape of the pit giving information on the ion species. Absolute numbers are retrievable, with longer etching times giving higher ion energies.

Work in this thesis uses a third method for detection of ions. A Thomson parabola [230] magnetic spectrometer is used in combination with a scintillator, as described below. Unlike radiochromic film and CR-39, this samples only a small portion of the ion beam, but have the added benefit of increased ion energy resolution.

3.4.1 Magnetic Spectrometer

A Thomson spectrometer allows for the detection of ions through their dispersion via magnetic and electric fields. Both fields are perpendicular to the incoming ion beam and parallel to each other. Consider an incoming ion of charge q, mass m, travelling in the $\hat{z}$ direction through perpendicular electric and magnetic fields, orientated in the $\hat{y}$ direction. Assume magnetic and electric fields of length L_B and L_E, respectively, also in the $\hat{z}$ direction, with the propagation distance from the respective field regions to the detector plane given by ξ_B and ξ_E. These are illustrated in figure 3.11.

Ions in the fields will experience a Lorentz force (equation 2.55), and the equations of motion can be expressed as

$$\ddot{x} = \frac{q}{m} v_z B_y \tag{3.32a}$$

$$\ddot{y} = \frac{q}{m} E_y \tag{3.32b}$$

The dispersion of ions occurs in two steps, first during the region of the field and second between the field and detector. These are denoted by the subscripts i and ii, respectively. The velocity in x due to the deflection of the magnetic field is given by

$$\dot{x} = \frac{q}{m} v_z B_y \int dt = \frac{q B_y}{m} z \tag{3.33}$$

where $z = v_z t$. The deflection within the magnetic plates, assuming constant velocity

v_z, is then given by

$$x_i = \frac{qB_y}{m} \int_0^{t=\frac{L_B}{v_z}} z \cdot dt \tag{3.34a}$$

$$x_i = \frac{qB_y}{mv_z} \int_0^{L_B} z \cdot dz \tag{3.34b}$$

$$x_i = \frac{qB_y}{mv_z} \frac{{L_B}^2}{2} \tag{3.34c}$$

Similarly, the deflection between the field region and the detector can be expressed as

$$x_{ii} = \frac{\xi_B}{v_z} \dot{x} L_B = \frac{qB_y}{mv_z} L_B \xi_B \tag{3.35}$$

Finally, the complete deflection can be expressed as

$$x = \frac{qB_y}{mv_z} L_B \left(\frac{L_B}{2} + \xi_B \right) \tag{3.36}$$

Similarly, the deflection due to the electric fields follows the equivalent procedure. As such, it can be expressed as

$$y = \frac{qE_y}{m{v_z}^2} L_E \left(\frac{L_E}{2} + \xi_E \right) \tag{3.37}$$

By eliminating the velocity from equations 3.36 and 3.37 the complete dispersion profile can be expressed as

$$y = \frac{mE_y}{q{B_y}^2} \frac{L_E}{L_B} \frac{\frac{L_E}{2} + \xi_E}{\left(\frac{L_B}{2} + \xi_B \right)^2} x^2 \tag{3.38}$$

This says that ions of equivalent charge-to-mass ratio are dispersed on a parabolic trajectory. Multiple ion species with differing ratios will therefore result in multiple traces. In practice, however, for the work in this thesis only proton acceleration is considered. As such, only the magnetic deflection, as given in equation 3.36, is of interest.

Proton data extraction

The ion spectrometer used on experiments presented in this thesis has the ability to provide both electric and magnetic field deflection, although in practice only the magnetic field is required. The ion spectrometer set-up specific to experiments at the ATF is shown in figure 3.11.

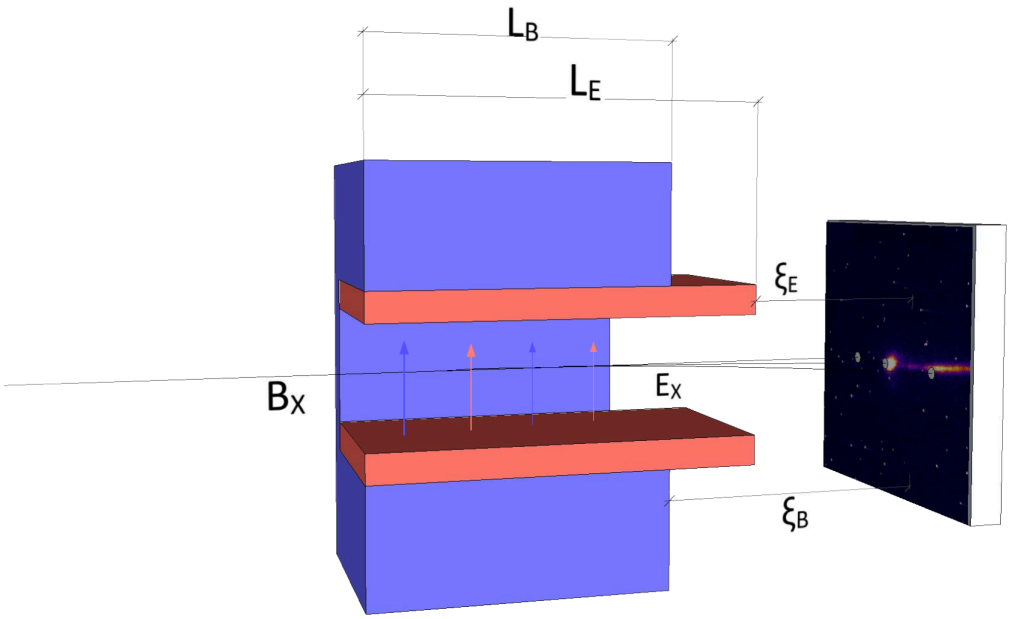


Figure 3.11: A schematic of the magnetic ion spectrometer used for experiments at the ATF. The magnet is depicted in blue, while the electric field plates are in red. An image of a raw proton trace image is displayed at the scintillator plane. Figure by Chaya Kelly.

The ion acceleration experiments conducted were using hydrogen gas and hence only proton acceleration was observed. Given only a single species is expected, the need for the electric field dispersion is removed. Typically the proton beam is passed through a 600 µm pinhole or 1 cm × 600 µm slit, located along the laser axis. The size of the pinhole or slit is a compromise between larger sizes to maximise the fraction of the beam observed and smaller sizes to improve spatial and therefore spectral resolution. For multi-species traces the additional requirement on the size is imposed; it must be small enough that ions tracks do not cross. Protons pass through the magnetic field and are dispersed onto a BC − 422Q scintillator from Saint-Gobain crystals [231]. The scintillator is flash coated; this is a thin layer of aluminium deposited on the surface aimed at stopping stray laser light exciting the scintillator. The ions deposit energy which causes electron excitation and subsequent emission which is imaged with an Andor iXon CCD camera. Further information about the choice of scintillator can be found in the paper by Cook et al. [232].

The dispersion of ions through the magnetic field was calculated using the measured magnetic field profile, a quasi-flat top profile with peak field strength 0.44 ± 0.005 T, and analytic proton tracking simulations for the specific field profile. This gives a relation for the energy, E [MeV], as a function of the dispersion, x [mm], taking the form of a polynomial given by equation 3.39 and plotted in figure 3.12.

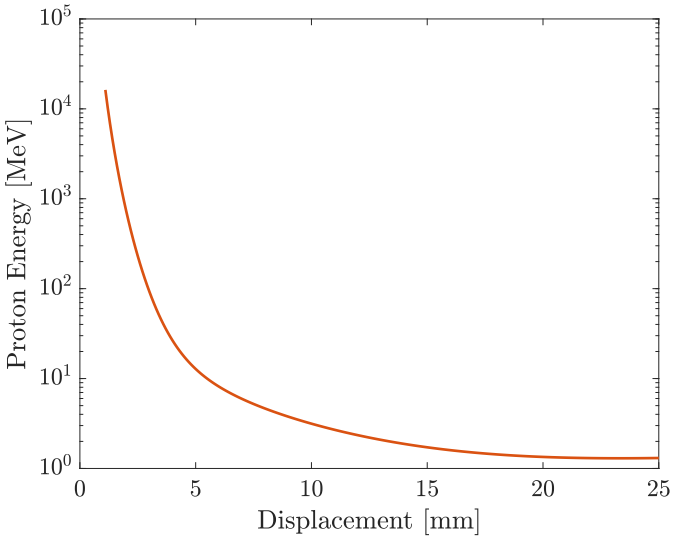


Figure 3.12: The proton energy as a function of dispersion displacement for the magnetic ion spectrometer used on experiments at the ATF.

$$E(x) = \frac{28390}{x^5} - \frac{2605}{x^3} + \frac{715.5}{x^2} - \frac{21.61}{x} + 0.004760x \tag{3.39}$$

Raw images typically consist of an zero point, produced by neutral particles which are not deflected by the fields, then the proton signal. This is illustrated in figure 3.11. Spurious signal is also often present, caused by laser light activating the scintillator due to defects in its flash coating, along with so called hard hits on the image, which are produced by bremsstrahlung x-rays incident on the camera CCD. Noise present in the image is typically significantly higher in counts than the real signal and localised to a region spanning only a few pixels. Before analysis, these features are removed from the image by the application of a median filter, the size optimised to remove the spurious signal while minimising the effect on real data. These regions are then interpolated over to give an expected real signal level.

Proton fluxes were extracted through vertical integration over the signal trace (the spatial dimension) for each energy bin. This total count level was then adjusted to compensate for the optical imaging system and the CCD response of the camera. The scintillator response was previously calibrated at the ATF with slotted CR-39 using the proton spectrum from a foil target to give a comparison of absolute proton counts as a function of energy [233]. The response was shown to be broadly linear over the energies concerned. An angularly resolved signal is then obtained in the direction perpendicular to magnetic dispersion, assuming the source size is much smaller than the slit/pinhole size. Subsequently, a full integrated spectrum can be achieved by considering the sampling angle of the diagnostic. The energy resolution is determined by the resolution of the scintillator imaging system. Given the dispersion is non-linear with energy, so too the energy resolution is non-linear, with increased resolution at lower energies. A full

Parameter	Value
Laser focus to pinhole/slit	$150 \pm 0.5\,\text{mm}$
Pinhole diameter	$600\,\mu\text{m}$
Slit dimensions	$10 \times 0.5\,\text{mm}$
Pinhole to magnet	$30 \pm 0.5\,\text{mm}$
Length of magnet, L_B	$50 \pm 0.5\,\text{mm}$
End of magnet to scintillator, ξ_B	$45 \pm 0.5\,\text{mm}$
Magnetic field strength	$0.44 \pm 0.005\,\text{T}$
Length of electric field, L_E	$65 \pm 0.5\,\text{mm}$
End of E-field to scintillator, ξ_E	$30 \pm 0.5\,\text{mm}$
Electric field strength	$0 - 2500\,\text{V}$
Scintillator to CCD	$100\,\text{mm}$

Table 3.1: Magnetic ion spectrometer parameters for experiments conducted at the ATF.

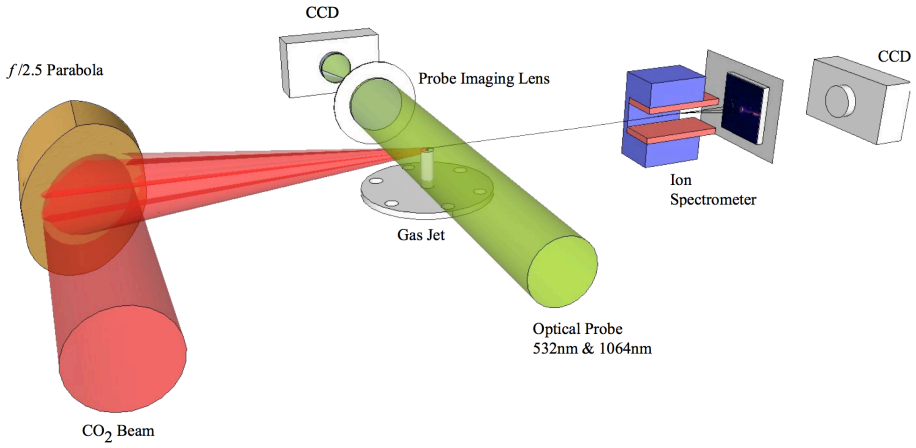


Figure 3.13: Diagram of the basic experimental setup for the experiments presented in this thesis. Figure by Chaya Kelly.

list of the diagnostic parameters are given in table 3.1.

The detector limit can also be found. The noise is said to be two standard deviations of the spatially dependent background of the image, which is applied to each energy bin to give the energy dependent detection limit.

3.5 Experimental Layout

The previous sections of this described the components of the experiments presented in this thesis. A complete experimental layout is given in figure 3.13 for reference.

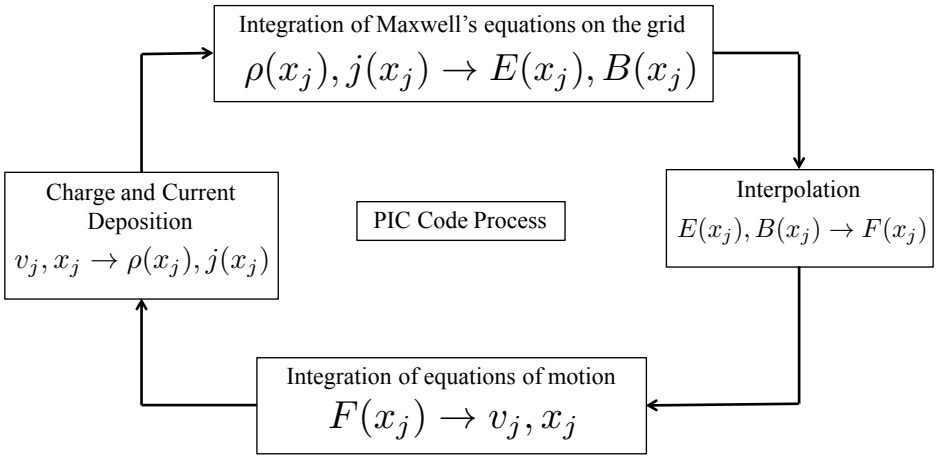


Figure 3.14: Schematic of the feedback loop followed by a PIC code such as EPOCH, proceeding in the clockwise direction, starting from the top of the diagram.

3.6 Particle in Cell Modelling

Complimenting the experimental work conducted for this thesis, numerical simulations have been carried out and will be presented. The complex nature of ion acceleration can make deconvolution of the relevant underlying mechanisms driving the interaction challenging. For any given experimental scenario, it is often difficult to interpret all of the physics occurring. Numerical simulations can provide information unattainable by experimental diagnostics and often important in understanding the subtleties of a situation. Furthermore, they allow for broad scans of a given parameter space beyond those which might be available experimentally, which can allow scalings to be determined and reveal interesting new routes to be explored experimentally.

The numerical simulations presented here were conducted using the particle-in-cell (PIC) code 'Extendable PIC Open Collaboration' (EPOCH) [234]. EPOCH, like similar PIC codes (e.g. OSIRIS [235]) used for laser-plasma interaction simulations, calculates the kinetic properties of charged particles within a system through their interaction with electromagnetic fields [236]. Since for critical densities the number of particles in a plasma is high, it would be computationally prohibitively expensive to attempt to simulate all these particles individually. As such, a given number of the plasma particles are grouped together into so called macroparticles. These occupy a finite volume of the plasma and are given a weighting function. Furthermore, the effects of electromagnetic forces on these particles are solved only at discrete points on a user defined grid superimposed over the plasma. The process followed by a typical PIC code is shown in figure 3.14.

First, the electric and magnetic fields are calculated on the grid using Maxwell's equations and integrating the charge and current densities. The next step is interpolation; the fields are interpolated onto the particle positions and then the Lorentz equation is solved to determine the particle push, i.e. the force on the particles. Finally, the motion

of the particles and their new positions can be used to update the electric and magnetic fields felt by the particles, which can be used to feed back into the loop and the cycle is repeated for the next time step.

For any given scenario to be simulated, the user is able to define a set of starting conditions, for example the laser temporal and spatial parameters, plasma particle distributions etc. Also defined are the grid upon which to solve the problem and any number of given outputs as a function of spatial and temporal co-ordinates, such as the laser and plasma fields, and particle velocity distributions. The result is a set of temporal snapshots of the interaction.

While PIC simulations offer the most practical solution for theoretical modelling of laser-plasma interactions, they have a number of limitations. These are primarily related to unphysical plasma heating effects within the simulations. There are two main sources of plasma heating in PIC codes:

1. The grouping of particles into macroparticles results in a loss of resolution of the particle fluxes through the cells of the grid, leading to 'noisy' current density profiles. These stochastic features can be imposed onto the calculated electromagnetic fields resulting in the anomalous transfer of energy to the particles and heating of the plasma. Clearly, the greater the number of macroparticles used, the less of an effect this is. Furthermore, the problem can be suppressed through the use of a higher order particle weighting functions to smooth out these unwanted fluctuations in current density. The particle weighting functions describe the distribution function that describes any given macroparticle.

2. Similarly, if the Debye length (equation 2.2) is not resolved, plasma heating can also occur. If the size of the grid is insufficient to resolve the Debye length then high frequency plasma oscillations may not be resolved and a low frequency mode may be assumed instead. Grid heating can then occur.

To resolve these issues then, it seems logical to simply use a combination of more macroparticles, shape functions with higher order terms for resolving the fields on the grid and by ensuring the grid can resolve the Debye length. This last condition can become particularly challenging for cold, dense plasmas given the Debye length becomes extremely small and the grid required equally fine. Furthermore, the time-step required between solutions is also linked to the grid size through the Courant condition, $\Delta t_{em} \leq \Delta x/c$. The Courant condition stipulates that the time-step, Δt_{em} is less than the time required for an electromagnetic wave to traverse any given cell of size Δx meaning more required timesteps for a smaller grid. Here, the computational power required to solve the problem becomes expensive. The grid size is therefore chosen to be as large as possible such to minimise computation requirements, but small enough that no unphysical effects, such as numerical heating, arise on the timescales of interest. This is achieved by fully resolving the Debye length and the Courant condition is met.

4 Radiation pressure acceleration of protons at near critical densities using a CO_2 laser

One of the major challenges for laser-driven ion sources is the requirement for high repetition rate operation to facilitate their use for applications. Conventional thin metal and plastic foil targets are by their nature not suitable; manufacture and alignment are time consuming. A number of solutions have been posited, for example a tape drive or a moving, larger area target which can be shot multiple times. However, these present new challenges pertaining to accurate positioning of the target at the laser focus. Gas targets offer the chance for higher shot rates, while also offering the benefits of simple species selection and a lower propensity for contamination. However, if left unmodified, their quasi-triangular density profile [180] is not conducive to efficient ion acceleration. To achieve radiation pressure acceleration the target must exhibit substantial reflection and as such be very near- or over-critical in density to the laser. These densities for near-IR lasers ($\sim 10^{21}\mathrm{cm}^{-3}$) have until now proved challenging to achieve with gas targets, although near [237] and over critical [238] densities have been reported. Recent experiments have also demonstrated the production of MeV level collisionless shock accelerated protons from over-critical density targets [239], while other authors have suggested sub critical gas targets ($\sim 0.01 n_c$) can be used to produce higher energy ions produced through low density collisionless shock [240] and later in combination with sheath acceleration [241].

With their increased wavelength, CO_2 lasers exhibit a factor 100 lower critical density, which is readily achievable with standard gas delivery equipment. This has made possible the study of RPA in gas targets. Previous work by Imperial College and collaborators [141], [180] [181] [182] [242] and others [167] established the ability to produce radiation pressure accelerated ion beams through HB-RPA and collisionless shock acceleration. Palmer et al. [141] demonstrated proton beams of energies $\approx 1\,\mathrm{MeV}$ with very narrow energy spreads $\Delta E/E \approx 4\,\%$. Furthermore the authors were able to demonstrate an I_L/n_i scaling of the proton energy, which is indicative of hole-boring.

The work in this chapter originates from a follow-up experiment intended to further this work. The results presented here will demonstrate increased proton energies over those obtained on previous experiments, and an excellent agreement with the $4I/nc$ hole-boring scaling.

Parameter	Value
Laser energy to chamber	1.45 - 4.01 J
Energy in focal spot	0.51 - 1.4 J
Focal spot size	35 µm
Pulse length	3.5 ps
Laser intensity at focus	1.5 - 4.16 $\times 10^{16}$ Wcm^{-2}
a_0 at focus	1.06 - 1.77

Table 4.1: CO_2 laser parameters for the results presented in Chapter 4

4.1 Experimental Overview

4.1.1 Laser Parameters

Work presented in this chapter used the CO_2 laser at the ATF, operating in the 10R branch at 10.2 µm. A 3.5 ps beam with a mean measured energy at the chamber entrance of 2.76 ± 0.6 J, ranging between 1.45 J and 4 J was used. The laser energy is delivered in the form of a pulse train, with pulses separated by 25 ps containing ~ 70 % of the energy in the main pulse and a further 30 % in post-pulses [243]. No on-shot measurements of the focal spot were possible, so a best case scenario is assumed, with 50 % energy contained in the focal spot as would be the case for a perfect gaussian. This is an upper bound and in practice is likely to be lower. Using this assumption, the mean energy on target was equivalent to ~ 1 J, ranging between 0.5 J and 1.4 J, with a measured spot size of $\omega_0 \approx 35$ µm. This equates to intensities of 1.5 - 4.6 $\times 10^{16}$ Wcm^{-2} and normalised vector potential values of $a_0 = 1.06$ - 1.77. The complete range of laser parameters for the results presented in this chapter are given in table 4.1.

Also present in the temporal profile were a number of parasitic pre-pulses. These originate from leakage of the seed pulse on the latter passes through the regenerative amplifier. These are subsequently amplified in the main amplifier. The separation between the main and any pre-pulses is fixed to ~ 27.5 ns steps, equivalent to the length of a double pass of the regenerative amplifier chain. An example of the laser temporal structure, including pre-pulses, is shown in figure 4.1. This was obtained using a photodiode and was used to provide on shot pulse train information, allowing measurement of the pre-pulse energy. Note that the peak pulse signal is saturated and its relative height compared to the pre-pulse is not representative. This was to ensure a measurement of the pre-pulse energy could be obtained on each shot; the dynamic range of the diode was such that simultaneous measurement of the pre-pulse and main pulse energy ($\sim 10^3$ difference) was not possible. However, these pre-pulse energies were subtracted from the total integrated energy measurement used to obtain the main pulse energies given in table 4.1.

Unlike in previous studies [141], the laser was linearly p-polarised. Recent laser developments have resulted in the introduction of chirped pulse amplification (CPA) to the

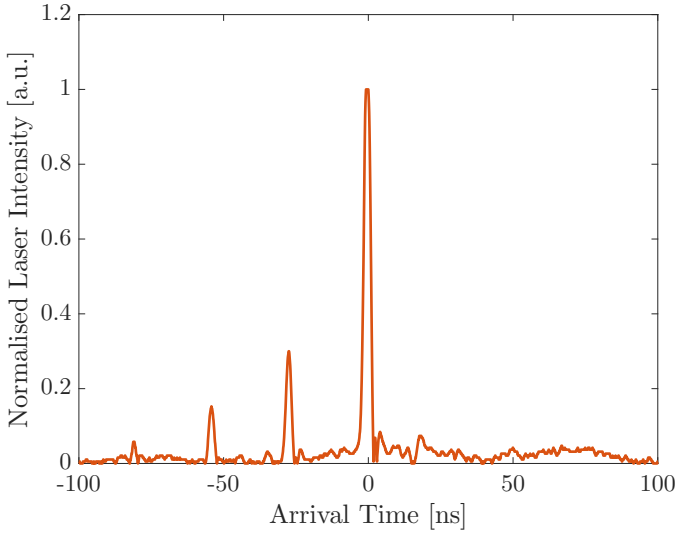


Figure 4.1: An example CO_2 temporal profile spanning 200 ns, showing the presence of parasitic pre-pulses at ~ 27.5 ns intervals before the main laser pulse.

laser system [193], the first time that this has been achieved with a CO_2 laser. The beam transport lines are all in air. Previously the beam was not stretched and susceptible to high levels of B-integral, with the result being the potential for a strongly modulated spatial profile of the laser. The introduction of CPA has worked to reduce this effect, but at the cost of no longer being able to achieve circular polarisation. The wave-plate used has a low damage threshold and must be used before the main amplifier. However, the polarisation cannot be maintained after the recompression gratings, limiting current experiments to linear polarisation.

4.1.2 Targetry

The experiments in this chapter employed the "1 mm" nozzle design, as outlined in section 3.2 with hydrogen gas with absolute backing pressures ranging from $2 - 7$ bar, giving density profiles as demonstrated in figure 3.5. As stated in section 3.2, the density has previously been shown to scale linearly with backing pressure; backing pressures not shown in figure 3.5 can be linearly interpolated to achieve the required density profiles. Therefore peak molecular gas densities between $1.7 \times 10^{18}\text{cm}^{-3}$ and $1.3 \times 10^{19}\text{cm}^{-3}$ were achievable.

Target shaping occurred through the use of the optical pre-pulse, forming a blast wave. An example interferogram is shown in figure 4.2. The pre-pulse energy is tuneable through control of the discharge voltage of the regenerative amplifier. The non-linear amplification process makes control of the relative intensity levels possible, although in practice suffers from a great deal of shot to shot variability. Fortunately, since the blast wave expansion is a weak function of the absorbed laser energy ($r_b \propto E^{\frac{1}{5}}$ from equation 3.7), this variation in the pre-pulse energy does not translate into large variability in the

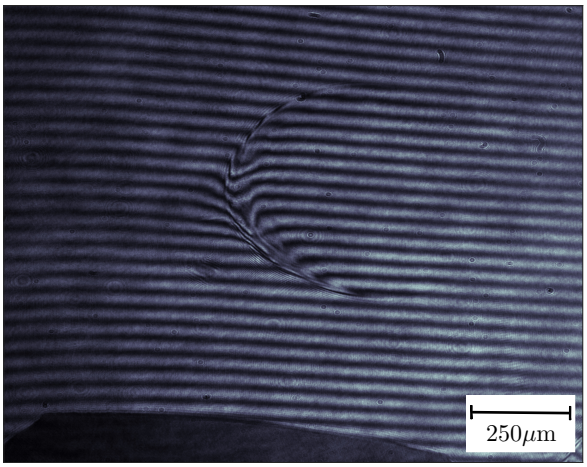


Figure 4.2: An example interferogram of a pre-pulse driven blast wave, 10 ps before the arrival of the main CO_2 pulse.

shock motion for a given gas density. The pre-pulse energy was set such that it ranged between $0.3 - 3.7$ mJ for all shots on which protons were observed (both thermal and peaked beams), with a mean value of 1.4 ± 0.4 mJ. These energies were between the target range of $1 - 5$ mJ, previously demonstrated to be favourable for radiation pressure acceleration of protons from a hydrogen gas jet by Tresca et al. [181]. The pre-pulse energies are at the lower end of the range given by Tresca et al. because the densities in this work were lower. Subsequently, less energy is required to achieve equivalent expansion conditions, as demonstrated by equation 3.7.

4.1.3 Diagnostics

This experiment utilised the magnetic ion spectrometer, as described in section 3.4.1. A 1 cm by 500 µm slit was used at the entrance to the spectrometer, providing energy and limited spatial information about the proton beam.

Optical probes were also used, consisting of an ~ 8 ps, fundamental 1064 nm and frequency doubled, 532 nm probe beam providing variable four time shadowgraphy through wavelength and polarisation selection. Two time interferometry was also used at second harmonic. This beam was synchronised to the CO_2 laser such that it could be timed to arrive before or up to 5 ns after the main CO_2 pulse responsible for ion acceleration. The beams were chosen to arrive such that the early beam arrived at the same time as the main CO_2 pulse, while the second beam was employed at various times to study the post acceleration structure. Imaging of the acceleration process was not directly possible since the probe beam is longer than the CO_2 beam; any features are consequentially blurred out due to the long integration time of the probe. However, this is not an issue for studying hydrodynamic features, such as the density profile resulting from the BW.

The important timescales here are on the order of ns.

4.2 Experimental Results

During the experimental campaign a total of 946 shots were taken. Of these, 351 were commissioning shots to test the installation of new features aimed at combatting high levels of laser back-reflection which had hindered previous experiments, along with testing new laser capabilities. As such, 595 shots were considered "data shots", aimed at characterising the new region of parameter space and attempting to produce radiation pressure accelerated ions. Of these shots, 497 produced observable protons, equivalent to 84 % of shots and significantly better than the 10 % achieved in earlier work [233]. Most proton spectra took the form of low energy (< 1MeV) thermal traces. However, ~ 30 % of shots demonstrated spectral peaking of the proton energy, indicative of radiation pressure driven acceleration of the protons.

Presented here are a selection of 12 shots which exhibited strong spectral peaking of their energy. The laser conditions varied as given in section 4.1.1, with the gas jet backing pressure for these shots taking values between 2.15 and 7 bar; equivalent to peak gas densities between $1.9 \times 10^{18}\,\mathrm{cm}^{-3}$ and $1.3 \times 10^{19}\,\mathrm{cm}^{-3}$.

Three examples of these data shots are shown in figure 4.3. Presented are raw proton energy traces from the magnetic ion spectrometer. These are the raw scintillator images with the horizontal spatial scale converted to energy.

The only data manipulation carried out is the removal of hot pixels from the images through use of a median filter. Subsequent interpolation was then carried out over these modified pixels. These hot pixels are believed to be due to x-rays generated in the interaction process.

Analysis of the raw spectra presented in figure 4.3 can be carried out as discussed in section 3.4.1, providing raw energy spectra as shown in figure 4.4.

4.2.1 Spectral Characterisation

The raw proton spectra shown in figure 4.4 show the unconvolved spectrum of the traces shown in figure 4.3. The width of the spectral features in the direction of magnetic dispersion are similar. Given that a slit was used as the entrance aperture to the spectrometer, the instrument function of the spectrometer can be taken as the width of the zero deflection feature in the direction of magnetic dispersion. Since the scintillator is coated to stop activation by laser light, the zero point is the product of neutral particles, which experience no deflection; thus the instrument function can be extracted. This takes the form of a gaussian fitted to the integrated signal to provide a smooth

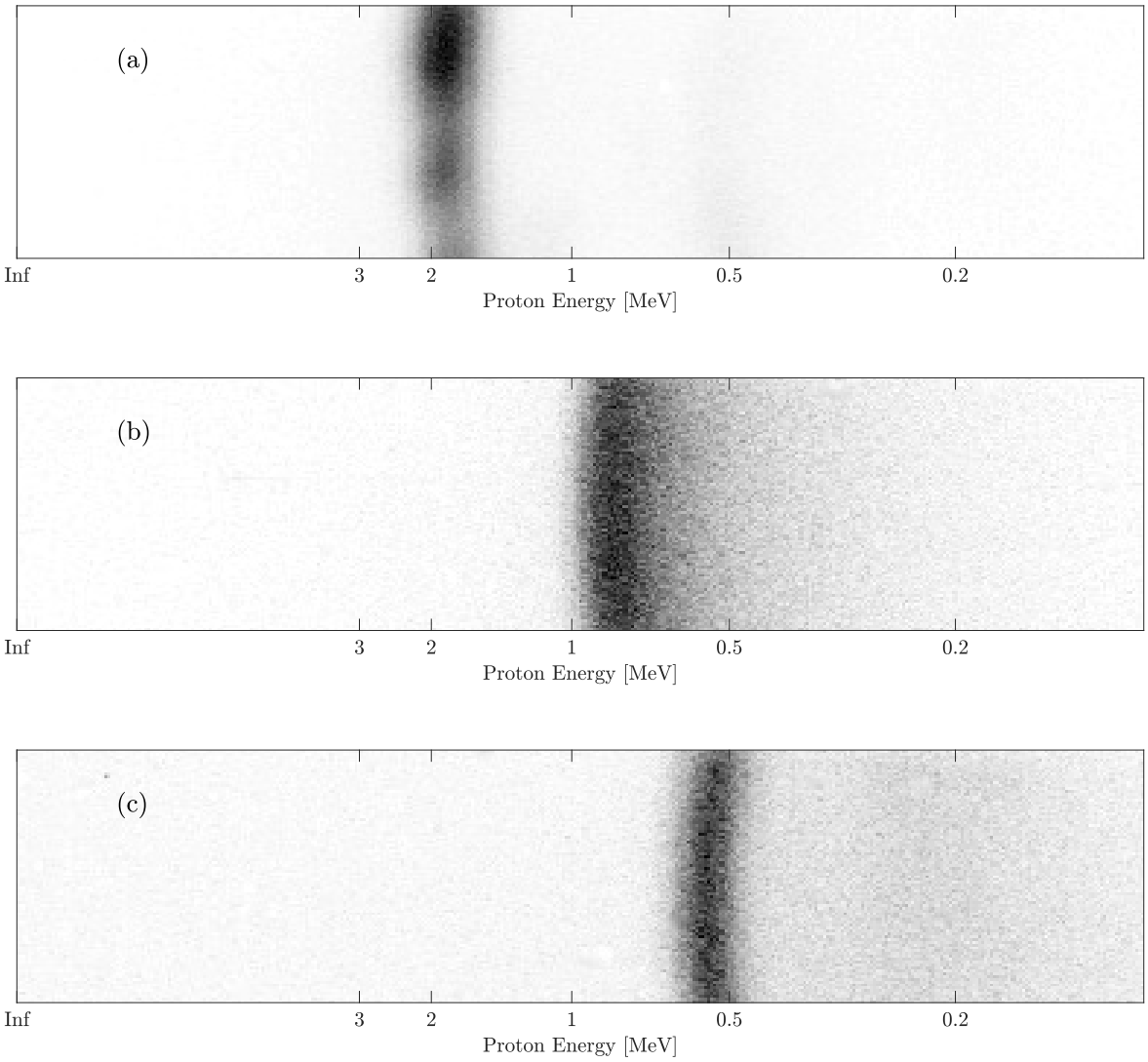


Figure 4.3: Example magnetic spectrometer proton energy traces which demonstrate the mono-energetic peaked spectra. For the three shots presented, the peak bunch energies are 1.84, 0.83 and 0.55 MeV for (a), (b) and (c), respectively.

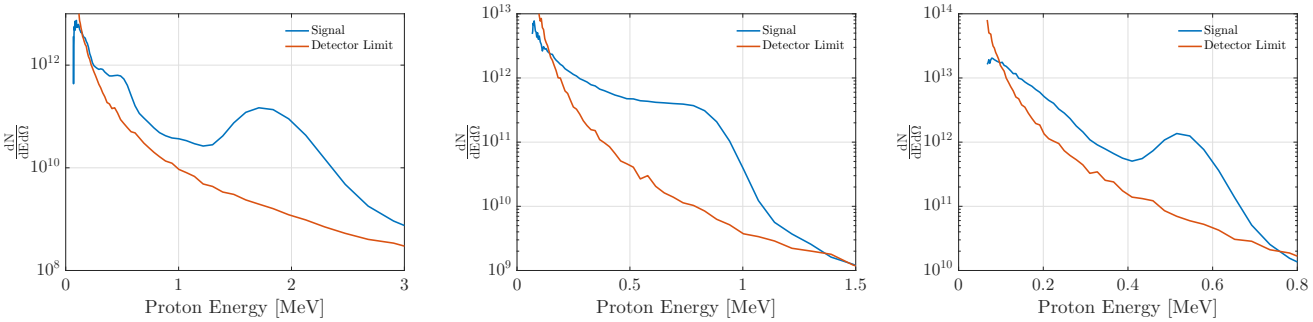


Figure 4.4: Example proton energy spectra for the three shots presented in figure 4.3. Peak energies of 1.84 MeV, 0.83 MeV and 0.55 MeV were observed for the top, middle and bottom profiles, equivalent to shots (a), (b) and (c) in figure 4.3, respectively.

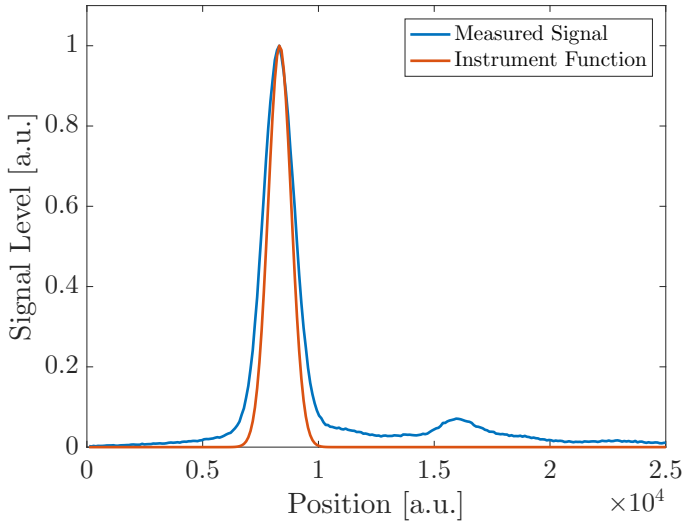


Figure 4.5: Integrated lineout of the raw spectrum shown in figure 4.3(a), compared to the instrument function of the spectrometer. This was taken to be the integrated lineout of a zero point, also in the direction of magnetic dispersion.

function. An instrument function without noise is important for deconvolution, which will become evident in the next section.

Taking the high energy shot in figure 4.3, comparison of the spectral features with the instrument function shows these to be similar, with the signal only slightly broader. This is shown in figure 4.5. This similarity implies the width of the spectral feature is dominated by the instrument function; the true width of the spectral feature is assumed to be smaller than measured. It is therefore important to remove this broadening of the signal to extract the true energy spread of the spectral features; this is termed the "true" signal.

Deconvolution Method

Extraction of the "true" signal can be obtained through deconvolution of the measured signal with the instrument function. The measured signal takes the form $S(x) = \int s(x, y)\,\mathrm{d}y$, where $s(x, y)$ is the spatially dependent signal level of each pixel on the raw image. The measured signal is related to the true signal, $T(x)$, through the relation,

$$S(x) = \int_{-\infty}^{\infty} I(x - x_1)T(x_1)\,\mathrm{d}x_1 = I(x) * T(x) \tag{4.1}$$

where $I(x)$ is the instrument function and the $*$ operator indicates convolution. Theoretically, classical deconvolution could be applied to extract the true signal. However, in reality this is not practical. The method requires the division of Fourier transforms and

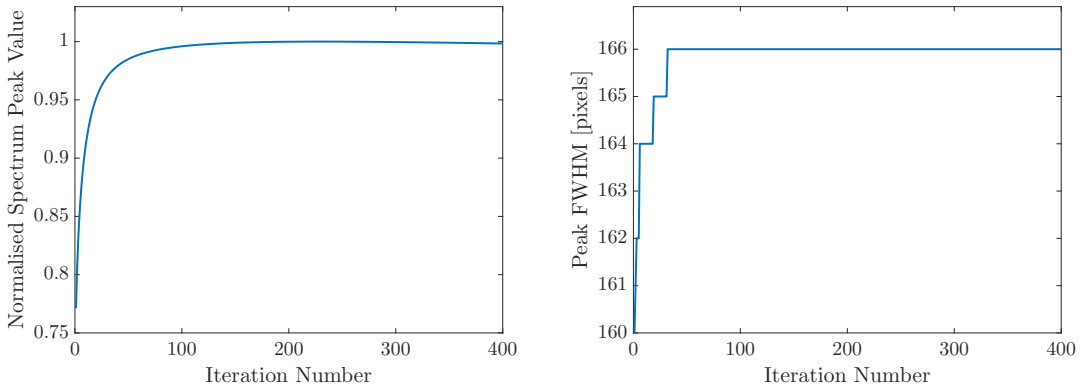


Figure 4.6: Left: The peak height of the spectral feature as a function of iteration step for the supposed "true" signal obtained by the Richardson-Lucy method. Right: The FWHM of the spectral feature as a function of iteration step.

high frequency noise is amplified in Fourier space; the resultant true signal is susceptible to the noise introduced by the signal, $S(x)$.

Another method for deconvolution of the true signal from a noisy image is through the Richardson-Lucy method [244] [245]. The instrument function of the detector must be known. The approach uses Poisson statistics to estimate the probability of the measured signal, $S(x)$, given a known $I(x)$ and $T(x)$, before maximising the probability with respect to $T(x)$. The process is iterative, with the associated algorithm taking the form

$$T_{n+1}(x) = T_n(x) \left(\frac{S(x)}{I(x) * T_n(x)} * I(-x) \right) \tag{4.2}$$

It was shown by Shepp and Vardi [246] that if the solution converges, it converges to the most likely solution for $T(x)$.

This approach has been widely studied and is common in astronomy, where it has been used to process images from the Hubble Space Telescope [247] [248], and microscopy [249] [250].

The measured signal and instrument function can be fed into the algorithm given by equation 4.2. The number of iteration steps for the algorithm are chosen to ensure the true signal is accurately recovered. This was achieved using a trial set of measured, instrument and true signal functions. Tests of the algorithm with a known true input spectrum demonstrated that ~ 100 iterations are required to accurately recreate this signal from the convolved function. After this number of iterations, the spectrum remains essentially constant.

Testing of the algorithm demonstrated that even small variations in the instrument function can result in an unstable solution, with the algorithm never converging to a unique solution, even for thousands of steps. For the real data, the first step is

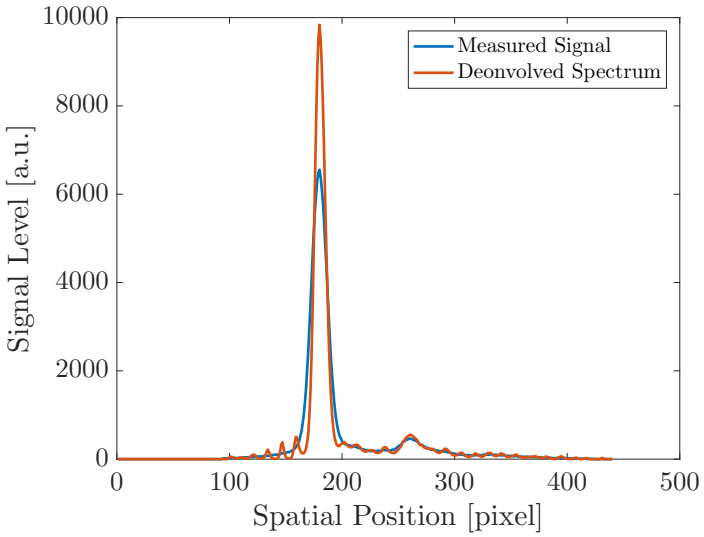


Figure 4.7: The retrieved true spectral profile as a function of spatial position after 100 iterations for the shot presented in 4.3(a).

therefore to test the convergence of the solution. The results of this for the raw data and instrument function from figure 4.5 are shown in figure 4.6. The peak width is shown to stabilise within ~ 40 steps. The peak height does so in ~ 100, showing good agreement with the test case.

The estimated true signal profile as a function of spatial position on the detector is given in figure 4.7. As would be expected if the instrument function is dominating the observed signal, the deconvolved spectrum exhibits a narrower spectral feature. The profile also exhibits spurious peaks either side of the main peak; this is termed ringing. These features appear due to a background on the image. A spatially dependent background subtraction has been carried out over the image. However, this takes the mean signal level from a region on the scintillator above the proton trace, where only noise exists. In practice this method is imperfect and noise still persists. An added background to the test case algorithm demonstrated the introduction of this ringing. The effect is essentially a form of spatial aliasing introduced by the high frequency components within the signal. When converted into Fourier space, should the frequency of the noise be greater than half that of the signal, the aliasing effect can occur. The iterative method of the Richardson-Lucy algorithm is particularly susceptible to this effect since the algorithm can attempt to deconvolve the high frequency components in the same manner as the spectral feature. Over time these can surpass the aforementioned frequency condition, seeding the ringing.

The importance of the ringing depends on the objective of the deconvolution. Clearly, if one is attempting to extract a full spectrum, it cannot be ignored; the peaks have the ability to artificially create spectral features at high energies and modified particle fluxes in the low energy component. To verify the effect, a predicted measured spectrum can be plotted with the original measured spectrum. The predicted measured spectrum is

the expected trace that would be observed on the scintillator, if a beam with a spectral profile of the retrieved true spectrum was imaged by the spectrometer. This is obtained by conducting the deconvolution process in reverse, i.e. by convolving the obtained true spectrum and the instrument function. As would be expected they demonstrate good agreement, although it is possible to observe low level oscillations in the background due to this ringing effect.

To get around this problem, the algorithm could be halted before the appearance of these features, which is dependent on the background conditions for any given shot. A spectrum unaffected by this ringing can then be extracted. However, the occurrence of the ringing features typically precedes a stable solution for the true spectrum. As such, stopping before the initiation of the ringing results in a lower peak value for the spectral feature and the estimated true signal profile is inaccurate.

This ringing feature is commonly observed with the Richardson-Lucy method, and a number of methods have been proposed to get around the problem. The obvious solution is to smooth the data. The problem with this method is associated smoothing of the spectral feature. Subsequently, it is not possible to reach a true signal solution that can accurately resolve the peak signal level of the unsmoothed measured data. Testing, to ensure the raw spectrum can be recovered, demonstrates a decreased peak value of the spectral feature.

One further such method that was trialled attempts to solve the problem of ringing by looking at the difference in subsequent iteration steps. For the local regions where iteration does not improve the solution, i.e. $I(x) * T_{n+1}(x) \approx I(x) * T_n(x)$, the algorithm is halted. For regions where this condition is not met, convolution is allowed to continue unrestrained. However, again the method proves unsuccessful in accurately converging to the true solution, with the peak signal level of the spectral feature underestimated. The resultant 'true' signal, when convolved with the instrument function, cannot then accurately reproduce the initia measured spectrum. This arises from the required choice of the variance between iterative steps that denotes iteration not appreciably improving the solution. This can be chosen to be relatively large, but then the peak will be under-resolved. Similarly, it can be chosen to be small, but this then allows the ringing to develop.

Fortunately, the ringing does not affect the retrieved true signal at the spectral features of interest; the raw signal features can be accurately recreated by convolution of the true signal with the instrument function. Information about the peak flux and rms energy spread can still be obtained. This was demonstrated in the test case, with the assumed raw signal level accurately retrievable, despite this ringing. This was only possible, however, because the signal level is much greater than the noise. Should this condition be broken, extraction of the true signal is no longer possible.

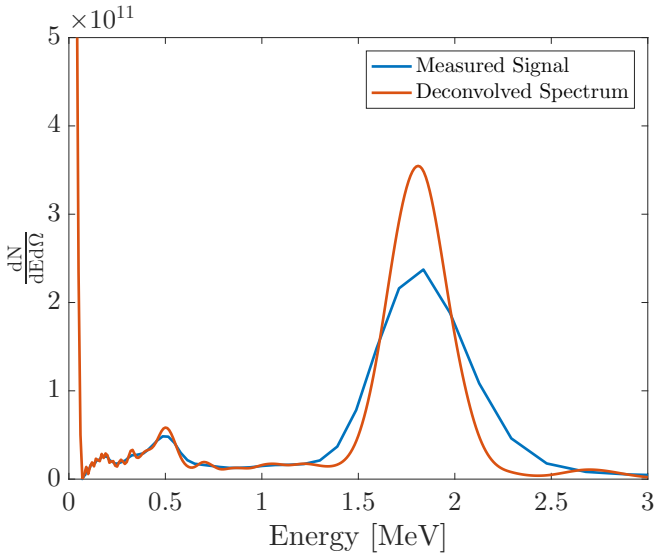


Figure 4.8: The true and unconvolved energy spectra for the experimental data presented in figure 4.3(a). The true signal demonstrates a peak energy of 1.84 MeV, peak flux of 3.55×10^{11} protons/MeV/sr and an rms energy spread of 12.2%.

Final Results

Once the true spatial signal is obtained, it can be treated as the raw spectrum would, as outlined in section 3.4.1. A true spectrum can then be produced for the spectral feature. The true energy spectrum, plus the raw spectrum for comparison, are shown in figure 4.8. The true signal demonstrates a peak energy of 1.84 MeV, peak flux of 3.55×10^{11} protons/MeV/sr and an rms energy spread of 12.2%, equivalent to a spectral width of 0.23 MeV. This is compared to the unconvoluted signal peak flux of 2.4×10^{11} protons/MeV/sr and spectral width of 0.34 MeV, equivalent to an rms energy spread of 18.5%.

True spectra were obtained for all 12 shots which exhibited clear spectral peaking. The shot presented in figure 4.3(c) demonstrated the narrowest rms energy spread of all the shots sampled. The peak energy was 0.55 MeV, with an rms energy spread of $\sigma = 5.3\%$. The peak flux for this shot was 1.92×10^{11} protons/MeV/sr. By comparison, the highest peak flux observed on the sample shots was 5.86×10^{11} protons/MeV/sr.

The inherent variability of the experiment meant a variation in rms energy spread was observed, with the mean rms for the shots sampled found to be $23.5 \pm 3.4\,\%$. The rms energy spread as a function of target density is plotted in figure 4.9. This demonstrates an apparent decrease in the energy spread as the target density increases. For narrow energy spreads to be possible, the HB-RPA front must collapse rapidly so that reflection abruptly stops. If this is not the case, the shock gradually slows, reflecting at a broad range of velocities and producing a broadband energy spectrum. The amount of energy stored in the propagating hole-boring front can be assumed to be a function of the time

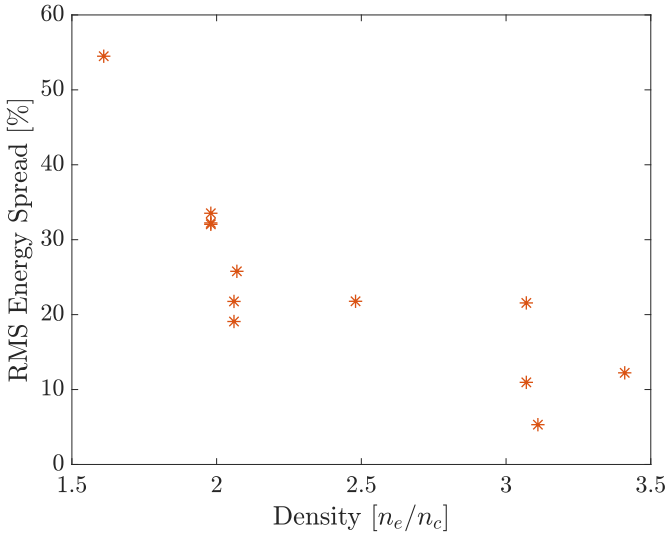


Figure 4.9: The rms energy spread of each shot demonstrating spectral peaking, as a function of the assumed density at the critical surface.

it is under the action of the laser, giving a finite amount of energy at the critical surface. Higher densities result in greater particle fluxes being reflected, with the relative energy loss being higher. Consequently, the shock slows more rapidly before it ceases being able to reflect the upstream ions, producing narrower energy spread features.

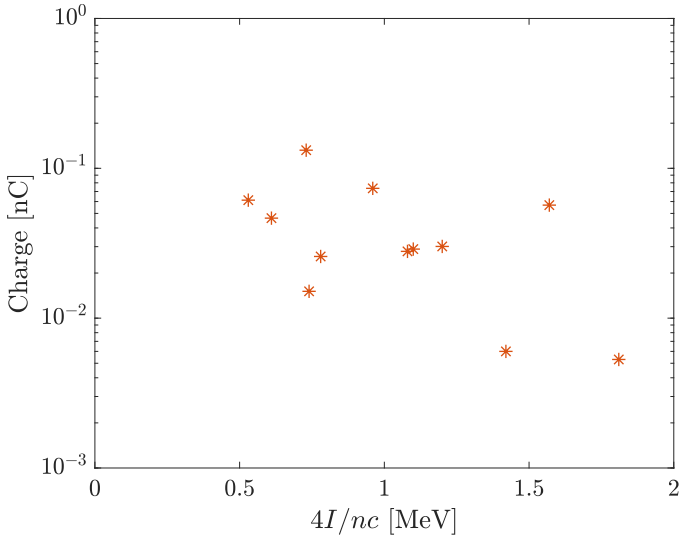


Figure 4.10: Proton bunch charge estimates compared with the predicted proton energy, assuming a beam divergence of $\sim 3.75°$, as indicated from simulations.

For each shot the beam charge can be calculated. While no measure of the experimental divergence of the proton bunch was possible, a minimum estimate can be made from the vertical dimensions of the slit. Since the vertical dimension of the slit is filled, the beam divergence must be greater than 1.9°. Through 2D PIC simulations, a beam divergence of $\sim 3.75°$ is expected. For all 12 shots the bunch charge was calculated

using this expected divergence, the results of which are shown in figure 4.10. These are plotted against the predicted proton energies for each shot, which scales as I/n_i. This might perhaps be expected to be a good metric of the bunch charge, since the strength of the potential associated with the propagating shock front, from which particles are reflected, is related to these quantities. The charge separation between the co-moving electron and ion layers is determined by the strength of the ponderomotive force, which scales with intensity. Despite this, for these results, no clear correlation was observed. Higher energy proton beams might appear to have a lower average charge, although enough shots do not exist to state this conclusively. A mean bunch charge of 0.043 nC (3×10^8 protons per bunch) was observed, with a standard deviation of 0.036 nC.

4.2.2 Comparison to theoretical scaling

The measured proton energy against the predicted energy from HB-RPA scaling, $E_\mathrm{p} = 4I/n_i c$, is shown in figure 4.11. Also plotted is the line of equivalence for the measured and predicted energies. The experimental energy is taken as the central value of a given spectral peak.

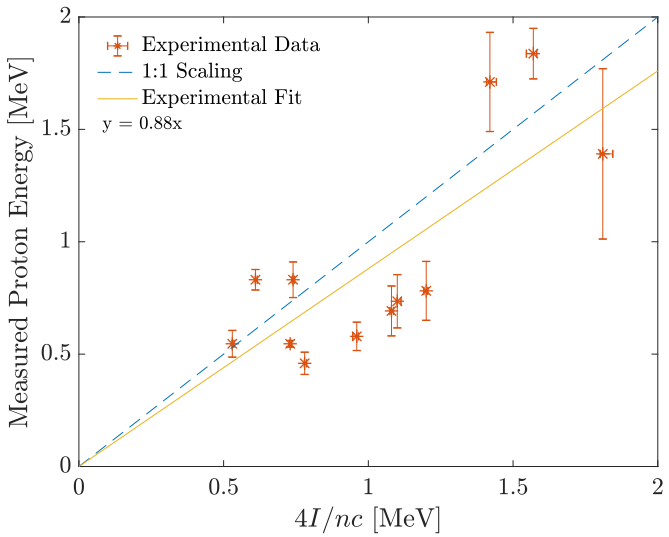


Figure 4.11: The measured proton energy compared with the predicted proton energy scaling for HB-RPA, $E = 4I/n_i c$. Also plotted a linear fit through the data and the line of equivalent scaling for reference.

The predicted scaling was calculated using the on-shot laser conditions and the assumed shock density. The laser intensity was calculated from the assumed spot size of 35 µm and 35 % of the on-shot laser energy measurement. The ion density comes from the predicted peak blast wave density from the observed shock front position.

Extraction of density profiles for all shots was not possible; the low backing pressures on some shots combined with poor fringe contrast made density retrieval impossible. However, for higher backing pressures the density was sufficient to observe significant

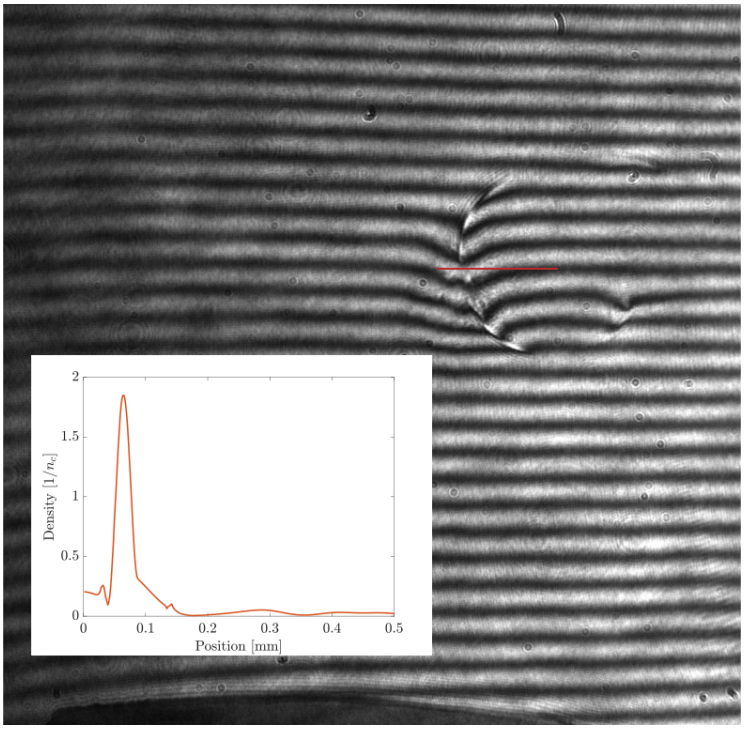


Figure 4.12: An example interferogram of a pre-pulse driven blast wave used for target shaping of the gas density profile for optimal ion acceleration. Inset: The density profile for the presented interferogram along the laser axis (marked by the red line), demonstrating a scale length of $18.6 \pm 5.3\,\mu m$.

fringe shift, while for lower densities the shock front location could often still be observed. The density profile of the shock and associated scale length can be extracted experimentally through interferometry, as described in section 3.3.2.

An example interferogram and associated density lineout along the laser axis is given in figure 4.12. The information presented is for one of the highest measured energy shots presented in figure 4.11, with a peak gas jet pressure of $5.8 \times 10^{18}\,cm^{-3}$ and a pre-pulse energy of 2.75 mJ. The mean measured scale length is $19 \pm 5\,\mu m$ across the width of the focal spot. To test the validity of this result a comparison with the analytical solution presented in section 3.2.1 can be made. From interferometry the shock radius along the laser axis can be retrieved, and is found to be $339 \pm 5\,\mu m$. Assuming spherical shock expansion the assumed scale length is $19.3 \pm 0.3\,\mu m$, in good agreement with the measured values. The error arises due to the uncertainty in the measured shock radius. Similarly good agreement was found between the densities; the measured and predicted peak densities were $1.88\,n_c$ and $1.93\,n_c$, respectively. It is concluded the pre-pulse driven shocks match the predicted analytical scaling in spherical geometry given the close agreement with results extractable from interferometry; the strong shock limit can reasonably be applied for those shots where the density is not retrievable.

Given the difficulty in extracting information from the low density interferograms, the peak density component of the presented scaling in figure 4.11 comes from extraction of

the shock front position from the optical probes. The relative position of the shock in the gas can be found, from which the equivalent proton density can be derived. The strong shock limit is applied to obtain an expected peak ion density, using $\rho/\rho_0 = (\gamma+1)/(\gamma-1)$. As such, only shots where the shock front can be located are presented in figure 4.11. It is worth commenting that a large number of shots exhibited clear spectral peaking, but are not presented due to the inability to accurately locate the shock front.

The vertical error bars for the measured proton energy are the rms energy for each shot, obtained after the deconvolution of the real spectrum as described previously. The analytical errors are a combination of the measured laser energy uncertainty and the range of possible densities from the associated shock front location measurement error.

Over a density range from $1.6\,n_c$ to $3.45\,n_c$ and laser intensities between $a_0 = 1.07$ and $a_0 = 1.77$, the proton energy was shown to match well with the predicted I/n_i scaling. This is indicative of radiation pressure acceleration via the so called hole-boring mechanism (see section 2.4.2). Furthermore, the presence of peaked spectra is a further indication of a radiation pressure based mechanism; sheath acceleration follows an $I^{\frac{1}{2}}$ (see section 2.4.1 and references therein) scaling and does not provide the possibility for spectral peaking in such simple targets.

The discrepancy between the predicted and measured energy can be explained by the laser energy within the focal spot being over-estimated. Based on the ratio between the measured and actual proton energies in figure 4.11 being 0.88, the actual energy in the focal spot can be estimated as $\sim 31\%$. This equates to a mean energy of 0.86 ± 0.19 J.

4.2.3 Proton Beam Filamentation

Those shots not presented but still exhibiting some form of spectral peaking were omitted for two reasons. Firstly if the location of the shock front was not retrievable from the optical probes, no estimate of the shock front density could be inferred; a value for the predicted energy could not be obtained.

Secondly, a number of shots exhibited spatial modulation of the proton beam across the vertical dimension of the slit. The reason for this is not completely clear, but believed to be due to spatial variation in the laser intensity leading to filamentation of the laser and subsequent proton beam. This is likely to be a result of spatial variations in the laser near-field profile.

Reflections from the experimental interactions were observed to propagate back down the laser chain, experiencing re-amplification in the main amplifier. The system geometry results in subsequent down-collimation on the exit of the amplifier in the back-propagation direction, which causes damage centres to form on the amplifier input

window. The damage formation itself is a run-away process, with the effect rapidly worsening once initial damage occurs. Subsequent shots demonstrate a measurable decrease in the uniformity of the laser near-field profile. The forward propagating beam spatial intensity will be inhomogeneous on entry to the amplifier due to varying transmission caused by the damage. The subsequent amplified beam will exhibit the same properties; the effect is accentuated by the non-linear amplification process. Three example images of the laser near-field profile at the entrance to the experimental chamber are shown in figure 4.13, demonstrating an incremental deterioration of the spatial uniformity with increased damage, from left to right. As the laser propagates the low density plasma preceding the critical surface, this inhomogeneity results in spatial variations in the laser intensity and equivalently the refractive index (see section 2.3.5); the laser is susceptible to filamentation causing acceleration from multiple locations with variations in the intensity.

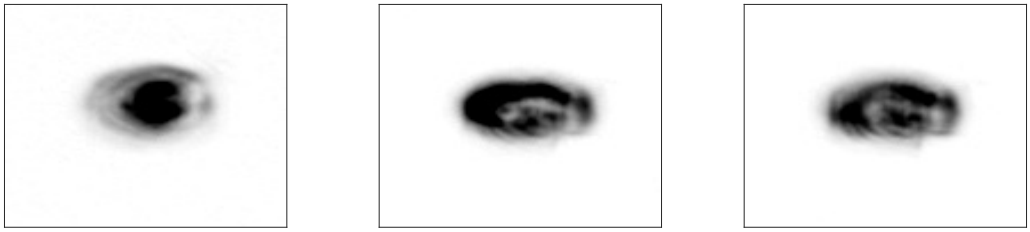


Figure 4.13: Images of the laser near-field profile for, from left to right, the cases of zero, partial and large damage to the main amplifier input window. The resultant imprint on the spatial profile of the laser near-field is suggested to cause modulation of the proton beam due to laser filamentation in the low density plasma preceding the critical surface.

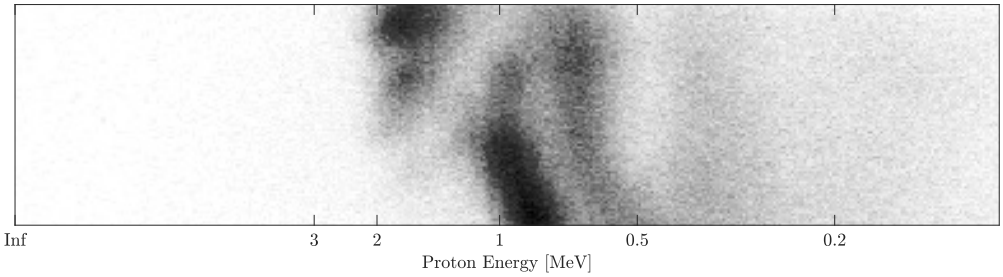


Figure 4.14: Magnetic spectrometer proton trace demonstrating the observation of strong spatial modulation of the proton beam in the non-dispersed direction. This is thought to be due to inhomogeneity of the laser near-field caused by non-uniform amplification of the pulse.

These spatially varying shots were subsequently omitted since the laser spot size, and consequently the intensity at the critical surface, cannot accurately be inferred, despite the observation of high energies, $> 1\,\mathrm{MeV}$. An example raw magnetic spectrometer image is given in figure 4.14 for reference.

4.2.4 Comparison to previous work

The results presented in this chapter were from an experiment with the purpose of furthering the previous work by Palmer at al. [141] [233] and Tresca et al. [181]. It is therefore interesting to compare the results from those experiments with the results presented here. A full comparison of a number of relevant parameters is given in the table 4.2. The work by these authors was carried out at the same facility, although the laser conditions were slightly different. The beam was operating in the 10P branch, at a wavelength of 10.6 µm, with a focal spot size of $\omega_0 \approx 70\,\mu\text{m}$, pulse duration of 7 ps, laser energies between 2.5-2.9 J and on target intensities of 5.4-6.3 $\times 10^{15}\,\text{Wcm}^{-2}$ ($a_0 \simeq 0.47$-0.51).

Palmer et al. and Tresca et al. present peak proton energies of 1.1 MeV and 1.2 MeV, respectively. By comparison, the peak proton energies observed in the results presented here was > 1.8 MeV, showing an improvement of $> 50\%$ over the previous work.

Palmer et al. also studied the relationship between the predicted and observed proton energy using the $4I/n_i c$ hole-boring scaling, as shown in figure 4.11. They demonstrated a linear correlation between the measured and predicted energies, although the measured energies were ~ 11 times higher than those predicted. This was partially explained by the observation via simulation of self-focussing in the density ramp preceding the critical surface. This provided a factor of ~ 2 increase in the laser intensity, enough to at least in part explain the discrepancy. The additional difference was explained by Palmer [233] through 2D PIC simulations, which suggested that acceleration occurred at lower than expected densities, owing to a long scale length density ramp preceding the critical surface. The work by Tresca et al. provided further analysis of these experiments, suggesting that when linear polarisation was used, acceleration was dominated by a laser-driven collisionless shock. The shock speeds are expected to exceed those of an RPA-HB front, providing explanation for the higher than expected energies. This is perhaps unsurprising. Consider the relation given by equation 2.74. It would be expected that collisionless shock acceleration would dominate for $n_e/n_c \gtrsim 4$. The nature of these previous experiments means they occur in the transition regime between when collisionless shock and HB-RPA acceleration are expected to dominate. By contrast, the work presented here occurred at higher a_0, with all densities below $3.5\,n_c$. We therefore expect the interaction to occur in the HB-RPA regime. This assumption is verified by the scaling observed in figure 4.11; the results agree well with the $4I/n_i c$ scaling.

No measure of the mean proton bunch energy spread is given by Palmer et al., so direct comparison is not possible. However, the range of energy spreads, $\Delta E/E$, is given as 3-19%. The mean from the work presented here was $21 \pm 3.5\,\%$, at the upper end of the work by Palmer et al.. The range of $\Delta E/E$ was 5.3-54.5%, although the upper value was a clear exception to the trend; hence the relatively high mean. Perhaps most interestingly was the observation of one shot with extremely low energy spread; 5.3%.

Author	Acceleration Mechanism	Species	Peak Energy [MeV/u]	Energy Spread [%]	Peak Signal [particles/MeV/sr]
Schwoerer et al. [129]	Sheath Acceleration	protons	1.2	40	5×10^{12}
Hegelich et al. [132]	Sheath Acceleration	protons	3	17	5×10^{9}
Henig et al. [251]	LS-RPA	C^{6+}	2.9	35	5×10^{9}
Palmer et al. [141]	HB-RPA	protons	1.1	4	3.5×10^{12}
Haberberger et al. [167]	CSA	protons	20	1	1×10^{7}
This work - lowest spread	HB-RPA	protons	0.55	5.3	5.9×10^{11}
This work - highest energy	HB-RPA	protons	1.85	12.2	3.6×10^{11}

Table 4.2: Comparison of previously observed peak enegies, energy spreads, $\Delta E/E$, and peak signal levels for mono-energetic spectral features observed in a number of laser-driven ion acceleration experiments.

For comparison, the lowest energy spreads observed by Palmer et al. and Tresca et al. were 3.2% and 4%, respectively. The results are roughly comparable, although slightly higher in this work. However, the peak proton energy of the bunch was roughly half that observed by Palmer et al. and Tresca et al., at $\sim 0.55\,\mathrm{MeV}$. The energy spread of the highest energy bunch was 12.2% at $\sim 1.85\,\mathrm{MeV}$. The work presented here produced higher energy proton bunches than previously observed with this laser system, although the measured energy spread is ~ 3.5 times higher.

The energy spread results still perform favourably when compared to results obtained by other authors. Table 4.2 provides information on other work which has produced narrow energy spread beams. As can be seen, the results presented here perform extremely favourably when compared to work by Schwoerer et al. [129] and Hegelich et al. [132] using structured targets to produce mono-energetic spectral features with the sheath acceleration mechanism. These produced energy spreads of 40% and 17%, respectively. Work by Henig et al. [251] demonstrated C^{6+} beams through the light-sail mechanism with a best observed energy spread of 35%. One final result for comparison is the work by Haberberger et al. [167]. Here the authors observed a $\sim 20\,\mathrm{MeV}$ proton beam with $\sim 1\%$ energy spread. However, the particle fluxes achieved were very low at $< 10^{7}\,\mathrm{protons/MeV/sr}$, measured not with an ion spectrometer but with CR-39. This was achieved through collisionless shock acceleration. The work used the high power Neptune CO_2 laser [191], although the mode of operation is significantly different to that at the ATF. The beam consists of a train of 3 ps pulses, separated by 18 ps over an $\sim 100\,\mathrm{ps}$ window. The total energy was 60 J, with the peak normalised vector potential of the pulses ranging from $a_0 = 1.5$-2.5 over the $\sim 100\,\mathrm{ps}$ temporal window. The experiment also used a near-critical gas target, although no separate target shaping was employed. Instead, the successive pulses were used to first steepen the density gradient, then subsequently drive the acceleration. As such, despite their use of a CO_2 laser, the acceleration scheme is markedly different and perhaps describes this discrepancy. Also of interest is the conversion efficiency of laser energy into the mono-energetic proton bunch. The work presented here has a conversion efficiency ~ 5 orders of magnitude higher than the work by Haberberger et al., while a factor of 10 higher than in the work by Palmer et al..

The measured peak proton counts were lower than in previous work. For comparison, the highest peak signals observed in the work presented here was 5.86×10^{11} protons/MeV/sr. By comparison, the highest peak signal observed by Palmer et al. was $\sim 3.5 \times 10^{12}$ protons/MeV/sr. However, this difference is explainable. The flux can reasonably be assumed to scale with the density of the target and the area over which the interaction occurs; the focal spot size. The focal spot size in the work presented here was approximately half that of the previous work, while the densities were $\sim 3.1\, n_c$ and $6.8\, n_c$, respectively. The difference in focal spot area, $\sim 3.5\times$, and density, $\sim 2.2\times$, result in a relative difference of $\sim 8\times$; this brings the results to comparable levels and higher than from foil targets in the work presented by Schwoerer et al. [129], Hegelich et al. [132] and Henig et al. [251]. The peak flux is also 4 orders of magnitude greater than in the work by Haberberger et al. [167], despite the higher observed energies. This result is understandable, given the requirement for high plasma temperature for fast collisionless shock propagation and associated high ion energies. Higher upstream plasma temperatures also result in fewer ions whose kinetic energy meets the condition for reflection, $e\phi > k_B T_i$, giving lower fluxes. It should be noted, however, that this effect is somewhat mitigated by the time that collisionless shock propagation is sustained, with the authors claiming times of the order 100 ps. This is substantially longer than the lifetime of the spatially driven critical surface in hole-boring, with the lifetime of the order of the laser pulse length, in this case 5 ps.

The generally observed trend of lower peak fluxes also translates to the measured beam charge; these are generally an order of magnitude lower than in the work by Palmer et al. [141].

4.3 Simulations

The results presented in this chapter suggest that HB-RPA is the dominant acceleration mechanism, as argued previously. However, the nature of these experiments is that they occur around the transition between two acceleration schemes; hole-boring and collisionless shock acceleration. Simulations were conducted to study the experimentally observed results, to investigate and verify both the dominant ion acceleration mechanism and also the energy scaling relative to the density profile and intensity.

Two different scenarios were considered; a basic plasma slab and a slab with preceding density ramp. The first represents an idealised case which maximises energy transfer to the critical surface and should produce optimal shock generation and acceleration conditions. The second case more realistically represents the density profile of a shaped gas target. The blast wave exhibits a characteristic density profile which is approximated here as a decaying exponential with an associated scale length. This scale length is 20 µm, chosen from the experimental scale lengths, extracted from observation of the shock expansion. The experimental scale lengths ranged from 18 - 24 µm, obtained as

Parameter	Value
Electron particles per cell	16
Proton particles per cell	16
Box size x	150 µm
Box size y	50 µm
Grid size x	$120\,\lambda_L = 83.3$ nm
Grid size y	$120\,\lambda_L = 83.3$ nm
Laser wavelength	10.2 µm
Laser focal spot size	35 µm
Laser pulse length	3.5 ps
Laser intensity	2.08 - $4.07 \times 10^{16}\,\mathrm{Wcm^{-2}}$
a_0	0.62 - 2
Laser polarisation	linear and circular
Initial electron/proton temperatures	0 eV
Peak electron densities	1.5, 2, 2.5 and $3\,n_c$

Table 4.3: Particle-in-cell simulation parameters used for studies of radiation pressure acceleration of protons from shaped gas targets.

described in section 3.3.2.

In each case the peak shock density was varied, assuming values of 1.5, 2, 2.5 and $3\,n_c$. Simultaneously the laser intensity was varied, with a_0 chosen to be 1.25, 1.5 and 1.75. These values represent the range of the experimentally realised conditions.

In all cases the plasma was formed of a pre-ionised hydrogen plasma. The approximation is reasonable given the laser intensity is sufficiently above the ionisation threshold that rapid ionisation would be expected at the rising edge of the pulse. This would be induced by barrier suppression ionisation (see section 2.3.2). The electrons and ions are assumed initially cold; their temperatures are initialised at 0 eV. A grid size of 85-85 nm was chosen to properly resolve the shock front, while 16 particles per cell were chosen for both electrons and protons to minimise numerical heating. Steps were also taken to minimise the effects of sheath acceleration, with the plasma extending to the rear of the box. Simulations were run for a total of 7.5 ps, equivalent to twice the laser pulse length, with an additional 0.5 to compensate for the time required for the laser to propagate the vacuum to the target.

The full list of simulation parameters are summarised in table 5.2.

4.3.1 Results and Discussion

Acceleration with a step density profile

Acceleration was initially studied for the idealised case, with a step density plasma profile from zero to varying peak densities, situated at the laser focus. A typical example

of acceleration from a slab target is given in figure 4.15. A linearly polarised pulse with $a_0 = 1.25$ is incident on a plasma slab with density $n_e = 1.5n_c$, focussed to a spot size of 35 µm. The initial setup is shown in the top panel of figure 4.15, with the on-axis electron density and 2D electron density shown, demonstrating the initial conditions.

Initially, as the laser intensity begins to increase, electromagnetic radiation reflects off the over-critical vacuum-plasma interface, the so-called critical surface. The associated radiation pressure causes density steepening to occur at the critical surface. This is shown in row two of figure 4.15, which gives the plasma profile at 1.1 ps. Electrons within the skin depth are accelerated forward creating a space charge field which drags along the ions behind the electrons. As time progresses, the laser intensity increases and the critical surface is accelerated further into the target at high velocity. Hole-boring occurs. As the critical surface propagates into the plasma, the associated potential profile reflects upstream ions to twice the critical surface velocity. The on-axis and full 2D density profiles are given in the third row of figure 4.15. This represents the plasma conditions at 1.8 ps, just after the arrival of the peak of the laser pulse. As the laser intensity subsequently drops, the critical surface continues to be driven into the target. Once the associated potential increases to the point that it exceeds the upstream kinetic energy of the protons, $e\phi > k_B T_i$, upstream ions cannot pass through the shock, but instead get reflected. At this point, the shock front can accelerate large numbers of protons. The bottom row in figure 4.15 shows the electron density conditions around the point when peak proton energies are produced, at 3.1 ps.

The associated x-p_x phase space plots for the three non-zero timesteps in figure 4.15 are given in figure 4.16. As can be observed in the two early timesteps, the critical surface begins to be accelerated, before upstream protons are reflected to twice the critical surface velocity, as shown in the 3.1 ps output. At later times protons can still be reflected, although to lower energies and in lower numbers, as the shock loses energy. This occurs for two reasons; the laser intensity drops and the shock loses energy through reflections.

It is also interesting to highlight the late stage dynamics of these interactions. The on-axis density lineout, 2D density profile, on-axis longitudinal electric field and potential profiles, and x-p_x phase space for this simulation are given in figure 4.17, for a time of 5 ps. At this late time, the laser pulse has finished and the dynamics are purely driven by the plasma conditions; the fields, density gradients and temperature gradients. As can be observed, a collisionless shock structure has formed. This is demonstrated by the oscillatory proton density profile in figures 4.17(a). These density modulations exist in both the proton and electron profiles, although the proton modulations are narrower in longitudinal size at <1 µm, due to the greater thermal energy of the electrons; these essentially equilibrate to form a sheath around each proton density modulation. Similarly, this oscillatory feature exists in the longitudinal electric field profile, seen in the blue curve in figure 4.17(c), as a result of these electron and proton plasma perturba-

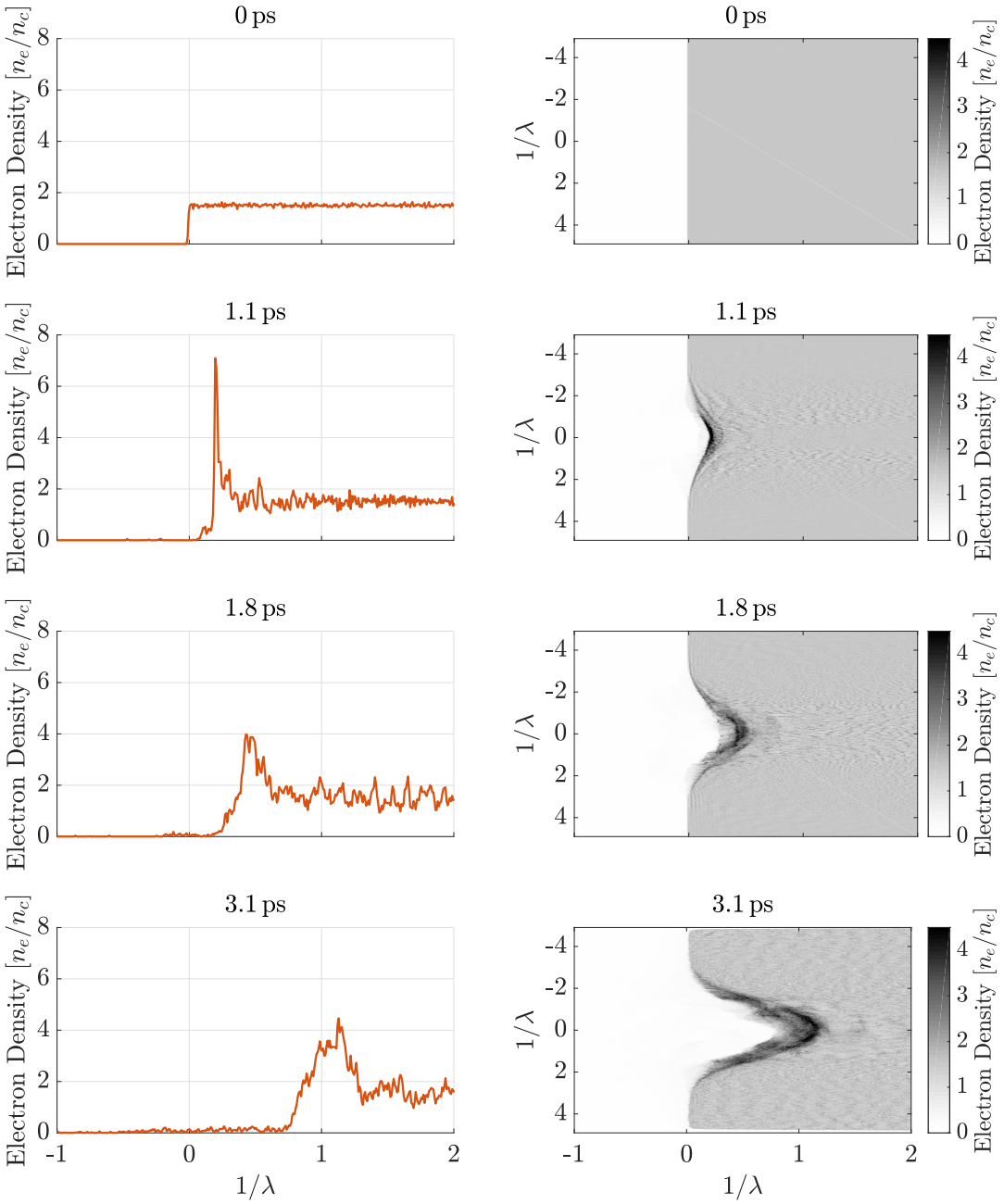


Figure 4.15: On-axis electron density lineouts and 2D density plots for the interaction of a CO_2 laser pulse with $a_0 = 1.25$, incident on a step profile plasma with density $n_e = 1.5n_c$, focussed to a spot size of 35 µm. The dynamics are shown at 0 ps, 1.1 ps, 1.8 ps and 5 ps. These demonstrate the initial conditions, density accumulation and the formation of a hole-boring front, the profile at the peak of the laser pulse and the profile around peak acceleration, respectively.

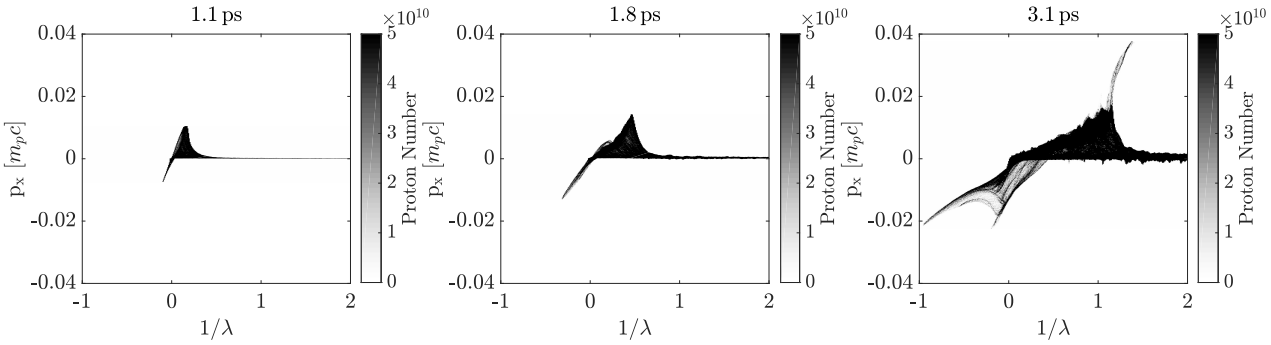


Figure 4.16: The proton x-p_x phase space plots for 1.1 ps, 1.8 ps and 3.1 ps for the equivalent temporal outputs from figure 4.15. At early times the protons at the critical surface are observed to be accelerated, before at 3.1 ps upstream protons are reflected off the shock potential to twice the velocity of the critical surface.

tions. The potential profile associated with this longitudinal electric field structure is also oscillatory, as anticipated in section 2.2.3. This is also shown in figure 4.17(c) as the red curve.

It is important to recognise that the collisionless shock forms at late times, near the end of the laser pulse, i.e. > 3.1 ps, when the peak acceleration off the critical surface occurs. However, there is a transition regime while the laser is still driving the critical surface and the collisionless shock is launched. During these early stages, while the laser persists, electrons become effectively trapped between the shock potential and the laser, confining the expansion of the shock in the direction opposite to the laser propagation. As can be seen from the x-p_x phase space plot in figure 4.17(d), protons are accelerated off the collisionless shock front by the associated potential, given by the red curve in figure 4.17(c). Those which are not reflected can be sufficiently slowed, becoming trapped within the shock structure, propagating at the shock velocity. This is also observed in figure 4.17(d), with a high flux component moving forwards with the collisionless shock velocity. However, it can be seen that the energies obtained by the reflected protons are lower than from the laser accelerated critical surface. A clear, detached bunch of protons are seen to propagate upstream from the collisionless shock, which were previously reflected off the hole-boring front at earlier times. These protons are those observed undergoing strong acceleration off the hole-boring front in figure 4.16 at 3.1 ps. While a component of the proton energy spectrum from the collisionless shock then exists, they do not exceed the energies of those accelerated through hole-boring.

The observed combination of acceleration mechanisms occurring in the above simulation highlights the nature of these near-critical density interactions, as was alluded to previously in section 4.2.4. Recall figure 2.13, which showed two regimes in which radiation pressure and collisionless shock acceleration are expected to dominate as a function of plasma density and laser intensity, given by equation 2.74. This suggests for

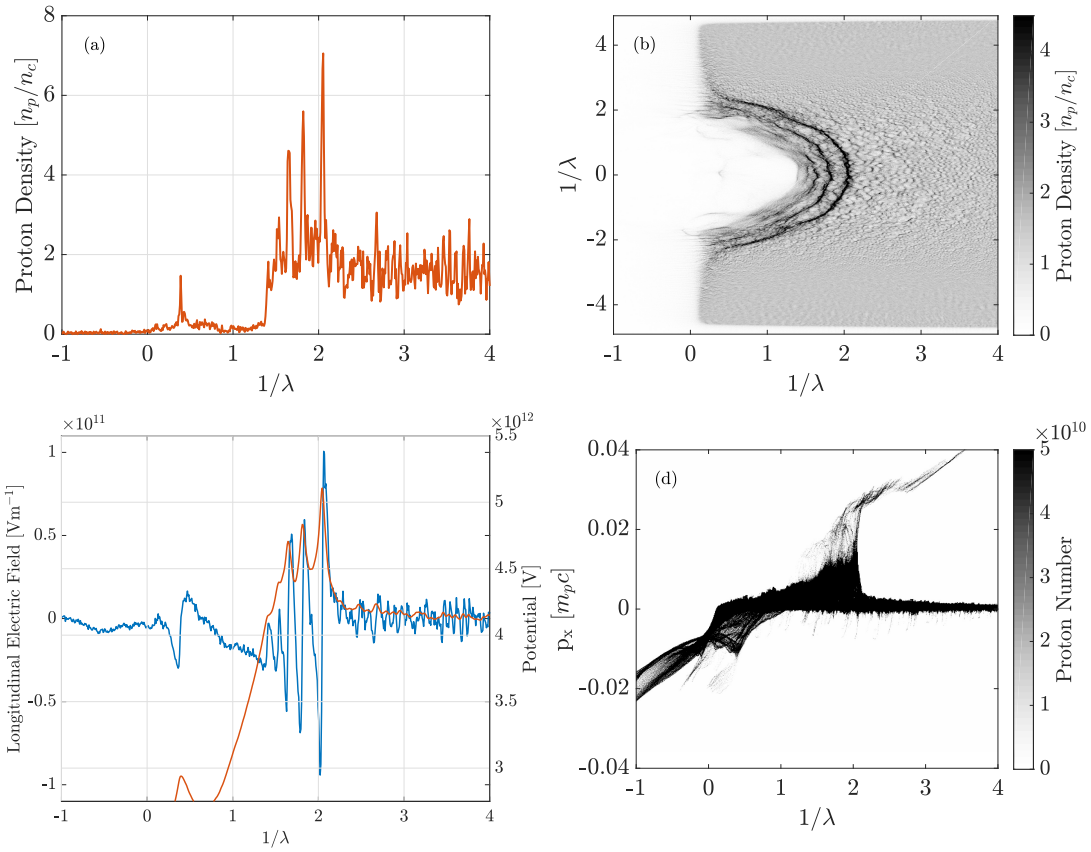


Figure 4.17: Simulation outputs at 5 ps for a CO_2 laser pulse with $a_0 = 1.25$, incident on a step profile plasma with density $n_e = 1.5n_c$. These demonstrate the formation of a collisionless shock structure. The subplots are (a) the on-axis proton density lineout, (b) the full 2D proton density profile. (c) the longitudinal electric field and (d) the x-p_x proton phase space.

$1 < a_0 < 2$ and for $n_e/n_c \lesssim 4$, hole-boring is expected to be the dominant acceleration mechanism. In practice, a transition regime will exist over a finite distance either side of this equality. For $a_0 \approx 1$ and near critical densities, the interactions appear to be in this transition regime, with both HB-RPA and collisionless shock acceleration occurring. However, HB-RPA still dominates because the conditions sit below the equality given by equation 2.74.

The effect of a density gradient

As previously discussed, in practice the density profile of the shaped gas target is not a step function, but instead assumes a decaying profile from the critical surface with an associated scale length. To model the effect of this finite scale length, an exponential ramp was assumed with a scale length of 20 µm. This was chosen as it sits between the range of experimentally measured scale lengths for the shots presented earlier in this chapter; these were between $\sim$ 18-24 µm.

Acceleration with the preceding density ramp shares similarities with the slab scenario, with acceleration being first driven by hole-boring before the late time formation of a collisionless shock. A number of differences also exist however. The laser propagates up the density ramp to the critical surface, denoted by $n_e = \gamma n_c$, where reflection occurs. This has two effects, the first being the critical surface is accelerated into the target and a hole-boring front is formed. Secondly, the reflected component of the laser interferes with itself, at very early times forming a static standing wave. This seeds periodic oscillations in the electron density, although these are quickly destroyed as the critical surface begins to move. The rapidly varying standing wave field causes turbulent motion in the plasma ramp, as can be seen in figure 4.18 for $t = 0.7$ ps. Consequently, early times are dominated by the interaction of the laser with the underdense plasma preceding the critical surface. As the intensity increases further, these low density perturbations dissipate and the interaction is dominated by the interaction at the critical surface. This is shown in the bottom row of figure 4.18 at 2.3 ps. Density continues to pile-up and the hole-boring front is accelerated further into the target. As in the slab case, the hole-boring front can reflect upstream ions to high energies. This is demonstrated in figure 4.19 at 2.3 ps.

An interesting aspect of the inclusion of the density ramp is the increased energies from the late time collisionless shock. Figure 4.20(a) shows the two-dimensional density profile at 6 ps, highlighting the formation of such a collisionless shock. Figure 4.20(b) shows the increased collisionless shock accelerated proton energies, comparable with those from hole-boring. A clear bunch, accelerated at earlier times off the hole-boring front is seen ahead of a broad energy beam accelerated off the collisionless shock. Peak energies in this specific case are comparable with the step density plasma case as seen in figure 4.16, with equivalent peak density and laser conditions. This observation has an interesting effect on the proton energy spectrum. Figure 4.21 shows the energy spectra

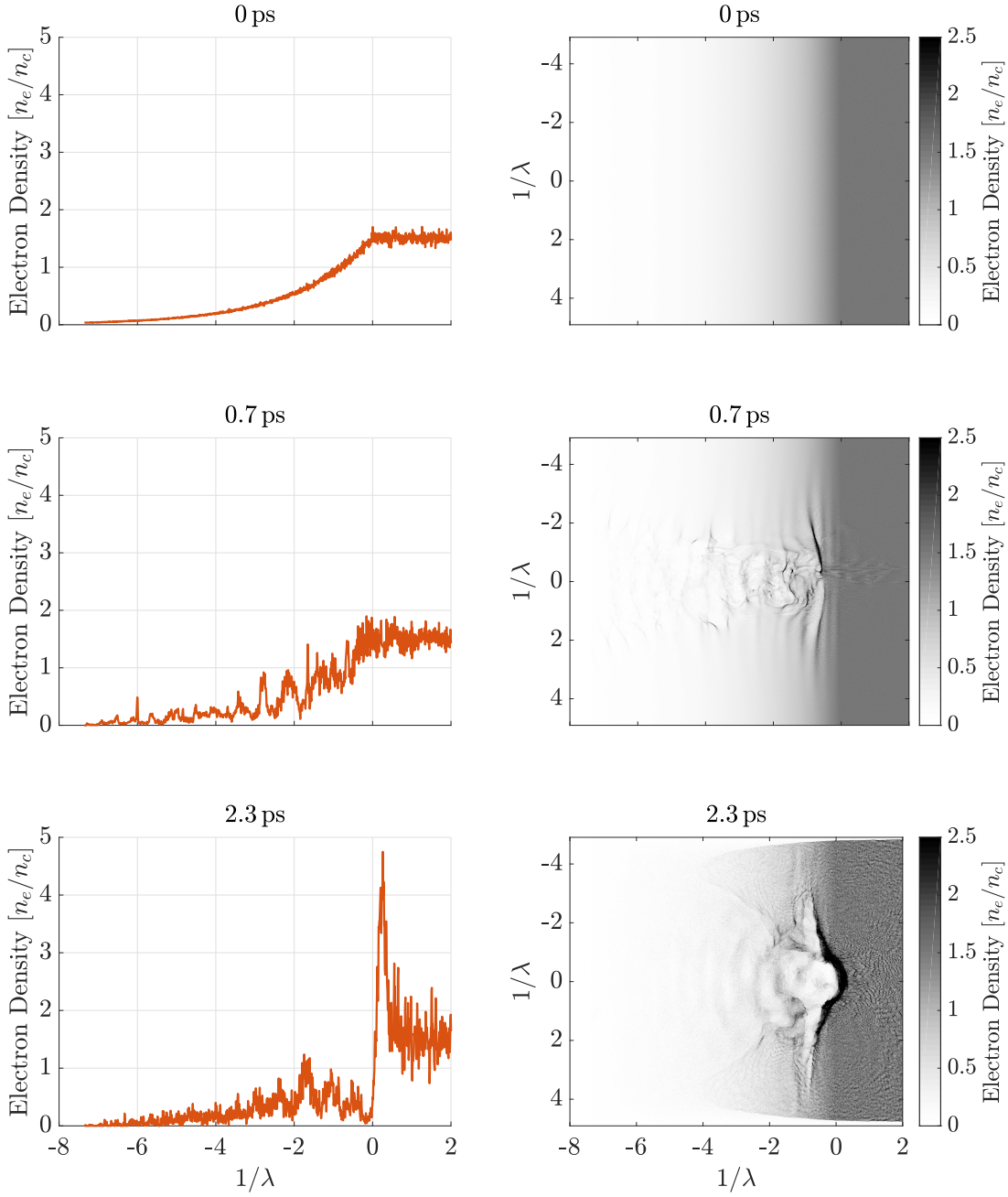


Figure 4.18: The on-axis electron density lineouts and 2D density plots for the interaction of a CO_2 laser pulse with $a_0 = 1.25$, incident on a plasma with peak density $n_e = 1.5n_c$ and 20 µm preceding density ramp. The dynamics are shown at 0 ps, 0.7 ps and 2.3 ps. These demonstrate the initial conditions, the perturbation of the density ramp preceding the initial critical surface and the profile around peak acceleration, respectively.

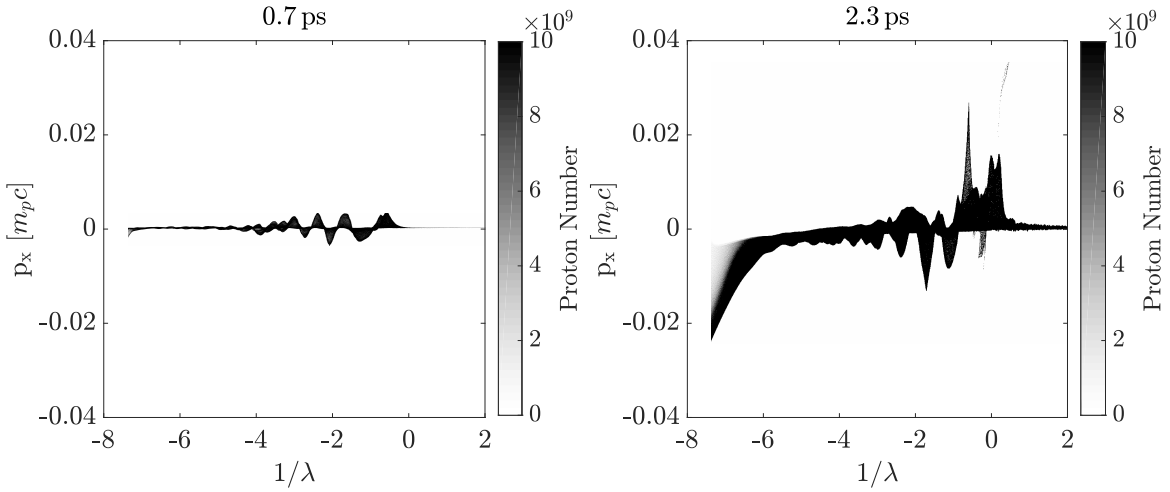


Figure 4.19: The proton x-p_x phase space plots for 0.7 ps and 2.3 ps for the equivalent temporal outputs from figure 4.18.

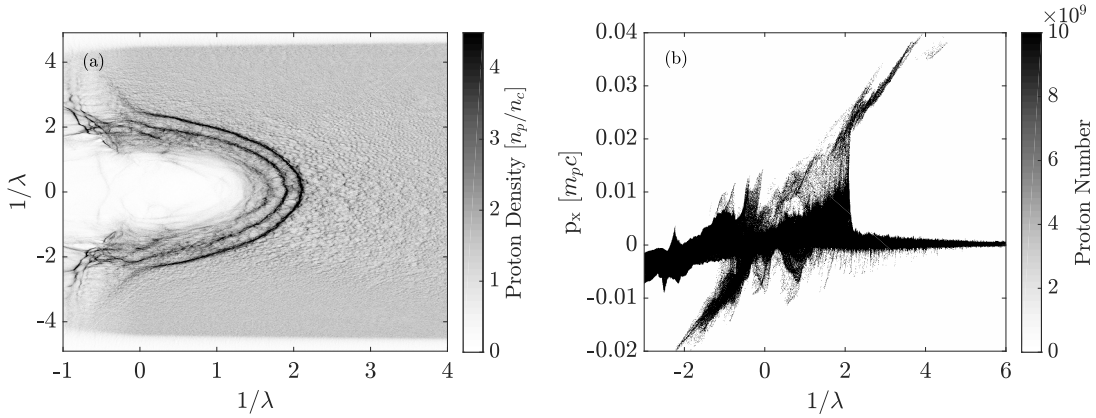


Figure 4.20: (a) The two-dimensional density profile at 6 ps for the late time collisionless shock formed in simulations with a 20 µm density ramp preceding a 1.5 n_c plasma slab. The incident laser has $a_0 = 1.25$. (b) The phase space plot for the same simulation, showing a bunch of protons previously accelerated by HB-RPA and a broad energy component accelerated off the collisionless shock potential.

at two times for both (a) the step density profile in the previous section and (b) the 20 µm scale length exponential ramp preceding the plasma slab. In both cases at early times spectral peaking is observed, with a narrower energy spread for the ramp case. This occurs because at the time of peak acceleration, the potential profile associated with the critical surface is steeper in the ramp case; upstream protons are more rapidly accelerated, giving a narrow energy spread. At late times, the spectral features are no longer observable. In the case of the slab target, the peak energy of shock accelerated protons coincides with that of the low energy end of the spectral feature. Appreciable numbers of protons are accelerated to these energies and the spectrum is smoothed. For the ramp case, as previously discussed, the peak shock accelerated proton energies match that of the hole-boring accelerated component, blurring out the spectral feature. This trend is observed throughout the parameter space simulated. Early time spectral features produced by HB-RPA are subsequently masked by the late time collisionless shock which is formed.

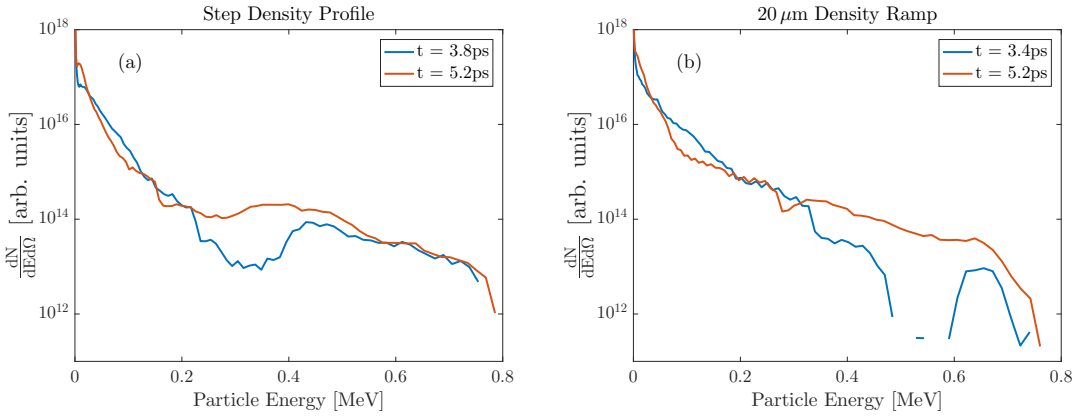


Figure 4.21: (a) The proton energy spectra at 3.8 ps and 5.2 ps for a step density profile. (b) The proton energy spectra at 3.4 ps and 5.2 ps for a 20 µm exponential density profile preceding the plasma slab. In both cases the early time energy peaking is not observed to be maintained at later times.

Results are presented in figure 4.22 for the maximum observed proton energies for the region of parameter space studied. This shows a number of interesting features. As is to be expected from HB-RPA scaling ($E_i = 4I/nc$), a linear decrease in proton energy with peak initial plasma density is observed for the plasma slab case. As the density drops below $n_e = \gamma n_c$, the radiation pressure exerted on the plasma is lower as the laser can propagate further into the plasma. While the density is reduced in this case, the acceleration is less effective owing to the reduced radiation pressure. Eventually, the laser can propagate in the underdense plasma, with no over-critical surface forming and no appreciable RPA.

The ramp case does not follow the same scaling. In this case, the critical surface initially forms not at the location of peak density, but instead where the density goes overcritical in the ramp preceding the slab. Acceleration begins at the same density independent of the peak density, although there is a dependence on the laser intensity due $n_{cr} = \gamma n_c$.

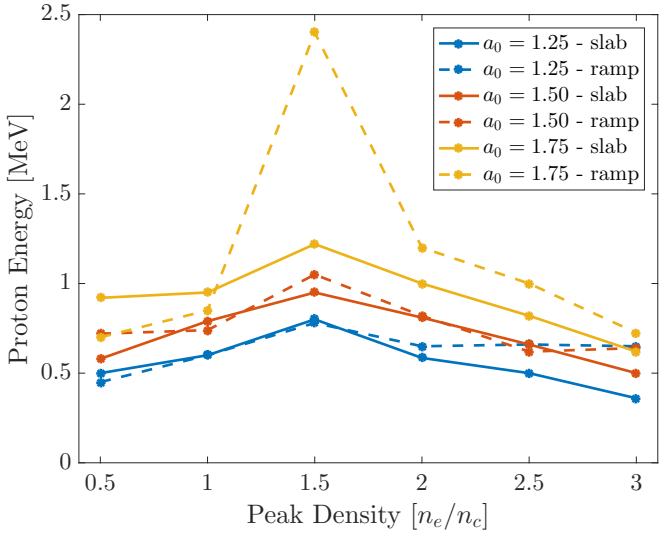


Figure 4.22: Peak proton energies observed in simulations, for $a_0 = 1.25$, $a_0 = 1.50$ and $a_0 = 1.75$, for densities over the range 1.5-3 n_c.

This helps explain why the peak proton energies become approximately constant for the case of higher densities. Here, acceleration is always occurring at approximately the same density, giving quasi-constant energies.

The exceptionally high relative energy for laser condition $a_0 = 1.75$ and peak density of $n_e = 1.5n_c$ arises due to the turbulent motion in the low density plasma ramp. The field structure is such that material is pulled from the edge of the hole drilled in the plasma into the centre of the laser field. This is subsequently accelerated in the forward direction by the laser, its limited mass facilitating the strong acceleration. While the effect is interesting, in reality it relies on a number of factors coinciding; hence it is not observed in any other case, where the scaling follows the same broad trend. Material is required to be pulled from the wall of the shock front into the centre of the laser field on a trajectory that allows it to gain significant forward momentum. While interesting, in practice the effect is not dependable as an acceleration mechanism.

It can be concluded that the interaction with a density ramp is sensitive to the ramp profile and laser conditions. While the dominant acceleration in the ramp always initially occurs at the critical surface, the time it takes for density steepening to occur and the formation of an accelerated hole-boring front clearly determines the energy spectrum observed. At lower intensities and longer ramps more energy will be coupled to the low density plasma in the preceding ramp and it will take longer for these effects to occur. Concurrently, high intensities and shorter ramps should allow this process to occur faster. This may help explain some of the variability in the experimental data, and give some indication of why HB-RPA is dominant in some situations, giving peaked energy spectra, and not in others.

The difference between the observed experimental and simulation scaling must also be

addressed. The experimental results demonstrated good agreement with the predicted HB-RPA scaling, $4I/nc$. Simulations suggest similar linear scaling for overdense ($n_e > n_c$) slab targets, as seen in figure 4.22.

The more realistic density ramp simulations do not follow this predicted scaling but for the highest laser intensity of $a_0 = 1.75$; lower intensities show quasi-constant proton energies at higher densities, attributed to acceleration occurring not at the peak of the ramp, but instead the critical surface location. This provides a quasi-constant density. Clearly the simulations and experimental results do not agree. The most probable explanation is that undiagnosed laser pre-pulses resulted in density steepening of the plasma, giving an effective slab like profile at the arrival of the main pulse. No high temporal resolution laser diagnostics were available making diagnosis of these structures impossible. However, previous experiments have demonstrated low energy, ~ 25 ps pre-pulses arriving before the main pulse [233] (see also Chapter 5). As described in section 3.1, these are formed due to the inclusion of multiple rotational lines from the gain spectrum in the extracted pulse. It has been shown that these act to steepen the density sufficiently such that upon the arrival of the main pulse, the interaction occurs with an effective slab target [150] [233]. It would then be possible to explain the observed experimental scaling.

Circular vs. Linear Polarisation

The effect of going to circular polarisation was also considered. Circular polarisation limits the effect of $\vec{J} \times \vec{B}$ electron heating, in theory reducing the upstream bulk plasma temperature. The lower thermal plasma pressure results in the critical surface propagating faster, generating higher energy protons. Reflection is also expected to be less efficient with increased plasma temperature; fewer particles can be reflected by the shock potential.

For these tests, the step density profile was used, to minimise computational resources. Circular polarisation was modelled by including two, identical but orthogonal laser components. By setting these to be $\pi/2$ out of phase with one another, a circularly polarised pulse is produced.

Results show a number of important differences between circular and linear polarisation. Firstly, circular polarisation demonstrates increased proton energies compared with the linear case. For a laser with $a_0 = 1.25$ and slab density $n_e = 1.5n_c$, the maximum proton energy is > 1.5 MeV. This is shown in figure 4.23. Compare this with the linear polarisation case for the same conditions in figure 4.21(a), where the peak energy is < 0.8 MeV. Suppressed heating of the upstream plasma in the case of circular polarisation results in a lower thermal plasma pressure, allowing faster propagation of the hole-boring front, giving higher proton energies. Furthermore, the suppressed plasma heating results in the condition $e\phi > k_B T$ being valid at earlier times, resulting in sub-

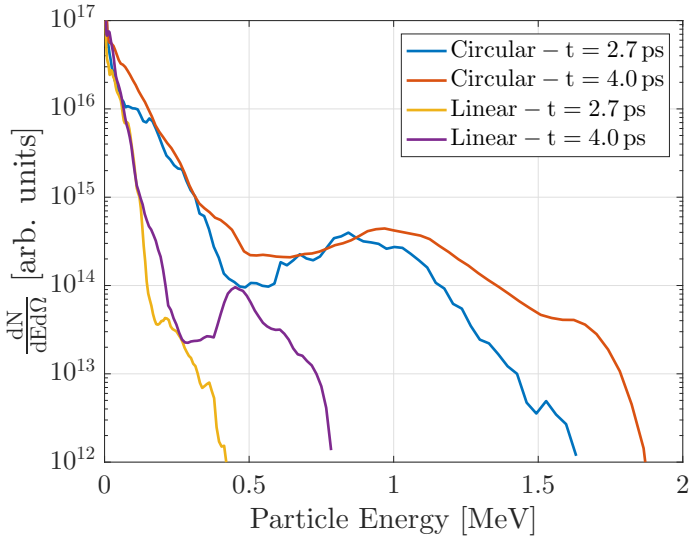


Figure 4.23: Proton energy spectra at two times from 2D PIC simulations, for both circularly and linearly polarised laser pulses with $a_0 = 1.25$ at a density of $1.5\,n_c$.

sequent particle reflection also being at earlier times. The shock continues reflecting at late times as the potential decays, again possible due to the upstream kinetic proton energy, $k_B T_i$, being lower and generating a broad spectrum beam component. This dominates the peaked spectrum at late times.

A collisionless shock structure is still formed in this case, although at later times than for linear polarisation, again owing to the reduced bulk plasma heating. Particle energies in this case are also lower.

4.4 Conclusions

This chapter presented experimental results studying near-critical density proton acceleration with a CO_2 laser. The results demonstrated a number of shots with spectral peaking of the proton energy. Mono-energetic features are indicative of a shock acceleration mechanism, in this case hole-boring or collisionless shock acceleration. The experimental density and laser intensity conditions suggest hole-boring should dominate, which was verified using 2D PIC simulations. Further evidence of this comes from the measured proton energies. These demonstrated good agreement with the predicted proton energies using the $E_p = 4I/n_i c$ hole-boring scaling, as shown in figure 4.11.

Higher peak proton energies than previously observed on the CO_2 laser at the ATF were produced. The highest peak proton bunch energy seen was $\sim 1.85\,\text{MeV}$, with an energy spread of 12.2%. This demonstrates a $> 50\%$ increase in the maximum previously observed peak energy.

The spectral features also demonstrated narrow energy spreads, with the lowest being

$\Delta E/E = 5.3\%$ at a peak energy of $\sim 0.55\,\mathrm{MeV}$. This compares slightly less favourably with the previous work by Palmer et al. [141] and Tresca et al. [181], who observed narrowest spreads of $\Delta E/E \simeq 4\%$ at a peak energy of $\sim 1.1\,\mathrm{MeV}$.

Simulations highlight the nature of these experiments, demonstrating that for the near-critical densities studied and laser intensities of $a_0 \approx 1$, multiple acceleration mechanisms can exist. Simulations suggest these experiments operate in a regime still dominated by HB-RPA, as also indicated by the observed experimental proton energy scaling. However, at late times, collisionless shocks are observed to form, accelerating upstream protons, albeit to lower peak energies and with no observable spectral peaking. These broad energy beams at late times dominate the spectral energy features from the hole-boring front. This observation provides an explanation of the high numbers of experimental shots on which no spectral peaking was observed. While these beams could perhaps be explained by sheath acceleration at the rear of the gas jet, no ionisation is observed here in the interferometry, as would be expected in the case of sheath expansion. These broad energy spread beam components from simulations help explain this observation. The shots where spectral features are clear must exist in a regime where acceleration from the critical surface is extremely fast, generating high energy protons above any low energy thermal component which does not dominate. These narrow energy spread beams require rapid dissipation of the shock [181], such that no gradual deceleration occurs producing a broad energy beam. This would explain the observations in figure 4.4. Shots (a) and (c) demonstrate very clear spectral peaking. Shot (b) is less pronounced, with a higher background component. These shots perhaps demonstrate different levels of broadband acceleration.

5 Enhanced ion acceleration from an induced grating structure in a near-critical density plasma ramp

It was previously stated in section 3.2.1 that short scale lengths at the critical interaction surface were important for efficient ion acceleration. This section will present experimental and simulation results which show this is not strictly true for all cases. In fact, this chapter hopes to demonstrate that for certain near-critical density interactions a front surface scale length can be beneficial to the ion acceleration process, providing superior ion energies to an equivalent slab target scenario. Experimental results demonstrated ion energies which consistently exceeded those predicted by the theoretical HB scaling, with a strong dependence on the relative timing between the BW generation and main pulses, despite the shock moving of the order of one Rayleigh length; the intensity can therefore be assumed quasi-constant. The reason for this is suggested to be a periodic modulation in the low density plasma preceding the critical surface, and the subsequent acceleration of one or more of these structures. Their limited areal density, when combined with a favourable formation time, allows for superior ion acceleration relative to a plasma slab. For certain regions of parameter space, this method can consistently provide superior ion energies, with a dependence on the ramp profile and laser intensity.

5.1 Experimental Overview

5.1.1 Laser Parameters

The work presented in this chapter used the CO_2 laser at the ATF, operating in the 10P branch at 10.6 µm. A linearly polarised train of pulses was delivered to the interaction chamber with a mean energy of 3.5 J, focussed to a 70 µm spot, with Rayleigh length ∼385 µm. The train of pulses arises due to spectral modulation in the regenerative amplifier; pulse extraction overlaps with multiple peaks on the gain spectrum (see figure 3.3), resulting in a train of pulses, separated by ~ 25 ps. An example of the laser temporal structure is given in figure 5.1. Typically most of the energy ($> 85\,\%$) is contained within the first two pulses, with the relative levels varying shot to shot due to the non-linear nature of the CO_2 amplification system. For the shots on the day

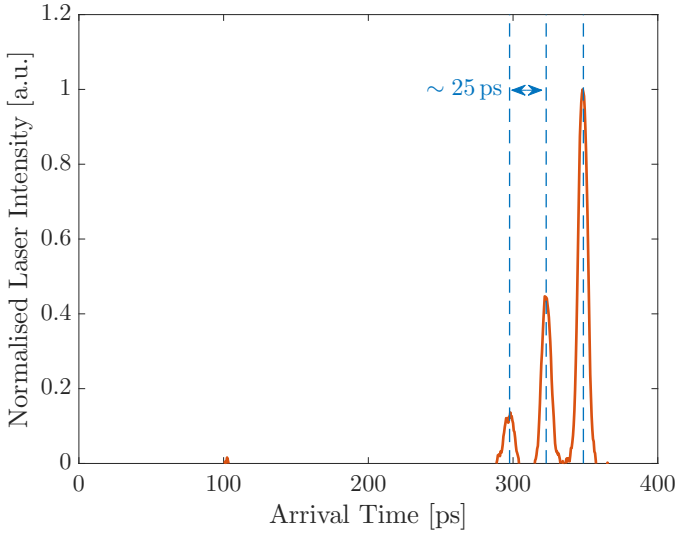


Figure 5.1: An example CO_2 temporal profile. Modulation of the gain spectrum results in temporal modulation and a laser train. The given example contains 7 %, 28 % and ~ 65 % energy in the first, second and third pulses, respectively.

Parameter	Value
Laser energy to chamber	2.1 - 4.2 J
Energy in focal spot	0.68 - 1.37 J
Focal spot size	70 µm
Pulse length	5 ps
Laser intensity at focus	$3.5 - 7 \times 10^{15}$ Wcm^{-2}
a_0 at focus	0.51 - 0.72

Table 5.1: CO_2 laser parameters for the results presented in Chapter 5

the experimental data was obtained, the mean laser energies were 12 ± 6 %, 23 ± 6 % and 65 ± 9 % for the first, second and third pulses, respectively. The information on the pulse structure was obtained using a streak camera. This is a device often used to measure the temporal evolution of the power or intensity of a laser pulse. Laser light incident on a cathode can generate electrons, the flux of which is related to the intensity of the incident light. The electrons are accelerated towards a detector, traversing a pair of electrodes which experience a temporally varying voltage which acts to spatially deflect the electrons. It is then possible to infer the temporally varying intensity from the spatial profile of the signal.

The inherent variability of the laser system gave a range of laser intensities for any given "equivalent" target conditions. The range of parameters are given in table 5.1. The mean energy of 1.1 ± 0.1 J gives an equivalent mean intensity of 5.9×10^{15} Wcm^{-2}, or equivalently, a mean vector potential, a_0, of 0.65.

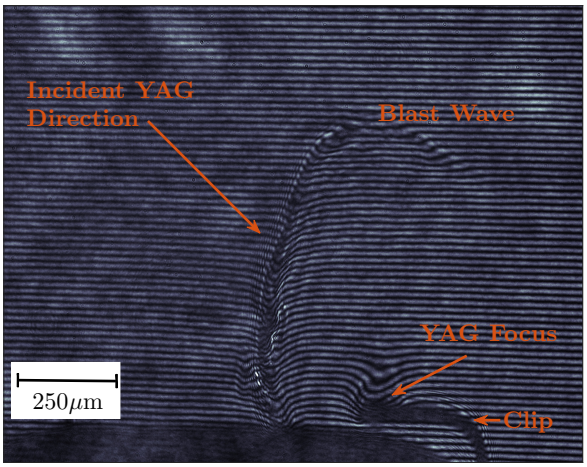


Figure 5.2: An example interferogram from the experiment, showing a blast wave launched into the gas jet 30 ns before the main CO_2 pulse. The clip, which is shot with a seperate Nd:YAG laser to heat the clip and generate the shock is clearly visible protruding into the gas flow. This laser is incident from above and to the side of the gas jet, with variable energy and timing.

5.1.2 Targetry

The experiments in this chapter employed the "1 mm" nozzle as outlined in section 3.2, with hydrogen gas at 4 bar backing pressure giving a density profile as demonstrated in figure 3.5. For these conditions, the gas reaches a peak molecular density of $3.4 \times 10^{18}\,\mathrm{cm}^3$, equivalent to $0.6\,n_c$. The scale length of the gas profile is 0.55 mm, with the profile extending out to 1.5 mm.

Target shaping occurred through the use of an external Nd:YAG laser on to a stainless steel clip, positioned at the edge of the gas flow. An example interferogram of this process is shown in figure 5.2. The YAG beam has energy ~ 80 mJ and pulse length $\tau_{\mathrm{YAG}} = 5$ ns. It is focussed using an $f/10$ geometry from above such that it passes through the side of the gas flow to the clip. The clip is heated, causing hot material to be ablated into the surrounding gas and subsequent localised heating. This can be seen at the YAG focus in figure 5.2. The heating causes a blast wave to be launched into the gas, as seen in the interferometry. The energy of the YAG pulse could be controlled through the use of polarisation based splitting, with a variable polariser and polarisation dependent beam-splitter used. However, in practice the full energy was always used to cause the fastest expansion possible. At the same time, the relative timing between this and the main CO_2 pulse was variable, with a delay range of $20 - 70$ ns studied. The CO_2 focus is fixed, which provides the opportunity to scan the BW position relative to focus, or, given the long Rayleigh range of the CO_2 beam, allows a study of the effect of a scale length preceding the critical surface to be investigated.

5.1.3 Diagnostics

The main diagnostics for this experiment were the magnetic ion spectrometer (see section 3.4.1) and optical probes. The ion spectrometer operated with a 500 µm pinhole at its entrance to sample the on-axis proton beam profile.

The optical probes consisted of an ~ 8 ps, frequency doubled, 532 nm probe beam providing variable two time shadowgraphy and interferometry. This beam is synchronised to the CO_2 laser such that it can be timed to arrive before, during or after the main pulse driving ion acceleration. The beams were chosen to arrive such that the early beam arrived ~ 30 ps before the main CO_2 pulse, while the second beam was employed at various times to study the post acceleration structure. Imaging of the acceleration process was not directly possible since the probe beam is longer than the CO_2 beam; any features are effectively blurred out due to the long integration time of the probe. However, this is not an issue for studying hydrodynamic features, such as the BW, since the important timescales for this case are orders of magnitude longer ($\sim$ ns).

5.2 Experimental Results

The results presented in this chapter originated from an experiment in July 2015, aimed at studying radiation pressure acceleration of protons from a near-critical density gas target. This work focusses specifically on studies aimed at studying the effect of differing target shaping conditions on the generated proton beams, namely the blast wave position in the gas and expansion time. Peaked proton spectra, indicative of a radiation pressure driven acceleration mechanism as earlier discussed in Chapter 4, were observed on $\sim 30\%$ of shots. A peaked proton trace constituted those with a clearly defined bunch of protons in the energy spectrum, typically at an energy exceeding a lower energy thermal spectrum. To illustrate this more clearly, figure 5.3 shows three raw proton traces on which various levels of spectral peaking were observed. Figure 5.3(b) shows the effect particularly clearly.

Also plotted in figure 5.3 are the energy spectra for the same shots. Data is extracted from the raw images as described in section 3.4.1. These demonstrate peak bunch energies of 0.77 ± 0.04 MeV, 1.47 ± 0.11 MeV and 0.88 ± 0.05 MeV for shots (a), (b) and (c), respectively. For each shot, measured peak fluxes of $\sim 5 \times 10^{12}$ protons/MeV/sr, $\sim 4 \times 10^{12}$ protons/MeV/sr and $\sim 6 \times 10^{12}$ protons/MeV/sr were observed. These are equivalent to the observed fluxes in solid target experiments [115].

5.2.1 Multiple ion bunches

For a sharp vacuum-plasma interface, induced by shaping of the target, it would be expected that protons would be accelerated due to RPA for the given experimental

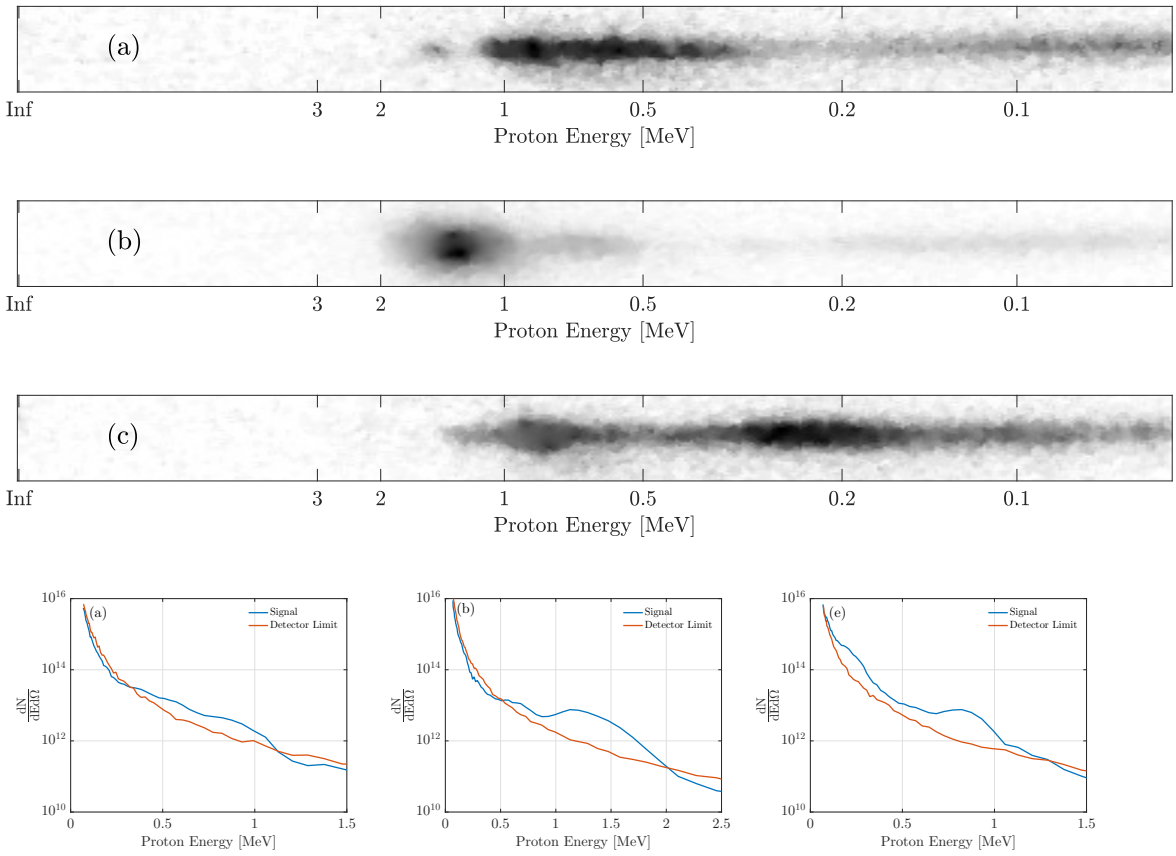


Figure 5.3: Experimental magnetic ion spectrometer traces illustrating the effect of high energy proton energy bunches, with a lower energy, thermal tail. The peak observed bunch energies were $0.77 \pm 0.04\,\mathrm{MeV}$, $1.47 \pm 0.11\,\mathrm{MeV}$ and $0.88 \pm 0.05\,\mathrm{MeV}$ for shots (a), (b) and (c), respectively.

conditions. An equilibrium could be expected between the laser photon and plasma thermal pressures, driving the critical surface at a quasi-constant velocity until the laser energy is depleted and the shock front collapses. The energy spectrum would consist of a narrow energy spread bunch of protons at high energy [252]. It is also possible a lower energy thermal component is present, produced as the shock front slows creating a broad energy spread. This is demonstrated in figure 5.3.

A further interesting signature in the experimental proton spectra is the observation of multiple peaks in the energy spectrum for a number of shots. Figure 5.4 demonstrates two shots containing examples of this observation. These were chosen from a sample of 8 shots exhibiting this effect from data taken during scans of the longitudinal and transverse nozzle position and the shock timing. This totalled 80 shots. As such, it can be said that these multiple bunches were observed on 10 % of shots.

Henceforth, two main examples will be discussed, termed shots (i) and (ii), which represent data in figures 5.4(a) and 5.4(c), plus 5.4(b) and 5.4(d), respectively. Both shots are for equivalent conditions; 5 bar absolute backing pressure giving a peak molecular gas density of $4.2 \times 10^{18}\,\mathrm{cm}^{-3}$, equivalent nozzle positions (0 mm relative longitudinal position) and 40 ns blast wave expansion time.

The two shots presented in figure 5.4 were chosen as follows; (i) represents the only shot with three bunches observed, while shots (ii) represents a typical example of the remaining shots which all demonstrate two bunches. These shots do not represent those with the highest proton energies or peak counts, but act to provide the clearest illustration of the phenomenon. For reference, the highest proton energy observed was 1.96 MeV with a peak proton number of 1.9×10^{12} protons/MeV/sr. The highest flux was observed on a shot with peak bunch energy of 0.38 MeV with a peak proton counts of 1.2×10^{13} protons/MeV/sr. As is evident from figure 5.4, lower energy bunches can exhibit higher proton numbers than this value.

Three energy bunches were observed above the thermal tail for shot (i), peaked at 0.38, 0.64 and 1.06 MeV with peak proton numbers of 4.2×10^{13} protons/MeV/sr, 6.7×10^{12} protons/MeV/sr and 2×10^{12} protons/MeV/sr, respectively.

Similarly, two energy bunches were observed for shot (ii), peaked at 0.38 and 0.61 MeV with peak proton numbers of 2.3×10^{13} protons/MeV/sr and 4.5×10^{12} protons/MeV/sr, respectively.

The presence of a peaked bunch with relatively narrow energy spread is typically indicative of a shock based mechanism constituting a sustained shock front moving at constant velocity from which protons are reflected by the associated potential. Classical hole-boring acceleration at the critical surface does not facilitate multiple bunches. Particle reflection is only sustainable during the quasi-stable period while the laser is driving the shock front, after which time the shock front rapidly dissipates. This model is not conducive to multiple bunches since there is no apparent mechanism for the shock

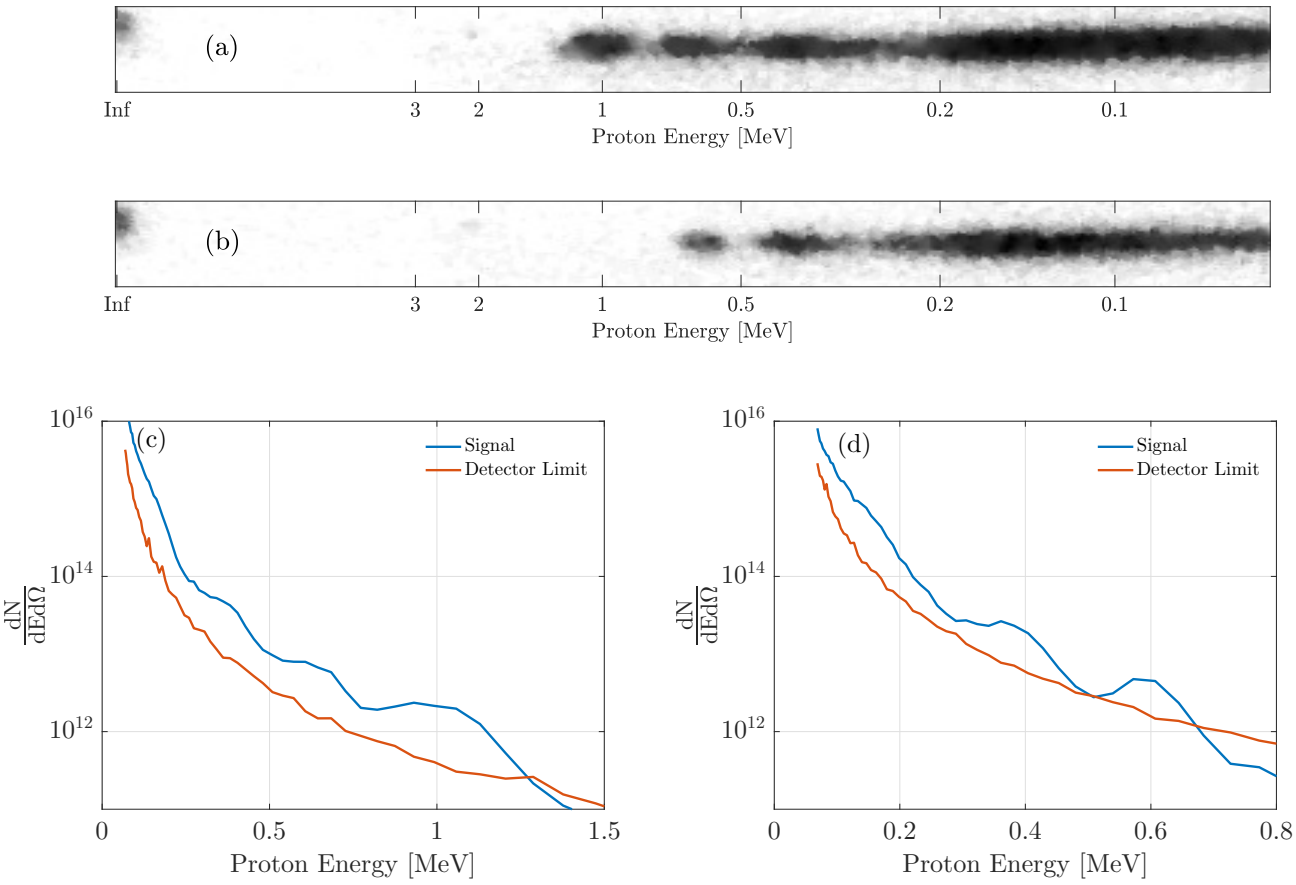


Figure 5.4: Experimental data demonstrating the observation of multiple proton bunches. (a) raw proton energy image from the magnetic ion spectrometer, with three proton energy bunches, (b) raw proton energy image with two energy bunches, (c) and (d) proton energy spectra as a function of counts per MeV per steradian for (a) and (b), respectively.

front velocity to transition between constant, discrete levels during the acceleration process.

Collisionless shock acceleration is a second mechanism by which bunches in the ion energy spectrum could be expected. The shock moving at constant velocity can snow-plough upstream ions. Again though, one would assume a quasi-equilibrium to be achieved between the up- and down-stream electron pressures, sustained by heating from the laser. After the laser intensity drops, one would assume the shock would dissipate due to loss of energy from reflections. One possible argument in favour of multiple bunches could be that protons which are not swept up by the shock front can become trapped in the potential behind the shock. It could be suggested that these particles are accelerated to energies significantly above the background, but below those achieved at the shock front. In reality however, these ions are trapped until such time as the shock decays, at which point the accelerating potential is not sufficient to accelerate sufficiently large particle fluxes to the required energies that they are quantitatively significant. Since the observed lower energy bunches are always higher in flux than the most energetic bunch, this further suggests a collisionless shock cannot be a mechanism by which to observe these multiple energy peaks.

The presence of a the pulse train structure described in section 5.1.1 could point to multiple successive acceleration stages. In either a hole-boring or collisionless shock acceleration based scheme, acceleration could occur from each pulse, with the proton energy expected to scale with the laser intensity of each successive pulse. In practice however, the experimentally observed results do not agree with this expected scaling; the peak energy ratio between the experimentally observed bunches does not match that of the intensity ratio between successive pulses. To illustrate this, the intensity of the second laser pulse is 0.36 times that of the main pulse, but the proton energy of the second to the first bunch is 0.62 times. As such, the pulse train structure does not provide sufficient means to explain the observed multiple bunches.

5.2.2 Proton energy vs. scale length

The use of an external YAG laser to drive a BW from the metal clip provides the advantage of stable energies delivered with simple temporal control between the arrival of the YAG and CO_2 pulses. Changing the Q-switch timing of the YAG laser by adjusting the time an input trigger is delivered, it was possible to adjust the relative temporal delay. For the purposes of the results presented here, the relative delay was changed from 20 ns to 70 ns. For such a timing scan the proton energies are given in figure 5.5. As can be observed, a strong proton energy dependence on the expansion time exists.

The data presented is the mean value of all shots on which peaked proton energy traces were observed for a given expansion time. The plotted errors are a combination of

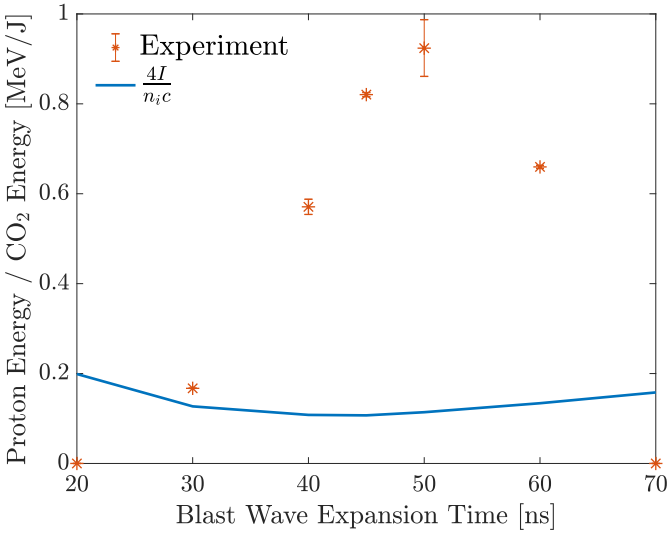


Figure 5.5: Experimental proton energy scaling as a function of relative blast wave timing; analogous to scaling versus the scale length. Also plotted is the predicted proton energy from HB-RPA ($E_p = 4I/n_i c$), using the estimated peak density from the shock front location.

the sample standard deviation for all shots at a given time and the uncertainty in determining the peak proton energy, determined by the energy bin size of any given pixel. Also plotted is the predicted proton energy for each given time, assumed to follow the HB-RPA scaling $E_p = 4I/n_i c$. The intensity is calculated in each case assuming the mean measured laser energy for each expansion time. The density is the assumed peak density of the blast wave, calculated by using the expected density increase in the strong shock limit, $\rho/\rho_0 = (\gamma+1)/(\gamma-1) \simeq 6$, using the unperturbed gas density at the average location of the shock front for each time. Clearly, the experimentally obtained results do not match the expected scaling.

During the 50 ns expansion window, the BW radius changes by $508 \pm 8\,\mu$m, or alternatively, $1.31 \pm 0.02\, z_R$. It might be thought that the change in intensity due to a variation in laser focal spot size through focus is the cause of the observed energy dependence. If this were the case, for fixed shock expansion conditions a change in longitudinal nozzle position (i.e. along the laser axis) would result in an equivalent energy scaling dependence as in figure 5.5. In reality, this is not observed, with the measured proton energies decreasing much slower than in figure 5.5. Figure 5.6 shows the change in ion energy as a function of nozzle position over 2 mm, equivalent to $5.2\, z_R$. The positions are relative to that for the peak observed proton energy per unit CO_2 energy. Positive values represent a shift in the laser focus towards the rear of the gas. The energies are again the mean value of bunched proton spectra. The error in energy comes from a combination of the sample standard deviation and the energy uncertainty of the detector. Again, also plotted is the predicted proton energy from HB scaling. Given the shock front location in the gas was fixed, the expected peak blast wave density was used from the

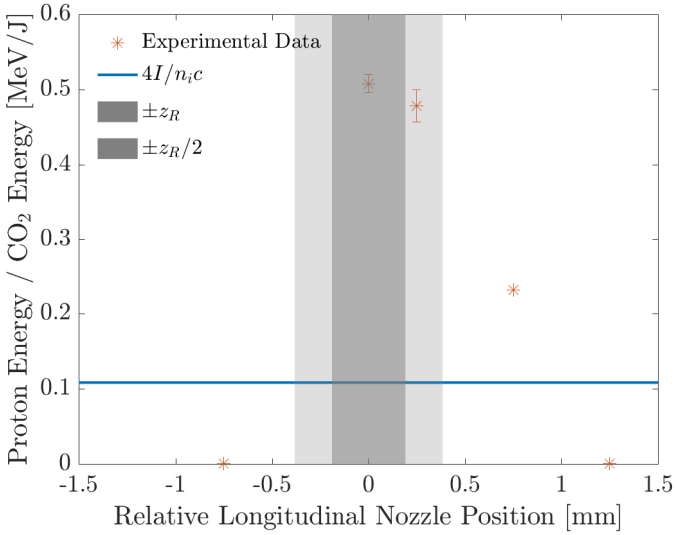


Figure 5.6: Experimental proton energy scaling as a function of the nozzle position along the axis of laser focus. Proton energies are not observed to appreciably decrease over two Rayleigh lengths. Also plotted is the predicted proton energy from HB-RPA ($E_p = 4I/n_ic$). A mean laser energy of 1.1 J was used. The shock expansion was fixed in this case, with the estimated peak density calculated from the average shock front location across all shots.

mean shock front location on all shots. This was found to be $\sim 3.5n_c$. The intensity was calculated using the mean laser energy of ~ 1.1J.

The difference in peak energy between figures 5.5 and 5.6 arises from a transverse optimisation of the nozzle position between the longitudinal and temporal scans. It should also be noted that for all shots presented here, except the shortest BW expansion time, the peak density in the shock remains above the relativistically correct critical density. For the 20 ns case, the assumed peak density is $0.9\,n_c$. Even for this case, density steepening, as presented by Robinson et al. [149], suggests RPA-HB should be possible. Since scaling suggests an inverse dependence on the density of the plasma being accelerated, it would be expected that the 20 ns or 30 ns case would provide the highest proton energies. Clearly then, given the 6-fold increase in proton energy between 30 ns and 50 ns, another phenomenon must be involved.

While a decrease in proton energy is observed over z_R, the relative difference when compared to the temporal scan is less. To quantitatively illustrate this, for the longitudinal scan the proton energy decreased by 7.2 % over 250 µm. By comparison, the proton energy in the temporal scan is observed to decrease by 67 % over a distance of ∼280 µm. Perhaps more clearly, the proton energy decreases from its peak value to zero in 752 µm and 254 µm for the longitudinal and temporal scans, respectively. It is therefore reasonable to assume that the observed proton energy depends on another time-dependent parameter. From the shock scaling presented in section 3.2.1, this is attributed to the density scale length, which is shown to be self-similar with time.

Experimentally observed density scale lengths

To test the hypothesis that the density scale length approaching the critical surface is a deterministic factor in the observed proton energy scaling, it is important to obtain values for these for each given expansion time. However, real experimental scale lengths are difficult to extract from the interferometric images. A number of challenges exist when attempting to retrieve the experimental density profile. The steep gradients at the shock front provide a major obstacle. Phase shifts significantly greater than 2π can be observed for the steepest gradients, making deconvolution more complicated. Furthermore, the ablated material from the clip which drives the expansion remains ionised, even after $> 20\,\text{ns}$. This is observed even for shots with no ionisation at the shock front from the CO_2 beam, and consequently makes density retrieval without ionisation from the shock impossible. The phase modulation at the peak of the shock is also such that fringe cuts are possible; the process by which two fringes appear to join in the shock, despite their being from two separate fringes when no perturbation is present. Information is also often totally lost at the shock front, with no fringes observed. This is due to the probe beam deflection being such that the information is outside the collection angle of the imaging optic. Finally, the fringe contrast on the images is poor, making fringe identification challenging.

To overcome these issues and retrieve the density scale lengths, a number of solutions were trialled. The fringe contrast issues were overcome with a process of computational image manipulation. It was possible to manually adjust the brightness and contrast of the image to optimise the fringe contrast. Automatic fringe tracing was also employed to the images, which first divided the raw image by a copy of itself which had a gaussian filter applied to blur the image; this acted to boost the contrast. A Fourier filter could then be applied, with only the region of interest in frequency space selected and the rest masked to remove noise. Finally, the fringes could be automatically traced by looking for the maximum and minimum levels above and below a threshold value set to be between these two values in regions of poor contrast. This allowed the automatic tracing of fringes for all regions of the image except at the shock front and those regions with the poorest contrast.

To resolve the information lost in the shock front, fringes were manually drawn on to the image, ensuring that the ends of a given fringe either side of the shock front were joined. The paths traced by the fringes in this instance was estimated from the information available on the raw image. While information is often lost in the very densest part of the shock, the fringes could be traced in the preceding regions. By utilising the fringes that were not obscured and the traces up to the point of information loss, it was possible to manually interpolate the fringes over the shock front. The level of phase shift could then be measured and density estimates retrieved. Figure 5.7 shows the estimated scale lengths for the given expansion times. The errors are a combination of the difference in scale length obtained through manual interpolation on the same image multiple times

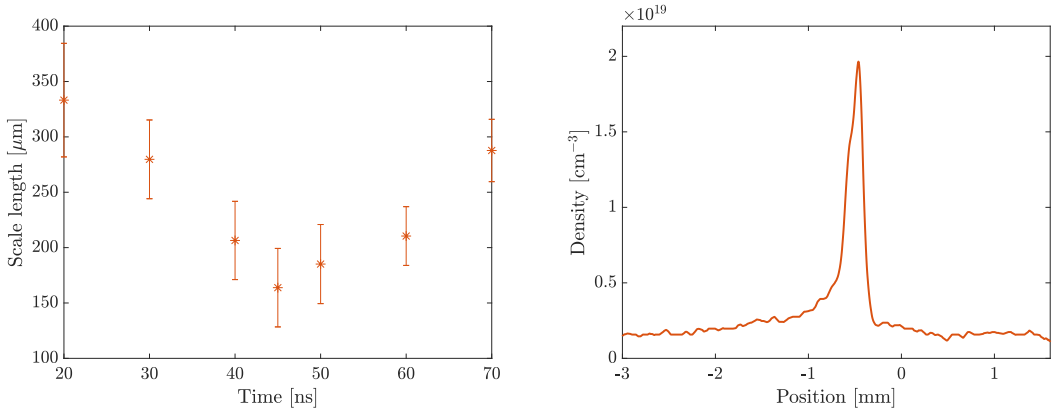


Figure 5.7: Left: Experimental density scale lengths obtained using interferometry ~ 30 ps before the main CO_2 pulse. Right: An example density lineout for the case of 50 ns expansion.

to assess the reproducibility, the variation in scale length across the focal spot and the resolution limit of the diagnostic. Figure 5.7 also shows the density profile achieved for the 50 ns case. The low upstream density is due to lack of ionisation; the relatively low density of the cold gas is not sufficient to produce measurable phase shifts to detect. For 50 ns expansion, the mean shock front position is ∼150 µm from the centre of the gas jet. Using the strong shock condition (equation 3.5b) and the unperturbed gas density profile, the expected peak density of the shock would be $4.5 \times 10^{19}\,\mathrm{cm}^{-3}$. The extracted peak density in this case is a factor of ~ 2.25 lower than expected. This is likely due to inaccurate interpolation over the shock front, with the phase shifts underestimated.

For expansion times of 45 ns and above, the scale length is observed to increase with time as would be expected. For times between 20 ns and 45 ns, the scale length decreases. This effect will be explained in the next section.

Analytic density scale lengths

While the true scale lengths are difficult to extract, it is possible to infer relative information from the experimental results. From the assumption that the shock originates from a point source at the clip surface, the expansion radius can be calculated by measurement of the front surface of the shock on the interferometric images. While the estimation of a point source is not strictly true, the ablated material heats a finite region of gas above the clip, the calculation will act as an informative tool to estimate the expected scale lengths.

The measured shock radius is plotted in figure 5.8(a), along with the analytical solution for the radius given by equation 3.7. The analytical solution was calculated using the YAG energy of $E = 80$ mJ, deposited in a 10 µm spot. The gas density was assumed to be $5.6 \times 10^{18}\,\mathrm{cm}^{-3}$. This represents the mean unperturbed gas density across all

shock front locations, obtained from the experimentally obtained interferograms. The experimental results show good agreement with the analytical solution, but for a constant offset in the radius across the 50 ns of 370 µm. This offset can be explained by the assumption of a point source expansion from the clip surface. In practice, the expansion volume is finite. This constant offset provides evidence for the size of the volume heated by the ablated material from the clip, which has a size of 370 µm.

The shock velocity can also be estimated. Through the assumption ionisation in the upstream gas is negligible, the upstream sound speed is given as $c_s = \sqrt{\gamma k_B T/2m_i}$, where γ is the ratio of heat capacities. At 300 K, the bulk sound speed is thus $c_s \simeq 1300\,\mathrm{ms}^{-1}$. By comparison of the measured shock speed to the sound speed, one can test the validity of the strong shock approximation; for $M > 1$, the shock is assumed strongly driven. Figure 5.8(b) shows the mean shock velocity for all given times, showing the strong shock limit is applicable. This is the mean velocity for the temporal window between timesteps e.g. between 50 ns and 60 ns, not the mean total velocity. This is justified by our interest in determining whether the shock is still strongly driven during any given temporal window. Also plotted is the analytical shock velocity from equation 3.8. Again, this used the same laser and density assumptions as for the expansion radius. This shows good agreement with the measured shock velocities.

The experimental velocity is observed to decrease over each temporal expansion window, as would be expected from the relation given in equation 3.8, but never drops below $M = 1$. The shock is assumed strongly driven at all times.

Based on the strong shock condition being met, it is possible to obtain an estimate of the density scale length using the expansion radius. Assuming spherical expansion, as earlier stated in section 3.2.1, the scale length is $0.057r_1$. The theoretical scale length takes the form as shown in figure 5.8(c). Also plotted for comparison are the experimental scale lengths, as given previously in figure 5.7.

A clear difference between the experimentally obtained and analytical solutions for the scale length exist. The experimentally measured values are > 2 times higher than predicted analytically. Furthermore, the analytic values increase with time, while the experimental values decrease, before later increasing.

The reasons for these differences are not immediately clear, although a number of possible explanations exist. Firstly, it might be expected that the analytical solution is not perfectly applicable in this case, given the Sedov-Taylor solutions introduced in section 3.2.1 arise from consideration of a homogeneous medium. In reality, this is not an issue; hydrodynamic simulations using the FLASH code suggest that the blast wave expansion is still well predicted by the Sedov-Taylor solutions, even for a linear ramp. The results presented in figures 5.8(a) and (b) also suggest good agreement between the experiment and theory. Previous authors have also demonstrated pre-pulse driven cylindrical blast wave expansion in a gas jet fits the predicted Sedov-Taylor scaling [253].

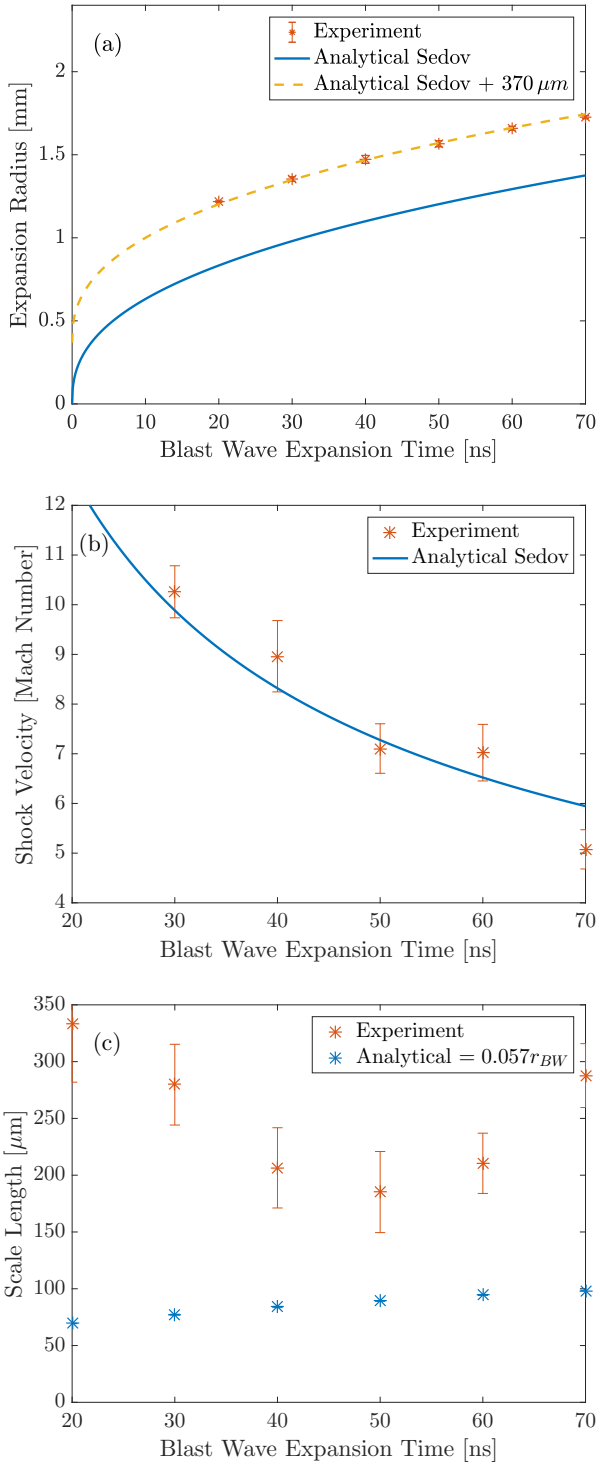


Figure 5.8: (a) The experimental shock radius, along with the analytical prediction obtained from equation 3.7. (b) The mean experimental blast wave expansion velocity for the temporal scan, demonstrating the shock continues to propagate in the strong shock limit up to the end of the temporal window. Also plotted is the predicted shock velocity from equation 3.8. (c) The theoretical scale length for a spherically expanding shock, assuming the expansion radius from a point source at the clip, using the radius measured in figure (a). For comparison the experimental results are also plotted. All analytical solutions use the YAG energy of $E = 80\,\mathrm{mJ}$ and a density of $5.6 \times 10^{18}\,\mathrm{cm}^{-3}$, which represents the mean unperturbed gas density across all shock locations.

Secondly, the long energy deposition time of the YAG laser (5 ns) used to produce the blast wave results in a longer scale length. The analytical solutions assume an instantaneous point explosion, however in this situation the energy deposition is on a hydrodynamically significant timescale. Other authors have claimed scale lengths less than 50 µm are not achievable with this shock generation method [182]; something readily achievable with CO_2 pre-pulse driven shocks, as demonstrated in Chapter 4. This is believed to be due to the significantly shorter deposition times with a pre-pulse scheme, of the order $\sim$ ps, compared to 5 ns in this case.

Finally, perhaps the most obvious answer lies in the extraction of the scale lengths from the experimental data. As explained previously, the conditions were such that fringe cuts and total lack of signal were observed on the interferometric images around the shock front. As such, the author was required to manually trace these fringes using the information available. An inherent level of inaccuracy exists in this method, since there is no way to assess with absolute certainty the accuracy of these interpolations, and the method is by its very definition subjective. The measured peak density in figure 5.7 is less than half the expected value from the unperturbed gas density profile. This suggests the level of fringe shift in the shock was underestimated. If this is true, the increased phase shift and the finite spatial size of unresolved shock front region implies the peak density would increase relative to the resolved portion of the interferogram, producing shorter scale lengths. As such, it would be reasonable to argue the scale lengths could be shorter than those presented here, while the peak shock densities are higher.

The decreasing of measured scale length at early times, before subsequently increasing is also in stark disagreement with the analytical predictions. This is believed to be not due to accurate representation of the shock profile, but in fact due to the generation mechanism. Heating occurs through the hot ablated clip material which is ejected into the gas. This heating can in fact be observed above the clip in the interferogram presented earlier in figure 5.2. It is believed that at early times this ablated material persists behind the shock front, providing greater phase shifts than would otherwise be observed. This hot, high-Z material modifies the apparent density profile, giving the impression of longer scale lengths. The effect is verified by interferograms obtained at earlier times, before the main CO_2 pulse, where the only ionisation is from this ablated material. These interferograms show ionisation extending towards the shock front and helps explain the longer than expected scale lengths. This effect would also explain the decreasing scale length at early times; shorter expansion times result in a higher density of the ablated material and an apparent longer scale length. As the shock expands over an ever increasing volume, the contribution decreases.

Given the uncertainty in the experimentally measured scale lengths, along with the good agreement between the other shock expansion properties and Sedov-Taylor blast wave solutions, the preceding work will utilise the analytic scale lengths. These results

will be used to help establish a region of parameter space over which to study the effect of scale length on proton acceleration through simulations.

5.2.3 Summary of experimental results

The preceding sections have presented experimentally observed results demonstrating the proton energy scales with both the longitudinal nozzle position and the temporal expansion of the BW. The scaling of the latter was shown to be stronger than the former, suggesting the position of the shock relative to the laser focus is not the dominant factor in deciding the temporal scaling for this study. Aside from the position of the BW, a temporal change will result in a variation in the density profile preceding the critical surface. From measurement of the shock front position, the expansion is predicted to be in the strong shock regime for the studied temporal window. The scale length is consequently predicted to increase self-similarly with radius, or equivalently, expansion time. Experimentally obtained scale lengths show longer than predicted values, although this is suggested to be due to challenges in density extraction under-resolving the peak density. The scale length appears to decrease, before subsequently increasing again. The reason the earliest times show these increased scale lengths is believed to be due to the hot, ablated material from the clip dominating the phase shift from the shock density profile, giving the appearance of more material and a longer scale length.

Multiple peaks in the proton energy traces were observed. While single high energy bunches are expected for a shock accelerated spectrum, multiple peaks are more challenging to explain from conventionally held acceleration theory.

The discussion in this section illustrates a lack of clarity on the mechanism behind the observation of these higher than expected proton energies, the strong dependence on the expansion time (scale length) and the observation of multiple mono-energetic features. Therefore, to better understand the underlying physics behind these experiments, particle-in-cell simulations were conducted. This work is presented in the following section and provides a possible explanation for the results presented above.

5.3 Particle-in-cell Simulations

Typically simulation based investigations into radiation pressure driven acceleration schemes consider “top-hat” or “slab” density profiles as this maximises reflection and simplifies the interaction physics somewhat. Clearly for these results a slab profile is not sufficient; the density profile preceding the critical surface must be considered also.

Three different scenarios were considered; a plasma slab, then linear and exponential ramps. These shapes were chosen to represent the idealised case, previously studied

Parameter	Value
Electron particles per cell	16
Proton particles per cell	16
Box size x	220 - 470 µm
Box size y	180 µm
Grid size x	$120\,\lambda_L = 83.3$ nm
Grid size y	$120\,\lambda_L = 83.3$ nm
Laser wavelength	10 µm
Laser focal spot size	65 µm
Laser pulse length	5 ps
Laser intensity	0.53 - 5.5×10^{16} Wcm^{-2}
a_0	0.62 - 2
Laser polarisation	Linear, p-polarised
Initial electron/proton temperatures	0 eV
Peak electron/proton densities	$1.8\,n_c$
Scale length	0 - 200 µm

Table 5.2: The particle-in-cell simulations used for studies into the effect of a scale length preceding the critical surface and subsequent studies into the observed density bunching phenomenon.

scenarios [150], and a profile which more accurately represents that of a blast wave, respectively. The density ramps were characterised by their scale length, again the distance over which the density drops from its peak to $1/e$ of the same value. These were simulated for a range of intensity values, corresponding to a_0 values of 0.62, 1.25 and 2. The full list of simulation parameters are summarised in table 5.2.

In all cases the plasma was formed of cold, pre-ionised hydrogen with initial electron and ion temperatures of 0 eV. The assumption of a pre-ionised plasma is reasonable given the peak intensity of the laser is sufficiently high to facilitate rapid ionisation of the target at the rising edge of the laser pulse. While interferometry indicated the presence of hot, high Z material behind the shock front due to the ablated clip, this was ignored for these simulations. While some of this material would indeed be present behind this shock front, the fraction relative to the hydrogen is assumed to be very small. The interferometric images are so affected due to their integration along the length of the shock front, while the interaction occurs at only a fraction of this; the contribution to the target conditions at the interaction point is assumed negligable.

Initial studies were interested in the effect of this scale length on the RPA driven ion energy spectrum. As such, the target rear-surface was not considered and the BWs were assumed infinitely thick; the plasma continues to the rear of the box in an attempt to suppress sheath effects. A BW with peak density of $1.8\,n_c$ with scale lengths from 0 - 200 µm was studied. These were chosen to span the range of analytically predicted scale lengths and the experimentally measured scale length for the case of the highest

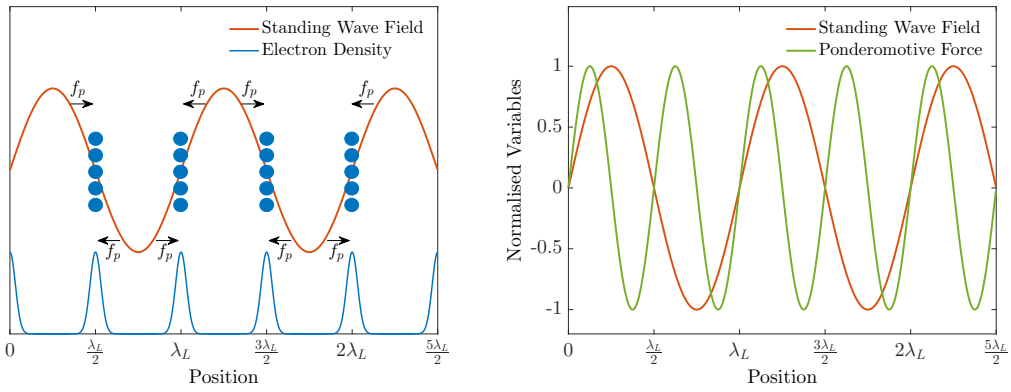


Figure 5.9: (a) A cartoon of the forces due to a standing wave on the plasma electrons, inducing density bunching at the standing wave nodes. (b) The ponderomotive force for the depicted standing wave.

observed proton energies.

5.3.1 Standing wave induced plasma grating structure

Grating formation

Consider first the case of a plasma slab, going from zero to a peak density, n_{peak} as a step function at the laser focus. In this case, if $n_{\text{peak}} > \gamma n_c$, an incident laser pulse will be reflected, forming a standing wave. Assuming the critical surface is stationary and total reflection, the standing wave will have a wavelength of half the incident beam, with a peak amplitude twice that of the incident pulse. However, for the slab case the standing wave profile has little influence on the plasma, since the effect is occurring in vacuum.

Now consider the same case but with a density ramp preceding the critical surface. In this case the standing wave can influence the plasma conditions. Electrons within the density ramp will experience the ponderomotive force from the standing wave; the ponderomotive force scaling goes as $\vec{\nabla}E^2$ and electrons are accelerated from regions of high field amplitude towards the standing wave nodes. This acts like a pinching force on the electrons, inducing localised density enhancement at the nodes and cavitation in regions of high field strength; the formation of a plasma grating structure due to "density bunching". This is illustrated by the cartoon in figure 5.9. Ions are comparatively slow to respond given their greater inertia; the induced charge separation fields are the dominant driving force behind their motion. As the charge separation increases the ions are also accelerated towards the standing wave nodes. This induced grating structure is formed of a variable number of bunches, dependent on the ramp shape, length and laser intensity. The formation of the density modulation is similar to that described by Estabrook and Kruer [254], who showed the formation of electron perturbations due

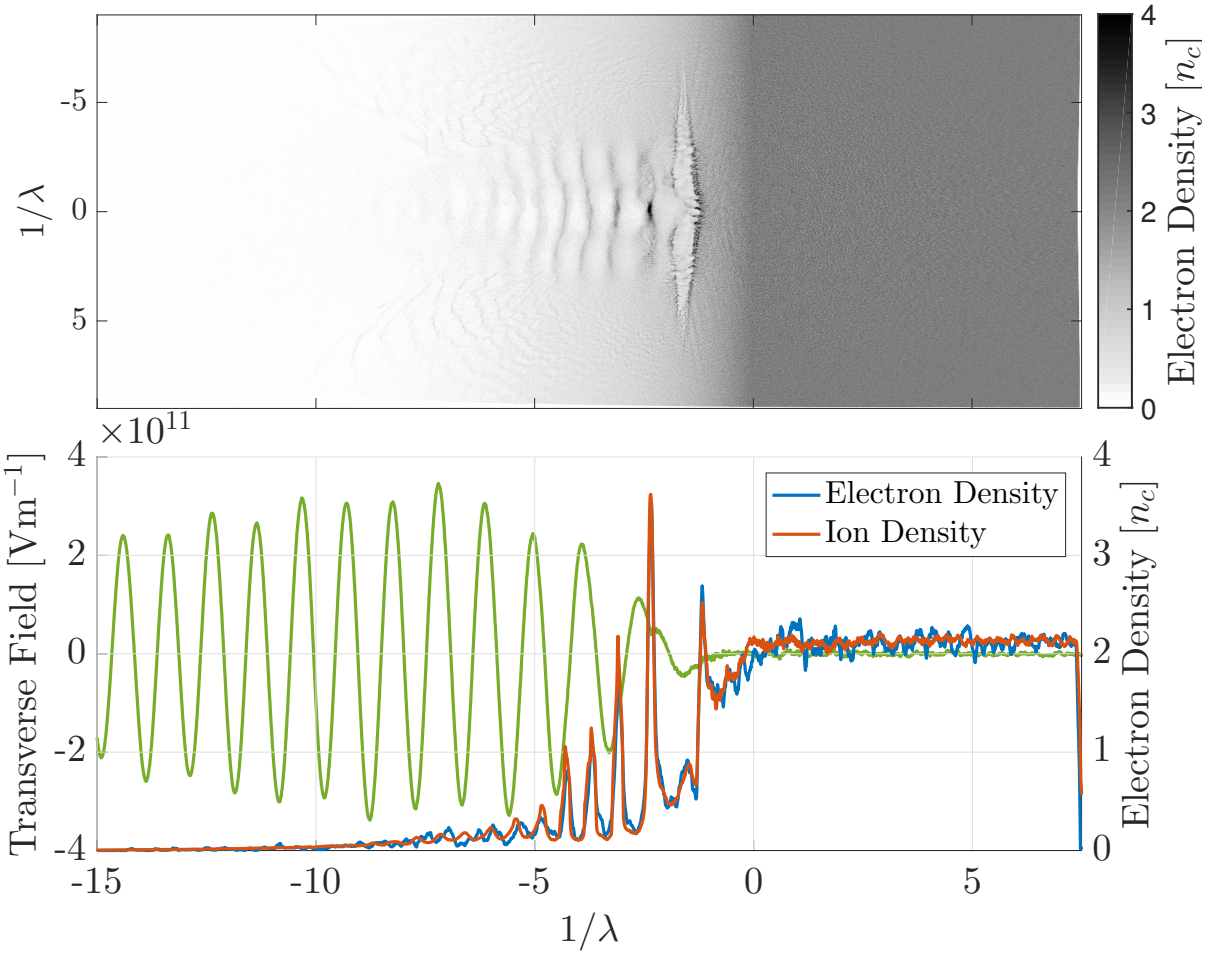


Figure 5.10: Simulation output at 2.7 ps showing the 2D density electron profile for a 25 µm scale length exponential density ramp preceding the critical surface. Also shown are 1D lineouts of the on-axis transverse component of the laser field, the electron and ion densities. A 10 µm, 5 ps CO_2 laser pulse with $a_0 = 0.62$ is incident on the plasma. A standing wave is formed between the incident and reflected pulse components, producing a grating structure in the electron and ion densities.

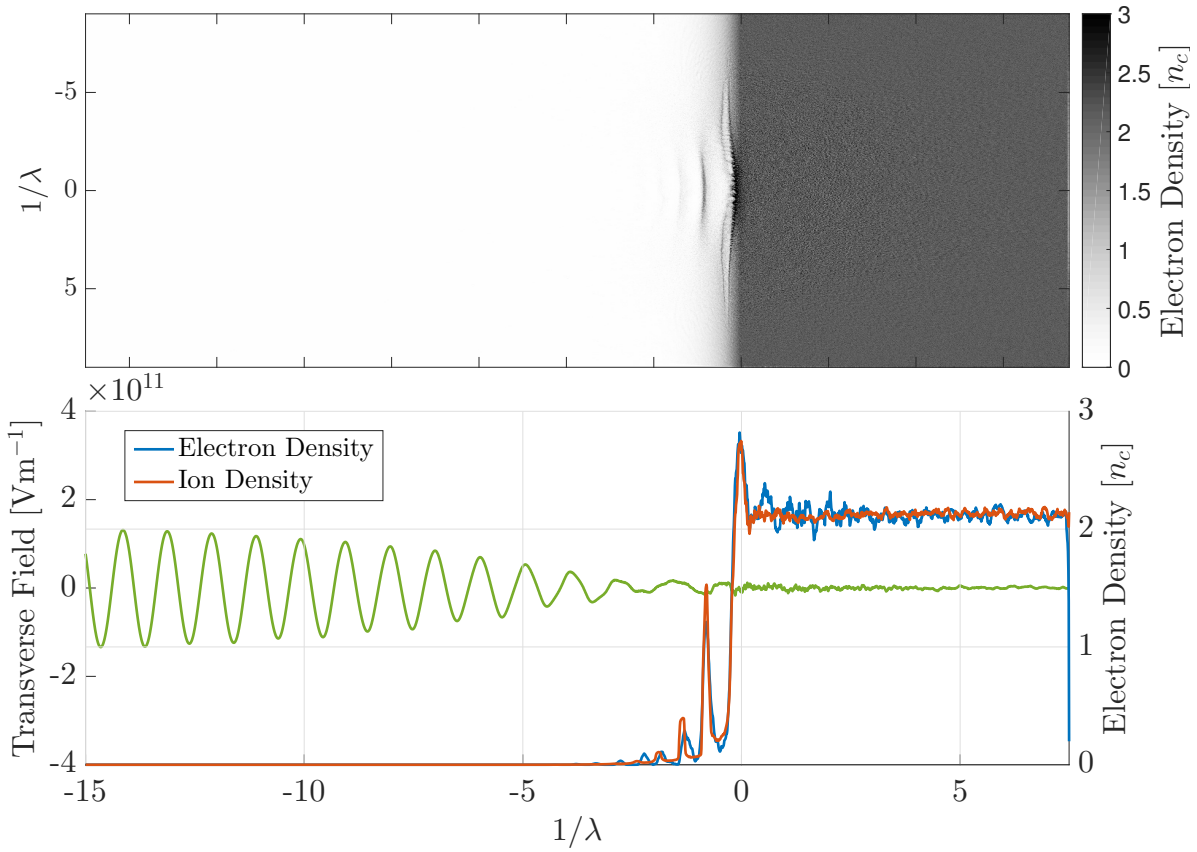


Figure 5.11: Simulation output at 2.3 ps showing the 2D density electron profile for a 5 µm scale length exponential density ramp preceding the critical surface. Also shown are 1D lineouts of the on-axis transverse component of the laser field, the electron and ion densities. A 5 ps CO_2 laser pulse with $a_0 = 0.62$ is incident on the plasma.

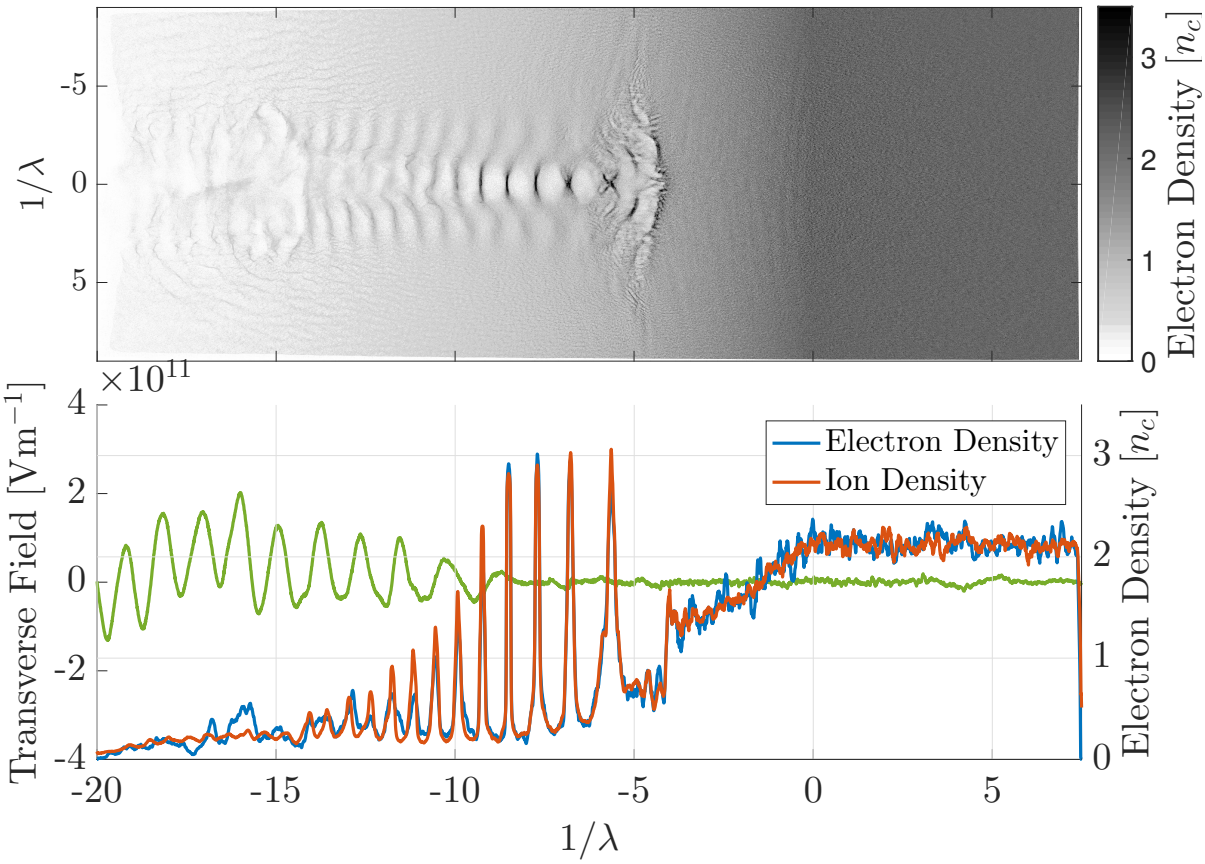


Figure 5.12: Simulation output at 3.3 ps showing the 2D density electron profile for a long, 75 µm scale length exponential density ramp preceding the critical surface. Also shown are 1D lineouts of the on-axis transverse component of the laser field, the electron and ion densities. A 5 ps CO_2 laser pulse with $a_0 = 0.62$ is incident on the plasma.

to an induced standing wave from the reflection of a laser off the critical surface. The density of the induced grating elements is also dependent on ramp shape, length and laser intensity, with the structures tending to a full width at half maximum size on the order of the electron skin depth of the plasma for the given structure peak density ($c/\omega_{p_e} \simeq 1\,\mu\text{m}$). An example grating structure is shown in figure 5.10 for a 25 µm ramp. This demonstrates the formation of a grating structure at 2.7 ps for a 10 µm, 5 ps pulse with $a_0 = 0.62$. This equates to an intensity of $5.3 \times 10^{15}\,\text{Wcm}^{-2}$ in a 65 µm focal spot. Figure 5.10 represents the near idealised case for perfect acceleration. For comparison, a shorter 5 µm ramp and significantly longer 75 µm ramp are shown in figures 5.11 and 5.12, respectively. These are shown at 2.3 ps and 3.3 ps, respectively, owing to the variation in formation times due to the ramp profile.

Ramp shape and length are clearly deterministic factors; the amount of plasma preceding the critical surface dictates the number of periods of the standing wave within the ramp and so number of bunches that can be formed. The incident laser intensity is important for a number of reasons. Sufficient intensity is required to provide a force that is capable of inducing the bunching within the period of the laser. Ideally this occurs within half the laser pulse duration, as will be described later in this section. However the intensity must not be such that the critical surface begins moving before the bunches are formed; this modifies the interference condition of the standing wave such that no stable nodes can form and bunching does not occur. Assuming these conditions are met, a grating structure can be formed. A series of snapshots demonstrating the temporal evolution of the grating structure is shown in figures 5.13 and 5.14. This is for the same conditions as in figure 5.10, with four temporal snapshots showing the initial ramp structure at 0 ps, the beginning of bunch formation at 1.7 ps, stable formation of multiple overcritical bunches at 2.4 ps and finally the point of peak density enhancement in the bunch closest to the initial critical surface, at 3 ps. This reaches a maximum density of $n_e = 3.59\,n_c$. After this time, the density begins to decrease; the same effect can be observed to have already occurred in the preceding density bunches.

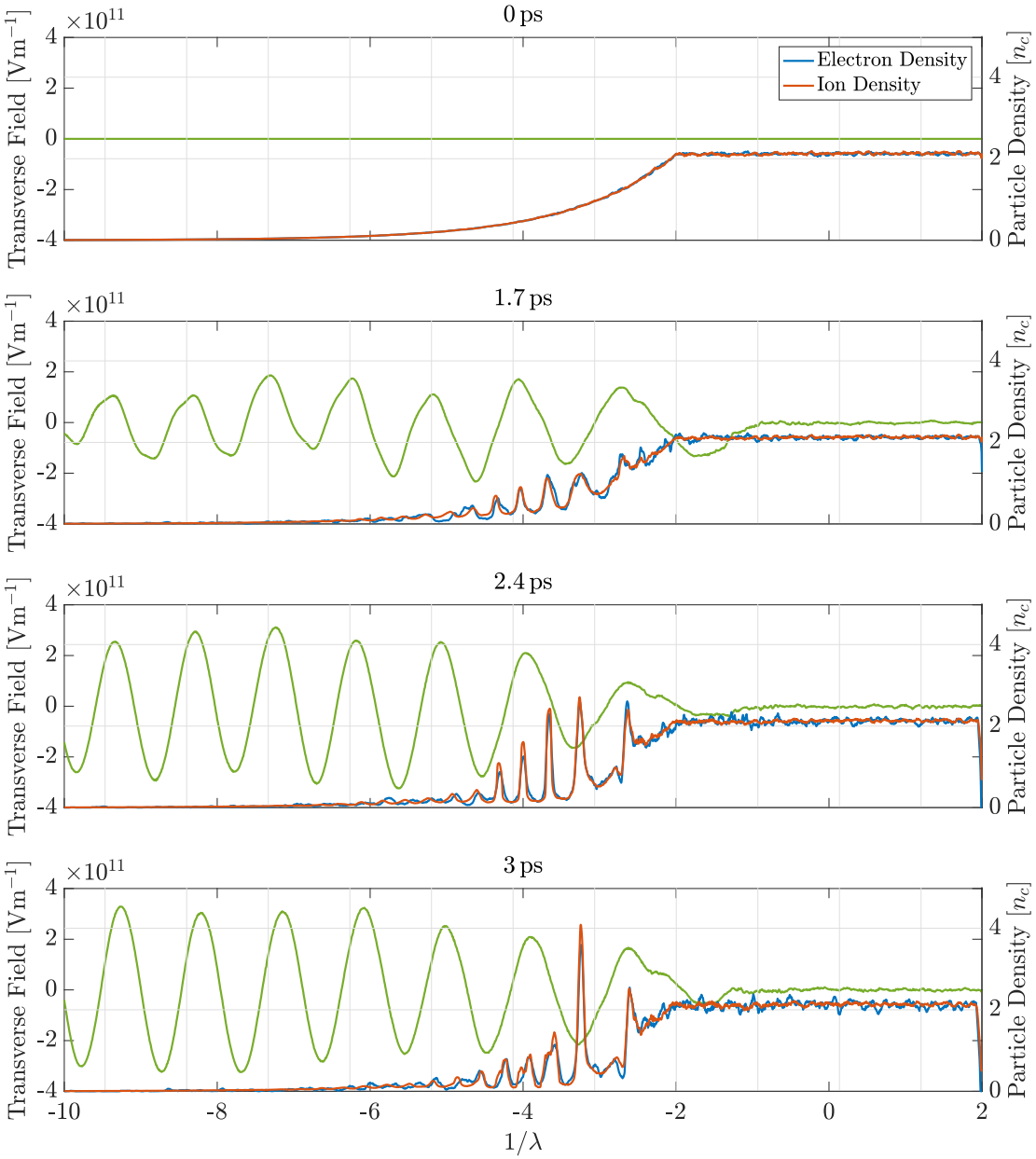


Figure 5.13: Simulation outputs showing the temporal evolution of bunch formation from the initial conditions through to the time of maximum density in the structure closest to the critical surface. 1D lineouts of the on-axis transverse laser field, ion and electron densities at 0, 1.7, 2.4 and 3 ps are shown. A 10 µm, 5 ps CO_2 laser pulse with $a_0 = 0.62$ is incident on the plasma, as in figure 5.10.

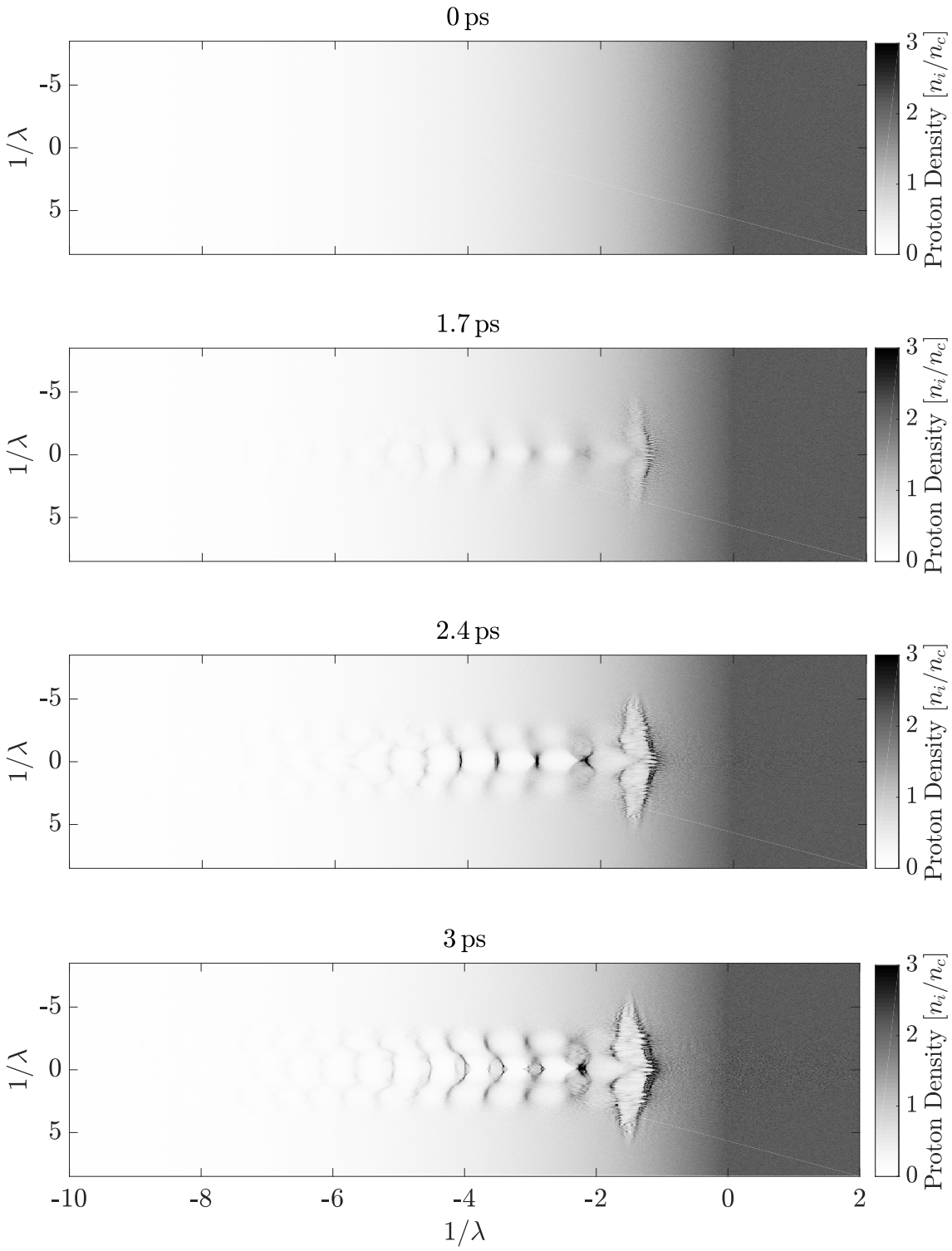


Figure 5.14: The 2D density profile for the grating structure formation, for equivalent temporal snapshots from the same simulation as shown in figure 5.13. The temporal evolution of the grating structure is depicted, with formation up to 2.4 ps, before the structure begins to collapse at 3 ps. Note the colour scale is saturated to highlight the effect.

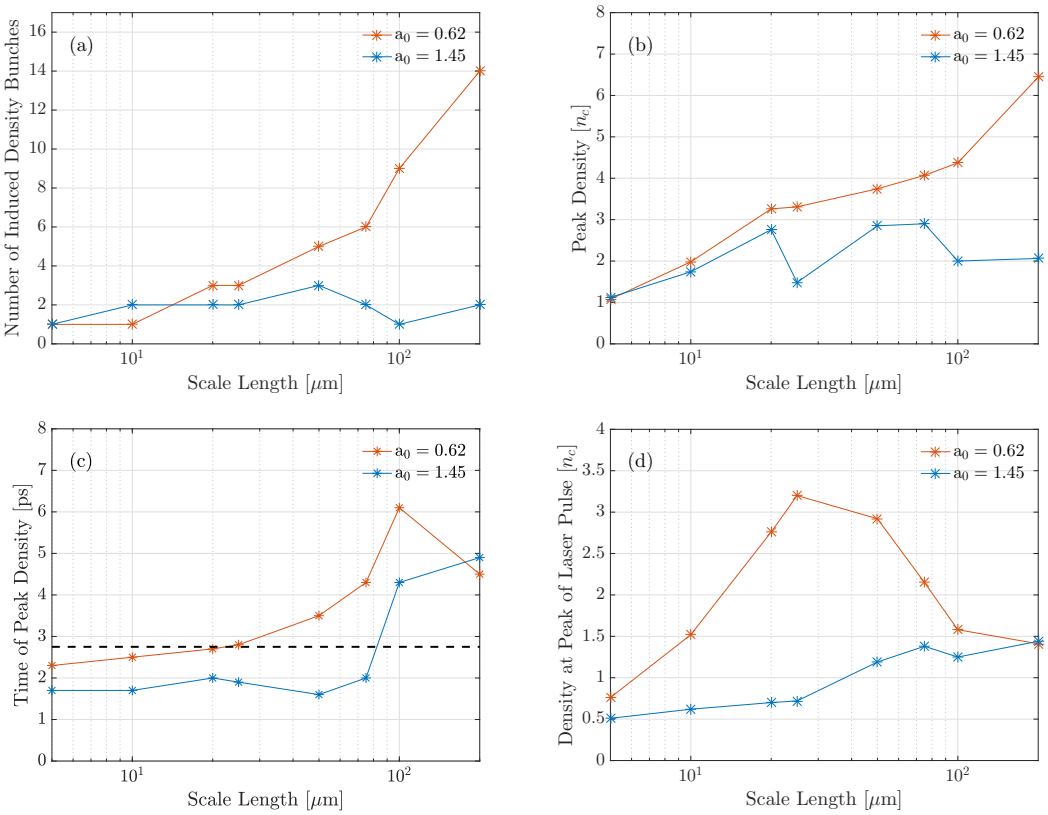


Figure 5.15: (a) The number of over-critical density bunches formed for a given exponential density scale length. (b) The peak density for the highest density grating structure. (c) The corresponding time of the peak density value shown in (b) relative to the scale length. The time of peak laser intensity is shown as the dashed black line for comparison. (d) The density of the highest density structure at the peak of the laser pulse.

Figure 5.15 helps illustrate the optimal formation conditions for the grating structure. The number of bunches is shown to scale quasi-linearly with the scale length for $a_0 = 0.62$, while is roughly constant for $a_0 = 1.45$ in figure 5.15(a). This can be attributed to the increased intensity in the latter case, with no stable grating structure formed as a result.

Figure 5.15(b) shows the highest density observed in the closest bunch preceding the critical surface as a function of scale length. This can be understood through simple consideration of the system. In 1D, equating the mean initial density contained within one wavelength of the standing wave to the unknown density, n_b, within the width of a bunch, $\sim c/\omega_{p_e}$, gives $\langle n_{e0}\rangle \lambda_L/2 = n_b c/\omega_{p_e}$. The peak density of a grating element is estimated by

$$n_b \simeq \frac{\alpha \lambda_L^2}{4c^2} \frac{e^2}{m_e \epsilon_0} \langle n_{e0}\rangle^2 \tag{5.1}$$

where α is a multiplication factor to compensate for the variation in thickness of the

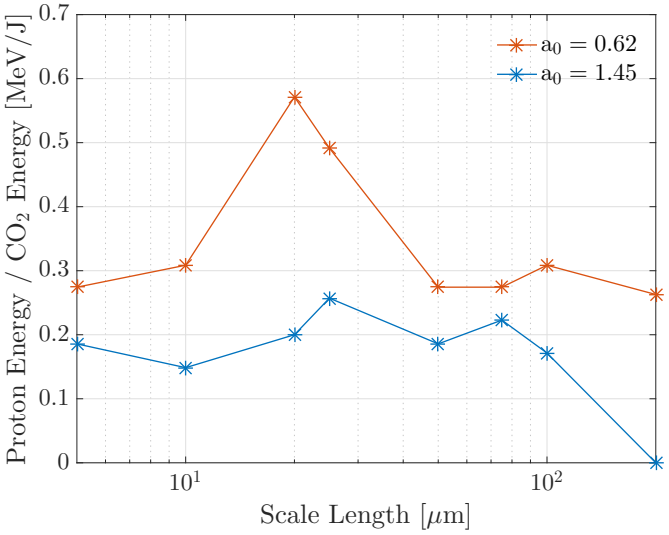


Figure 5.16: Proton energy scaling vs. scale length from 2D PIC simulations for exponential density ramps with $a_0 = 0.62$ and $a_0 = 1.45$. The $a_0 = 0.62$ case shows a peaked dependence on the scale length, as for the experimental results, albeit for shorter scale lengths.

grating element. This variation occurs because the peak density is dependent on the formation time. These simple considerations perform well in predicting the peak density, although knowledge of the grating element thickness is required. For the 20 µm case, the first bunch preceding the initial critical surface is predicted to reach a peak density of $3.17\,n_c$, while in the simulation actually reaches a peak density of $3.26\,n_c$.

Figure 5.15(c) shows the corresponding time at which these peak densities are achieved. When combined with the proton energy scaling in figure 5.16, this helps to illustrate the point made previously; sufficient mass is required in the overcritical grating element to oppose significant motion before the peak of the pulse, but not too high as to hinder the subsequent acceleration. The 20 µm example reaches its modest peak density just as the peak of the pulse arrives, but is dense enough not to move significantly before this point to destroy the standing wave condition and suppress acceleration. Finally, figure 5.15(d) further reinforces this point, with the density at the peak of the laser pulse.

Proton acceleration off the grating structure

Results demonstrated a strong dependence on the ion energy with scale length, as shown in figure 5.16.

The formation of the grating structure still facilitates radiation pressure driven acceleration, although this now occurs not at the location of the initial critical surface but at the induced over-critical density spikes. The reduced areal density of the bunches results in enhanced proton energies accelerated by these structures when compared to

a slab. The slab acceleration process is equivalent to the step-density simulations presented previously in Chapter 4. Density is piled up at the vacuum-density interface, and this overdense, reflecting critical surface is accelerated into the upstream plasma, accelerating upstream ions off the shock potential.

For the case of $a_0 = 0.62$, proton energies are enhanced by 3.3 times, as shown in figure 5.16. For $a_0 = 1.45$, the trend is much less clear, a fractional 0.39 increase in proton energy is observed between no ramp and a 25 µm ramp. No grating structure is observed for $a_0 = 2$ as the intensity is too great to meet the formation conditions. Here, the intensity is too great and the critical surface begins moving too soon in the laser pulse; no long lived stationary standing wave nodes exist and the grating cannot form. The information is subsequently omitted here.

Acceleration is not limited to the induced grating structure. Even for the optimised scenario in which over-critical bunch formation at the peak of the laser pulse occurs, the accelerated structures rapidly drop below the critical density. As the density of the spikes goes sufficiently overcritical, the standing wave condition is broken and there is no force compressing the bunch from the upstream side; the previously induced sharp density gradient is then dissipated and the bunch collapses. The density of the spike and time in the laser intensity profile at which this occurs determines the time it takes for the feature to collapse. After the collapse, it is not uncommon for the laser to subsequently accelerate the initial critical density surface, also accelerating protons. However, these protons are consistently lower in energy than those accelerated from the grating structure. In some cases, the accelerating phase from the initial critical surface can also occur in the form of a collisionless shock as outlined in section 2.4.2. This typically occurs after the laser pulse has finished, when the density and temperature gradient at the HB front causes the RPA front to decay into a collisionless shock. This structure only produces low energy protons with no observable spectral peaking, significantly less in number than those accelerated from the density structures.

To optimise the acceleration process, the density bunches are required to form on a timescale which coincides with the arrival of the peak of the laser pulse. Since acceleration occurs from these bunches directly, this ensures they are accelerated by the highest intensity portion of the laser pulse, providing maximum ion energies. With this, it is desirable that the peak density is close to critical, to ensure optimal acceleration conditions. However, the density must be sufficient such that the bunch does not get accelerated in a lower intensity portion of the pulse or decay too quickly. This latter condition ensures stable acceleration to produce peaked energy spectra. Consider the results plotted in figure 5.15(b) and (c). The 10 µm case is an interesting example of this. The peak density is reached near the most intense part of the laser pulse, while the density is lower than the 20 µm or 25 µm cases. This lower density means the structure begins moving too early and the standing wave condition is broken, causing destructive interference and a lower intensity for acceleration. For longer ramps the gradient

is shallow enough that multiple bunches can go overcritical, making the acceleration occur away from the laser focus and limiting its efficiency. More energy is also given up to the grating formation, again suppressing efficient acceleration. The bunch formation is dependent on a number of competing factors; most importantly the ramp shape and the laser intensity.

5.3.2 Comparison to experiment

A number of similarities exist between the experimental results presented earlier in this chapter and the previous simulation section. Firstly, both demonstrate a strong scaling with the scale length of the density ramp preceding the critical surface. The experimental results demonstrate a 6-fold increase in the proton energy between 30 ns and 50 ns expansion times, or equivalently scale lengths of 280 µm and 185 µm. Simulation results show similar scaling, although only a 3.3-fold increase is observed between 0 µm and 20 µm scale lengths. The increased energy scaling in the experiment could perhaps be explained by low level self-focussing in the plasma. The laser near-field profile during the experiment was susceptible to modulation. The beam was subject to high levels of B-integral due to the beam transport lines being in air. This can result in spatial variation of the near field intensity profile, creating regions of high intensity facilitating stronger self-focussing and filamentation in the low density plasma preceding the critical surface. If self-focussing were to be an explanation for the discrepancy in the observed energy scaling, the radius would need to collapse to $\sim 25\,\mu m$.

For longer scale lengths, simulations predict quasi-constant proton energies between $\sim 75\,\mu m$ and $\sim 200\,\mu m$. Experimentally this is not observed.

The experiment demonstrates longer scale lengths than those predicted to be required for optimal acceleration using the density grating scheme. In fact, simulations suggest that for these long ramps no obvious scaling with density profile should be observed (see figure 5.16). This can be explained by considering the pulse train structure of the CO_2 pulse. While the relative energies for all shots is not available, using the mean values presented in section 5.1.1, it was possible to simulate the effect of a 25 ps pulse containing 23 % of the total measured energy, equivalent to 0.4 J on target. It can be shown that modulation of the density profile is observed, reducing the scale length. For ramps equivalent to the shortest measured experimentally ($\sim 150\,\mu m$), the scale length is shown to decrease to $\sim 100\,\mu m$. However, scale lengths are expected to be shorter than the measured levels as earlier discussed. With initial scale lengths of the order $\sim 90\,\mu m$, as predicted analytically for the 50 ns case, this number decreases to $\sim 22\,\mu m$. This matches the optimal conditions obtained from simulations extremely well. This result, combined with the good agreement demonstrated between the shock expansion radius with time in figure 5.8(a), suggests that experimental scale lengths are those given by the analytic solution in figure 5.8(c). It is then possible to explain both the experimentally observed higher than expected proton energies and the multiple proton

energy bunches.

The effect of self focussing

One possible explanation for the observed enhancement in proton energy as a function of the scale length could be the effect of self-focussing in the low density plasma preceding the critical surface. For the CO_2 parameters on the experiment, assuming the mean laser energy of 1.14 ± 0.05 J is contained within the focal spot on target, the critical power for self focussing is ~ 230 GW. This corresponds to a density threshold of $\sim 0.075\, n_c$, above which self focussing can occur.

As demonstrated by the proton energy results from the temporal scan presented in figure 5.5, a $\sim$ 6-fold increase in proton energy is observed between 30 ns and 50 ns. From the predicted scaling, the spot radius would need to decrease to 0.41 times its initial value; it would have to decrease from 35 µm to 14.3 µm. It is possible to estimate the distance over which the beam would self-focus to this given spot size through equation 2.64. For a mean density of $0.5\, n_c$, the beam would collapse to this spot size in $\sim$150 µm. Similarly, for a mean density of $0.25\, n_c$, the beam would collapse in $\sim$230 µm.

Similar logic can be applied to the simulation results presented in figure 5.16. In this study, the ramps are not long enough to observe sufficient self-focussing to provide the intensity increase required to explain the enhanced ion energies. This is reasoned both through consideration of the theoretical scaling and from observation in simulations. Using an equivalent approach to above, the level of self-focussing required to achieve a $\sim$ 3.3 fold increase in proton energy as observed in figure 5.16 can be calculated. This difference occurred for the exponential ramp case between 0 µm and 20 µm. Here, the laser focal spot would need to decrease in radius by a factor $\sqrt{1/3.3} = 0.55$ (from $E_i \propto I \propto 1/\sigma_0^2$); it would need to decrease from 35 µm to 17.8 µm. Again assuming a mean laser power of $\sim$ 230 GW, for a mean density of $n_e/n_c = 0.5$, the distance required for focussing needed would be $\sim$ 139 µm, increasing to $\sim$ 216 µm for $n_e/n_c = 0.25$. Self-focussing is therefore unlikely to explain these improved ion energies alone.

This can further be verified directly within the simulations through analysis of the laser for different ramp lengths. The peak electric field amplitude can be calculated for the given laser pulse. By comparison of the forward travelling wave field at any given instant with this maximum limit, the level of self-focussing can be calculated. For the simulations presented in this work equivalent to expected on target conditions (i.e. $a_0 \simeq 0.65$), self focussing does not provide an appreciable increase to the laser intensity and cannot describe the enhanced proton energies observed. Self focussing is observed with the spot radius decreasing down to 33 µm; this cannot explain the proton energy scaling.

While these scale lengths are of the order of those extracted experimentally, the pulse train and preceding 25 ps pulses cause significant density steepening as earlier alluded

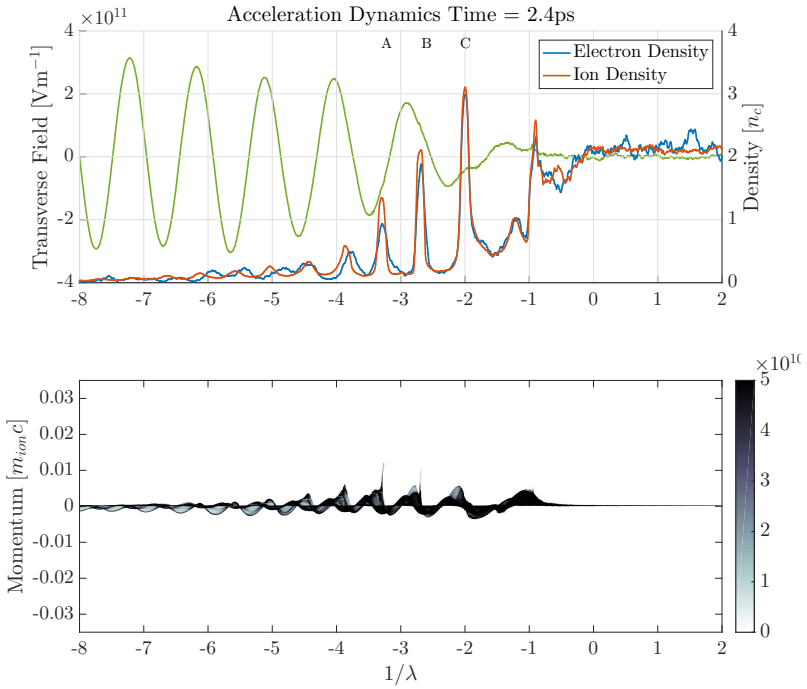


Figure 5.17: Top: the on-axis electron and proton densities, plus the transverse electric field profile at 2.4 ps for a 20 µm density ramp with a 10 µm, 5 ps CO_2 laser pulse of $a_0 = 0.62$ incident on the plasma. Bottom: the proton phase space for the equivalent time.

to. These shorter scale lengths are much more suited to the formation of the grating structure.

Multiple Proton Energy Peaks

The induced gating structures also demonstrate the ability to produce multiple proton energy peaks. Figures 5.17 to 5.19 present three phases of the proton acceleration process to help demonstrate the effect. After the grating formation the laser intensity continues to increase, in turn enhancing the force exerted on the density structures. Figure 5.17 shows the on-axis densities and equivalent proton phase space at 2.4 ps for a 20 µm density ramp; the optimal proton energy example for $a_0 = 0.62$. As can be seen in the phase space plot in figure 5.17, two bunches are beginning to undergo acceleration, located at $-3.3\,\lambda_L$ and $-2.7\,\lambda_L$. A third, higher density structure is located at $-2\,\lambda_L$. Let these be termed A, B and C, respectively, for the subsequent discussion. Structure A is under-critical in density, but high enough that the reflection is sufficient for acceleration. However, since this bunch remains under-critical, structure B also experiences a significant accelerating force. These two bunches are driven forwards, and acceleration off the two structures occurs.

As time progresses, the force on the up and downstream sides of structure B (for clarity,

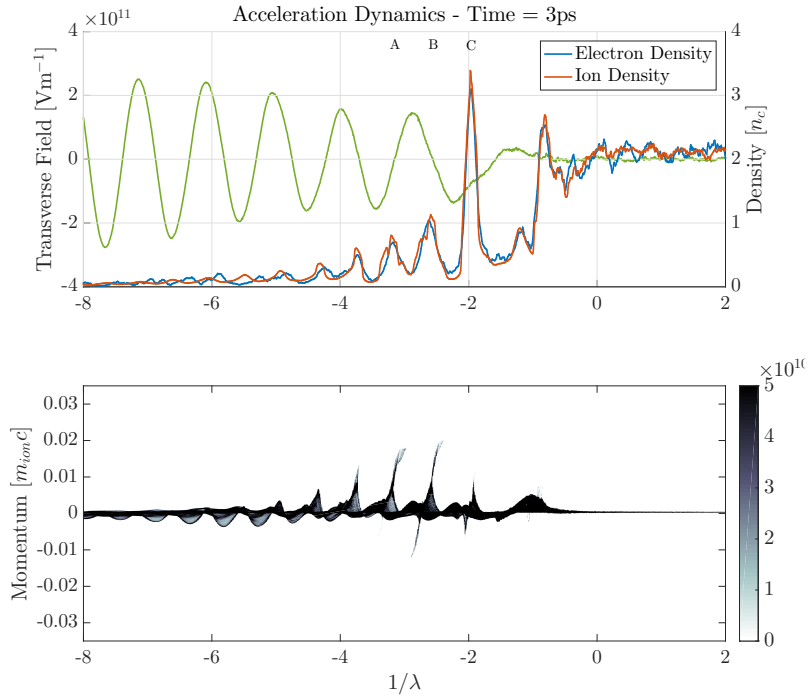


Figure 5.18: Top: the on-axis electron and proton densities, plus the transverse electric field profile at 3 ps for a 20 µm density ramp with a 10 µm, 5 ps CO_2 laser pulse of $a_0 = 0.62$ incident on the plasma. Bottom: the proton phase space for the equivalent time.

these denote the left and right hand sides in space) results in a drop in density; the structure is sufficiently overdense that the force on the downstream side drops and it expands. Figure 5.18 shows the same simulation at 3 ps. At this time, the density of structure B has dropped to the critical density. While acceleration of this and the preceding bunch can still continue, the effect is reduced as the reflectivity decreases; consider the $(1 + R)$ reflection coefficient scaling of RPA. The greatest force is now experienced by the highest density feature, structure C. This grating element begins to be accelerated, coincidentally with the peak of the laser pulse. Bunches preceding structure A also experience lower levels of acceleration.

The final time presented is at the end of the laser pulse, shown in figure 5.19. This demonstrates the proton phase space at 5.2 ps. As can be observed, strong acceleration has occurred off structure C, with energies exceeding those accelerated off the earlier grating structures. This is attributed to this density feature being accelerated by the most intense part of the laser pulse. This can result in reflection of significant fluxes off upstream protons to high energies. Note that despite steepening and some propagation of the initial critical surface, no significant acceleration occurs here since the preceding overcritical bunches have shielded it from the peak accelerating force of the laser.

The energy spectrum for this case is shown in figure 5.20(a). This shot does not demonstrate multiple ion energy peaks, because the early time acceleration from multiple

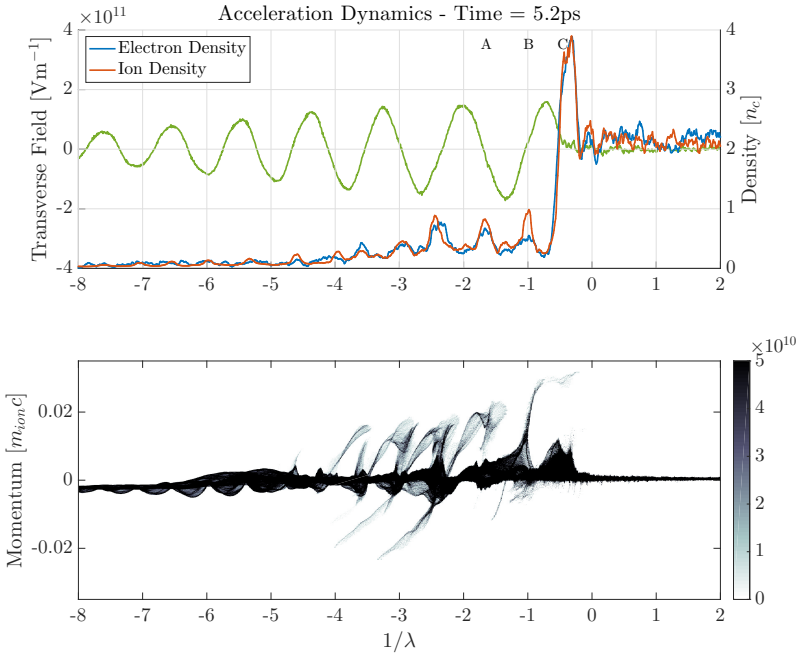


Figure 5.19: Top: the on-axis electron and proton densities, plus the transverse electric field profile at 5.2 ps for a 20 µm density ramp with a 10 µm, 5 ps CO_2 laser pulse of $a_0 = 0.62$ incident on the plasma. Bottom: the proton phase space for the equivalent time.

bunches is not sustained long enough to generate monoenergetic features. Instead, a single, high energy bunch is observed, with a peak energy of 0.49 MeV. This is accelerated through reflection off structure C, as can be observed in the phase space plot in figure 5.19. A lower energy thermal component is also present due to the bulk motion of the grating elements. These are not accelerated for sufficiently long times that upstream ions can reflect and outrun the shock front and a broad spectrum of energies is produced.

These multiple stages of acceleration off the various grating elements do also facilitate the observation of multiple proton bunches. The forward propagating integrated proton spectrum for the 25 µm case is given in figure 5.20(b). Unlike in the case of the 20 µm ramp, multiple bunches are accelerated for sustained periods, allowing the creation of multiple proton energy features. Whether this phenomenon occurs or not is dependent on the grating formation conditions. While there is a relatively small difference in the density profile between the 20 µm and 25 µm cases, in the latter the density features preceding the critical surface reach a higher peak density, sufficient to allow longer, sustained acceleration before they decay. The most effective acceleration still occurs from the primary bunch, formed closest to the critical surface as in the 20 µm case. However, the increased lifetime of the preceding structures results in enhanced acceleration from these, with slightly lower acceleration from the primary bunch. This lower acceleration is because the feature experiences the laser at later times, when the laser intensity has

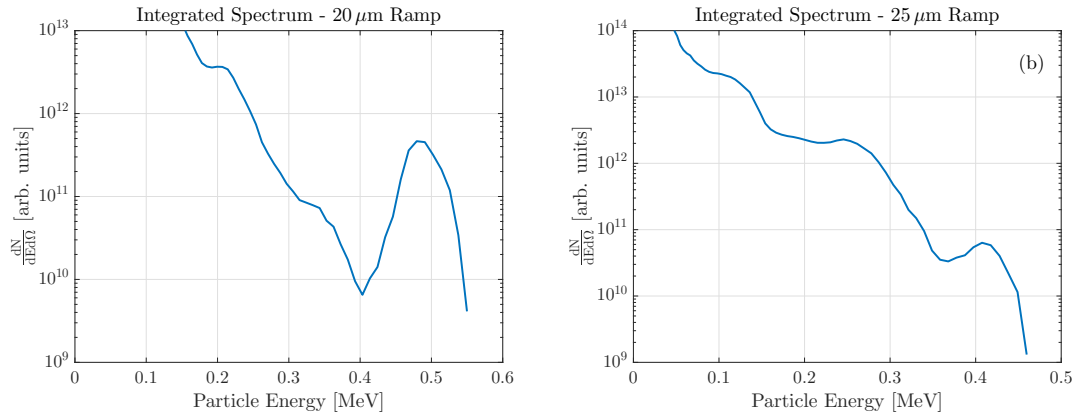


Figure 5.20: (a) The proton energy spectrum for a 25 µm exponential ramp, showing a peaked spectrum at 0.48 MeV (b) Integrated proton energy spectrum for a 20 µm exponential ramp, demonstrating multiple ion energy bunches.

dropped, and also due to the higher reflectivity off the preceding bunches. This provides less effective acceleration. It is interesting to compare the relative energies of the bunches between simulation and experiment. The ratio of peak energy of the second to first and third to second bunches from the presented simulation is 0.62 and 0.5, respectively. Similarly, for the experimental results, the same ratios are 0.58 and 0.62, in reasonable agreement. The larger discrepancy between the second and third bunches could perhaps be due to the density profile in the experiment not following the idealised exponential profile.

Therefore, the formation of these plasma grating structures could help explain the results observed in the experiment. The multiple ion spectral features can be explained from acceleration off multiple grating elements. The higher than originally expected energy scaling can also be explained. The limited mass and lower background density of the grating elements results in an increase in proton energy compared to if the peak blast wave density were assumed.

While multiple bunches can be explained by this effect, they are only observed on some shots. This is the case for all but one of the highest energy shots, with most exhibiting only one proton energy feature. It is possible these highest energy shots found conditions equivalent to the 20 µm case presented in this section. While a grating structure is formed, dominant acceleration occurred at a single structure, coinciding with the peak of the laser pulse.

5.4 Conclusions

Experimental results were presented which demonstrate enhanced proton energies when compared to theoretical HB-RPA scaling. Also shown was a strong dependence of the proton energy on the expansion time of the blast wave used for target shaping of the gas

jet. A 6-fold increase in proton energy was observed through increase of the expansion time from 30 ns to 50 ns, with these then falling to zero over a further 20 ns. This effect is thought to be due to the variation in density scale length as expansion increases. Also observed were multiple ion bunches on a number of shots. This is a difficult phenomenon to explain with classical HB-RPA or collisionless shock acceleration, even with the presence of multiple pre-pulses. While these pre-pulses act to steepen the density profile, they do not perform efficient acceleration due to the long scale length and low intensity.

Simulations of the experimental conditions suggest a pre-cursor effect occurs; the formation of a density grating from which enhanced HB-RPA can occur. The stable formation of these structures is highly dependent on the intensity profile of the laser and density scale length of the target. HB-RPA can be achieved from these grating elements, with their limited mass and the low background density leading to enhanced proton acceleration. As shown in figure 5.16, simulations demonstrate a similar enhancement of proton energy with scale length, albeit less strongly than in the experiment. Multiple ion energy peaks can also be formed from these grating structures, with multiple density spikes accelerated to varying degrees. From these structures, ion bunches can be accelerated through HB-RPA, potentially explaining the experimentally observed results.

Figure 5.16 illustrates the benefit of this scheme well. Despite ultimately higher proton energies in the case of $a_0 = 1.45$, the efficiency of the mechanism is worse, with no obvious enhancement of the proton energy for a given ramp length. The increased intensity leads to no long lived stationary nodes of the standing wave in the density ramp, prohibiting formation of a grating structure and acceleration is due to HB-RPA about the initial critical surface.

6 Proton acceleration from shaped gas targets produced through colliding blast waves

6.1 Context

The preceding chapters have demonstrated the ability to produce mono-energetic protons at near-critical densities through hole-boring. Chapter 4 first showed that for thick targets, HB-RPA could produce narrow energy spread proton beams, demonstrating good agreement with the predicted theoretical $4I/n_i c$ scaling. Chapter 5 subsequently showed that under certain conditions, modification of a plasma density ramp by a standing wave produces a plasma grating structure, from which enhanced radiation pressure driven acceleration occurs. The limited areal density of the structures, coupled with the low background density, allows these structures to be accelerated to higher velocities than in the unmodified case, giving superior proton energies. By way of comparison, the highest observed proton energies were $\sim 20\%$ higher than shots at > 5 times higher intensity where no grating structure was expected to form. Thin, near-critical density targets have the potential to optimise the acceleration process and produce the highest energies.

Thin solid density targets are relatively simple to make and are routinely used in ion acceleration experiments at thicknesses down to the nanometre scale in order to study radiation pressure acceleration [251] [255]. However, these targets are thin foils, susceptible to contamination and difficult to operate at high repetition rates. They are also considerably above critical density, $n_e > 100\, n_c$. Thin gas targets would again allow many of these obstacles to be overcome.

While acceleration is promising from the grating structures described in Chapter 5, their formation is inextricably linked to the accelerating laser pulse, which places restrictions on the both the grating formation and acceleration phases. Ideally then, the phases would be decoupled, allowing greater, independent control over each. An ideal situation would be the formation of a very thin, near-critical density target, independently produced, from which to accelerate protons. This could be achieved through separate or temporally shaped laser pulses, to form the grating structure before the arrival of the accelerating pulse. Alternatively, thin gas targets could be pursued as an alterna-

Parameter	Value
Laser energy to chamber	2 - 4.9 J
Energy in focal spot	0.61 - 1.5 J
Focal spot size	65 µm
Pulse length	5 ps
Laser intensity at focus	$3.7 - 8.8 \times 10^{15}$ Wcm^{-2}
a_0 at focus	0.55 - 0.85

Table 6.1: CO_2 laser parameters for the results presented in Chapter 6

tive target shaping approach. The requirements for these targets are the need for thin, low areal density structures. Furthermore, in this scenario a scale length would not be expected to be beneficial since the target would already have all the desired properties; maximum energy transfer to the thin slab would be optimal to maximise the acceleration. In this best case scenario, a situation in which very thin gas targets were produced might be envisaged, such that a transition from the hole-boring to light-sail regime occurred. This would allow the exploitation of the superior intensity scaling of this mechanism.

This chapter presents results from preliminary attempts to produce thin gas targets through the collision of two, counter-propagating blast waves. Experimental efforts are outlined, both in the production of these colliding shocks and the effect of proton acceleration. Particle-in-cell simulations are also presented, which studied the effects of thin, near-critical density targets on proton acceleration.

6.2 Experimental Overview

6.2.1 Laser Parameters

For work in this chapter, the CO_2 laser at the ATF was operating in the 10P branch at 10.6 µm. A linearly polarised beam was delivered to the target chamber with a mean total integrated energy of 4.2 ± 0.5 J. Again, the laser temporal profile consisted of a train of pulses, separated by ~ 25 ps. An example of the pulse train on this experimental run is given in figure 6.1. Typically, most of the energy (~ 90 %) was contained within the first two pulses, with the relative levels varying shot-to-shot due to the non-linear nature of the CO_2 amplification system. For the shots relevant to the results presented in this chapter, 10 ± 6 %, 30 ± 12 % and 60 ± 17 % of the total laser energy was contained within the first, second and third pulses, respectively.

A full list of parameters for the results presented are given in table 6.1. Assuming 60% energy in the main pulse, with 50% energy contained within the full width at half maximum of the focal spot, a mean laser energy of 1.25 ± 0.14 J was delivered to the target, focussed to a spot size of 65 µm. This factor of half the energy delivered to the

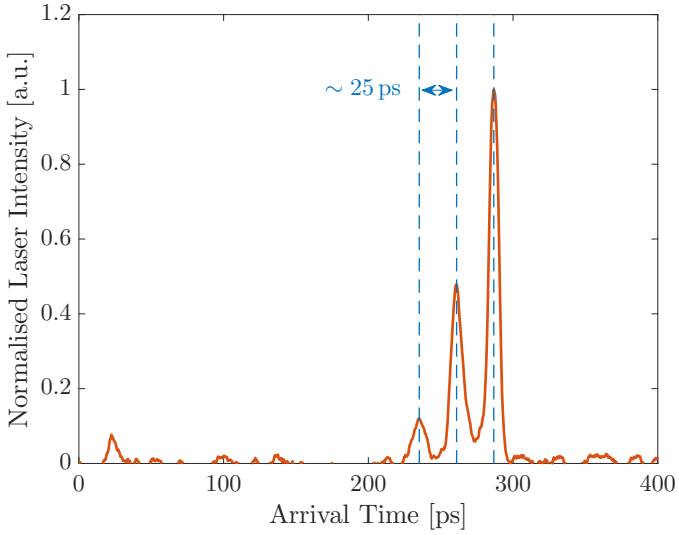


Figure 6.1: An example CO_2 temporal profile for the experimental conditions in Chapter 6. Pulse trains typically consisted of 3 pulses, separated by ~ 25 ps. The given example contains $10 \pm 6\,\%$, $30 \pm 12\,\%$ and $\sim 60 \pm 17\,\%$ of the total energy in the first, second and third pulses, respectively.

chamber being in the focal spot is validated by previous experimental measurement, which, as shown for example in section 4.2.2, is a reasonable estimate. This gives an equivalent mean intensity of $7.5 \pm 0.8 \times 10^{15}\,\mathrm{Wcm^{-2}}$, or equivalently, a mean vector potential, a_0, of 0.78 ± 0.04.

6.2.2 Targetry

The experiments in this chapter employed the "1 mm" nozzle as outlined in section 3.2. Hydrogen gas at backing pressures ranging from 2-4.5 bar were employed, giving a density profile equivalent to that shown in figure 3.5. For these conditions, the peak electron density ranged from $4 \times 10^{18}\,\mathrm{cm^3}$ to $7.4 \times 10^{18}\,\mathrm{cm^3}$. This equated to peak unperturbed densities between 0.35-0.65$\mathrm{n_c}$. The unperturbed gas profile had a scale length of 0.55 mm, with the profile extending out to ~ 1.5 mm in all directions from the centre of the nozzle.

Again, target shaping occurred through the use of an external Nd:YAG laser. Here, the beam was split in two, with half the energy in each pulse. The YAG beam had a total energy ~ 80 mJ, with ~ 40 mJ in each of the two beams, and a pulse length, $\tau_{\mathrm{YAG}} = 5$ ns. The beams were focussed using an $f/10$ geometry, onto two stainless steel foils, placed in the edge of the gas flow. The two clips were positioned at the front and rear of the gas nozzle, relative to the laser propagation direction. As in Chapter 5, the YAG beams cause heating and ablation of the clip, resulting in two, counter-propagating blast waves. An example of the two clip system, and two counter-propagating, colliding shocks, are shown in figure 6.2. The total energy of the YAG pulses could be controlled

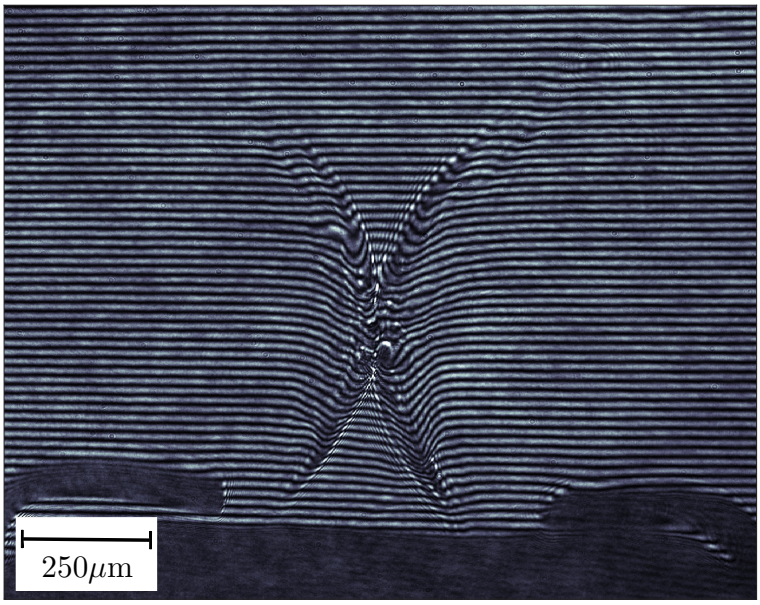


Figure 6.2: An example interferogram from the experiment, demonstrating two colliding blast waves. Two clips were shot with an Nd:YAG laser, with ~ 40 mJ each, to generate the shocks.

through the use of polarisation based splitting, although for the work presented here the full energy was always used. No relative timing between the two shocks was possible, but control of the timing between the two shocks and the arrival of the main CO_2 pulse was achievable.

6.2.3 Diagnostics

Shadowgraphy, interferometry and the magnetic ion spectrometer were the main diagnostics for these studies.

The ion spectrometer operated as explained in section 3.4.1, with a 1 cm by 500 µm slit at its entrance to sample the on-axis proton beam profile.

The optical probes consisted of an ~ 8 ps, frequency doubled, 532 nm probe beam providing variable two-time shadowgraphy and interferometry. It was possible to control the arrival of the probe beams relative to the main CO_2 pulse, allowing observation of the target conditions before, during and after the arrival of the main pulse. The early time probe was set such that it was 25 ps before the arrival of the main pulse. This ensured that the blast wave profile was measurable before any effect of the main or 25 ps pre-pulse occurred. The late time was variable, and allowed the study of late time effects of the interaction up to ~ 2 ns after the main pulse.

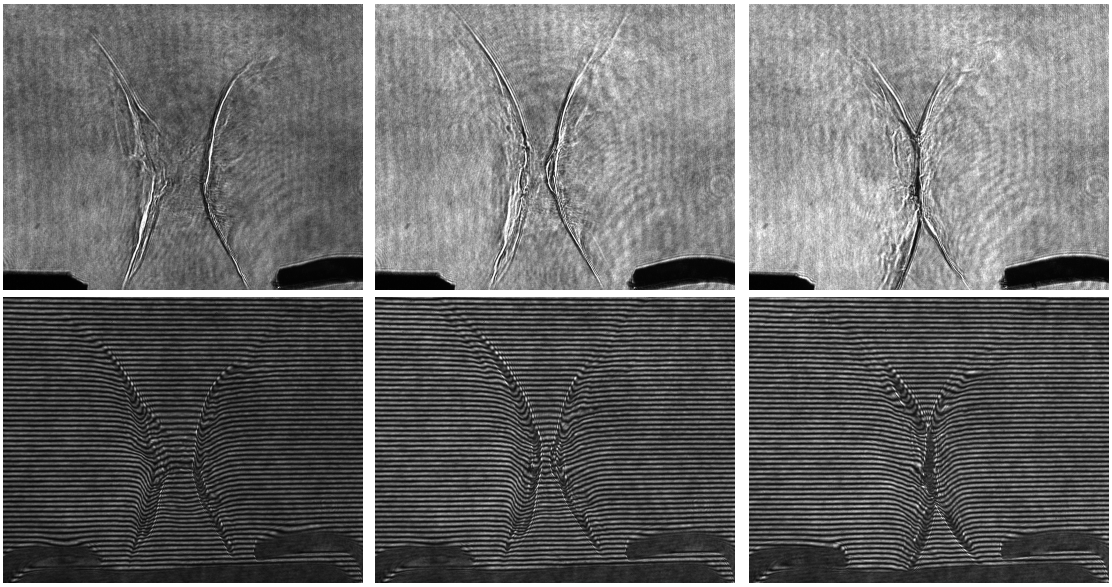


Figure 6.3: Top: shadowgraphy optical probe images of the shock expansion for three increasing expansion times, showing evolution up to the point of collision. Bottom: the equivalent interferometry images corresponding to the shadowgraphy images above. Shots were taken at 4.5 bar backing pressures, corresponding to peak gas densities of $7.4 \times 10^{18}\,\mathrm{cm}^{-3}$, or $\sim 0.65\,n_c$.

6.3 Experimental Results

The experiment was aimed at creating two, counter-propagating blast waves in an attempt to produce thin gas targets for optimised proton acceleration. Figure 6.3 shows optical probe images for increasing expansion radii up to the point of collision. These images are the early time probe images, demonstrating the target conditions $\sim 25\,\mathrm{ps}$ before the arrival of the main CO_2 pulse. The blast waves are propagating in a gas with a gas jet backing pressure of 4.5 bar, corresponding to a peak density of $7.4 \times 10^{18}\,\mathrm{cm}^{-3}$, or $\sim 0.65\,n_c$. As can be observed, with increasing relative delay between the YAG and CO_2 main pulse, the shocks become incrementally closer until they collide.

For the three stages of shock expansion, given in figure 6.3, density retrieval was attempted to ascertain the shock conditions for each case. The retrieved two-dimensional densities and density profile along the laser axis are given in figure 6.4 for the three stages of expansion shown in figure 6.3.

Density retrieval was achieved with the same method as outlined previously for the YAG driven shocks in Chapter 5. As can be observed in figure 6.3, at the highest shock densities, it is common for fringe 'cuts' to be observed. Furthermore, in the case of these highest densities, for example in the case of the colliding shock, total loss of probe signal is observed. Again, this is due to the refraction of the probe light being such that the light escapes the collection angle of the imaging optic ($\sim 5°$). To overcome such issues, fringes were required to be manually traced in these unresolved regions. By its very nature such a method is highly subjective. In an attempt to minimise errors,

fringes whose paths can be fully resolved on either side of the affected region are used to provide information about the maximum possible deflection; fringes can never cross. Since one is also often tracing up a density gradient, these allow inference of the likely general path of the fringes. Once full fringe maps were obtained, the interferograms were analysed using the Magic code developed by George Swadling, formerly of the MAGPIE group at Imperial College London. This calculates the level of phase shift from the deflection of each fringe to obtain a phase map, which with knowledge of the size of the plasma structure allows the density to be retrieved.

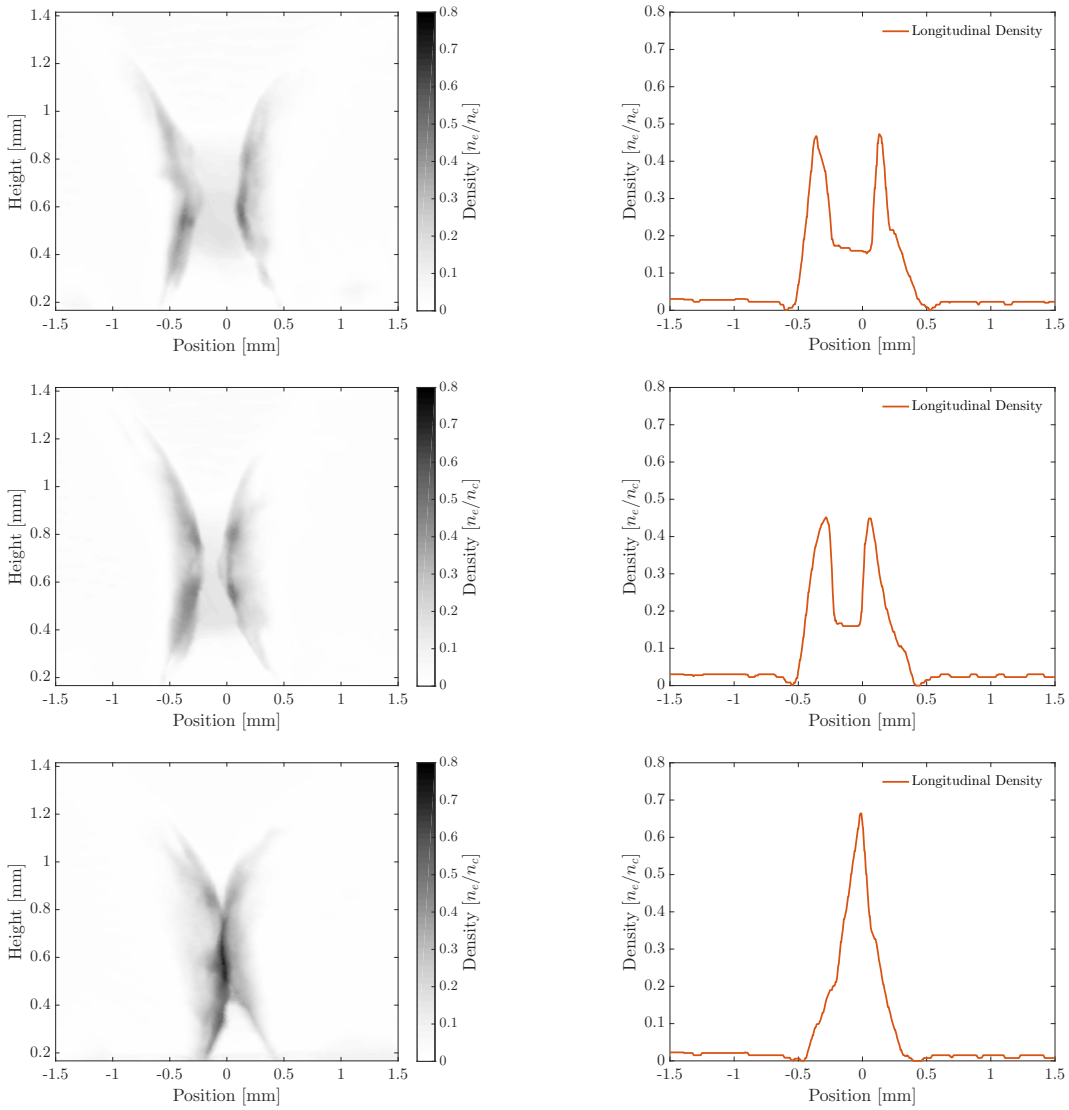


Figure 6.4: Left: two dimensional density profiles for three different shock expansion radii. Right: lineouts of the density profile in the direction of laser propagation for the same density profiles. The profiles are for the raw interferometry images given in figure 6.3 and demonstrate increased convergence of the shocks until they collide.

However, the density retrieval suffers from a number of issues which makes obtaining accurate values for the density challenging. Firstly, the method of drawing on fringes

is inaccurate, making them susceptible to errors. Consequently multiple attempts to interpolate over the same region can give substantially different results. Furthermore, the images are limited by their finite resolution. Since extraction of the density requires each fringe path to be distinct, with no overlap, when tracing the fringes they must be separated by at least one pixel width. However, for very steep density gradients, such as at the front of the shock, the paths traced by the fringes make it possible that the separation is below this limit. For the case of multiple consecutive fringes exhibiting these features, this constraint can limit the retrievable density gradients, which has implications for the obtained scale lengths. In regions of high density, it also constrains the observable maximum density.

The peak measurable densities from figure 6.4 are on the order of 0.5-0.7 n_c. Inference suggests these maximum retrieved densities are lower than the actual values. Firstly, the unperturbed gas densities were shown to be roughly equivalent to this level for all shock front positions. This was measured during calibration, as outlined in section 3.2. Secondly, the addition of a strongly driven shock gives a predicted density increase of ~ 6 at the shock front, making these measured values even less reliable. For this to be the case, one is required to know if the strong shock limit still applies, which provides this density jump condition.

For the experimentally retrieved shock front locations, the expansion time between the two temporal extremes in figure 6.4 is 30 ns. During this time, the shock travels $\sim$250 µm, giving an average shock velocity of $M = v/c_s \approx 6$, where c_s is the upstream gas sound speed, found to be $\sim 1300\,\mathrm{ms}^{-1}$ for $T = 300\,\mathrm{K}$, assuming no significant upstream heating. The shock expansion also shows good agreement with the predicted scaling given by equation 3.7, as demonstrated in figure 6.5. The vertical offset in the predicted and experimental results originates due to the non-zero source size of the explosion; this is shown to be $\sim$250 µm. Heating of the clip causes ablation of the ionised material into the surrounding gas. The region this ablated material heats is the source size of the explosion. Note the smaller size of the explosion centre compared to the results in section 5.2.2. This is explained by the heating of the clip being performed with half the energy.

The previous calculations imply the strong shock limit is indeed applicable. As such, given the ratio of specific heats for hydrogen is 1.4, peak densities ~ 6 times higher than the measured unperturbed background could be expected at each shock front position. This is equivalent to up to $\sim 4\,n_c$ at the centre of the gas jet; the peak shock density is thought to be significantly under-resolved.

This assumption of lower than expected density measurements can also be validated through consideration by a second method. Since the unperturbed gas is characterised, assuming there is no upstream change to the density between the shocks, the average difference in density between the experimentally measured and calibrated densities can be estimated. This assumption is believed to be valid since no radiative effects should

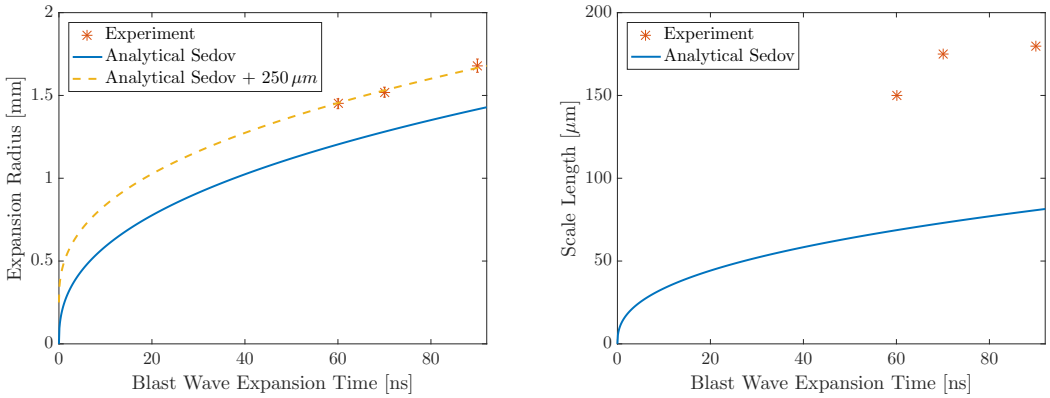


Figure 6.5: Left: the experimentally obtained shock radii as a function of expansion time, along with the theoretical scaling as predicted by Sedov (equation 3.7), showing good agreement when the finite explosion centre size is accounted for. Right: the experimentally obtained density scale length and predicted scale lengths from the Sedov scaling.

be present and so the upstream density profile should be unaffected by the shocks. For the case of the earliest time, 60 ns, as shown in the top row of figure 6.4, the mean retrieved density is $\sim 0.15\, n_c$. This is a factor of ~ 4 times less than expected for full ionisation of the measured neutral density. Similarly, for the second time in figure 6.4, $t = 70$ ns, the density is also underestimated by ~ 4 times. Obviously this estimate cannot be made for the late time at which collisions occur.

Despite the expected unresolved peak densities, estimated scale lengths can be extracted. The retrieved scale lengths are ∼150 µm, ∼175 µm and ∼180 µm for 60 ns, 70 ns and 90 ns, respectively. For comparison, these are plotted with the predicted scale lengths in figure 6.5. As can be observed, poor correlation exists, with the experimental results ~ 2 times higher. Again, as in section 5.2.2, this can be rationalised. Given the underestimation in the region of peak shock densities by a factor of approximately 4, the relative scale lengths could reasonably be assumed to be shorter. Resolution of the density is expected to be accurate in the region preceding the highest density portion of the shock front since the fringes can be accurately traced, but the profile at the shock front is unresolved. Hence, the density peak around the shock front is the only portion expected to increase; the scale length would subsequently drop.

6.3.1 The point of collision

Discussion to this point has largely focussed on the conditions of the two blast waves and the surrounding medium at times preceding the shock collision. However, to make the thinnest gas targets possible, the case where a collision occurs between the two counter-propagating blast waves was investigated. This is shown in the final panels in figures 6.3 and 6.4.

Colliding strong shocks are of general interest due to their applicability in a number of astrophysical situations, for example colliding supernova remnants [256] and stellar bow jets [257]. The scalable nature of these structures makes their study through numerical simulations and experiments possible, so long as the dimensionless parameters associated with these shocks, for example the Mach and Reynolds numbers, are consistent; the underlying dynamics can then be shown to be invariant in space, time and velocity [258].

Specifically, experimental investigations are of interest to study these phenomena, since their scalable nature makes the investigation of the shock evolution possible over short time scales. These interactions could otherwise take decades or longer to observe in real astrophysical events. Furthermore, numerical modelling of colliding shocks is particularly challenging [259], motivating experiments to assist in benchmarking of these codes. However, despite these motivations for the problem of colliding blast waves, their experimental study is still fairly limited [260] [261] [262].

Experimental determination of the target conditions for the time that coincides with the collision of two blast waves also presents challenges. Firstly, limited shots were available during the study and this focussed not on measuring the shock collision dynamics themselves, but the accelerated proton beams (see section 6.3.2 later). Furthermore, for the data that is available, the lack of optical probe information to extract the density profile of the gas makes understanding the exact proton acceleration conditions impossible. It is only possible to infer information based either on the experimental results obtained or in combination with theory. Consider, for example, the case of the peak density of the structure at the point of collision. Since no accurate information about the density profile was retrievable from the interferometry, this must be inferred. Smith et al. [261] and Elton et al. [263] conducted experiments of colliding blast waves and suggest the peak density of the collision structure is ~ 1.5 times that of a single incident blast wave, assuming symmetric shocks are used. Therefore, based on the assumed peak density of a single blast wave at the centre of the gas jet, the peak density of the collision structure can be estimated to be equivalent to $\sim 5.8\, n_c$. It is worth noting that despite the inaccuracies in the retrieval process, the measured relative peak shock densities for the single and colliding blast wave cases are ~ 1.5 times different, as predicted, perhaps suggesting systematic underestimation of the density in the high density regions.

The shock thickness and scale length are more challenging to estimate. The full width at half maximum thickness of the shock from the retrieved density profile in figure 6.4 is $\sim$250 µm. In reality, an underestimation of the peak density will result in this being smaller, although how thin the target will become is not easy to ascertain. However, assuming accurate retrieval in the low density section of the target far from the shock front, where clear fringe paths are visible, an estimate of the structure width can be made. A function of the form $n_e \propto n_{max}\, e^{-|r|}$ was plotted with the experimentally obtained data to get an estimate of the structure width. This is shown in figure 6.6.

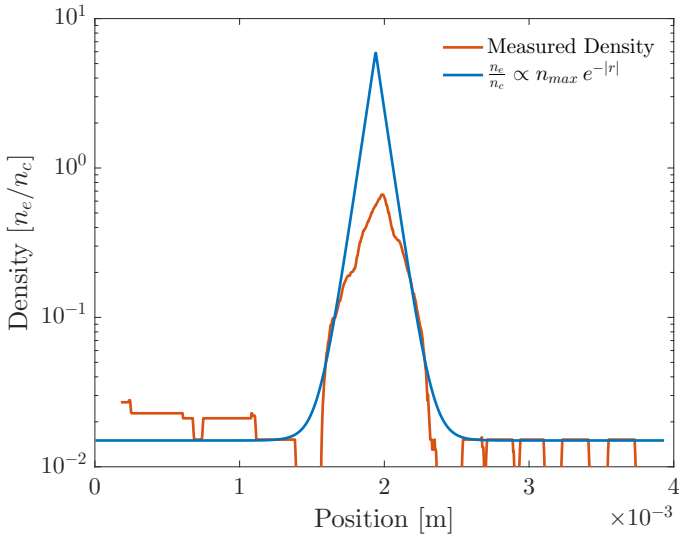


Figure 6.6: The retrieved density profile for the case of two colliding blast waves, along with a fitted function of the form $n_e/n_c \propto n_{max}\, e^{-|r|}$, fitted to match the resolvable, low density portion of the interferogram and set to a peak density of $5.8\, n_c$

By assuming the previously discussed peak density of $5.8\, n_c$, and fitting the function to trace a path as close as possible to that followed by the shock in the low density regions, the density profile is estimated. This gives the colliding shock structure a full width at half maximum of ∼85 µm. Clearly, however, this number should only act as a guide to the size of the structure given the number of assumptions made. However, some confidence can be drawn from the fact it demonstrates reasonable agreement with similar work by Helle et al. [264], who used a near identical method to produce thin gas "foils" of width 75 µm for ion acceleration experiments at 800 nm wavelengths. Also of interest were the scale lengths in this case, ∼35 µm. For a single shock at the same location, it is also possible to perform the same process, giving a full width at half maximum shock width of ∼120 µm, ∼ 40% larger than the colliding case.

In fact, the thickness of the colliding shock structure might be expected to be even smaller than this. The three-dimensional nature of the colliding shocks might be expected to result in material being ejected outwards from the point of collision, towards the regions where shock collision has not yet occurred. This might result in wider, dense regions away from the centre of the shock, which could give the appearance of a thicker shock front. Collisions of these spherical shock fronts might be expected to result in the formation of a Mach stem [265]. A shock front incident on a surface at an oblique angle, in this case the other shock, does not reflect directly away. Instead, the shock is deflected such that it propagates along the surface, and extends between the surface to the point it interacts with the incident shock [266]. While these structures might be expected, in practice they are not observed. This is possibly because no late time optical probe images exist without the arrival of the main CO_2 pulse. Due to the high

intensity of this pulse, the target is totally destroyed and with it, potentially, so are these structures.

The relative scale length is measured not to appreciably increase between the 70 ns and 90 ns expansion times, equivalent to before and during the collision, when compared to the difference measured between 60 ns and 70 ns. In fact the measured scale length increase is less than predicted by the analytical scaling provided by Sedov. This could be purely due to the inaccuracy of the density retrieval, although it may indicate a change in target conditions due to the collision. This, along with the possible lower thickness of the collision structure is perhaps not to be unexpected. Consider the collision dynamics. To do this, the mean free path of the shock can be estimated. The ion temperature can, in the immediate post shock region, be inferred using the relation [267]

$$k_B T_i = \frac{2(\gamma-1)}{(\gamma+1)^2}\frac{Am_p}{Z+1}u_{BW}^2 \tag{6.1}$$

where A is the atomic weight, γ is the ration of specific heats and u_{BW} is the blast wave velocity. The shock velocity is approximated as $\sim 7.5\,\mathrm{kms}^{-1}$, obtained from the change in shock radius over the latter two interferometric images. This gives an ion temperature of the order $\sim 0.04\,\mathrm{eV}$. The mean free path can be calculated using the ion-ion collision time, $\tau_{ii} = 6.6\times10^{-10}(A^{\frac{1}{2}}T_i^{\frac{3}{2}})/(n_i Z_i^4 \ln\Lambda_i)$ [98], and the ion thermal energy, $v_i = \sqrt{k_B T_i/m_p}$, for protons at $\sim 0.04\,\mathrm{eV}$, giving a result on the order of $\sim$1 µm. Therefore, at the point of collision, limited inter-penetration between the shocks might be expected, with instead stagnation occurring at the interface between the two. While these particles slow, the material behind continues to rush into the collision region, creating a narrowing of the shock front structure and a decrease in the expected scale length for a given shock radius. Given the short mean free path, the collision between two shocks can be treated as equivalent to the reflection of a single shock by a rigid surface, so long as the colliding shocks were produced by two explosions of equal energy, located the same distance from the point of collision [265]. A useful analogy to better understand the collision between the two shocks is the case of a water wave hitting a harbour wall. As the wave reaches the wall, the front of the wave rapidly slows, while the trailing portion of the wave, unaware of the obstruction continues to rush into the collision region. Density accumulates and a region of higher amplitude forms at the wall, before subsequently relaxing and a reflected wave is launched. In the case of the colliding shocks, these would be reverse shocks.

These interaction dynamics would help explain the observation of a narrowing of the shock structure size at the point of collision, despite this being formed of two shock fronts. It also helps explain the expected density increase. Given the predicted density increase of $\sim$ 1.5 times, the shock front might be expected to decrease in width by a factor of $\sim 2/3$ from its original size.

This effect might also help explain why the scale length was not estimated to apprecia-

bly increase over 20 ns of expansion between the second and third temporal snapshots analysed.

Clearly then, the lack of clear interferometric data makes extracting meaningful density profiles challenging. Subsequently, only inferences can be made with the information that is available and theoretical considerations.

6.3.2 Proton acceleration results

The results in this chapter were mainly focussed on observing the effect on the proton energy spectra for the case of relative expansion of two blast waves up to the point of collision. This was performed at the end of an experiment in July 2015, intended as an investigative study to determine the benefit, if any, of the modified gas structures. As such, only a limited number of shots were available, with 74 shots taken. Of these shots, 48 produced protons, while only 14 produced mono-energetic proton features. These shots constituted both colliding shocks, as shown in figure 6.2, and single shocks generated at the front of the gas jet, similar to those presented in Chapter 5. In total, 8 shots demonstrated mono-energetic proton features with the presence of colliding shocks, while 25 produced broad energy spectra.

Measurements were made of the peak proton energy for the peaked spectral data as a function of the blast wave expansion radius for two different gas backing pressures, 2 bar and 4.5 bar. These correspond to peak unperturbed electron densities of $4.5 \times 10^{18}\,\mathrm{cm}^{-3}$ and $7.4 \times 10^{18}\,\mathrm{cm}^{-3}$, respectively. Example proton traces and the associated proton energy spectra are given in figure 6.7. The proton energy spectra were extracted as described in section 3.4.1. These two shots were representative of the peaked spectral data, and demonstrate peak energies of $0.46 \pm 0.06\,\mathrm{MeV}$ and $0.74 \pm 0.08\,\mathrm{MeV}$.

Deconvolution of the observed energy spectra was also possible for those shots demonstrating spectral peaking to obtain the true energy spread of these beams. This was conducted using the Richardson-Lucy deconvolution method, as outlined previously in section 4.2.1. Convolution of the raw proton signal trace from the scintillator with the magnetic spectrometer instrument function allows the 'true' spectral profile of the proton beam to be retrieved. The approach uses an iterative algorithm to conduct the convolution, in an attempt to converge on a most probable solution. This process was performed on the two example shots given in figure 6.7, the results of which can be observed in figure 6.8. Here, figures (a) and (b) represent the raw traces 6.7(a) and 6.7(b). The spectral features on these shots were shown to have rms energy spreads of 17.4% and 16.8%, respectively.

The proton energy as a function of shock radius, up to and including the collision of a blast wave, can also be plotted. This was done for all peaked proton spectra observed in the case of colliding shocks. These are shown in figure 6.9, and are given for both 2 bar and 4.5 bar backing pressures. The results from the 4.5 bar backing pressures correspond

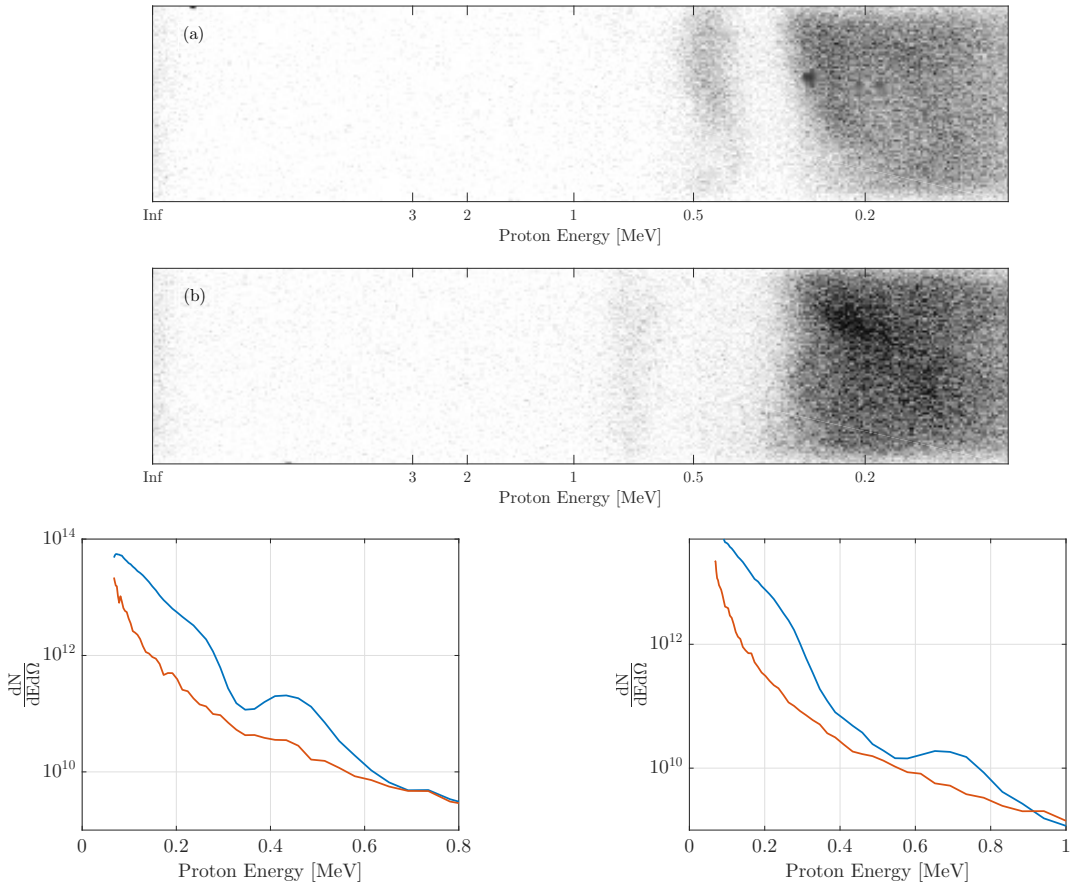


Figure 6.7: (a) & (b): example raw proton energies traces observed with the magnetic ion spectrometer. (c) & (d): the corresponding proton energy spectra for (a) and (b), with peak bunch proton energies of 0.46 MeV and 0.74 MeV, respectively.

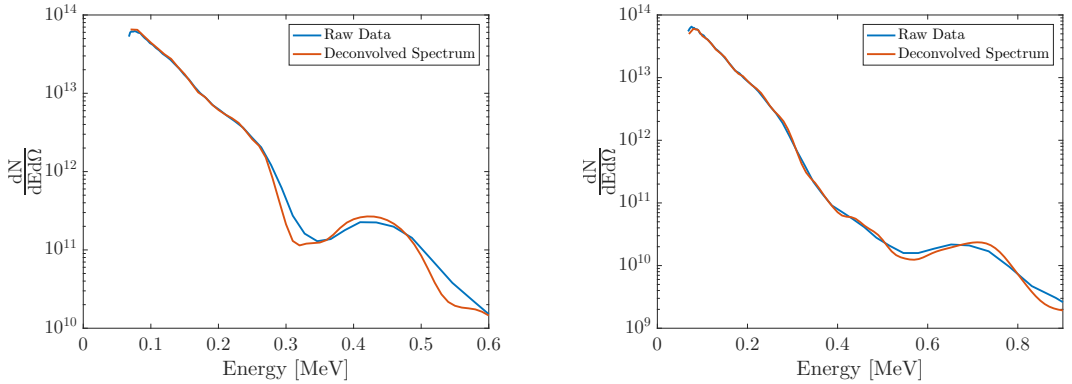


Figure 6.8: The deconvolved proton energy spectra for the equivalently labelled shots in figure 6.7. RMS energy spreads of 17.4% and 16.8% were found for each shot, respectively.

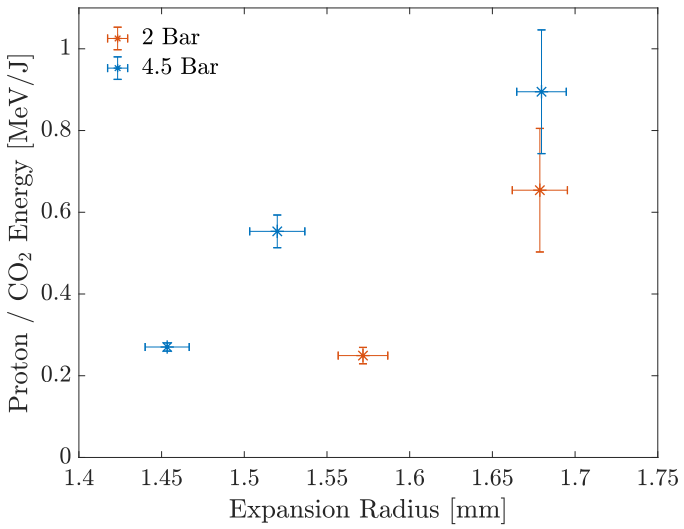


Figure 6.9: The experimentally obtained peak proton energy versus the expansion radius for colliding shocks in the case of spectral peaking of the proton energy.

to the three expansion scenarios presented previously in figures 6.3 and 6.4. The errors in the measured energy correspond to the uncertainty in the peak energy of the peaked spectral feature and, where applicable the energy variation observed on multiple shots for the same expansion conditions. The errors in the expansion radius come from the uncertainty in the shock front location for a given time.

The results demonstrate increasing proton energy with the expansion radius, with the highest observed energies for the case of the colliding shocks. This could be explained in one of two ways. Firstly, given the similarity in laser conditions, the induced grating phenomenon presented in Chapter 5 could again be influencing the interaction dynamics. In this instance, the peak observed proton energies per unit CO_2 energy are near equivalent. However, the point of collision coincides with an expansion radius which gives a predicted scale length 10 µm shorter than found to be optimal (90 µm before steepening from a laser pre-pulse with energy $E/E_{tot} \approx 23\%$ pre-pulse) in this previous work. Couple this shorter scale length with an increased fraction of the laser energy in the 25 ps pre-pulse and this explanation seems less plausible. Furthermore, the interferometry hints at the scale length not appreciably increasing at collision, so the near doubling of the proton energy at collision compared to the preceding expansion radius suggests the scale length is not a dominant factor in the acceleration in this instance.

Conversely, the increased proton energies with expansion radius also corresponds with an increase in proton energy with the target density. The production of the observed spectral peaking would be expected to arise due to a radiation pressure driven mechanism, as in previous chapters. However, the proton energy for hole-boring scales as $E_p = 4I/n_i c$; an increase in density should result in lower proton energies for constant intensities. Perhaps then, the density bunching phenomenon described previously is

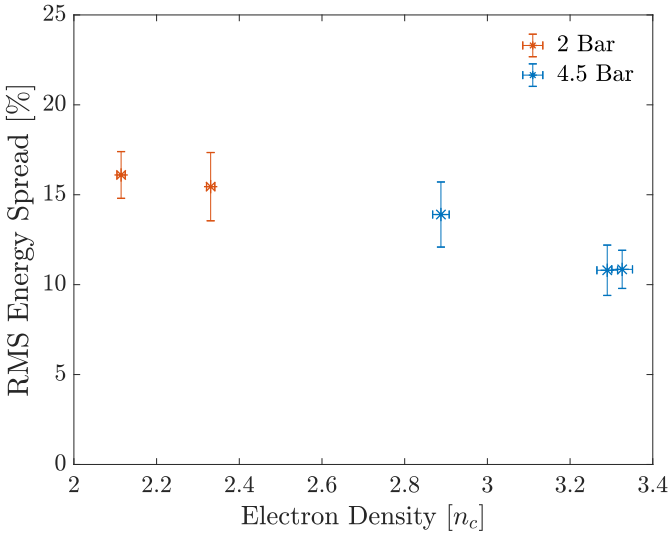


Figure 6.10: The experimentally obtained proton bunch rms energy spread values for the shots presented in figure 6.9, demonstrating a decrease in the rms energy spread with increasing target density.

the cause of the acceleration. Higher peak densities would result in more, low density plasma to be present preceding the critical surface. Therefore, favourable grating formation conditions might occur with the increased expansion. Furthermore, if this were the case, enhanced proton acceleration when compared to that observed in Chapter 5 may be possible, with the maximum energies observed roughly equivalent. With further target modification through variation in the initial density, it might be possible to enhance the peak proton energies further.

A second explanation is that the modification of the target density profile has again produced enhanced conditions which optimise the proton acceleration. Particularly in the case of the colliding shock, a relatively thin gas target with a low density at the rear surface might be possible. In the extreme case, this would be broadly similar to the acceleration off one of the grating structures as described in section 5, although the thickness of the plasma slab in this case is expected to be more than 50 times larger.

The rms energy spread of these shots was also calculated, with values of $\Delta E/E = 15.8 \pm 0.5\%$ and $\Delta E/E = 11.9 \pm 1.8\%$ for 2 bar and 4.5 bar backing pressures, respectively. The rms energy spread for all shots presented in figure 6.9 are shown as a function of the assumed target density in figure 6.10. The assumed target density is calculated using the shock front position and the estimated peak density, as outlined earlier in this chapter. This result shows good agreement with the observation in section 4.2.1, where a similar correlation was observed. This is believed to be due to the higher upstream density resulting in higher levels of reflection off the shock potential, causing more rapid energy loss and subsequently narrower energy spreads.

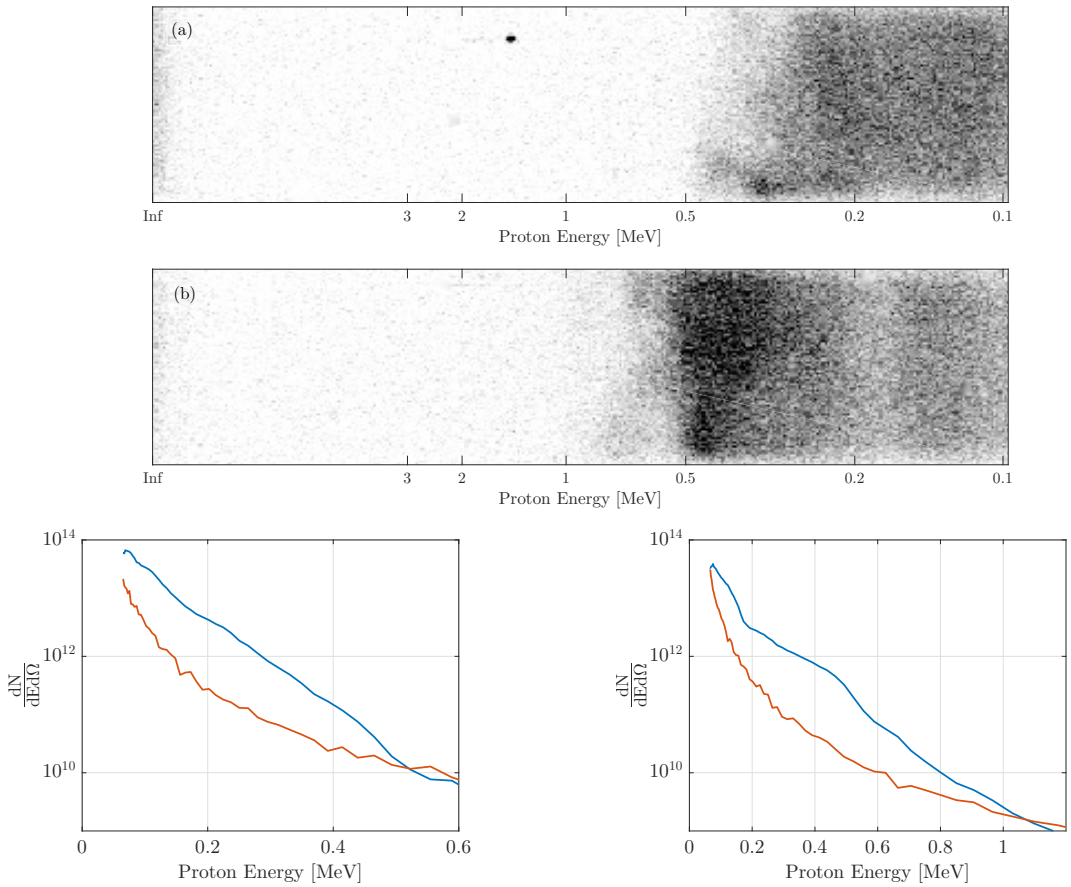


Figure 6.11: (a) & (b): example raw proton energies traces observed with the magnetic ion spectrometer. (c) & (d): the corresponding proton energy spectra for (a) and (b), with maximum observed proton energies of $0.49 \pm 0.03\,\mathrm{MeV}$ and $0.97 \pm 0.05\,\mathrm{MeV}$, respectively.

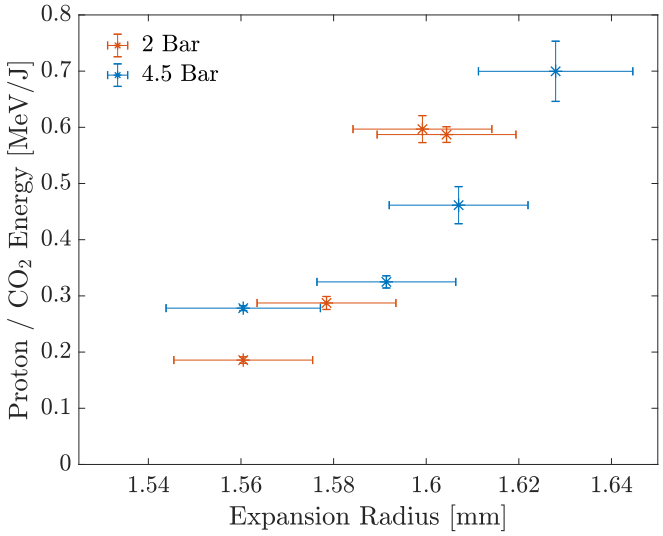


Figure 6.12: The experimentally obtained maximum proton energy versus the expansion radius for colliding shocks in the case of no observed spectral peaking. Instead, broadband energy spread beams are observed.

A number of shots also demonstrated no mono-energetic features. Example spectra for this case are shown in figure 6.11. Both cases presented are for a backing pressure of 4.5 bar, with an expansion radius of 1.55 mm for figures (a) and (c), and 1.6 mm for figures (b) and (d). These shots demonstrated maximum observed proton energies of 0.49 ± 0.03 MeV and 0.97 ± 0.05 MeV, respectively.

The presence of these broadband energy features does not preclude hole-boring as the dominant acceleration mechanism. Instead, it possibly indicates lower background densities. With lower densities, less upstream reflection occurs and a slower decay of the shock potential is expected. As such, lower peak fluxes and a broader energy spread proton beam is to be expected. The shot represented by figures 6.11(b) and (d) perhaps shows signs of this effect. While the overall energy spectrum is broadband in nature, some spectral peaking around ~ 0.4 MeV is perhaps observed. In this case, the critical surface could have been driven at a quasi-constant velocity until the laser energy depletes and subsequently begins slowing due to energy loss from the upstream ions. At low upstream densities, relatively few particles are reflected and this energy loss occurs less rapidly, giving a broader range of energies.

The maximum proton energy versus expansion radius for the shots demonstrating no spectral features are plotted in figure 6.12. Again, a correlation between the shock expansion radius and proton energy is observed, as with the case of observed spectral features. This suggests the cause of these broad energy spread beams is again through the formation of a reflecting potential structure in the upstream plasma. However, for the generation of these structures, the potential is expected to decay more gradually, reflecting upstream protons for longer over a broader range of energies; a broadband energy spectrum is observed.

Additionally, the measured increase in proton energy as a function of expansion radius when broadband energy spectra are observed is ~ 2.5 times faster than when spectral features are present. This is true for both backing pressures. No clear explanation for this observation exists.

The lack of clear interferometric data to extract accurate target conditions for these shots makes direct inference of the exact experimental conditions challenging. Therefore, particle-in-cell simulations were used to first ascertain the target conditions at the time of interaction with the main CO_2 pulse, before subsequently studying the proton acceleration mechanisms. These results are presented in the subsequent section of this chapter.

6.4 Particle in cell simulations

To better understand the results presented in this chapter, particle-in-cell simulations were carried out. Given the long relative length of the optical probes, coupled with the low resolution, it was not possible to observe fine features of the interaction. At 8 ps, the integration time of the probe was such that any large spatial, short timescale features would be effectively blurred out.

First, the effect of the laser pulse train was considered to assess the effect on the plasma profile preceding the critical surface. Subsequently, simulations were carried out to better understand the proton acceleration mechanisms. Finally, the idealised case of thin, near-critical density plasma targets and their interaction with a CO_2 laser was also studied.

In all cases the plasma was formed of cold, pre-ionised hydrogen with initial electron and ion temperatures of 0 eV. Where applicable, the front and rear target density ramps were estimated from the experimental results and theoretical scaling. These were characterised by their scale length, the distance over which the density drops from its maximum to $1/e$ of the peak value. A grid size of $120 \times 120\,\lambda_L = 88 \times 88$ nm was chosen. This ensured that the fine features of the HB-RPA shock front were resolved, while 16 particles per cell were chosen for both electrons and protons. These values were chosen to minimise numerical heating, and also to minimise the computational resources required. Simulations were run for a total of 15 ps for the cases studying proton acceleration, equivalent to three times the laser pulse length. For initial studies on the density steepening effect of the 25 ps pre-pulse, the total simulation time was 30 ps to encompass the pulse and subsequent plasma evolution.

The full list of simulation parameters are summarised in table 6.2.

Parameter	Value
Electron particles per cell	16
Proton particles per cell	16
Box size x	100 - 350 µm
Box size y	100 µm
Grid size x	$120\,\lambda_L = 88.3$ nm
Grid size y	$120\,\lambda_L = 88.3$ nm
Laser wavelength	10.6 µm
Laser focal spot size	65 µm
Laser pulse length	5 ps
Laser intensity	$7.5 \times 10^{15}\,\mathrm{Wcm^{-2}}$
a_0	0.78
Laser polarisation	Linear, p-polarised
Initial electron/proton temperatures	0 eV

Table 6.2: The particle-in-cell simulation parameters used for the simulation results presented in Chapter 6.

6.4.1 Effect of the laser train

Regardless of the challenges in extraction of the target density profile from the interferometric images, the front surface scale length is not retrievable at the time of arrival of the main CO_2 pulse. The arrival of the early time probe ~ 25 ps before the main pulse was intended to allow characterisation of the blast wave. However, this gives no insight into the effect of the 30% pre-pulse. This was studied using particle-in-cell simulations to better understand the target conditions at the time of the main pulse.

Given the challenges with characterising the density profile from the experimental images, and the good agreement of the shock radius with the predicted scaling, the analytical scale lengths were again assumed, as in Chapter 5. For the case of the colliding shocks, the true density profile was even more challenging to obtain, although the scale length was measured to be roughly equivalent to that of the preceding time. From the scaling outlined in section 3.2.1, the assumed scale lengths from figure 6.5 are 68 µm, 73 µm and 80 µm. Therefore, a range of initial density ramps were simulated with associated scale lengths ranging from 50-100 µm. A linearly polarised, CO_2 beam was incident on the plasma, focussed at the nominal position of the top of the ramp, with 30% of the mean laser energy, equivalent to 0.38 J. This corresponds to a peak laser intensity of $2.3 \times 10^{15}\,\mathrm{Wcm^{-2}}$. The peak density of the target was assumed to be $4\,n_c$, equivalent to the peak density of the gas jet at 4.5 bar with a 6-fold density increase due to a blast wave.

Simulations demonstrate that the density profile is indeed steepened in all cases. Since laser propagation cannot occur to the peak of the density ramp, the density accumulates at the location of the critical surface. While some relaxation occurs over the 25 ps the laser is not present, the profile exhibits significant steepening. In practice, a second ramp forms, with the "peak" formed around where the initial critical surface was located. The

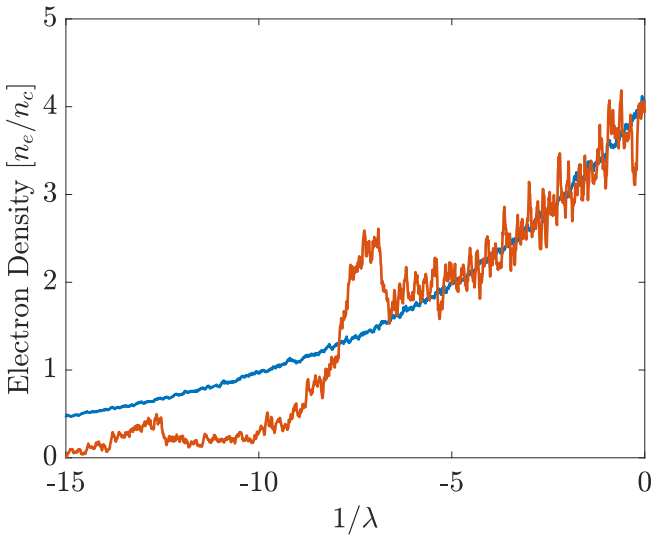


Figure 6.13: The steepened density profile of a target with a peak density of $4\,n_c$ and scale length of 70 µm at the arrival of the main CO_2 pulse. This was induced by a pre-pulse with 30% of the total integrated laser energy, 25 ps before the main pulse. A new density profile emerges, with scale length of 7 µm.

scale length of this structure ranges from ∼5 µm to ∼15 µm, dependent on the initial scale length. For illustration, the assumed density profile of a target with initial scale length of 70 µm is given in figure 6.13. The final scale length is ∼7 µm.

6.4.2 Experimental comparison

From the experimentally obtained optical probe images, the target structure for the early times is equivalent to the standard blast wave case, with a steepened density profile leading to a shock front which appears infinitely thick to the incident laser; the interaction never traverses the entire shock front. Similarly, even for the case of colliding shocks, the target thickness, > 50 µm, is such that the acceleration is expected to be dominated either by hole-boring RPA or collisionless shock acceleration, as in Chapters 4 and 5. Therefore, simulations were conducted using the experimental parameters to determine the dominant acceleration mechanism. A plasma of peak density $5.8\,n_c$ was assumed, equivalent to the estimated peak density in the colliding shock case. This was simulated with an exponential density ramp preceding the critical surface with a scale length of 7 µm, as found in the previous section. The incident laser was linearly polarised with a peak intensity of $I = 7.5 \times 10^{15}\,\mathrm{Wcm}^{-2}$, focussed to a spot of radius 32.5 µm.

Simulations indicate that for the expected experimental conditions, an analogous situation to that observed in Chapter 5 occurs. Again, a standing wave is induced between the incident and reflected components of the laser, forming a plasma grating structure.

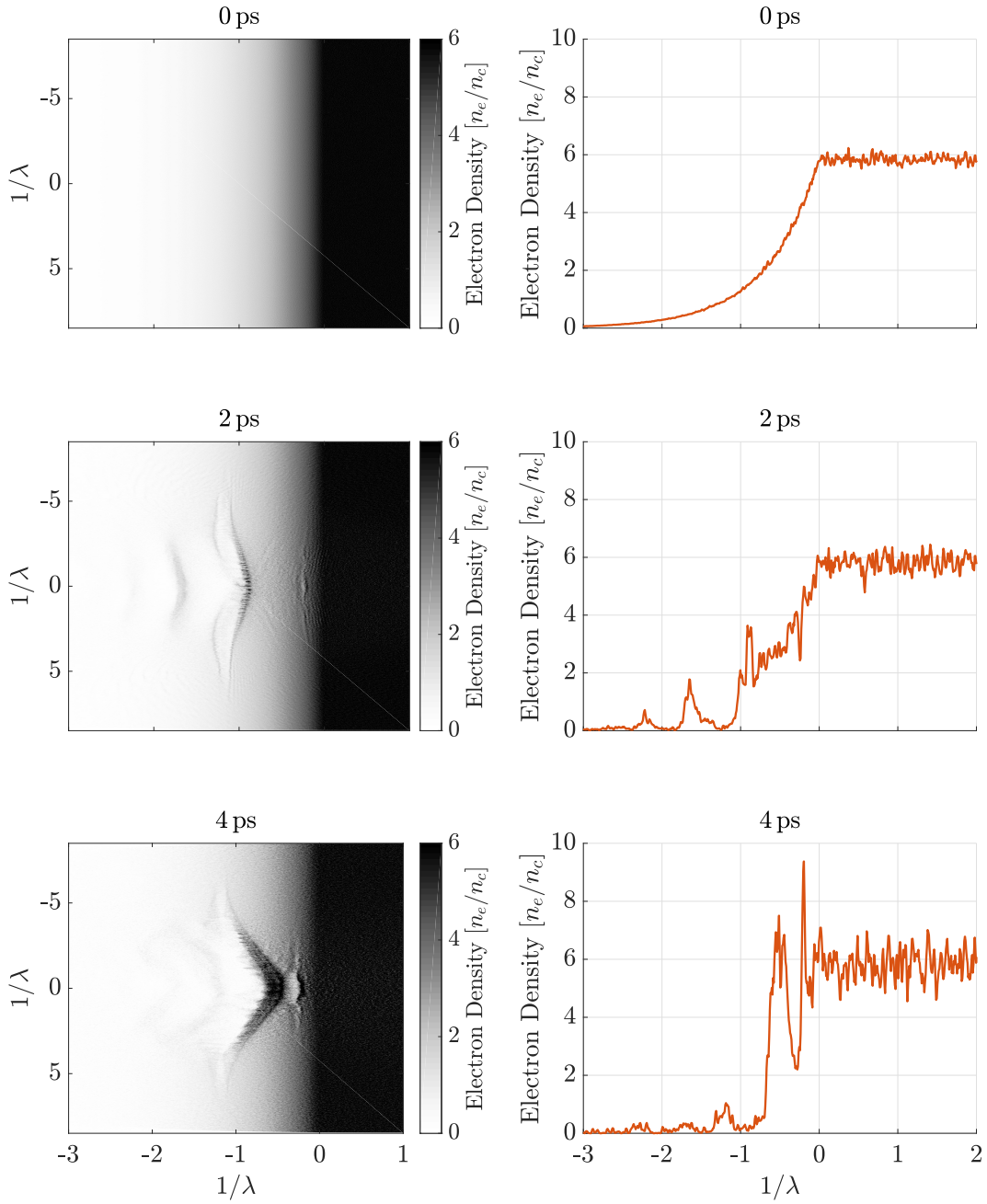


Figure 6.14: The full 2D and on-axis electron density lineouts for the interaction of a CO_2 laser pulse with intensity $I = 7.5 \times 10^{15}\,\mathrm{Wcm^{-2}}$, incident on a target with peak density $n_e = 5.8\,n_c$ with a front surface exponential density gradient with a scale length of 7 µm. The dynamics are shown at 2 ps and 4 ps, along with the initial density profile. These demonstrate the formation of a single density structure due to a standing wave, which is subsequently accelerated. Note the 2D density images are on a saturated colour scale to better illustrate the interaction

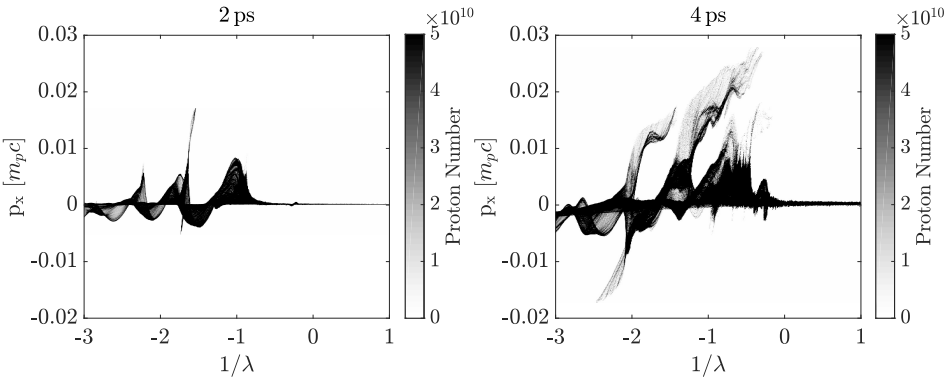


Figure 6.15: The x-p_x proton phase space for at 2 ps and 4 ps for the interaction conditions given in figure 6.14.

Figure 6.14 demonstrates the full two-dimensional and on-axis density profiles of the plasma. For the case of the relatively short, 7 µm density ramps assumed in this scenario, only two grating elements are observed to form, with one exceeding the critical density. This is observed in the 2 ps profile shown in figure 6.14. At subsequent times, the laser intensity increases to a level that the radiation pressure causes this density structure to be accelerated in the direction of laser propagation, generating high energy protons. The onset of this effect is observable in the x-p_x proton phase space at 2 ps in figure 6.15. Subsequently, this density structure is destroyed, with density steepening then occurring at the initial critical surface. This is also accelerated, with hole-boring acceleration occurring, but to lower energies. The 4 ps outputs given in figures 6.14 and 6.15 illustrate this effect. Along with modest acceleration off the near-critical density secondary grating structure, this results in the total integrated proton energy spectrum appearing broadband.

Acceleration was modelled for two further, higher intensity cases, equivalent to twice and four times the laser energy, or $I = 1.5 \times 10^{16}\,\mathrm{Wcm^{-2}}$ and $I = 3 \times 10^{16}\,\mathrm{Wcm^{-2}}$, respectively. These demonstrated the same density modulation effect, and subsequent acceleration off a limited-mass grating element. Increased maximum proton energies are observed, although not at the expected $4I/n_i c$ scaling, i.e. a doubling in laser energy did not result in a doubling in the proton energy. This is a result of the coupled nature of the grating formation and acceleration. For the higher intensity cases, the grating structure forms more rapidly, but subsequently is accelerated earlier in the pulse; it is destroyed before the highest laser intensities are reached. As such, the maximum observed proton energies do not scale linearly with the maximum laser intensity, as might be expected.

As in previous chapters, whether mono-energetic spectral features are present or not is thought to be dependent on the target conditions, grating element formation time and the overall density profile, and the speed at which the shock front decays. In simulations, mono-energetic proton features are not observed, with radiation pressure acceleration off multiple structures to differing energies resulting in the total integrated proton beam

energy profile appearing broadband. To observe spectral peaking, efficient acceleration must occur off these grating elements, before a rapid decay of the shock front to ensure these narrow energy spread features are preserved.

In summary, results suggest at the experimental intensities, acceleration was due to hole-boring off an induced plasma grating structure. This in fact perhaps helps explain the observation of increased proton energy with expansion radius, and as such, density. This is an unexpected observation given the predicted $E_i = 4I/n_i c$ scaling of hole-boring. With increasing density and expansion radius, the density profile preceding the critical surface will logically change. It is easy to imagine a situation where with increasing shock radius and density, conditions become more favourable for the formation of these near-critical density structures around the peak of the laser pulse, resulting in higher proton energies.

6.4.3 Proton acceleration from thin gas targets

Now, let us now consider the more idealised case of perfect, thin, near-critical density plasma slabs. While it was not possible to produce these, the ultimate goal of optimal proton acceleration would suggest moving into the light-sail regime. For this, thin, steep density gradient plasma targets would be required.

Particle-in-cell simulations were carried out to study the effect of acceleration from thin slab targets on the proton energy. These ranged from 2-50 µm, and were initialised with a peak density of $5.8\,n_c$, with all other parameters as described previously. Two laser intensities were simulated, first at the expected experimental conditions, with $I = 7.5 \times 10^{15}\,\mathrm{Wcm^{-2}}$, and secondly with 4 times the laser energy, giving an intensity roughly equivalent to the current intensities now available, at $I = 3 \times 10^{16}\,\mathrm{Wcm^{-2}}$. These were initially studied for linear polarisation, given circular polarisation is not currently possible to realise experimentally.

Figure 6.16 shows the electron density profile, longitudinal electric field and x-p_x phase space for a 5 µm target at 2.3 ps. The peak laser intensity is $I = 7.5 \times 10^{15}\,\mathrm{Wcm^{-2}}$. As can be observed, for the case of the expected experimental intensities, the proton acceleration is dominated by the rear surface sheath which forms. This arises due to strong electron heating by the laser at the front surface. The hot electrons traverse the target and exit at the rear, forming the sheath. This formation of the sheath field can clearly be observed in figure 6.16(c). Also present is a radiation pressure driven component, seen at the front of the target. The combination of these two effects can be observed most clearly in the x-p_x proton phase space in figure 6.16(d). Here, a low energy hole-boring front is seen forming at the front surface, although no significant reflection occurs at this time. The dominant acceleration arises due to the target expansion at the rear surface, producing a broad range of proton energies. These sheath accelerated beams reach ~ 5 times higher energies than those driven by hole-boring.

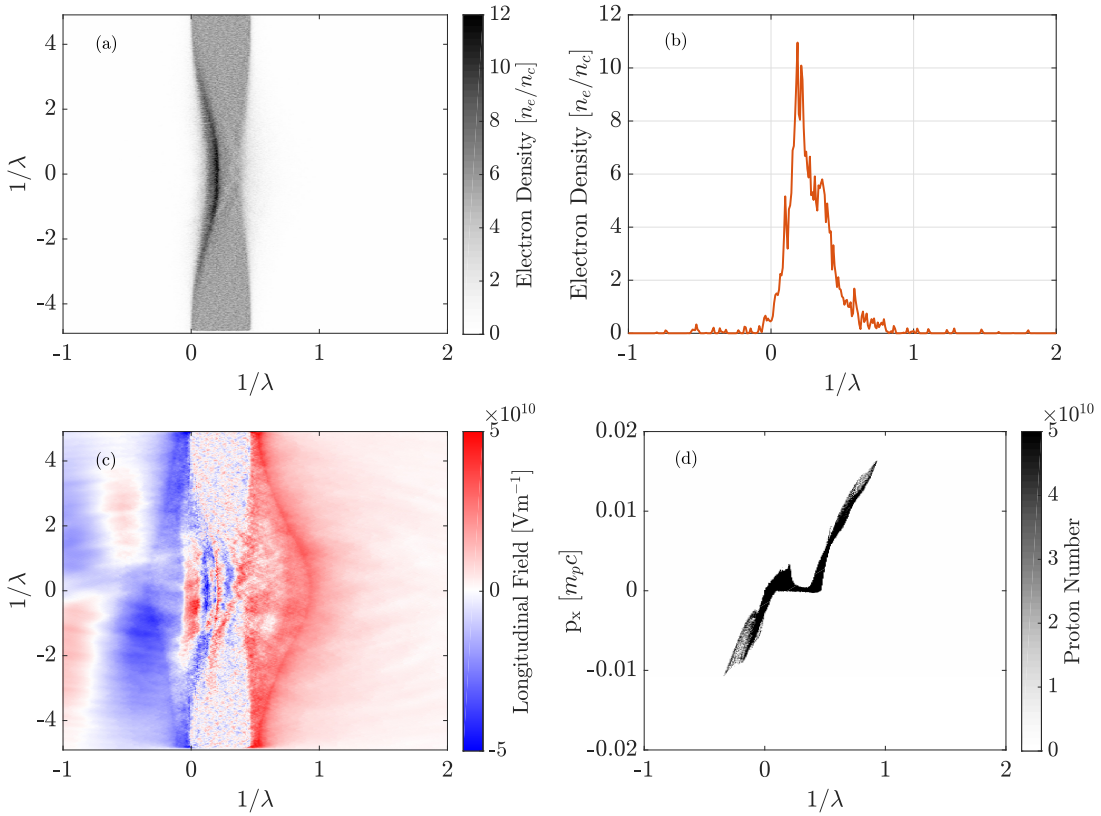


Figure 6.16: Example target conditions at 2.3 ps, for the interaction of a CO_2 laser pulse of peak intensity $I = 7.5 \times 10^{15}\,\mathrm{Wcm^{-2}}$, incident on a 5 µm plasma slab of density $5.8\,n_c$. (a) The full 2D electron density of the target, illustrating density steepening at the front surface, (b) the on-axis electron density, (c) the longitudinal electric field, demonstrating the formation of a sheath field at the rear of the target due to expansion, (d) the x-p_x proton phase space for the temporal snapshot. This illustrates that the protons gain energy from two mechanisms, at the critical surface due to the radiation pressure, and more significantly, at the target rear due to the sheath formation.

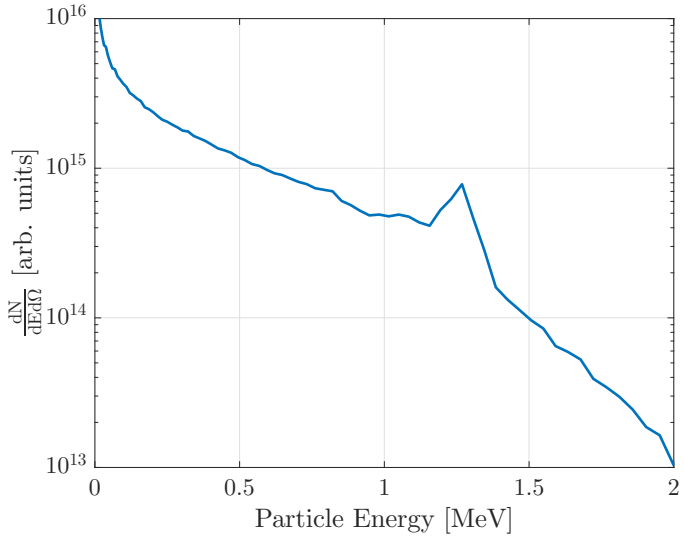


Figure 6.17: The proton energy spectrum for a 2 µm slab target with density of $5.8\,n_c$. The incident laser had a peak intensity of $I = 3 \times 10^{16}\,\mathrm{Wcm}^{-2}$. A thermal energy spectrum is observed due to the expansion of the heated target, while also present is a narrow energy spread feature due to radiation pressure acceleration at the front surface of the target.

In the case of the thinnest targets, $\leqslant 5\,\mu\mathrm{m}$, the bulk of the target is accelerated by this effect, while for thicker targets, $\geqslant 10\,\mu\mathrm{m}$, the critical surface is driven into the target, with a subsequent collisionless shock structure formed. This is not a surprising result, given the laser intensity and density conditions (see equation 2.74). However, regardless of the target thickness, the acceleration is dominated by the sheath field, with the shock accelerated ions lower in energy. The linear laser polarisation results in considerable heating, while the intensities are low enough that the radiation pressure cannot dominate for these thin targets.

In the higher intensity case, for the thinnest targets, the interaction is somewhat different. Take, for example, the 2 µm case. Here, acceleration is still dominated by the expansion of the target due to heating. However, also present is a radiation pressure driven feature. The bulk of the target is spatially driven in the direction of propagation as a single entity, producing a narrow energy spread feature within the sheath accelerated beam. This can be observed in figure 6.17.

For the thinnest targets, $< 10\,\mu\mathrm{m}$, radiation pressure effects result density steepening at the critical surface and the bulk of the target being accelerated forward during the early portion of the laser pulse. Simultaneously, the target rapidly expands with heating effects dominating and the target going underdense to the incident laser ($n_e < \gamma n_c$); for the case of the 2 µm target, this occurs around the peak of the laser pulse. This acceleration mechanism is termed relativistic transparency, also known as the laser breakout afterburner regime, and is a form of enhanced sheath acceleration. This was first investigated through numerical simulations by Yin et al. [268] [269]. The mechanism exhibits

three distinct phases. Initially the target is overdense to the incident laser. Target expansion due to sheath effects results in a reduction in the density, while simultaneously an increase in the laser intensity gives an increase in the Lorentz factor, γ, reducing the plasma frequency by a factor $\gamma^{\frac{1}{2}}$, although for the modest intensities relevant to this work, this effect is negligible. For sufficiently thin targets, the second phase arises when the plasma skin depth (see section 2.1.3) becomes comparable with the target thickness; the laser field heats all the electrons confined within a region equivalent to the size of the laser focal spot. This is termed the "enhanced sheath acceleration" phase. Finally, as the target expands still further the density drops below the critical density, $n_e = \gamma n_c$, and the laser can penetrate the target, heating the sheath electrons to very high temperatures. This effect is illustrated in figure 6.18, where first the initial radiation pressure driven phase is observed at 1 ps. At 3 ps, sufficient heating has occurred that the target has expanded to the point of the critical density, before finally, the target goes underdense and the bulk of the target can be heated. Despite the laser intensity decreasing at this point, a significant jump in the peak proton energy from ~ 1.4 MeV to > 2.5 MeV is observed between 3 ps and 4 ps, due to this effect.

For thicker targets, $\gtrsim 10\,\mu$m, the interaction conditions are insufficient for relativistic transparency to occur. The target does not go underdense to the incident laser pulse at any point during the interaction. As such, two mechanisms again occur. Sheath acceleration dominates, with the highest energies determined by the target expansion. Also present are shock driven components, both due to hole-boring and the late time formation of a collisionless shock. However, these features are lower in energy than the sheath beams. The interaction looks similar to that in figure 6.16, except the stronger electron heating produces stronger sheath fields and subsequently, higher proton energies.

For both intensities, the maximum proton energies are plotted as a function of target thickness. These results are given in figure 6.19. For the experimentally applicable case, the proton energy is observed to decrease with increasing target thickness. Since the classical sheath effects dominate, with increasing thickness the divergence of the hot electron beam means that the effective strength of the sheath that can form diminishes [123]. For the higher intensity case, a clear transition is visible, indicating the two regimes in which acceleration occurs. For thicknesses $< 10\,\mu$m and $\geqslant 10\,\mu$m, these are the relativistic transparency and classical sheath acceleration regimes, respectively.

An interesting final point of note is the expected benefit of thin targets in the collisionless shock acceleration regime. This is of interest because thin targets are believed to offer a number of benefits for this mechanism. Furthermore, as shown in Chapter 4, the current operating regime for the laser results in both hole-boring and collisionless shock acceleration occurring, with a move to higher densities making this the most probable acceleration mechanism. Thin targets are particularly suitable due to the requirements for high shock velocities to produce high energy proton energies, with the need for uni-

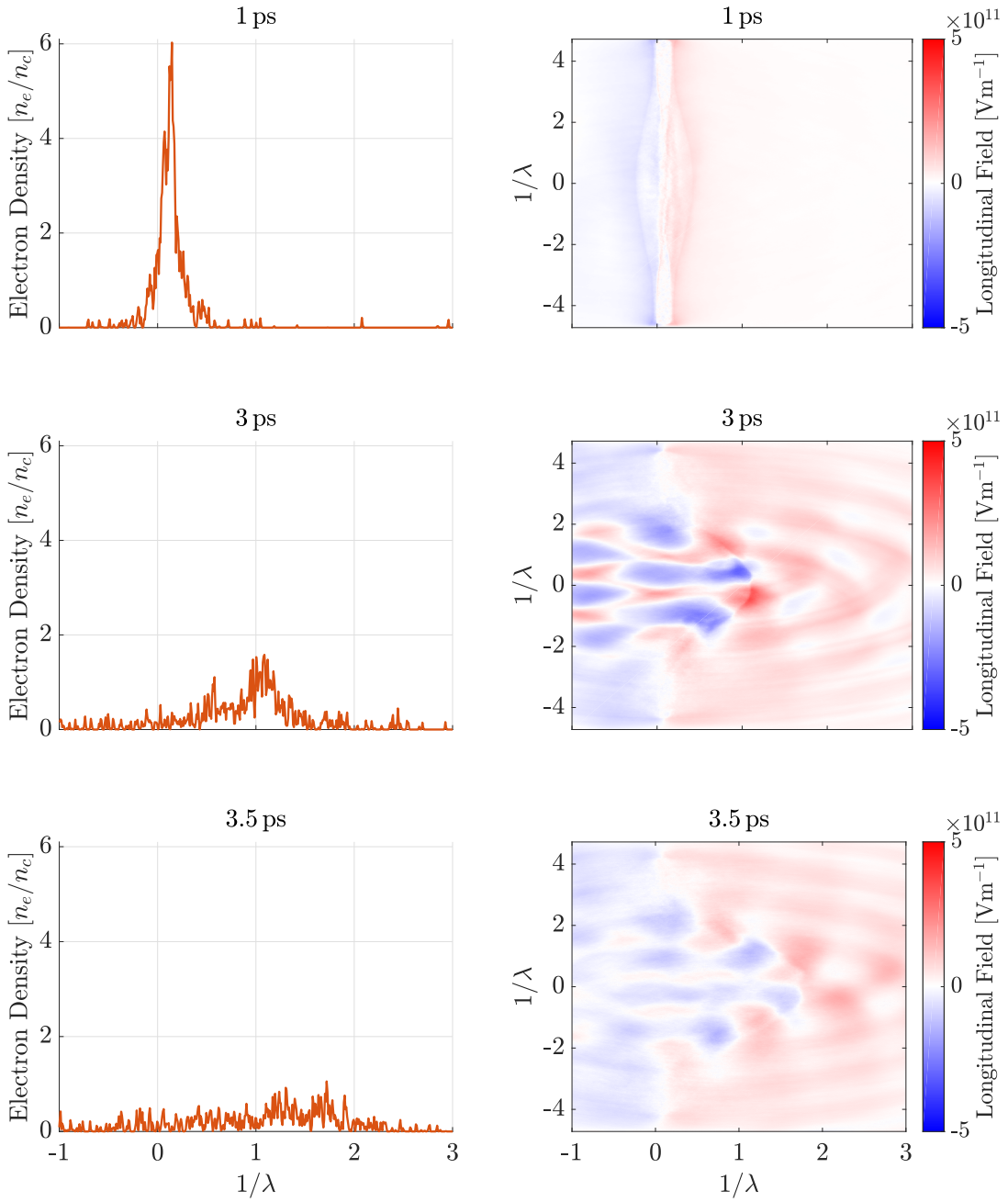


Figure 6.18: The on-axis electron density lineouts and on-axis longitudinal electric field for the interaction of a CO_2 laser pulse with intensity $I = 3 \times 10^{16}\,\mathrm{Wcm}^{-2}$, incident on a 2 µm thick plasma with peak density $n_e = 5.8\,n_c$. The dynamics are shown at 1 ps, 3 ps and 3.5 ps. These demonstrate the initial density steepening, the point the target expands to the critical density and later subcritical phase, where bulk electron heating due to relativistic transparency is possible.

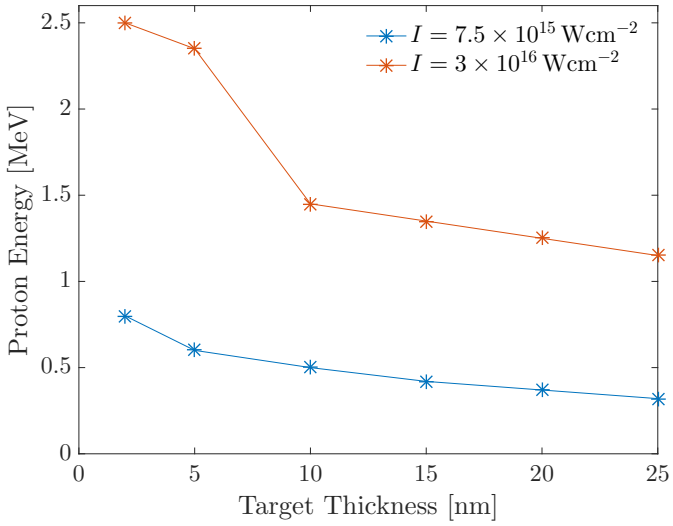


Figure 6.19: The maximum proton energy versus target thickness for the case of slab targets. Results are given for two intensities, $I = 7.5 \times 10^{15}\,\mathrm{Wcm}^{-2}$ and $I = 3 \times 10^{16}\,\mathrm{Wcm}^{-2}$, equivalent to the estimated experimental parameters and an intensity with 4 times higher energy, roughly equivalent to the currently available intensities.

form heating of the upstream plasma [157]. As shown with thin foil targets, recirculation of electrons can lead to increased target heating [115] [270]. The same is true from thin near-critical density targets, with steep front and rear density gradients promoting the formation of sheaths which induce electron recirculation. Silva et al. [157] suggest that for high shock velocities the shock formation time, approximately two ion plasma periods for $M \approx 1$, i.e. $\sim 4\pi/\omega_{p_i}$ [86], needs to be longer than the electron recirculation time, with even a single transition cycle enough to provide more uniform heating of the target. This gives a limit of the target thickness equivalent to $L_{target} < \sqrt{m_i/m_e}\lambda_L$ for MeV electrons at critical densities [156]. Given the time for electron traversal scales with the target thickness, thin targets ensure the formation time condition is met and produce enhanced shock velocities. Therefore, the production of high density, thin gas targets could allow for efficient collisionless shock acceleration of ions.

The idealised case

The idea of thin targets can be taken one step further, to the extreme case of the optimal situation to achieve light-sail acceleration, as earlier described in section 2.4.2. Equation 2.95 gives an expression for the optimal thickness of a target for a given density and laser intensity, with $L_{opt} \propto \sqrt{I_L/{n_i}^2}$.

For the case of the assumed peak density of a colliding blast wave, $n_i = 5.9\,n_c$, the optimal target thickness can be calculated; this is shown to be $L_{opt} \approx 0.4\,\mu\mathrm{m}$ in the low intensity case. Simulations were conducted for both linear and circular polarisation.

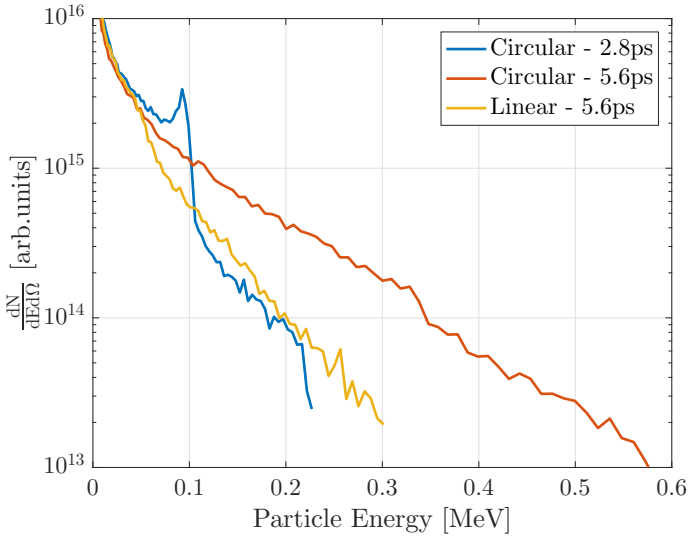


Figure 6.20: The proton energy spectra for the case of an idealised thin slab target at a peak density of $n_i = 5.9\,n_c$ and peak intensity of $I = 7.5 \times 10^{15}\,\mathrm{Wcm}^{-2}$. Energy spectra for both linear and circular polarisations are presented at a time of 5.6 ps, equivalent to the energy at time of the end of the laser pulse. Also presented is the energy spectrum at the peak of the laser pulse, 2.8 ps, corresponding to the peak of the laser pulse. This demonstrates a radiation pressure driven component to the interaction.

The higher intensity case was also studied, using a thicker target due to the increased intensity, with $L_{opt} \approx 0.8\,\mu\mathrm{m}$. While circular polarisation was not available on the experiment, light-sail requires minimal heating of the thin target to suppress expansion and ensure the acceleration is dominated by radiation pressure effects. The proton energy spectra for the low intensity cases are shown in figure 6.20.

As can be seen from figure 6.20, for the low intensity case, acceleration is dominated by the target heating and subsequent expansion. At late times, at the end of the laser pulse (5.8 ps), the spectra are broadband in nature which signifies the expansion being dominant. For the linear polarisation case, acceleration is always primarily driven by the sheath that forms. However, for the circular polarisation case, heating is sufficiently suppressed due to a reduction in $\vec{J} \times \vec{B}$ heating. At early times up until the peak of the pulse, radiation pressure effects also occur, driving a mono-energetic ion feature. This can be observed in the third trace in figure 6.20(a), from 2.8 ps, equivalent to the arrival of the peak of the laser pulse.

For the higher intensity case, the interaction is similar, with the target expansion dominating the interaction. While the bulk of the target is accelerated due to the radiation pressure, heating effects still dominate and the target rapidly expands. In this case, the peak proton energies are ~ 1.5 MeV and ~ 3 MeV, for linear and circular polarisation, respectively.

One obvious question to address is why the acceleration in the case of these thin slabs

is not dominated by shock acceleration mechanisms, unlike in the roughly analogous case in Chapter 5. This is despite almost identical laser conditions in both cases. For the case of the thin slabs, the structures are initialised at the optimal conditions at the start of the pulse. Conversely, in the case of the induced plasma grating structure, these must be formed in the rising edge of the laser pulse. Consequently, unlike in the case of the thin slabs, in the idealised case, no appreciable heating of these structures can occur before the peak of the laser pulse. The radiation pressure mechanism can then dominate. In the case of these thin slabs, the intensities are such that the radiation pressure can never dominate the heating effects, even for the case of circular polarisation. The gradual increase in intensity results in strong heating, driving target expansion effects. To overcome this limitation, shorter pulses, with higher peak intensities and a switch to circular polarisation would be required to ensure minimal heating and radiation pressure based effects dominate.

6.5 Conclusions

This chapter has presented results from attempts to use colliding blast waves to favourably modify the density profile of gas jet targets to enhance proton acceleration. Work presented in Chapter 5 demonstrated that the formation of narrow, limited areal density structures through the formation of a plasma grating structure could indeed give enhanced proton energies. However, the formation of these plasma grating structures was directly linked to the accelerating CO_2 pulse, with strict requirements on the laser parameters to permit the formation of the grating. With this, decoupling the formation of these thin, limited mass structures from the main accelerating laser pulse is important for full control of the interaction conditions. Collisions between two, counter-propagating blast waves were considered in an attempt to make thin gas targets.

Colliding blast waves were formed using the external YAG driven scheme, where two metal foils, placed on opposite sides of the nozzle at the edge of the gas flow, were heated with a YAG beam. Ablation of the foil caused localised heating, and the formation of two counter-propagating shocks. Examples of the shock structure for different expansion times are given in figure 6.3. Accurate retrieval of the density profiles of these shocks was challenging, due to the poor quality of the interferometric images. However, the shock expansion showed reasonable agreement with the scaling given by Sedov [206] (see section 3.2.1) and velocities of $\sim 7.5\,\mathrm{kms}^{-1}$, indicating the strong shock limit can be applied and the shock density scales as the result given in equation 3.5b. This allowed estimates of the peak density and scale length to be inferred, and an estimate of the thickness of the structure formed during shock collision; this was found to be $85\,\mu\mathrm{m}$.

The observed proton energy as a function of expansion radius up to the point of collision was studied. Mono-energetic features were observed for the relative expansion

scenarios for two differing initial gas density profiles, with peak unperturbed densities of $4.5 \times 10^{18}\,\mathrm{cm}^{-3}$ and $7.4 \times 10^{18}\,\mathrm{cm}^{-3}$, corresponding to nozzle backing pressures of 2 bar and 4.5 bar, respectively. This indicates acceleration through hole-boring or a collisionless shock structure. Peak proton energies were observed to increase with expansion radius, with the highest observed energies at the point of collision. Retrieval of the true energy spread of these spectral features was also possible through deconvolution. Mean rms energy spreads of $\Delta E/E = 15.8 \pm 0.5\%$ and $\Delta E/E = 11.9 \pm 1.8\%$ were observed for backing pressures of 2 bar and 4.5 bar, respectively. A clear scaling of the energy spread with target density was observed, with the rms energy spread observed to decrease with increasing intensity (see figure 6.10). Broadband energy proton beams were also observed on a number of shots. These again showed increased peak proton energies with increasing expansion radius, with the highest energies at the point of collision.

Particle-in-cell simulations were conducted to better understand the interaction dynamics and to attempt to explain the experimental observations. First, the modification of the target density profile was investigated, due to the effect of the 25 ps pre-pulse. This showed that for the analytically predicted scale lengths, the final density profile has a scale length of $\sim$ 5-10 µm. Using this modified density profile, the interaction dynamics were studied. This showed that, like in the results presented in Chapter 5, the formation of a limited number of plasma grating structures was observed. These were again the source of the highest energy protons, accelerated due to HB-RPA. This helps explain the observation of spectral peaking in the experiment, and also might provide explanation an of why the maximum proton energies were observed to increase with the shock radius and density. It is proposed that these greater expansion radii and peak densities result in more favourable grating formation conditions, resulting in higher proton energies.

Finally, simulations were carried out in the extreme case, if it were possible to make micron scale thin slab targets. These investigated the interaction dynamics between such near-critical density plasma structures at the experimentally achievable CO_2 laser intensities. Intensities of $7.5 \times 10^{15}\,\mathrm{Wcm}^{-2}$ and $3 \times 10^{16}\,\mathrm{Wcm}^{-2}$ were studied, equivalent to the experimentally relevant parameters and the currently achievable parameters, respectively. Owing to these relatively modest intensities and the long pulse length, 5 ps, strong target heating is observed and sheath expansion is the dominant mechanism for all but the thinnest targets, $\leqslant 5$ µm.

7 Conclusions and Future Avenues

This thesis has presented work using the CO_2 laser at the Accelerator Test Facility at Brookhaven National Laboratory, studying proton acceleration in near-critical density laser plasma interactions. These have demonstrated the possibility of producing mono-energetic ion features using radiation pressure driven acceleration from shaped gas targets. This chapter summarises the experimental results presented in the preceding chapters, and provides a number of potential avenues of pursuit to further this work.

7.1 Proton acceleration from pre-pulse shaped gas targets

Chapter 4 presented a continuation of earlier experimental work into ion acceleration at the Accelerator Test Facility. The experiment concerned the interaction of a CO_2 laser at relativistic intensities of $1 \lesssim a_0 \lesssim 1.8$, and at near critical densities, between $1.7 \times 10^{18}\,\mathrm{cm}^{-3}$ and $1.3 \times 10^{19}\,\mathrm{cm}^{-3}$ (0.15-1.15n_c). Target shaping was employed by means of a blast wave, generated with a 27.5 ns laser pre-pulse of varying energy between 0.3-3.7 mJ. This had the effect of steepening the density profile of the gas, which has previously been shown to be crucial in these experiments to produce mono-energetic ion features [181].

Previous results had demonstrated ~ 1.1 MeV, peaked proton spectra with energy spreads as low as $\Delta E/E \approx 4\%$ [141] [181]. By comparison, the results presented in Chapter 4 produced peak proton energies of > 1.8 MeV, demonstrating a $> 50\%$ increase in the previously best observed ion energies for this laser system. The best observed energy spread from the experimental results presented was $\Delta E/E \approx 5\%$, only slightly worse than those previously observed, although this shot had a peak energy of ~ 0.55 MeV. For comparison, the highest energy shot exhibited an energy spread of $\sim 12\%$.

Also observed was very good agreement between the experimentally observed proton energies and the theoretical hole-boring scaling, $4I/n_i c$. The fitted trend followed a gradient of 0.93, close to the expected 1 : 1 scaling. By comparison, previous work also demonstrated a linear scaling, although these results produced a gradient of ~ 11; i.e. measured energies were 11 times higher than predicted. The observed scaling indicates that the dominant acceleration mechanism for the results presented in Chapter 4 was HB-RPA. Simulations also verified this conclusion, showing dominant proton acceleration from the spatially driven critical surface due to hole-boring. Acceleration was also

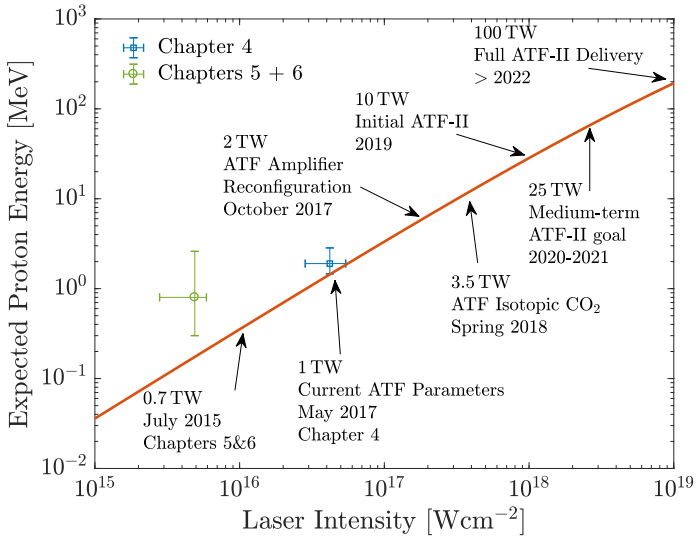


Figure 7.1: The predicted maximum proton energy scaling versus laser intensity for the CO_2 laser at the ATF for a critical density interaction. Experimental results from chapters 4, 5 and 6 are also given. The points correspond to the mean measured proton energy and on target intensity. The errorbars define the range over which these values varied. Important historic and future laser development milestones are also given.

observed to come from a collisionless shock at late times, although never at higher energies than those from HB-RPA over the parameter range studied. This structure forms at late times as the laser pulse depletes. This observation of multiple mechanisms driving acceleration highlights the transition regime which occurs, owing to the intensities and densities studied (see figure 2.13 and equation 2.74). However, the combination of the simulation observations and good agreement between the experimental results and theoretical scaling strongly suggests that HB-RPA is still the dominant acceleration mechanism. Simulations also provide explanation for the lack of spectral peaking on many shots, with a gradual deceleration of the hole-boring front or a collisionless shock capable of producing broad energy spread beams which drown out lower flux spectral features. Consequently, rapid dissipation of the acceleration structure is expected to be required in cases where the production of these narrow spectral features is desirable.

A number of possible interesting avenues of pursuit exist to extend the work presented in Chapter 4. Many of these should become feasible in the near future, with the development of the current ATF laser and the upgraded ATF-II [76] [271] facilities. Current ongoing upgrades to the ATF laser system include an increase of the current deliverable laser energy to provide up to $\sim 2\,\mathrm{TW}$ laser powers [272] at the current 3.5 ps pulse lengths. This equates to a peak intensity of $I \approx 2 \times 10^{17}\,\mathrm{Wcm^{-2}}$, or $a_0 \approx 3.9$. For comparison, the current best measured conditions are $\sim 1\,\mathrm{TW}$. Plans also exist within the next year to add isotopic CO_2 molecules to the main amplifier, which is expected to reduce the pulse length down to 2 ps, with no loss of deliverable energy

to the chamber. As such, peak powers as high as 3.5 TW could soon be achievable. This would give a maximum peak laser intensity of $I \approx 3.6 \times 10^{17}\,\mathrm{Wcm^{-2}}$, or $a_0 \approx 5.1$. Given the good agreement with the theoretical HB-RPA scaling, this ~ 3.5 times increase in laser power could also translate into an equivalent increase in the observed proton energy. Assuming the observed agreement with theoretical scaling holds, at critical densities, $n_i = n_c$, these improved laser energies could lead to proton energies of $> 6\,\mathrm{MeV}$ and $> 11\,\mathrm{MeV}$, respectively. For reference, figure 7.1 shows demonstrates the expected proton energies against laser intensity, along with the expected future CO_2 laser development milestones.

The future ATF-II laser system will go considerably further, with laser powers up to 100 TW anticipated from the completed system. This is expected to be delivered in the form of a $\sim 10\,\mathrm{J}$ beam in 100 fs (equivalent to 3 laser cycles) [76]. These would represent a 100-fold increase in the laser power compared to current levels. At these high intensities of $\sim 10^{19}\,\mathrm{Wcm^{-2}}$, the interactions become strongly relativistic, with $a_0 > 25$. Subsequently, the predicted proton energies are expected to scale less strongly with intensity, as outlined in section 2.4.2, with the proton energy dependence now scaling as $I^{\frac{1}{2}}$. For these intensities, proton energies of $\sim 20\,\mathrm{MeV}$ might be expected from HB-RPA.

Circular polarisation would also be an interesting avenue to explore. Previous experiments utilised this option [141], and simulations suggest that for the experimental conditions of the work in Chapter 4, a two-fold increase in the maximum observed proton energy could be achieved. This is due to decreased upstream plasma heating, reducing the thermal plasma pressure and allowing faster propagation of the critical surface. Circular polarisation in not currently possible at the ATF, due to the installation of the CPA system. This has the benefit of permitting higher peak powers to be delivered to target, with the beam less prone to non-linear effects in the air transport lines to the chamber. However, the previously used $\lambda/4$ waveplate is susceptible to damage with high power beams and can only be used before the main amplifier. Use of this would not be beneficial, since upon recompression of the CPA pulse, circular polarisation cannot be maintained. Acquisition of a suitable waveplate is challenging, since high power CO_2 lasers are extremely rare and often require custom beam optics to be made. However, it is hoped that in the near future the option of circular polarisation will become possible.

A further interesting avenue to explore is related to the use of multiple ion species. Esirkepov et al. [131] suggested double layer targets, with a high-Z first layer and thin low-Z coating on the rear. It was shown these could be used to control the low-Z energy spectrum, particle bunch charge and beam collimation. Robinson et al. [126] demonstrated that the proton beam spectral characteristics could be modified through the manipulation of relative concentrations of protons to higher-Z ions. A change in the accelerating field structure for different relative concentrations of the two ion species

facilitates modulation of the proton energy spectrum. Sahai et al. [273] [274] demonstrated that for a mixture of low and high-Z ion species, high proton energies could be possible. In this scheme, the high-Z ions are stationary, while an electron plasma wave is formed in a density ramp. As this structure propagates, protons can be pulled along via charge separation. This facilitates the production of high energy protons. The use of multiple ion species gas targets could therefore be an interesting avenue to pursue in the future.

Finally, current experiments have been limited to investigation with the CO_2 laser at the ATF due to the challenges with producing over-critical density gas targets for near-IR, $\sim$1 µm, lasers. Recent developments have allowed experiments of this kind [239], with $\sim$ MeV level protons produced from an over-critical hydrogen gas jet through collisionless shock acceleration. Experiments are also planned using the VULCAN Petawatt laser system at the Rutherford Appleton Laboratory ($a_0 \simeq 25$, $\lambda_L = 1.053\,\mu m$) using near-critical density gas jets along with target shaping as used in the experiment presented in Chapter 4. Simulations in this case suggest ~ 45 MeV protons could be produced, although producing short density scale lengths, important for producing mono-energetic features, could prove challenging.

7.2 Proton acceleration off a plasma grating structure

Chapter 5 presented experimental results again looking at proton acceleration at near-critical densities from hydrogen gas jets. Target shaping was again employed, although in this case through the use of a secondary laser. This 5 ns, 80 mJ YAG beam was focussed onto a stainless steel clip, positioned at the edge of the gas flow at the front of the gas nozzle. The relative timing of this secondary laser beam to the main CO_2 pulse was easily changeable, with $\sim$ ns precision. This allowed studies of the effect of the blast wave scale length on the measured proton energies.

Experimental results demonstrated a strong dependence on the measured proton energy with the shock expansion time. This is believed to be due to the variation in plasma scale length preceding the peak of the shock, which scales with the shock radius. The proton energies were shown to vary much faster than predicted by the focussing geometry of the CO_2 beam; the shock moved ~ 1.3 Rayleigh lengths during the full 50 ns expansion window, showing a strong optimum at 50 ns, with no protons observed at either temporal extreme. Since the scale length is ever increasing with expansion time, an optimal scale length clearly exists.

Simulations were carried out to model the experimental conditions, which demonstrated proton acceleration through a novel scheme based on the formation of a plasma grating structure. The pulse conditions were such that the incident laser reflects off the critical surface, forming a standing wave and inducing periodic density modulations in the ramp preceding the critical surface. It was found that the ramp profile and laser conditions

strongly influenced the formation of these structures, with the idealised case being the formation of a just over-critical density bunch, with $n_e \gtrsim n_c$, coinciding with the peak of the laser pulse. In these conditions, the limited mass of the grating element, coupled with the high laser intensity, facilitates strong RPA of the entire grating element, coupled with reflection of upstream protons to high energies.

Given the sensitivity of the formation of these structures to the experimental parameters, notably the laser intensity and target density profiles, optimal ramp conditions are observed for a given experimental scenario. The ideal case is the formation of a near critical density grating structure coinciding with the time of the peak of the laser pulse to ensure the maximum accelerating force is felt. For the laser conditions relevant to the experimental results presented, an optimal scale length of $\sim$20 µm was found. This is significantly shorter than measured through interferometry prior to the arrival of the main pulse, and also shorter than those predicted through the analytical Sedov-Taylor blast wave scaling. However, simulations demonstrated that the presence of 25 ps pre-pulses result in density steepening. For the highest observed proton energies, these showed that the analytically predicted density scale lengths shortened from $\sim$90 µm to $\sim$20 µm; the optimum case predicted from simulations.

7.2.1 Limitations of the acceleration scheme

While this induced density modulation phenomenon provides the opportunity for enhanced ion energies, the scheme is limited in its applicability. As stated previously, for the effective formation of the grating structure, two conditions must be simultaneously met. The intensity of the incident laser pulse must be low enough that the critical surface does not appreciably move, ensuring the ions have sufficient time to respond and form the grating. High intensity leads to a faster ion response and shorter formation time, but as this increases the critical surface moves sooner in the laser pulse such that the nodes in the standing wave are not spatially fixed but move; the grating structure cannot form. The intensity condition is a necessarily a compromise. Longer pulses are more suitable given a gradual intensity increase occurs over a long enough time for the grating structure to form.

The conditions for the experimental results presented in Chapter 5 met these requirements. In fact, simulations suggest relatively small changes in the laser parameters would result in this process not occurring. As presented, for an increase in a_0 from 0.62 to 1.45, equivalent to the total measured energy to the chamber contained within the focal spot within a single pulse, the intensity is such that the grating cannot efficiently form. In this case, the intensity increases too quickly and reaches a point where the critical surface begins moving too early in the process. Here, the nodes of the standing wave are not long enough lived to allow the formation of the density structures. In this case, electrons and ions from the ramp are piled up at the initial critical surface under the action of the laser and an effective zero ramp situation occurs. Acceleration occurs

at the front surface of a relatively high density, thick plasma. This is unlike acceleration off the grating structures, which are accelerated into a significantly lower background density, producing higher energies.

Simulations also suggest the scale length must be sufficiently short that only a few over-critical density bunches form, to coincide with the arrival of the peak of the pulse. For longer ramps, too much energy is given up to the formation of the grating and the relative density between the grating element and the background is not sufficient to assist in effective acceleration to high energies.

The work presented in Chapter 5 was concerned with the use of a relatively long wavelength CO_2 laser. While the effect presented here would not be limited to these wavelengths in theory, its application at near-IR would be challenging. Bunch formation occurs every half laser wavelength, with ramps exceeding a few laser wavelengths inefficient for acceleration. Production of these necessarily extremely short scale lengths is challenging and not achievable with the current target shaping method. It might, however, be possible to produce a suitable density profile at the front surface of a target through low intensity pre-heating and subsequent expansion.

Considering the above, target shaping through control of the incident laser pulse temporal profile could perhaps provide the opportunity to utilise this effect at higher intensities. Recent developments to the ATF CO_2 laser have resulted in a significant decrease in the laser pulse duration to 3.5 ps, with further plans to decrease this to 2 ps; too short for stable grating formation. It should be noted that this is confirmed by the lack of this feature in the results presented in Chapter 4. Control of the temporal profile of the laser pulse, with the addition of a low intensity pedestal preceding a shorter, intense pulse could facilitate stable grating formation and subsequent acceleration at higher laser intensities. Despite this possibility, it is obvious that a fundamental limit in the applicability of this scheme exists, limiting it to near critical density interactions. Reflection off the critical surface to produce the standing wave imposes a restriction on the initial density of the plasma from which a grating element can be formed, with $n_e \lesssim n_c$. Since the finite level of density exists within one half period of the standing wave and the structure thickness tends to the electron skin depth, a fundamental limit is imposed on the achievable peak density of a given structure. A transition to even longer wavelengths would help, as shown by the estimated peak density given by equation 5.1. The peak density scales with the incident laser wavelength, as a greater volume of plasma is then contained within one half laser wavelength. In practice, however, this is not a feasible solution, since no high power lasers exist at these wavelengths. As such, for appropriately high intensities, the structure will not remain sufficiently overcritical and HB-RPA can no longer occur. This applies to both the CO_2 laser or near-IR wavelengths.

One potential solution to this problem is the use of temporal laser pulse shaping. The grating formation is dependent on the incident laser intensity being low enough not to

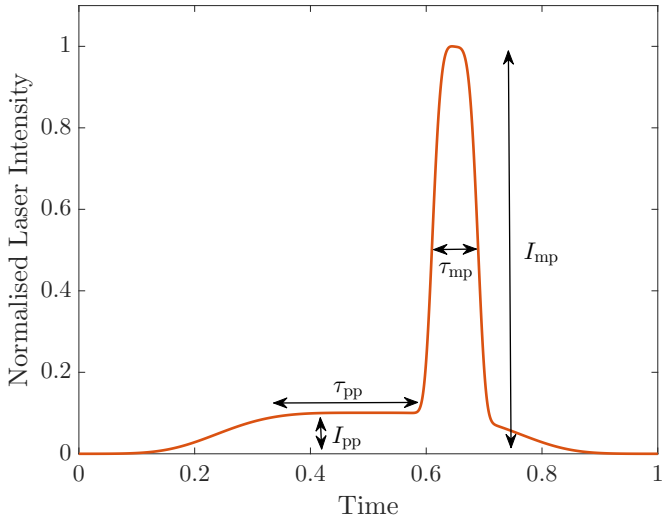


Figure 7.2: Example shaped temporal pulse structure for the ATF CO_2 beam to optimise the formation of a plasma grating structure for subsequent ion acceleration.

accelerate the critical surface too early, before the grating structure is formed. While at very high a_0 the density will still be below n_c, this acceleration scheme could be extended to include higher intensities through use of a low intensity pedestal preceding the main pulse. Through control of the intensity and temporal duration of this portion of the beam, a stable grating structure could be formed, before a short, high intensity pulse arrives, accelerating these grating elements to high velocities and producing high energy proton beams. An example possible laser temporal profile is shown in figure 7.2. Through control of the ratio of I_{pp}/I_{mp}, and the pedestal duration, τ_{pp}, it would be possible to control the grating formation. For a given target density profile, these conditions could be optimised to maximise the achievable proton energy. As an example, consider the case of the expected future ATF beam conditions after the addition of isotopic CO_2 into the main amplifier. A ~ 2 ps pulse is expected with up to 6 J of energy. Here, no grating structure could form without the use of pulse shaping to introduce a lower intensity pedestal given the predicted peak intensities of $\sim 3 \times 10^{17}\,\mathrm{Wcm^{-2}}$. This pedestal would comprise of a pulse a few picoseconds in duration and with an intensity of the order $10^{15}\,\mathrm{Wcm^{-2}}$. Subsequent to this, the intense, 2 ps pulse could be used to accelerate the already formed grating.

Production of these shaped pulses is believed to be possible at the ATF. By limiting the horizontal size of the dispersed beam in the stretcher with a hard aperture, the sharp edges in the spectrum should result in secondary peaks in the time domain. This can be thought of as analogous to the intensity distribution observed by Fraunhofer diffraction from a single slit [111]. It is hoped that experiments to test out this pulse shaping, and its ability to form these grating structures, can be carried out in the future at the ATF.

7.3 Colliding blast waves to produce thin gas targets

As already summarised, Chapter 4 demonstrated that radiation pressure acceleration of protons was possible at near-critical densities with a mid-IR wavelength CO_2 laser. Further to this, Chapter 5 showed that through modification of the target density profile, enhanced acceleration was possible from limited areal density structures. However, the formation of this modified density profile is intricately linked to the acceleration, owing to its formation during the foot of the laser pulse. The requirements for the laser conditions to facilitate effective formation of the grating structure in turn places restrictions on the accelerating pulse. Therefore, decoupling of the two effects is desirable to optimise both the grating formation and the acceleration conditions.

As such, Chapter 6 was motivated by the desire to produce thin, near-critical density gas targets independently from the CO_2 pulse. This chapter presented work relating to the collision between two blast waves, to favourably modify the target density profile. The experiment, much like in Chapter 5, used the heating of stainless steel foils placed at the edge of the gas flow to launch the strong shocks. However, unlike previously, two counter-propagating shocks were launched from the front and rear of the gas jet. The expansion time of the shocks relative to the main CO_2 pulse could be varied, allowing the separation between the shocks to be changed. In the extreme case, the shocks were allowed to expand to the point of collision. The expansion dynamics were studied for two initial gas profiles, with peak, unperturbed electron densities of $4 \times 10^{18}\,\mathrm{cm}^{-3}$ and $7.4 \times 10^{18}\,\mathrm{cm}^{-3}$. Retrieval of the shock density profiles was challenging, due to a number of issues relating to the poor quality of the experimentally obtained interferometric data. As such, only estimates of the shock density profile could be achieved. These were based on interpolation from the information obtained from regions in which the plasma profile was well resolved. The shock expansion was shown to be in the strong shock limit, suggesting the density in the case of no collision was underestimated by more than a factor of 5. For the case of collision, the peak shock density was expected to be under-resolved by a factor of ~ 8. Through fitting to the density profile in the well resolved regions preceding the peak of the shock, and interpolation over the unresolved regions, the thickness of the collision structure could be estimated. This was shown to be $\sim$85 µm.

Spectral peaking of the proton energy trace was again observed, due to hole-boring acceleration, with the highest observed proton energy being $\sim 1.3\,\mathrm{MeV}$. The maximum proton energy scaling was also studied as a function of shock expansion, with increasing energy observed with the shock radius. The highest energies were found for the case of the colliding shocks. This result is difficult to explain given the $E_p = 4I/n_i c$ scaling for hole-boring and the expected increasing shock density with expansion radius. However, simulations indicate the primary acceleration is again from an induced plasma grating structure, as described in Chapter 5. It was suggested that the increasing blast wave radius results in more favourable density conditions approaching the criti-

cal surface, resulting in more optimal grating formation and better proton acceleration conditions.

As demonstrated, the creation of colliding shock structures can enhance the proton acceleration conditions, producing higher energies. The work in Chapter 6 was intended as a preliminary run, at the end of another experiment, to test the validity of this approach. It is most likely not possible to create micron level targets on the order of 10's microns with this scheme. As demonstrated, however, even the experimentally produced thin structures offer enhancement of the observed energies. Future work would necessarily first better study the collision dynamics between these shocks, given the lack of available information from the presented experiment. This would allow more information about the target profile to be inferred. These experiments are planned at Imperial College in the near future. Subsequently, this would permit more accurate control of the main pulse interaction conditions, and future ion acceleration experiments to better study their effects. Different size gas jets could also be used, to vary the shock radius before expansion and allow the creation of variable scale length shocks. This might allow a more systematic study of the effect of the scale length for these relatively thin gas targets.

Other schemes could also be employed to provide alternative target shaping methods. One possible suggestion is the use of two, weakly focussed beams transverse to the main laser pulse, horizontally displaced by varying degrees. In this scheme, the long Rayleigh length of the beams would create two cylindrical blast waves, which would expand out radially and collide. With a suitably narrow gas jet, these could be positioned and the energy selected, such that they expand and collide in the centre of the jet with only a very low density plasma preceding the critical surface. Through careful selection of the target and laser conditions, this might facilitate the creation of more optimised targets.

7.3.1 Effect of a rear surface density ramp

The process of using colliding blast waves to produce thin gas targets necessarily also modifies the density profile at the rear of the target. In a radiation pressure driven scheme, the benefit of using thin plasma slabs lies predominantly in the reduced mass that the laser is required to accelerate, with less upstream material to resist the spatially driven critical surface. In the extreme limit of very thin targets, bulk motion of the whole target can occur.

However, in reality the experimentally produced density profiles are not perfect slabs. For single blast waves, the scale length at the front of the shock is approximately the mean free path of the ions, in this case on the order of $\sim$1 µm. This drops to the level of the upstream density, before following the gas density profile, which itself has a scale length of around 0.5 mm from the centre of the gas jet. For the case of colliding blast

waves, the density profile at the target rear is not so clear, but might be expected to form with a scale length equivalent to that of the incident shock counter-propagating with the laser. Analytically this was predicted to be ∼80 µm.

Section 6.4.3 suggested that, for thin slabs at the experimentally relevant and higher currently available intensities, sheath effects would dominate due to heating, especially for linear polarisation. Two potential solutions exist to ensure RPA is dominant. First, increasing the intensity would ensure that the radiation pressure is sufficient to overcome any target expansion effects. Secondly, rear surface scale lengths have previously been suggested to be beneficial to the ion acceleration process in terms of both the maximum energy observed and maintaining low energy spread spectral features. Reflection of upstream ions off a potential occurs as the shock structure propagates through the plasma, with the final velocity of an ion, v_{ion}, taking the form $v_{ion} = 2v_{shock} + v_0$, where v_0 is the upstream ion velocity. Typical plasma expansion at the rear target surface creates a sheath field, which induces a broad range of upstream ion velocities, v_0 [157], broadening the energy spectrum. The presence of an exponential plasma profile with a given ion density scale length, L_∇, was shown to modify the plasma expansion. In the case of sheath acceleration, Grismayer and Mora [275] demonstrated the final ion velocity decreases with L_∇ for the case of scale lengths greater than a few percent of the slab thickness, with the expansion slowed and the sheath fields suppressed. For acceleration dominated by the sheath expansion this is undesirable. However, for the case of shock accelerated ion beams in which mono-energetic features are expected to be observed, the sheath structure at the target rear surface have the potential to inhibit mono-energetic features due to a broad range of initial ion velocities; suppression of the sheath expansion is desirable.

The effect of such a rear density gradient has been studied specifically for the case of collisionless shock acceleration. Work by Fiuza et al. [156] demonstrated an optimal rear scale length for efficient electron heating and ion reflection, given $L_\nabla \approx \sqrt{m_i/m_e}\lambda_L/2$. The work was developed further, again by Fiuza et al. [161], which clearly showed the suppression of the sheath field due to a rear density ramp and its effect on the energy spread of accelerated ions. This work was furthered by Boella et al. [276], who identified a relation for the plasma scale length that can be used to identify regimes in which the fraction of reflected ions and the energy spread can be optimised. The authors demonstrated an optimal scale length, independent of the plasma temperature, $L_\nabla^{opt} = \pi c/\omega_{p_i}$. This minimises the energy spread of a shock accelerated beam. Conversely, in the limit $L_\nabla \ll L_\nabla^{opt}$, the reflected particle flux is maximised. The experimental proton acceleration results presented by Haberberger et al. [167] demonstrated the presence of an exponential density ramp at the rear of their gas target, and likely helped in the production of their reported low ($\sim$ 1%) energy spread, but also very low flux ($< 10^7$ protons/MeV/sr), proton beam.

Clearly then, a decaying density profile at the target rear surface has the potential to

influence the proton acceleration. In the colliding blast wave case presented earlier in this chapter, such features are expected, although their level of influence on the shock driven acceleration might reasonably be expected to depend on the thickness of the central overdense region of the target. The experimental conditions in this case differs from the work with collisionless shocks given hole-boring RPA is thought to be the dominant acceleration mechanism. However, should it be possible to produce suitably thin collision structures, with sufficient control over the front and rear surface scale lengths, these targets may make it practical for the experimental study of the effect of a rear surface scale length on the energy spread. With an increase in target density and appropriately low laser intensities, such that the equality given in equation 2.74 is not satisfied, it is possible to create a set of conditions in which ion acceleration is expected to be dominated by a collisionless shock structure. In this case, sufficient control of the target conditions would in theory allow manipulation of the ion beam flux and energy spread. Studies of this nature will be important, with control of these ion beam features crucial for any future applications.

One final point of note is that this effect should also be expected to occur for hole-boring driven acceleration, although for this to be relevant, the critical surface would need to reach the expansion region while still being driven by the laser. This places stricter restrictions on the maximum target thickness. In this case, using the same arguments as in [156], an expression for the maximum ion energy, accounting for the sheath expansion, can be obtained

$$E_i = \frac{1}{2} m_i \left(\frac{2(1+R) I_L}{n_i c} + \frac{k_B T_e \tau_{acc}}{m_i L_\nabla} \right)^2 \tag{7.1}$$

where τ_{acc} is the time at which acceleration of upstream ions occurs.

7.4 Concluding remarks

This thesis has described experimental results of interactions involving a CO_2 laser with near-critical density gas targets, with the intention of studying shock driven acceleration of protons. The unique nature of this high power, mid-IR laser made possible the study of these effects with gas targets. This is due to the favourable scaling of the critical plasma density; over-dense gas targets are only now just being realised for the much more common near-IR wavelengths. Gas targets offer a pathway to high repetition rate, single species operation, crucial for many applications such as hadron therapy. While the energies demonstrated from the current experiments are modest, at the MeV level, the conditions still allow the study of the underlying mechanisms and verification of the predicted theoretical scaling under these conditions, as demonstrated in Chapter 4. Furthermore, these conditions have facilitated the discovery of novel acceleration schemes, as in Chapter 5.

However, with the planned upgrades to the ATF, and the subsequent ATF-II facility predicted to start operation in the not too distant future, it will soon be possible to investigate new intensity regimes and with them, achieve higher ion energies. With this, the ability to now produce over-critical density gas targets for near-IR laser wavelengths will provide the opportunity to take this work further, opening up experiments on a much larger number of laser systems. As a result, experiments of this nature are planned on the VULCAN laser system in the near future. Clearly then, the future holds many interesting and exciting opportunities to further study these ion acceleration interactions. Furthermore, with the possibility to study these effects at higher intensities, it may soon be possible to produce ion beams with the required parameters to be relevant to a number of applications, for example hadron therapy. Finally, perhaps, the use of of laser-driven ion beams in real-world applications is in reach.

A The Debye Length

Assume a perfectly neutral volume of plasma i.e. $n_e = Zn_i$. This is a simple case since there are no net fields or currents. Now we introduce a positive test charge; this induces the relatively massless electrons neighbouring the charge to move towards it, shielding the electric field of the charge and thus minimising the potential energy of the system. This ensures that while the charge in the plasma is not homogeneous, it maintains overall quasi-neutrality. For the sake of simplicity, one can also assume that because the ion mass is much greater than that of the electrons, they do not have time to move before the field created by the test charge is shielded. This allows for the assumption $\mathrm{n_i} = \mathrm{n_0}$.

Consider the ideal case where the plasma is cold i.e. $T_e = T_i = 0$. This would have one important implication; the fields would be perfectly shielded, since there are no thermal fluctuations in the plasma.

Let us now assume the plasma has a temperature $T \neq 0$. Now there are thermal effects in the plasma and a Boltzmann distribution is required to describe the density of electrons,

$$n_e = n_0 e^{-\frac{E}{k_B T_e}} = n_0 e^{\frac{e\phi}{k_B T_e}} \tag{A.1}$$

One can use Poission's equation to calculate the electric potential, ϕ,

$$\nabla^2 \phi = -\frac{\rho}{\epsilon_0} = -\frac{(Zn_i e - n_e e)}{\epsilon_0} \tag{A.2}$$

Through substitution of A.1 into A.2 while remembering the earlier assumptions that $n_0 = Zn_i$ and assuming spherical geometry

$$\frac{1}{r^2}\frac{\mathrm{d}}{\mathrm{d}r}(r^2 \frac{\mathrm{d}}{\mathrm{d}r})\phi = \frac{-e}{\epsilon_0}\left[n_0 - n_0 e^{\frac{e\phi}{k_B T_e}}\right] \tag{A.3}$$

Except when very close to the test charge, we can assume $e\phi \ll k_B T_e$ since the potential energy is significantly smaller than the thermal kinetic energy at large distances. Therefore, one can make the expansion $e^{\frac{e\phi}{k_B T_e}} \backsimeq 1 + \frac{e\phi}{k_B T_e}$, giving

$$\frac{-e}{\epsilon_0}\left[n_0 - n_0 - \frac{n_0 e\phi}{k_B T_e}\right] = \frac{n_0 e^2}{\epsilon_0 k_B T_e}\phi \tag{A.4}$$

If one now considers the behaviour of the system in its limiting cases, there are two scenarios that need consideration.

1. If the distance from the test charge is large ($r \to \infty$), then $\phi \to 0$.
2. If the distance to the test charge is small ($r \to 0$), then the test charge looks like a point charge in the plasma and one sees the normal, unshielded potential $\phi \to \frac{q}{4\pi\epsilon_0 r}$

The result of these boundary conditions is to suggest a trial solution of the form $\phi = \frac{q}{4\pi\epsilon_0}\frac{1}{r}e^{\frac{-r}{\lambda}}$. Therefore, one can say

$$\frac{1}{r^2}\frac{\mathrm{d}}{\mathrm{d}r}(r^2\frac{\mathrm{d}}{\mathrm{d}r})\phi = \alpha\phi \tag{A.5}$$

where $\alpha = \frac{n_0 e^2}{\epsilon_0 k_B T_e}$. This is equivalent to

$$\frac{\mathrm{d}^2}{\mathrm{d}r^2}r\Phi = \alpha r\Phi \tag{A.6}$$

By substituting $\Phi = r\phi$, the trial solution becomes $\Phi = \frac{q}{4\pi\epsilon_0}e^{\frac{-r}{\lambda}}$

$$\frac{\mathrm{d}^2}{\mathrm{d}r^2}r\Phi = \frac{1}{\lambda^2}\frac{q}{4\pi\epsilon_0}e^{\frac{-r}{\lambda}} = \frac{n_0 e^2}{\epsilon_0 k_B T_e}\frac{q}{4\pi\epsilon_0}e^{\frac{-r}{\lambda}} \tag{A.7}$$

Therefore, $\frac{1}{\lambda^2} = \frac{n_0 e^2}{\epsilon_0 k_B T_e}$ and so we get our results for the Debye Length, λ_D

$$\lambda_D = \left(\frac{\epsilon_0 k_B T_e}{n_0 e^2}\right)^{\frac{1}{2}} \tag{A.8}$$

B Normalised Vector Potential and Laser Intensity

The normalised vector potential can be related to the intensity of a laser pulse through the use of the Poynting vector, which gives the rate of energy transfer by an electromagnetic wave

$$\vec{S} = \frac{1}{\mu_0}(\vec{E} \times \vec{B}) \tag{B.1}$$

Taking a linearly polarised plane wave, with $\vec{E} = E_0 sin(kz - \omega t)\hat{x}$ and $\vec{B} = B_0 sin(kz - \omega t)\hat{y}$, the Poynting vector can be rewritten as

$$|\vec{S}| = \frac{1}{\mu_0} E_0 B_0 sin^2(kz - \omega t) \tag{B.2}$$

Using the relation $B_0 = \frac{E_0}{c}$,

$$|\vec{S}| = \frac{1}{\mu_0 c} E_0^2 sin^2(kz - \omega t) = \epsilon_0 c E_0^2 sin^2(kz - \omega t) \tag{B.3}$$

The time averaged energy flow is therefore

$$\langle \vec{S} \rangle = \frac{\epsilon_0 c E_0^2}{2} \tag{B.4}$$

It should be noted the same applies for a circularly polarised laser. In this case, the electric and magnetic field components are the superposition of x and y components i.e. $\vec{E} = E_0 sin(kz - \omega t)\hat{x} + E_0 cos(kz - \omega t)\hat{y}$ and $\vec{B} = B_0 cos(kz - \omega t)\hat{x} + B_0 sin(kz - \omega t)\hat{y}$. Therefore, $\vec{S} = \frac{1}{\mu_0}(E_x B_y - E_y B_x)\hat{z}$ and following through $\langle \vec{S} \rangle = \epsilon_0 c E_0^2$.
Given the intensity is equal to the time averaged energy flow ($I_L = \langle \vec{S} \rangle$), it can also be equated to the peak electric field of the laser. This is the case for both types of polarisation, the only difference being the peak electric field oscillates in the linear case, while it is constant for circular polarisation. Therefore, the time averaged field magnitudes are found to be $\frac{E_0}{2}$ and E_0 for linear and circular polarisations, respectively. The time aveage of the normalised vector potential, squared, therefore differs for the two polarisations and takes the form (remembering $\langle a^2 \rangle \propto I_L$), for linear and circular

polarisation, respectively

$$\langle a^2 \rangle = \frac{a_0^2}{2} \rightarrow a_0^2 = 2\langle a^2 \rangle \rightarrow a_0 \propto \sqrt{2I_L} \tag{B.5}$$

$$\langle a^2 \rangle = a_0^2 \rightarrow a_0^2 = \langle a^2 \rangle \rightarrow a_0 \propto \sqrt{I_L} \tag{B.6}$$

These can be rewritten, respectively, as

$$a_0 \backsim 0.85(I_{10^{18}}\lambda_\mu^2)^{\frac{1}{2}} \tag{B.7}$$

$$a_0 \backsim 0.66(I_{10^{18}}\lambda_\mu^2)^{\frac{1}{2}} \tag{B.8}$$

C Single Particle Motion

Consider an electron within an electromagnetic field. Whether an electric or magnetic field, the electron will feel a force given by equation 2.55. Ions need not be considered given there relatively large mass; their movement within the timescales considered can be assumed negligible.

If a laser propagates in the z-direction, the E-field can be written as $\vec{E}(x,t) = \vec{E}_x e^{i(kz-\omega t)}\hat{x}$. From Faraday's law, $\vec{E}$, $\vec{B}$ and $\vec{k}$ are shown to be orthogonal and it can also be said that $\vec{B}(y,t) = \vec{B}_y e^{-i(kz-\omega t)}\hat{y}$. From 2.55, the equations of motion are given by

$$\begin{aligned} m\dot{v}_x &= -eE_x \cos(kz-\omega t) \\ m\dot{v}_y &= 0 \\ m\dot{v}_z &= -ev_x B_y \cos(kz-\omega t) \end{aligned} \tag{C.1}$$

Integrating the above expression, a result for v_x can be found to be $v_x = \frac{eE_x}{m\omega}\sin(kz-\omega t)$, or equivalently $v_x = a_0 c \sin(kz-\omega t)$. Here, a_0 is the normalised vector potential

$$a_0 = \frac{v}{c} = \frac{eE_0}{m_e \omega c} \tag{C.2}$$

The normalised vector potential (also sometimes called the normalised momentum) is another method of comparing laser pulses. It gives a measure of the electron response to the laser's electromagnetic field, or in other words, the 'strength' of a laser pulse. It can be related to the laser intensity for linear and circular polarisation, respectively, through

$$\begin{aligned} I &= \frac{1}{2} n_c m_e c^3 {a_0}^2 \\ I &= n_c m_e c^3 {a_0}^2 \end{aligned} \tag{C.3}$$

Similarly, the relation can be expressed as (see Appendix B)

$$a_0 \backsim 0.85 (I_{10^{18}} \lambda_{\mu m}^2)^{\frac{1}{2}} \tag{C.4}$$

$$a_0 \backsim 0.6 (I_{10^{18}} \lambda_{\mu m}^2)^{\frac{1}{2}} \tag{C.5}$$

for linear and circular polarisation, respectively.

Now, returning to single particle motion and considering the z-component of the equation of motion, substituting for v_x

$$m\dot{v}_z = -ev_x a_0 cB_y \sin(kz-\omega t)\cos(kz-\omega t) = -\frac{ev_x a_0 cB_y}{2}\sin[2(kz-\omega t)]$$

$$\dot{v}_z = -\left(\frac{a_0^2 c\omega}{2}\right)\sin[2(kz-\omega t)]$$

$$v_z = -\left(\frac{a_0^2 c}{4}\right)\cos[2(kz-\omega t)] + constant$$

Consider the initial case, where $v_x = v_z = 0$. From this, we can say

$$v_z = \left(\frac{a_0^2 c}{4}\right)(1-\cos[2(kz-\omega t)])$$

$$v_z = \left(\frac{a_0^2 c}{4}\right)\sin^2(kz-\omega t)$$

This gives the velocity components as

$$\begin{aligned} v_x &= a_0 c\sin(kz-\omega t) \\ v_y &= 0 \\ v_z &= \left(\frac{a_0^2 c}{4}\right)\sin^2(kz-\omega t) \end{aligned} \tag{C.6}$$

These show that the velocity components are parabolic tracks, with $v_z = \frac{v_x^2}{2}$. This means that the larger the transverse motion, the greater the acceleration of the electron in the direction of laser propagation. The components of the electron motion are found by integration, giving

$$\begin{aligned} x &= \frac{a_0 c}{\omega}(1-\cos(kz-\omega t)) \\ y &= 0 \\ z &= (\frac{a_0^2 c}{4})t - (\frac{a_0^2 c}{8\omega})\sin 2(kz-\omega t) \end{aligned} \tag{C.7}$$

Bibliography

[1] F. Braun, "On a process for the display and study of the course in time of variable currents (in German)," *Annalen der Physik*, vol. 296, no. 3, pp. 552–559, 1897. 3

[2] J. D. Cockroft and E. T. S. Watson, "Experiments with High Velocity Positive Ions (I). Further Developments in the method of obtaining High Velocity Positive Ions," *Proc. Roy. Soc. Lond. A*, vol. 136, pp. 619–630, 1932. 3

[3] J. D. Cockroft and E. T. S. Walton, "Experiments with High Velocity Positive Ions (II). The Disintegration of Elements by High Velocity Protons," *Proc. Roy. Soc. Lond. A*, vol. 137, pp. 229–242, 1932. 3

[4] M. Weiss, "Introduction to RF linear accelerators," *Proc. CAS*, vol. CERN 94-01, p. 105, 1994. 3

[5] R. J. England, R. J. Noble, Z. Wu, and M. Qi, "Dielectric Laser Acceleration," vol. 86, no. December, pp. 1337–1389, 2014. 4

[6] T. Tajima and J. Dawson, "Laser Electron Accelerator," *Physical Review Letters*, vol. 4, no. 4, pp. 267–270, 1979. 4

[7] D. Strickland and G. Mourou, "Compression of Amplified Chirped Optical Pulses," *Optics communications*, vol. 56, no. 3, pp. 219–221, 1985. 4

[8] A. Modena, Z. Najmudin, A. E. Dangor, C. E. Clayton, K. A. Marsh, C. Joshi, V. Malka, C. B. Darrow, C. Danson, D. Neely, and F. N. Walsh, "Electron acceleration from the breaking of relativistic plasma waves," 1995. 4

[9] E. Esarey, S. P., J. Krall, and A. Ting, "Review of Plasma-Based Accelerator Concepts," *IEEE Transactions on Plasma Science*, vol. 24, no. 2, p. 252, 1996. 4

[10] S. P. D. Mangles, C. D. Murphy, Z. Najmudin, A. G. R. Thomas, J. L. Collier, A. E. Dangor, E. J. Divall, P. S. Foster, J. G. Gallacher, C. J. Hooker, D. A. Jaroszynski, A. J. Langley, W. B. Mori, P. A. Norreys, F. S. Tsung, R. Viskup, B. R. Walton, and K. Krushelnick, "Monoenergetic beams of relativistic electrons from intense laserplasma interactions," *Nature*, vol. 431, no. 7008, pp. 535–538, 2004. 4

[11] W. P. Leemans, B. Nagler, A. J. Gonsalves, C. Tóth, K. Nakamura, C. G. R. Geddes, E. Esarey, C. B. Schroeder, and S. M. Hooker, "GeV electron beams

from a centimetre-scale accelerator," *Nature Physics*, vol. 2, no. 10, pp. 696–699, 2006. 4

[12] V. Malka, J. Faure, Y. A. Gauduel, E. Lefebvre, A. Rousse, and K. T. Phuoc, "Principles and applications of compact laser plasma accelerators," *Nature Physics*, vol. 4, no. 6, pp. 447–453, 2008. 4

[13] X. Wang, R. Zgadzaj, N. Fazel, Z. Li, S. A. Yi, X. Zhang, W. Henderson, Y.-Y. Chang, R. Korzekwa, H.-E. Tsai, C.-H. Pai, H. Quevedo, G. Dyer, E. Gaul, M. Martinez, A. C. Bernstein, T. Borger, M. Spinks, M. Donovan, V. Khudik, G. Shvets, T. Ditmire, and M. C. Downer, "Quasi-monoenergetic laser-plasma acceleration of electrons to 2 GeV.," *Nature communications*, vol. 4, p. 1988, jan 2013. 4

[14] A. Caldwell, K. Lotov, A. Pukhov, and F. Simon, "Proton-driven plasma-wakefield acceleration," *Nature Physics*, vol. 5, pp. 363–367, apr 2009. 5

[15] W. I. Linlor, "Ion energies produced by laser giant pulse," *Applied Physics Letters*, vol. 3, no. 11, pp. 210–211, 1963. 5

[16] S. J. Gitomer, R. D. Jones, F. Begay, A. W. Ehler, J. F. Kephart, and R. Kristal, "Fast ions and hot electrons in the laserplasma interaction," *Physics of Fluids*, vol. 29, no. 8, p. 2679, 1986. 5

[17] A. P. Fews, P. A. Norreys, F. Beg, A. R. Bell, A. E. Dangor, C. N. Danson, P. Lee, and S. J. Rose, "Plasma Ion Emission from High Intensity Picosecond Laser Pulse Interactions with Solid Targets," *Physical Review Letters*, vol. 73, no. 13, p. 1801, 1994. 5

[18] F. N. Beg, A. R. Bell, A. E. Dangor, C. N. Danson, A. P. Fews, M. E. Glinsky, B. A. Hammel, P. Lee, P. A. Norreys, and M. Tatarakis, "A study of picosecond laser solid interactions up to," *Physics of Plasmas*, vol. 4, no. 2, pp. 447–457, 1997. 5

[19] E. L. Clark, K. Krushelnick, J. R. Davies, M. Zepf, M. Tatarakis, F. N. Beg, A. Machacek, P. A. Norreys, M. I. K. Santala, I. Watts, and A. E. Dangor, "Measurements of energetic proton transport through magnetized plasma from intense laser interactions with solids," *Physical review letters*, vol. 84, pp. 670–673, jun 2000. 5

[20] E. L. Clark, K. Krushelnick, J. R. Davies, M. Zepf, M. Tatarakis, F. Beg, A. Machacek, P. A. Norreys, M. I. K. Santala, I. Watts, and A. E. Dangor, "Measurements of energetic proton transport through magnetized plasma from intense laser interactions with solids," *Physical Review Letters*, vol. 84, no. 4, p. 670, 2000. 5, 39, 40

[21] R. A. Snavely, M. H. Key, S. P. Hatchett, T. E. Cowan, M. Roth, T. W. Phillips, M. A. Stoyer, E. A. Henry, T. C. Sangster, M. S. Singh, S. C. Wilks, A. MacKinnon, A. Offenberger, D. M. Pennington, K. Yasuike, A. B. Langdon, B. F. Lasinski, J. Johnson, M. D. Perry, and E. M. Campbell, "Intense high-energy proton beams from Petawatt-laser irradiation of solids.," *Physical Review Letters*, vol. 85, p. 2945, oct 2000. 5, 40, 42

[22] S. C. Wilks, A. B. Langdon, T. E. Cowan, M. Roth, M. Singh, S. Hatchett, M. H. Key, D. Pennington, A. MacKinnon, and R. A. Snavely, "Energetic proton generation in ultra-intense lasersolid interactions," *Physics of Plasmas*, vol. 8, no. 2, p. 542, 2001. 5, 39, 61

[23] H. Daido, M. Nishiuchi, and A. S. Pirozhkov, "Review of laser-driven ion sources and their applications," *Reports on Progress in Physics*, vol. 75, no. 5, p. 056401, 2012. 5

[24] A. Macchi, M. Borghesi, and M. Passoni, "Ion acceleration by superintense laser-plasma interaction," *Reviews of Modern Physics*, vol. 85, no. 2, pp. 751–793, 2013. 5

[25] F. Wagner, O. Deppert, C. Brabetz, P. Fiala, A. Kleinschmidt, P. Poth, V. A. Schanz, A. Tebartz, B. Zielbauer, M. Roth, T. Stöhlker, and V. Bagnoud, "Maximum Proton Energy above 85 MeV from the Relativistic Interaction of Laser Pulses with Micrometer Thick CH2 Targets," *Physical Review Letters*, vol. 116, no. 20, p. 205002, 2016. 5, 44

[26] T. Cowan, J. Fuchs, H. Ruhl, A. Kemp, P. Audebert, M. Roth, R. Stephens, I. Barton, A. Blazevic, E. Brambrink, J. Cobble, J. Fernández, J.-C. Gauthier, M. Geissel, M. Hegelich, J. Kaae, S. Karsch, G. Le Sage, S. Letzring, M. Manclossi, S. Meyroneinc, A. Newkirk, H. Pépin, and N. Renard-LeGalloudec, "Ultralow Emittance, Multi-MeV Proton Beams from a Laser Virtual-Cathode Plasma Accelerator," *Physical Review Letters*, vol. 92, p. 204801, may 2004. 5, 43

[27] IRS, "IRS Barrel of oil equivalent energy value." 6

[28] J. Wesson, *Tokamaks*. Oxford: Claredon Press, 1987. 6

[29] C. Llewellyn-Smith and D. Ward, "Fusion power," *European Review*, vol. 13, no. 3, pp. 337–359, 2005. 6

[30] J. Nuckolls, L. Wood, A. Thiessen, and G. Zimmerman, "Laser Compression of Matter to Super-High Densities: Thermonuclear (CTR) Applications," *Nature*, vol. 239, pp. 139–142, 1972. 6

[31] J. Lindl, "Development of the indirectdrive approach to inertial confinement fusion and the target physics basis for ignition and gain," *Physics of Plasmas*, vol. 2, no. 11, pp. 3933–4024, 1995. 6

[32] M. Roth, T. Cowan, M. Key, S. Hatchett, C. Brown, W. Fountain, J. Johnson, D. Pennington, R. Snavely, S. Wilks, K. Yasuike, H. Ruhl, F. Pegoraro, S. Bulanov, E. Campbell, M. Perry, and H. Powell, "Fast Ignition by Intense Laser-Accelerated Proton Beams," *Physical Review Letters*, vol. 86, pp. 436–439, jan 2001. 6

[33] M. H. Key, "Status of and prospects for the fast ignition inertial fusion concept," *Physics of Plasmas*, vol. 14, no. 5, 2007. 6

[34] R. Kodama, P. A. Norreys, K. Mima, A. E. Dangor, R. G. Evans, H. Fujita, Y. Kitagawa, K. Krushelnick, T. Miyakoshi, N. Miyanaga, T. Norimatsu, S. J. Rose, T. Shozaki, K. Shigemori, A. Sunahara, M. Tampo, K. A. Tanaka, Y. Toyama, T. Yamanaka, and M. Zepf, "Fast heating of ultrahigh-density plasma as a step towards laser fusion ignition," *Nature*, vol. 412, no. 6849, pp. 798–802, 2001. 6

[35] R. Kodama, H. Shiraga, K. Shigemori, Y. Toyama, S. Fujioka, H. Azechi, H. Fujita, H. Habara, T. Hall, Y. Izawa, T. Jitsuno, Y. Kitagawa, K. M. Krushelnick, K. L. Lancaster, K. Mima, K. Nagai, M. Nakai, H. Nishimura, T. Norimatsu, P. A. Norreys, S. Sakabe, K. A. Tanaka, A. Youssef, M. Zepf, and T. Yamanaka, "Fast heating scalable to laser fusion ignition.," *Nature*, vol. 418, no. 6901, pp. 933–934, 2002. 6

[36] M. Tabak, J. Hammer, M. E. Glinsky, W. L. Kruer, S. C. Wilks, J. Woodworth, E. M. Campbell, M. D. Perry, and R. J. Mason, "Ignition and high gain with ultrapowerful lasers," *Physics of Plasmas*, vol. 1, no. 5, p. 1626, 1994. 6

[37] R. R. Wilson, "Radiological Use of Fast Protons," *Radiology*, vol. 47, no. 5, pp. 487–491, 1946. 6

[38] M. Jermann, "Particle Therapy Patient Statistics (per end of 2015)," tech. rep., 2016. 7

[39] K. Zeil, M. Baumann, E. Beyreuther, T. Burris-Mog, T. E. Cowan, W. Enghardt, L. Karsch, S. D. Kraft, L. Laschinsky, J. Metzkes, D. Naumburger, M. Oppelt, C. Richter, R. Sauerbrey, M. Schürer, U. Schramm, and J. Pawelke, "Dose-controlled irradiation of cancer cells with laser-accelerated proton pulses," *Appl. Phys. B*, vol. 110, pp. 437–444, 2013. 7

[40] Cancer Research UK, "World cancer factsheet," 2014. 7

[41] A. Giulietti, "Laser-driven particle acceleration for radiobiology and radiotherapy: where we are and where we are going," *Proc. of SPIE*, vol. 10239, 2017. 7

[42] M. Jermann, "https://www.ptcog.ch/index.php/patient-statistics." 7

[43] K. Epstein, "Is spending on proton beam therapy for cancer going too far, too fast?," *BMJ-British Medical Journal*, vol. 2488, no. April, pp. 1–2, 2012. 7

[44] U. Linz and J. Alonso, "Laser-driven ion accelerators for tumor therapy revisited," *Physical Review Accelerators and Beams*, vol. 19, no. 12, pp. 1–8, 2016. 8

[45] D. Sardari, R. Maleki, H. Samavat, and A. Esmaeeli, "Measurement of depth-dose of linear accelerator and simulation by use of Geant4 computer code," *Reports of Practical Oncology and Radiotherapy*, vol. 15, no. 3, pp. 64–68, 2010. 8

[46] J. F. Ziegler, M. D. Ziegler, and J. P. Biersack, "SRIM - The stopping and range of ions in matter (2010)," *Nuclear Instruments and Methods in Physics Research, Section B: Beam Interactions with Materials and Atoms*, vol. 268, no. 11-12, pp. 1818–1823, 2010. 8

[47] D. Schulz-Ertner and H. Tsujii, "Particle radiation therapy using proton and heavier ion beams," *Journal of Clinical Oncology*, vol. 25, no. 8, pp. 953–964, 2007. 9

[48] T. I. Yock, B. Y. Yeap, D. H. Ebb, E. Weyman, B. R. Eaton, N. A. Sherry, R. M. Jones, S. M. MacDonald, M. B. Pulsifer, B. Lavally, A. N. Abrams, M. S. Huang, K. J. Marcus, and N. J. Tarbell, "Long-term toxic effects of proton radiotherapy for paediatric medulloblastoma: A phase 2 single-arm study," *The Lancet Oncology*, vol. 17, no. 3, pp. 287–298, 2016. 9

[49] S. V. Bulanov and V. S. Khoroshkov, "Feasibility of using laser ion accelerators in proton therapy," *Plasma Physics Reports*, vol. 28, no. 5, pp. 493–496, 2002. 9

[50] S. V. Bulanov, T. Z. Esirkepov, V. S. Khoroshkov, A. V. Kuznetsov, and F. Pegoraro, "Oncological hadrontherapy with laser ion accelerators," *Physics Letters A*, vol. 299, no. July, pp. 240–247, 2002. 9

[51] V. Malka, S. Fritzler, E. Lefebvre, E. D'Humières, R. Ferrand, G. Grillon, C. Albaret, S. Meyroneinc, J.-P. Chambaret, A. Antonetti, and D. Hulin, "Practicability of protontherapy using compact laser systems," *Medical Physics*, vol. 31, no. 6, pp. 1587–1592, 2004. 9

[52] K. W. D. Ledingham, W. Galster, and R. Sauerbrey, "Laser-driven proton oncology - A unique new cancer therapy?," 2007. 9

[53] K. Ledingham, P. Bolton, N. Shikazono, and C.-M. Ma, "Towards Laser Driven Hadron Cancer Radiotherapy: A Review of Progress," *Applied Sciences*, vol. 4, no. 3, pp. 402–443, 2014. 9

[54] M. Murakami, Y. Hishikawa, S. Miyajima, Y. Okazaki, K. L. Sutherland, M. Abe, S. V. Bulanov, H. Daido, T. Z. Esirkepov, J. Koga, M. Yamagiwa, T. Tajima, and H. Daido, "Radiotherapy using a laser proton accelerator," *AIP Conference Proceedings*, vol. 1024, pp. 275–300, 2008. 9

[55] A. Koehler, "Proton Radiography," *Science*, vol. 160, no. 3825, pp. 303–304, 1968. 10

[56] D. West and A. Sherwood, "Radiography with 160 MeV protons," *Nature*, vol. 239, pp. 157–159, 1972. 10

[57] M. Borghesi, A. Schiavi, D. H. Campbell, M. G. Haines, O. Willi, A. J. MacKinnon, L. A. Gizzi, M. Galimberti, R. J. Clarke, and H. Ruhl, "Proton imaging: a diagnostic for inertial confinement fusion/fast ignitor studies," *Plasma Physics and Controlled Fusion*, vol. 43, no. 12A, pp. A267–A276, 2001. 10

[58] M. Borghesi, D. H. Campbell, A. Schiavi, M. G. Haines, O. Willi, A. J. MacKinnon, P. Patel, L. A. Gizzi, M. Galimberti, R. J. Clarke, F. Pegoraro, H. Ruhl, and S. Bulanov, "Electric field detection in laser-plasma interaction experiments via the proton imaging technique," *Physics of Plasmas*, vol. 9, no. 5, p. 2214, 2002. 10

[59] L. Romagnani, J. Fuchs, M. Borghesi, P. Antici, P. Audebert, F. Ceccherini, T. Cowan, T. Grismayer, S. Kar, A. Macchi, P. Mora, G. Pretzler, A. Schiavi, T. Toncian, and O. Willi, "Dynamics of Electric Fields Driving the Laser Acceleration of Multi-MeV Protons," *Physical Review Letters*, vol. 95, p. 195001, oct 2005. 10, 42, 43

[60] L. Romagnani, S. V. Bulanov, M. Borghesi, P. Audebert, J. C. Gauthier, K. Löwenbrück, A. J. MacKinnon, P. Patel, G. Pretzler, T. Toncian, and O. Willi, "Observation of collisionless shocks in laser-plasma experiments," *Physical Review Letters*, vol. 101, no. 2, pp. 1–4, 2008. 10, 52

[61] L. Willingale, P. M. Nilson, A. G. Thomas, J. Cobble, R. S. Craxton, A. Maksimchuk, P. A. Norreys, T. C. Sangster, R. H. Scott, C. Stoeckl, C. Zulick, and K. Krushelnick, "High-power, kilojoule class laser channeling in millimeter-scale underdense plasma," *Physical Review Letters*, vol. 106, no. 10, pp. 1–4, 2011. 10

[62] C. K. Li, F. H. Séguin, J. A. Frenje, J. R. Rygg, R. D. Petrasso, R. P. J. Town, P. A. Amendt, S. P. Hatchett, O. L. Landen, A. J. MacKinnon, P. K. Patel, V. A. Smalyuk, T. C. Sangster, and J. P. Knauer, "Measuring E and B fields in laser-produced plasmas with monoenergetic proton radiography," *Physical Review Letters*, vol. 97, no. 13, pp. 3–6, 2006. 10

[63] P. M. Nilson, L. Willingale, M. C. Kaluza, C. Kamperidis, S. Minardi, M. S. Wei, P. Fernandes, M. Notley, S. Bandyopadhyay, M. Sherlock, R. J. Kingham, M. Tatarakis, Z. Najmudin, W. Rozmus, R. G. Evans, M. G. Haines, A. E. Dangor, and K. Krushelnick, "Magnetic reconnection and plasma dynamics in two-beam laser-solid interactions," *Physical Review Letters*, vol. 97, no. 25, pp. 1–4, 2006. 10

[64] C. A. Cecchetti, M. Borghesi, J. Fuchs, G. Schurtz, S. Kar, A. Macchi, L. Romagnani, P. A. Wilson, P. Antici, R. Jung, J. Osterholtz, C. A. Pipahl, O. Willi, A. Schiavi, M. Notley, and D. Neely, "Magnetic field measurements in laser-produced plasmas via proton deflectometry," *Physics of Plasmas*, vol. 16, no. 4, 2009. 10

[65] T. F. Budinger, "Time-of-flight Positron Emission Tomography: Status Relative to Conventional PET.," *Journal of Nuclear Medicine*, vol. 24, no. 1, pp. 73–8, 1983. 10

[66] M. E. Raichle, "Positron Emission," vol. 2, no. August, pp. 1–12, 1983. 11

[67] G. Brownell and W. Sweet, "Localization of brain tumors with positron emitters," *Nucleonics*, vol. 11, pp. 40–45, 1953. 11

[68] D. Vaughan, "A Vital Legacy - Biological and Enviromental Research in the Atomic Age," tech. rep., 2010. 11

[69] G. L. Brownell, "A History of Positron Imaging," *Physics Research Laboratory, Massachusetts General Hospital*, pp. 1–11, 1999. 11

[70] Txchnologist, "A PET Prototype." 11

[71] I. Spencer, K. W. D. Ledingham, R. P. Singhal, T. McCanny, P. McKenna, E. L. Clark, K. Krushelnick, M. Zepf, F. N. Beg, M. Tatarakis, A. E. Dangor, P. A. Norreys, R. J. Clarke, R. M. Allott, and I. N. Ross, "Laser generation of proton beams for the production of short-lived positron emitting radioisotopes," *Nuclear Instruments and Methods in Physics Research, Section B: Beam Interactions with Materials and Atoms*, vol. 183, no. 3-4, pp. 449–458, 2001. 11

[72] K. W. D. Ledingham, "Applications for Nuclear Phenomena Generated by Ultra-Intense Lasers," *Science*, vol. 300, no. 5622, pp. 1107–1111, 2003. 11

[73] S. Fritzler, V. Malka, G. Grillon, J. P. Rousseau, F. Burgy, E. Lefebvre, E. D'Humières, P. McKenna, and K. W. Ledingham, "Proton beams generated with high-intensity lasers: Applications to medical isotope production," *Applied Physics Letters*, vol. 83, no. 15, pp. 3039–3041, 2003. 11

[74] K. W. D. Ledingham, P. McKenna, T. McCanny, S. Shimizu, J. M. Yang, L. Robson, J. Zweit, J. M. Gillies, J. Bailey, G. N. Chimon, R. J. Clarke, D. Neely, P. A. Norreys, J. L. Collier, R. P. Singhal, M. S. Wei, S. P. D. Mangles, P. Nilson, K. Krushelnick, and M. Zepf, "High power laser production of short-lived isotopes for positron emission tomography," *Journal of Physics D: Applied Physics*, vol. 37, pp. 2341–2345, aug 2004. 11

[75] C. Hernandez-Gomez, S. P. Blake, O. Chekhlov, R. J. Clarke, A. M. Dunne, M. Galimberti, S. Hancock, R. Heathcote, P. Holligan, A. Lyachev, P. Matousek,

I. O. Musgrave, D. Neely, P. A. Norreys, I. Ross, Y. Tang, T. B. Winstone, B. E. Wyborn, and J. Collier, "The Vulcan 10 PW project," *Journal of Physics: Conference Series*, vol. 244, no. 3, p. 032006, 2010. 12

[76] I. V. Pogorelsky, M. Babzien, I. Ben-Zvi, J. Skaritka, and M. N. Polyanskiy, "BESTIA - The next generation ultra-fast CO2 laser for advanced accelerator research," *Nuclear Instruments and Methods in Physics Research, Section A: Accelerators, Spectrometers, Detectors and Associated Equipment*, vol. 829, pp. 432–437, 2015. 12, 182, 183

[77] "Extreme light," *Nature Materials*, vol. 15, no. 1, p. 1, 2016. 12

[78] F. F. Chen, *Introduction to Plasma Physics and Controlled Fusion*. Boston, MA: Springer US, 1st ed., 1984. 15, 33, 36

[79] K. Miyamoto, "Fundamentals of Plasma Physics and Controlled Fusion," 2011. 15

[80] P. Gibbon, *Short Pulse Laser Interactions with Matter: An Introduction*. London: Imperial College Press, 1st ed., 2005. 20, 34, 36, 38, 57

[81] V. L. Ginzberg, *Propagation of Electromagnetic Waves in Plasma*. New York: Gordon and Breach, Scientific Publishers inc., 1961. 21

[82] W. L. Kruer, *The Physics of Laser Plasma Interactions*. Oxford: Westview Press, 2003. 21, 33, 34

[83] R. Z. Sagdeev, "Collisionless shocks in a rarified plasma," *Sov. Phys. Tech. Phys.*, vol. 6, p. 867, 1962. 25

[84] J. H. Adlam and J. E. Allen, "The structure of strong collision-free hydromagnetic waves," *Philosophical Magazine*, vol. 3, no. 29, pp. 448–455, 1958. 25

[85] S. S. Moiseev and R. Z. Sagdeev, "Collisionless shock waves in a plasma in a weak magnetic field," *Journal of Nuclear Energy Part C*, vol. 5, pp. 43–47, 1963. 27

[86] D. W. Forslund and C. R. Shonk, "Formation and Structure of Electrostatic Collisionless Shocks," *Physical Review Letters*, vol. 25, no. 25, p. 1699, 1970. 29, 176

[87] D. W. Forslund and J. P. Freidberg, "Theory of Laminar Collisionless Shocks," *Physical Review Letters*, vol. 27, no. 18, p. 1189, 1971. 29

[88] G. Sorasio, M. Marti, R. Fonseca, and L. O. Silva, "Very High Mach-Number Electrostatic Shocks in Collisionless Plasmas," *Physical Review Letters*, vol. 96, no. 4, p. 045005, 2006. 29

[89] W. Lotz, "An empirical formula for the electron-impact ionization cross-section," *Zeitschrift für Physik*, vol. 206, pp. 205–211, apr 1967. 31

[90] H. Ghaforyan, R. Sadighi, and E. Irani, "The effect of chirped intense femtosecond laser pulses on the Argon cluster," *arXiv*, pp. 1–27, aug 2016. 31

[91] L. Keldysh, "Ionization in the field of strong electromagnetic wave," *Sov. Phys. JETP*, vol. 20, no. 5, pp. 1307–1314, 1965. 32

[92] M. V. Ammosov, N. B. Delone, and V. P. Krainov, "Tunnel ionization of complex atoms and of atomic ions in an alternating electromagnetic field," *Sov. Phys. JETP*, vol. 64, no. December 1986, pp. 1191–1194, 1986. 32

[93] G. Gibson, T. S. Luk, and C. K. Rhodes, "Tunneling ionization in the multiphoton regime," *Physical Review A*, vol. 41, no. 9, pp. 5049–5052, 1990. 32

[94] T. P. Auguste, P. Monot, A. E. Lompre, G. Mainfray, and C. Manus, "Multiply charged ions produced in noble gases by a 1ps laser pulse at λ=1053nm," *Journal of Physics B*, vol. 25, pp. 4181–4194, 1992. 32

[95] L. Keldysh, "Ionization in the field of strong electromagnetic wave," *Zh. Eksperim. i Teor. Fiz.*, vol. Vol: 47, nov 1964. 32

[96] J. F. Drake, "Parametric instabilities of electromagnetic waves in plasmas," *Physics of Fluids*, vol. 17, no. 4, p. 778, 1974. 33

[97] D. W. Forslund, J. M. Kindel, and E. L. Lindman, "Theory of stimulated scattering processes in laser-irradiated plasmas," *Physics of Fluids*, vol. 18, no. 8, p. 1002, 1975. 33

[98] S. Atzeni and J. Meyer-Ter-Vehn, *The Physics of Inertial Fusion*. Oxford: Oxford University Press, 2004. 33, 50, 159

[99] W. Rozmus and V. T. Tikhonchuk, "Skin effect and interaction of short laser pulses with dense plasmas," *Physical Review A*, vol. 42, no. 12, pp. 7401–7412, 1990. 34

[100] K. Estabrook, "Critical surface bubbles and corrugations and their implications to laser fusion," *Physics of Fluids*, vol. 19, no. 11, p. 1733, 1976. 34

[101] J. J. Thomson, W. L. Kruer, A. B. Langdon, C. E. Max, and W. C. Mead, "Theoretical interpretation of angle- and polarization-dependent laser light absorption measurements," *Physics of Fluids*, vol. 21, no. 4, p. 707, 1978. 34

[102] N. G. Denisov, "On a Singularity of the Field of an Electromagnetic Wove," *JETP*, vol. 4, no. 4, pp. 544–553, 1957. 34

[103] F. Brunel, "Not-so-resonant, resonant absorption," *Physical Review Letters*, vol. 59, no. 1, pp. 52–55, 1987. 35

[104] E. S. Weibel, "Anomalous Skin Effect in a Plasma," *Physics of Fluids*, vol. 10, no. 4, p. 741, 1967. 35

[105] S. Wilks, W. Kruer, M. Tabak, and A. Langdon, "Absorption of Ultra-Intense Laser Pulses," *Physical Review Letters*, vol. 69, no. 9, pp. 1383–1386, 1992. 35, 42, 44, 50

[106] W. L. Kruer and K. Estabrook, "JxB heating by very intense laser light," *Physics of Fluids*, vol. 28, pp. 430–432, jan 1985. 36

[107] Y. Ping, R. Shepherd, B. Lasinski, M. Tabak, H. Chen, H. Chung, K. Fournier, S. Hansen, A. Kemp, D. Liedahl, K. Widmann, S. Wilks, W. Rozmus, and M. Sherlock, "Absorption of Short Laser Pulses on Solid Targets in the Ultrarelativistic Regime," *Physical Review Letters*, vol. 100, p. 085004, feb 2008. 36

[108] E. A. Startsev and C. J. McKinstrie, "Multiple scale derivation of the relativistic ponderomotive force," *Physical Review E*, vol. 55, pp. 7527–7535, jun 1997. 36

[109] J. Jackson, "From Lorenz to Coulomb and other explicit gauge transformations," *American Journal of Physics*, no. April, pp. 1–31, 2002. 36

[110] K. Krushelnick, A. Ting, C. Moore, H. Burris, E. Esarey, P. Sprangle, and M. Baine, "Plasma Channel Formation and Guiding during High Intensity Short Pulse Laser Plasma Experiments," *Physical Review Letters*, vol. 78, no. 21, pp. 4047–4050, 1997. 38

[111] E. Hecht, *Optics*. Pearson Education Inc., fourth ed., 2002. 38, 187

[112] S. P. Hatchett, C. G. Brown, T. E. Cowan, E. A. Henry, J. S. Johnson, M. H. Key, J. A. Koch, A. B. Langdon, B. F. Lasinski, R. W. Lee, A. J. Mackinnon, D. M. Pennington, M. D. Perry, T. W. Phillips, M. Roth, T. C. Sangster, M. S. Singh, R. A. Snavely, M. A. Stoyer, S. C. Wilks, and K. Yasuike, "Electron, photon, and ion beams from the relativistic interaction of Petawatt laser pulses with solid targets," *Physics of Plasmas*, vol. 7, no. 5, pp. 2076–2082, 2000. 39

[113] M. Zepf, E. L. Clark, F. Beg, R. J. Clarke, A. E. Dangor, A. Gopal, K. Krushelnick, P. A. Norreys, M. Tatarakis, U. Wagner, and M. S. Wei, "Proton Acceleration from High-Intensity Laser Interactions with Thin Foil Targets," *Physical Review Letters*, vol. 90, no. 6, p. 064801, 2003. 40

[114] E. Clark, K. Krushelnick, M. Zepf, M. Tatarakis, F. Beg, P. Norreys, and A. Dangor, "Clark et al. Reply:," *Physical Review Letters*, vol. 96, p. 249202, jun 2006. 40

[115] A. Mackinnon, Y. Sentoku, P. Patel, D. Price, S. Hatchett, M. Key, C. Andersen, R. Snavely, and R. Freeman, "Enhancement of Proton Acceleration by Hot-Electron Recirculation in Thin Foils Irradiated by Ultraintense Laser Pulses," *Physical Review Letters*, vol. 88, p. 215006, may 2002. 40, 118, 176

[116] P. Mora, "Plasma Expansion into a Vacuum," *Physical Review Letters*, vol. 90, p. 185002, may 2003. 40

[117] P. Mora, "Thin-foil expansion into a vacuum," *Physical Review E*, vol. 72, p. 056401, nov 2005. 41

[118] L. Robson, P. T. Simpson, R. J. Clarke, K. W. D. Ledingham, F. Lindau, O. Lundh, T. McCanny, P. Mora, D. Neely, C.-G. Wahlström, M. Zepf, and P. McKenna, "Scaling of proton acceleration driven by petawatt-laserplasma interactions," *Nature Physics*, vol. 3, no. 1, p. 58, 2006. 41

[119] C. Perego, A. Zani, D. Batani, and M. Passoni, "Extensive comparison among Target Normal Sheath Acceleration theoretical models," *Nuclear Instruments and Methods in Physics Research, Section A: Accelerators, Spectrometers, Detectors and Associated Equipment*, vol. 653, no. 1, pp. 89–93, 2011. 41, 42

[120] F. N. Beg, A. R. Bell, A. E. Dangor, C. N. Danson, A. P. Fews, M. E. Glinsky, B. A. Hammel, P. Lee, P. A. Norreys, and M. Tatarakis, "A study of picosecond lasersolid interactions up to 1019 Wcm2," *Physics of Plasmas*, vol. 4, no. 2, p. 447, 1997. 41

[121] P. Gibbon and E. Förster, "Short-pulse laser - plasma interactions," *Plasma Physics and Controlled Fusion*, vol. 38, no. 6, pp. 769–793, 1996. 42

[122] T. Kluge, T. Cowan, A. Debus, U. Schramm, K. Zeil, and M. Bussmann, "Electron temperature scaling in laser interaction with solids," *Physical Review Letters*, vol. 107, no. 20, pp. 1–5, 2011. 42

[123] J. Schreiber, F. Bell, F. Grüner, U. Schramm, M. Geissler, M. Schnürer, S. Ter-Avetisyan, B. Hegelich, J. Cobble, E. Brambrink, J. Fuchs, P. Audebert, and D. Habs, "Analytical Model for Ion Acceleration by High-Intensity Laser Pulses," *Physical Review Letters*, vol. 97, p. 045005, jul 2006. 42, 174

[124] M. Passoni and M. Lontano, "Theory of light-ion acceleration driven by a strong charge separation," *Physical Review Letters*, vol. 101, no. 11, pp. 1–4, 2008. 42

[125] B. J. Albright, L. Yin, B. M. Hegelich, K. J. Bowers, T. J. T. Kwan, and J. C. Fernández, "Theory of laser acceleration of light-ion beams from interaction of ultrahigh-intensity lasers with layered targets," *Physical Review Letters*, vol. 97, no. 11, pp. 1–4, 2006. 42

[126] A. P. L. Robinson, A. Bell, and R. Kingham, "Effect of Target Composition on Proton Energy Spectra in Ultraintense Laser-Solid Interactions," *Physical Review Letters*, vol. 96, p. 035005, jan 2006. 42, 183

[127] M. Roth, M. Allen, and P. Audebert, "The generation of high-quality, intense ion beams by ultra-intense lasers," *Plasma physics and ...*, vol. 99, 2002. 42

[128] F. Lindau, O. Lundh, A. Persson, P. McKenna, K. Osvay, D. Batani, and C. G. Wahlström, "Laser-accelerated protons with energy-dependent beam direction," *Physical Review Letters*, vol. 95, no. 17, pp. 1–4, 2005. 43

[129] H. Schwoerer, S. Pfotenhauer, O. Jäckel, K.-U. Amthor, B. Liesfeld, W. Ziegler, R. Sauerbrey, K. W. D. Ledingham, and T. Esirkepov, "Laser-plasma acceleration of quasi-monoenergetic protons from microstructured targets.," *Nature*, vol. 439, pp. 445–8, jan 2006. 43, 100, 101

[130] M. Borghesi, A. Mackinnon, D. Campbell, D. Hicks, S. Kar, P. Patel, D. Price, L. Romagnani, A. Schiavi, and O. Willi, "Multi-MeV Proton Source Investigations in Ultraintense Laser-Foil Interactions," *Physical Review Letters*, vol. 92, no. 5, p. 055003, 2004. 43

[131] T. Z. Esirkepov, S. V. Bulanov, K. Nishihara, T. Tajima, F. Pegoraro, V. S. Khoroshkov, K. Mima, H. Daido, Y. Kato, Y. Kitagawa, K. Nagai, and S. Sakabe, "Proposed Double-Layer Target for the Generation of High-Quality Laser-Accelerated Ion Beams," *Physical Review Letters*, vol. 89, p. 175003, oct 2002. 43, 183

[132] B. M. Hegelich, B. J. Albright, J. Cobble, K. Flippo, S. Letzring, M. Paffett, H. Ruhl, J. Schreiber, R. K. Schulze, and J. C. Fernández, "Laser acceleration of quasi-monoenergetic MeV ion beams.," *Nature*, vol. 439, pp. 441–4, jan 2006. 43, 100, 101

[133] J. Bin, K. Allinger, and W. Assmann, "A laser-driven nanosecond proton source for radiobiological studies," *Applied Physics . . .*, vol. 101, no. 24, p. 243701, 2012. 43

[134] D. Gabor, "A Space-Charge Lens for the Focusing of Ion Beams," *Nature*, 1947. 43

[135] J. Pozimski and M. Aslaninejad, "Gabor lenses for capture and energy selection of laser driven ion beams in cancer treatment," *Laser and Particle Beams*, pp. 723–733, 2013. 43

[136] G. Marx, "Interstellar Vehicle Propelled By Terrestrial Laser Beam," *Nature*, vol. 211, pp. 22–23, 1966. 44

[137] T. Esirkepov, M. Borghesi, S. Bulanov, G. Mourou, and T. Tajima, "Highly Efficient Relativistic-Ion Generation in the Laser-Piston Regime," *Physical Review Letters*, vol. 92, p. 175003, apr 2004. 44, 53

[138] X. Zhang, B. Shen, X. Li, Z. Jin, F. Wang, and M. Wen, "Efficient GeV ion generation by ultraintense circularly polarized laser pulse," *Physics of Plasmas*, vol. 14, no. 12, 2007. 44

[139] A. Macchi, F. Cattani, T. Liseykina, and F. Cornolti, "Laser Acceleration of Ion Bunches at the Front Surface of Overdense Plasmas," *Physical Review Letters*, vol. 94, p. 165003, apr 2005. 44

[140] T. V. Liseikina, D. Prellino, F. Cornolti, and A. Macchi, "Ponderomotive acceleration of ions: Circular versus linear polarization," *IEEE Transactions on Plasma Science*, vol. 36, pp. 1866–1871, 2008. 44

[141] C. Palmer, N. Dover, I. Pogorelsky, M. Babzien, G. Dudnikova, M. Ispiriyan, M. Polyanskiy, J. Schreiber, P. Shkolnikov, V. Yakimenko, and Z. Najmudin, "Monoenergetic Proton Beams Accelerated by a Radiation Pressure Driven Shock," *Physical Review Letters*, vol. 106, p. 014801, jan 2011. 44, 51, 55, 67, 83, 84, 99, 100, 101, 114, 181, 183

[142] A. Macchi, *A Superintense Laser-plasma Interaction Theory Primer*. 2013. 46

[143] T. Schlegel, N. Naumova, V. T. Tikhonchuk, C. Labaune, I. V. Sokolov, and G. Mourou, "Relativistic laser piston model: Ponderomotive ion acceleration in dense plasmas using ultraintense laser pulses," *Physics of Plasmas*, vol. 16, no. 8, 2009. 48

[144] A. P. L. Robinson, P. Gibbon, M. Zepf, S. Kar, R. G. Evans, and C. Bellei, "Relativistically correct hole-boring and ion acceleration by circularly polarized laser pulses," *Plasma Physics and Controlled Fusion*, vol. 51, p. 024004, feb 2009. 49

[145] J. Denavit, "Absorption of High-Intensity Subpicosecond Lasers on Solid Density Targets," *Physical review letters*, vol. 69, no. 21, 1992. 50, 52

[146] X. Zhang, B. Shen, X. Li, Z. Jin, and F. Wang, "Multistaged acceleration of ions by circularly polarized laser pulse: Monoenergetic ion beam generation," *Physics of Plasmas*, vol. 14, no. 7, 2007. 50

[147] T. V. Liseikina and A. Macchi, "Features of ion acceleration by circularly polarized laser pulses," *Applied Physics Letters*, vol. 91, no. 17, p. 171502, 2007. 50

[148] F. Cattani, A. Kim, D. Anderson, and M. Lisak, "Threshold of induced transparency in the relativistic interaction of an electromagnetic wave with overdense plasmas," *Physical review. E*, vol. 62, pp. 1234–7, jul 2000. 50

[149] A. P. L. Robinson, R. M. G. M. Trines, N. P. Dover, and Z. Najmudin, "Hole-boring radiation pressure acceleration as a basis for producing high-energy proton bunches," *Plasma Physics and Controlled Fusion*, vol. 54, p. 115001, nov 2012. 50, 124

[150] C. A. J. Palmer, N. P. Dover, I. Pogorelsky, M. J. V. Streeter, and Z. Najmudin, "Manipulation of laser-generated energetic proton spectra in near critical density

plasma," *Journal of Plasma Physics*, vol. 81, no. 01, p. 365810103, 2015. 51, 112, 131

[151] D. Montgomery and G. Joyce, "Shock-like solutions of the electrostatic Vlasov equation," *Journal of Plasma Physics*, vol. 3, pp. 1–11, 1969. 51

[152] H. Schamel, "Stationary solitary, snoidal and sinusoidal ion acoustic waves," *Plasma Physics*, vol. 905, 1972. 51

[153] R. Z. Sagdeev, "Cooperative Phenomena and Shock Waves in Collisionless Plasmas," *Reviews of Plasma Physics*, vol. 4, p. 23, 1966. 51

[154] D. A. Tidman and N. A. Krall, *Shock waves in collisionless plasmas.* Wiley-Interscience, 1971. 51

[155] S. Moiseev and R. Sagdeev, "Collisionless shock waves in a plasma in a weak magnetic field," *... of Nuclear Energy. Part C, Plasma ...*, vol. 43, 1963. 51

[156] F. Fiuza, R. Fonseca, J. Tonge, W. Mori, and L. Silva, "Weibel-Instability-Mediated Collisionless Shocks in the Laboratory with Ultraintense Lasers," *Physical Review Letters*, vol. 108, pp. 1–5, jun 2012. 51, 52, 176, 190, 191

[157] L. O. Silva, M. Marti, J. R. Davies, and R. A. Fonseca, "Proton Shock Acceleration in Laser-Plasma Interactions," *Physical Review Letters*, vol. 92, p. 015002, jan 2004. 52, 176, 190

[158] M. Chen, Z.-M. Sheng, Q.-L. Dong, M.-Q. He, Y.-T. Li, M. A. Bari, and J. Zhang, "Collisionless electrostatic shock generation and ion acceleration by ultraintense laser pulses in overdense plasmas," *Physics of Plasmas*, vol. 14, no. 5, p. 053102, 2007. 52

[159] M. Chen, Z. Sheng, and Q. Dong, "Collisionless electrostatic shock generation and ion acceleration by ultraintense laser pulses in overdense plasmas," *Physics of Plasmas (...*, vol. 053102, no. 2007, 2007. 52

[160] A. Macchi, A. S. Nindrayog, and F. Pegoraro, "Solitary versus shock wave acceleration in laser-plasma interactions," *Physical Review E*, vol. 85, p. 046402, apr 2012. 52

[161] F. Fiuza, A. Stockem, E. Boella, R. A. Fonseca, L. O. Silva, D. Haberberger, S. Tochitsky, W. B. Mori, and C. Joshi, "Ion acceleration from laser-driven electrostatic shocks," *Physics of Plasmas*, vol. 20, no. 5, p. 056304, 2013. 52, 190

[162] A. Zhidkov, M. Uesaka, A. Sasaki, and H. Daido, "Ion Acceleration in a Solitary Wave by an Intense Picosecond Laser Pulse," *Physical Review Letters*, vol. 89, no. 21, p. 215002, 2002. 52

[163] E. D'Humieres, E. Lefebvre, L. Gremillet, and V. Malka, "Proton acceleration mechanisms in high-intensity laser interaction with thin foils," *Physics of Plasmas*, vol. 12, no. 6, p. 062704, 2005. 52

[164] M.-P. Liu, B.-S. Xie, Y.-S. Huang, J. Liu, and M. Yu, "Enhanced ion acceleration by collisionless electrostatic shock in thin foils irradiated by ultraintense laser pulse," *Laser and Particle Beams*, vol. 27, no. 02, p. 327, 2009. 52

[165] M. S. Wei, S. P. D. Mangles, Z. Najmudin, B. Walton, A. Gopal, M. Tatarakis, A. E. Dangor, E. L. Clark, R. G. Evans, S. Fritzler, R. J. Clarke, C. Hernandez-Gomez, D. Neely, W. Mori, M. Tzoufras, and K. Krushelnick, "Ion Acceleration by Collisionless Shocks in High-Intensity-LaserUnderdense-Plasma Interaction," *Physical Review Letters*, vol. 93, no. 15, p. 155003, 2004. 52

[166] A. Henig, D. Kiefer, M. Geissler, S. G. Rykovanov, R. Ramis, R. Horlein, J. Osterhoff, Z. Major, L. Veisz, S. Karsch, F. Krausz, D. Habs, and J. Schreiber, "Laser-driven shock acceleration of ion beams from spherical mass-limited targets," *Physical Review Letters*, vol. 102, no. 9, pp. 100–103, 2009. 52

[167] D. Haberberger, S. Tochitsky, and F. Fiuza, "Collisionless shocks in laser-produced plasma generate monoenergetic high-energy proton beams," *Nature Physics*, vol. 8, no. 1, pp. 95–99, 2011. 52, 62, 83, 100, 101, 190

[168] Y. P. Zakharov, "Collisionless Laboratory Astrophysics With Lasers," *IEEE Transactions on Plasma Science*, vol. 31, no. 6 I, pp. 1243–1251, 2003. 52

[169] D. D. Ryutov, N. L. Kugland, H. S. Park, C. Plechaty, B. A. Remington, and J. S. Ross, "Basic scalings for collisionless-shock experiments in a plasma without preimposed magnetic field," *Plasma Physics and Controlled Fusion*, vol. 54, no. 10, p. 105021, 2012. 52

[170] A. Stockem, F. Fiuza, A. Bret, R. A. Fonseca, and L. O. Silva, "Exploring the nature of collisionless shocks under laboratory conditions.," *Scientific reports*, vol. 4, p. 3934, 2014. 52

[171] A. Grassi, M. Grech, F. Amiranoff, A. Macchi, and C. Riconda, "Radiation Pressure Driven Ion Weibel Instability and Collisionless Shocks," *arXiv*, pp. 1–5, 2017. 52

[172] P. M. Nilson, S. P. D. Mangles, L. Willingale, M. C. Kaluza, A. G. R. Thomas, M. Tatarakis, Z. Najmudin, R. J. Clarke, K. L. Lancaster, S. Karsch, J. Schreiber, R. G. Evans, A. E. Dangor, and K. Krushelnick, "Generation of ultrahigh-velocity ionizing shocks with petawatt-class laser pulses," *Physical Review Letters*, vol. 103, no. 25, pp. 1–4, 2009. 52, 66

[173] C. M. Huntington, F. Fiuza, J. S. Ross, A. B. Zylstra, R. P. Drake, D. H. Froula, G. Gregori, N. L. Kugland, C. C. Kuranz, M. C. Levy, C. K. Li, J. Meinecke,

T. Morita, R. Petrasso, C. Plechaty, B. A. Remington, D. D. Ryutov, Y. Sakawa, A. Spitkovsky, H. Takabe, and H. S. Park, "Observation of magnetic field generation via the Weibel instability in interpenetrating plasma flows," *Nature Physics*, vol. 11, no. January, pp. 1–13, 2015. 52

[174] E. S. Weibel, "Spontaneously growing transverse waves in a plasma due to an anisotropic velocity distribution," *Physical Review Letters*, vol. 2, no. 3, pp. 83–84, 1959. 52

[175] A. P. L. Robinson, M. Zepf, S. Kar, R. G. Evans, and C. Bellei, "Radiation pressure acceleration of thin foils with circularly polarized laser pulses," *New Journal of Physics*, vol. 10, no. 1 PG - 013021 (13pp), 2008. 53

[176] G. Chen, B. Kim, B. Ahn, and D. E. Kim, "Pressure dependence of argon cluster size for different nozzle geometries," *Journal of Applied Physics*, vol. 106, no. 5, p. 053507, 2009. 54

[177] F. Pegoraro and S. Bulanov, "Photon Bubbles and Ion Acceleration in a Plasma Dominated by the Radiation Pressure of an Electromagnetic Pulse," *Physical Review Letters*, vol. 99, pp. 1–4, aug 2007. 54

[178] X. Zhang, B. Shen, L. Ji, W. Wang, J. Xu, Y. Yu, and X. Wang, "Instabilities in interaction of circularly polarized laser pulse and overdense target," *Physics of Plasmas*, vol. 18, no. 7, p. 073101, 2011. 54

[179] I. V. Pogorelsky, M. Babzien, K. P. Kusche, I. V. Pavlishin, V. Yakimenko, C. E. Dilley, S. C. Gottschalk, W. D. Kimura, T. Katsouleas, P. Muggli, E. Kallos, L. C. Steinhauer, A. Zigler, N. Andreev, D. B. Cline, and F. Zhou, "Plasma-based advanced accelerators at the Brookhaven Accelerator Test Facility," *Laser Physics*, vol. 16, no. 2, pp. 259–266, 2006. 55

[180] Z. Najmudin, C. A. J. Palmer, N. P. Dover, I. Pogorelsky, M. Babzien, A. E. Dangor, G. I. Dudnikova, P. S. Foster, J. S. Green, M. Ispiriyan, D. Neely, M. N. Polyanskiy, J. Schreiber, P. Shkolnikov, and V. Yakimenko, "Observation of impurity free monoenergetic proton beams from the interaction of a CO2 laser with a gaseous target," *Physics of Plasmas*, vol. 18, no. 5, p. 056705, 2011. 55, 61, 83

[181] O. Tresca, N. Dover, N. Cook, C. Maharjan, M. Polyanskiy, Z. Najmudin, P. Shkolnikov, and I. Pogorelsky, "Spectral Modification of Shock Accelerated Ions Using a Hydrodynamically Shaped Gas Target," *Physical Review Letters*, vol. 115, no. 9, p. 094802, 2015. 55, 61, 67, 83, 86, 99, 114, 181

[182] A. Ting, B. Hafizi, M. Helle, Y. H. Chen, D. Gordon, D. Kaganovich, M. Polyanskiy, I. Pogorelsky, M. Babzien, C. Miao, N. Dover, Z. Najmudin, and O. Ettlinger, "Staging and laser acceleration of ions in underdense plasma," *AIP Conference Proceedings*, vol. 1812, 2017. 55, 67, 83, 129

[183] W. D. Kimura, L. P. Campbell, C. E. Dilley, S. C. Gottschalk, D. C. Quimby, A. Van Steenbergen, M. Babzien, I. Ben-Zvi, J. C. Gallardo, K. P. Kusche, I. V. Pogorelsky, J. Skaritka, V. Yakimenko, D. B. Cline, P. He, Y. Liu, L. C. Steinhauer, and R. H. Pantell, "Detailed experimental results for laser acceleration staging," *Physical Review Special Topics - Accelerators and Beams*, vol. 4, no. 10, pp. 1–12, 2001. 55

[184] M. Babzien, I. Ben-Zvi, K. Kusche, I. V. Pavlishin, I. V. Pogorelsky, D. P. Siddons, V. Yakimenko, D. Cline, F. Zhou, T. Hirose, Y. Kamiya, T. Kumita, T. Omori, J. Urakawa, and K. Yokoya, "Observation of the second harmonic in Thomson scattering from relativistic electrons," *Physical Review Letters*, vol. 96, no. 5, pp. 1–4, 2006. 55

[185] J. Duris, P. Musumeci, M. Babzien, M. Fedurin, K. Kusche, R. K. Li, J. Moody, I. Pogorelsky, M. Polyanskiy, J. B. Rosenzweig, Y. Sakai, C. Swinson, E. Threlkeld, O. Williams, and V. Yakimenko, "High-quality electron beams from a helical inverse free-electron laser accelerator," *Nature Communications*, vol. 5, p. 4928, 2014. 55

[186] W. Kimura, N. Andreev, M. Babzien, I. Ben-Zvi, D. Cline, C. Dilley, S. Gottschalk, S. Hooker, K. Kusche, S. Kuznetsov, I. Pavlishin, I. Pogorelsky, A. Pogosova, L. Steinhauer, A. Ting, V. Yakimenko, A. Zigler, and F. Zhou, "Inverse free electron lasers and laser wakefield acceleration driven by CO2 lasers," *Philosophical Transactions of the Royal Society A: Mathematical, Physical and Engineering Sciences*, vol. 364, no. 1840, pp. 611–622, 2006. 55

[187] P. Oliva, M. Carpinelli, B. Golosio, P. Delogu, M. Endrizzi, J. Park, I. Pogorelsky, V. Yakimenko, O. Williams, and J. Rosenzweig, "Quantitative evaluation of single-shot inline phase contrast imaging using an inverse compton x-ray source," *Applied Physics Letters*, vol. 97, no. 13, pp. 13–16, 2010. 55

[188] Y. Sakai, I. Pogorelsky, O. Williams, F. O'Shea, S. Barber, I. Gadjev, J. Duris, P. Musumeci, M. Fedurin, A. Korostyshevsky, B. Malone, C. Swinson, G. Stenby, K. Kusche, M. Babzien, M. Montemagno, P. Jacob, Z. Zhong, M. Polyanskiy, V. Yakimenko, and J. Rosenzweig, "Observation of redshifting and harmonic radiation in inverse Compton scattering," *Physical Review Special Topics - Accelerators and Beams*, vol. 18, no. 6, pp. 1–11, 2015. 55

[189] C. K. N. Patel, "High-Power Carbon Dioxide Lasers," *Scientific American*, 1968. 55

[190] W. Rath, "CO 2 Lasers : Modern Workhorses in the World of Industrial Manufacturing," *LTJ*, no. 3, pp. 34–39, 2007. 55

[191] D. Haberberger, S. Tochitsky, and C. Joshi, "Fifteen terawatt picosecond CO2 laser system.," *Optics express*, vol. 18, no. 17, pp. 17865–17875, 2010. 55, 100

[192] M. N. Polyanskiy and M. Babzien, "Ultrashort Pulses," in *CO2 Laser-Optimisation and Application*, pp. 139–162, InTech, 2016. 56, 58

[193] M. N. Polyanskiy, M. Babzien, and I. V. Pogorelsky, "Chirped-pulse amplification in a CO 2 laser," *Optica*, vol. 2, no. 8, pp. 657–681, 2015. 58, 59, 85

[194] R. K. Brimacombe and J. Reid, "Accurate Measurements of Pressure-Broadened Linewidths in a Transversely Excited CO_2 Discharge," *IEEE Journal of Quantum Electronics*, vol. 19, no. 11, pp. 1668–1673, 1983. 57

[195] R. L. Abrams and O. R. Wood, "Characteristics of a mode-locked TEA CO2 laser," *Applied Physics Letters*, vol. 19, no. 12, pp. 518–520, 1971. 58

[196] M. N. Polyanskiy, I. V. Pogorelsky, and V. Yakimenko, "Picosecond pulse amplification in isotopic CO2 active medium.," *Optics express*, vol. 19, no. 8, p. 7717, 2011. 59

[197] S. Semushin and V. Malka, "High density gas jet nozzle design for laser target production," *Review of Scientific Instruments*, vol. 72, no. 7, p. 2961, 2001. 60

[198] S. Göde, C. Rödel, K. Zeil, R. Mishra, M. Gauthier, F. Brack, T. Kluge, M. J. MacDonald, J. Metzkes, L. Obst, M. Rehwald, C. Ruyer, H. P. Schlenvoigt, W. Schumaker, P. Sommer, T. E. Cowan, U. Schramm, S. Glenzer, and F. Fiuza, "Relativistic electron streaming instabilities modulate proton beams accelerated in laser-plasma interactions," *Physical Review Letters*, vol. 118, no. 194801, pp. 1–5, 2017. 62

[199] N. P. Dover, N. Cook, O. Tresca, O. C. Ettlinger, C. Maharjan, M. N. Polyanskiy, P. Shkolnikov, I. Pogorelsky, and Z. Najmudin, "Optical shaping of gas targets for laserplasma ion sources," *Journal of Plasma Physics*, vol. 82, no. 01, p. 415820101, 2016. 62, 67

[200] G. Taylor, "The Formation of a Blast Wave by a Very Intense Explosion. I. Theoretical Discussion," *Proceedings of the Royal Society A: Mathematical, Physical and Engineering Sciences*, vol. 201, no. 1065, pp. 159–174, 1950. 62

[201] M. Dryer, "Interplanetary shock waves generated by solar flares," *Space Science Reviews*, vol. 15, pp. 403–468, 1974. 62

[202] J. von Neumann, "The point source solution," *NDRC Division B Report AM-9*, 1941. 62

[203] L. I. Sedov, "On certain unsteady compressible fluid motions," *Journal of Applied Mathematics and Mechanics*, vol. 9, no. 4, p. 294, 1945. 62

[204] L. I. Sedov, "Propagation of strong shock waves," *Journal of Applied Mathematics and Mechanics*, vol. 10, pp. 241–250, 1946. 62

[205] G. I. Barenblatt, *Similarity, Self-Similarity, and Intermediate Asymptotics*. New York: Consultants Bureau, 1979. 62

[206] L. I. Sedov, *Similarity and Dimensional Methods in Mechanics*. New York: Academic Press Inc., 1959. 62, 65, 178

[207] V. P. Korobeinikov, *Problems of Point Blast Theory*. New York: American Institute of Physics, 1991. 63

[208] Y. B. Zel'dovich and Y. P. Raizer, *Physics of Shock Waves and High-Temperature Hydrodynamic Phenomena*. New York: Dover Publications Inc., 2002. 63

[209] H. A. Bethe, K. Fuchs, J. O. Hirschfelder, J. L. Magee, R. E. Peierls, and J. von Neumann, "Blast Wave," *Los Alamos National Labs*, p. 304, 1947. 66

[210] G. I. Taylor, "The Formation of a Blast Wave by a Very Intense Explosion. II. The atomic explosion of 1945," *Proc. Roy. Soc. Lond. A*, vol. 201, 1950. 66

[211] A. S. Kompaneets, "A point explosion in an inhomogeneous atmosphere," *Soviet Phys. Doklady*, vol. 5, pp. 46–48, 1960. 66

[212] D. D. Laumbach and R. F. Probstein, "A point explosion in a cold exponential atmosphere," *J. Fluid Mech.*, vol. 35, pp. 53–75, 1969. 66

[213] T. A. Lozinskaya, "The Supernova Remnants IC 433 and VRO 42.05.01: Fast Filaments and High-velocity Gas," *Aust. J. Phys.*, vol. 32, pp. 113–121, 1979. 66

[214] G. S. Bisnovatyi-Kogan and S. A. Silich, "Shock-wave propagation in the nonuniform interstellar medium," *Reviews of Modern Physics*, vol. 67, no. 3, pp. 661–712, 1995. 66

[215] C. A. Olano, "The propagation of the shock wave from a strong explosion in a plane-parallel stratified medium: the Kompaneets approximation," *Astronomy and Astrophysics*, vol. 506, no. 3, pp. 1215–1228, 2009. 66

[216] A. Dubey, K. Antypas, A. Calder, B. Fryxell, D. Lamb, P. Ricker, L. Reid, K. Riley, R. Rosner, A. Siegel, F. Timmes, N. Vladimirova, and K. Weide, "The Software Development Process of FLASH, a Multiphysics Simulation Code," *ICSE 2013 Workshops*, pp. 1–8, 2013. 67

[217] T. Ditmire, K. Shigemori, B. A. Remington, K. Estabrook, and R. A. Smith, "The Production of Strong Blast Waves through Intense Laser Irradiation of Atomic Clusters," *The Astrophysical Journal Supplement Series*, vol. 127, no. 2, pp. 299–304, 2000. 66

[218] A. S. Moore, D. R. Symes, and R. A. Smith, "Tailored blast wave formation: Developing experiments pertinent to laboratory astrophysics," *Physics of Plasmas*, vol. 12, no. 5, pp. 1–7, 2005. 66

[219] A. S. Moore, E. T. Gumbrell, J. Lazarus, M. Hohenberger, J. S. Robinson, R. A. Smith, T. J. A. Plant, D. R. Symes, and M. Dunne, "Full-trajectory diagnosis of laser-driven radiative blast waves in search of thermal plasma instabilities," *Physical Review Letters*, vol. 100, no. 5, pp. 1–4, 2008. 66

[220] Y.-H. Chen, M. H. Helle, A. Ting, D. F. Gordon, M. N. Polyanskiy, I. Pogorelsky, M. Babzien, and Z. Najmudin, "Observation of monoenergetic protons from a near-critical gas target tailored by a hydrodynamic shock," *Proc. of SPIE*, vol. 9514, no. 95140C, 2015. 67

[221] D. Kaganovich, D. F. Gordon, M. H. Helle, and A. Ting, "Shaping gas jet plasma density profile by laser generated shock waves," *Journal of Applied Physics*, vol. 116, 2014. 67

[222] I. H. Hutchinson, "Principles of Plasma Diagnostics: Second Edition," *Plasma Physics and Controlled Fusion*, vol. 44, pp. 2603–2603, dec 2002. 68

[223] J. M. Cole, "Interpret," 2017. 74

[224] G. Swadling, *An experimental investigation of the azimuthal structures formed during the ablation phase of wire array z-pinches.* PhD thesis, 2011. 74

[225] G. F. Swadling, S. V. Lebedev, N. Niasse, J. P. Chittenden, G. N. Hall, F. Suzuki-Vidal, G. Burdiak, A. J. Harvey-Thompson, S. N. Bland, P. De Grouchy, E. Khoory, L. Pickworth, J. Skidmore, and L. Suttle, "Oblique shock structures formed during the ablation phase of aluminium wire array z-pinches," *Physics of Plasmas*, vol. 20, no. 2, 2013. 74

[226] F. C. Young, J. R. Boller, S. J. Stephanakis, T. G. Jones, and J. M. Neri, "Radiachromic film as a detector for intense MeV proton beams," *Review of Scientific Instruments*, vol. 70, no. 1, pp. 1201–1204, 1999. 74

[227] R. M. Cassou and E. V. Benton, "Properties and applications of CR-39 polymeric nuclear track detector," *Nuclear Track Detection*, vol. 2, no. 3, pp. 173–179, 1978. 75

[228] A. P. Fews and D. L. Henshaw, "High resolution alpha-particle spectroscopy using CR-39 plastic track detector," *Nuclear Instruments and Methods In Physics Research*, vol. 197, pp. 517–529, 1982. 75

[229] A. P. Fews, "Flexible analysis of etched nuclear particle tracks," *Nuclear Inst. and Methods in Physics Research, B*, vol. 72, no. 1, pp. 91–103, 1992. 75

[230] J. J. Thomson, "Rays of positive electricity," *Philosophical Magazine*, vol. 21, no. 122, pp. 225–249, 1911. 75

[231] S.-G. Crystals, "BC-422Q Scintillator." 77

[232] N. Cook, O. Tresca, and R. Lefferts, "Scintillator diagnostics for the detection of laser accelerated ion beams," *Journal of Instrumentation*, vol. 9, no. 09, pp. P09004–P09004, 2014. 77

[233] C. Palmer, *Approaching the radiation pressure regime of proton acceleration with high intensity lasers*. PhD thesis, Imperial College London, 2011. 78, 87, 99, 112

[234] C. S. Brady and T. D. Arber, "An ion acceleration mechanism in laser illuminated targets with internal electron density structure," *Plasma Physics and Controlled Fusion*, vol. 53, p. 015001, jan 2011. 80

[235] R. A. Fonseca, L. O. Silva, F. S. Tsung, V. K. Decyk, W. Lu, C. Ren, W. B. Mori, S. Deng, S. Lee, T. Katsouleas, and J. C. Adam, "OSIRIS: A Three-Dimensional, Fully Relativistic Particle in Cell Code for Modeling Plasma Based Accelerators," in *Lecture Notes in Computer Science*, pp. 342–351, Berlin: Springer, 2002. 80

[236] J. Dawson, "Particle simulation of plasmas," *Reviews of Modern Physics*, vol. 55, pp. 403–447, apr 1983. 80

[237] S. Chen, S. Atzeni, M. Gauthier, D. Higginson, F. Mangia, J.-R. Marques, R. Riquier, and J. Fuchs, "Proton stopping power measurements using high intensity short pulse lasers produced proton beams," *Nuclear Instruments and Methods in Physics Research Section A: Accelerators, Spectrometers, Detectors and Associated Equipment*, vol. 740, pp. 105–106, 2014. 83

[238] F. Sylla, M. Veltcheva, S. Kahaly, A. Flacco, and V. Malka, "Development and characterization of very dense submillimetric gas jets for laser-plasma interaction," *Review of Scientific Instruments*, vol. 83, no. 3, 2012. 83

[239] S. N. Chen, M. Vranic, T. Gangolf, E. Boella, and P. Antici, "Collimated protons accelerated from an overdense gas jet irradiated by a 1 m wavelength high-intensity short-pulse laser," pp. 1–22. 83, 184

[240] E. D'Humières, P. Antici, M. Glesser, J. Boeker, F. Cardelli, S. Chen, J. L. Feugeas, F. Filippi, M. Gauthier, A. Levy, P. Nicolaï, H. Pépin, L. Romagnani, M. Scisciò, V. T. Tikhonchuk, O. Willi, J. C. Kieffer, and J. Fuchs, "Investigation of laser ion acceleration in low-density targets using exploded foils," *Plasma Physics and Controlled Fusion*, vol. 55, no. 12, p. 124025, 2013. 83

[241] P. Antici, E. Boella, S. N. Chen, D. S. Andrews, M. Barberio, J. Boeker, F. Cardelli, J. L. Feugeas, M. Glesser, P. Nicolaï, L. Romagnani, M. Scisciò, M. Starodubtsev, O. Willi, J. C. Kieffer, V. T. Tikhonchuk, H. Pepin, L. O. Silva, E. D'Humières, and J. Fuchs, "Acceleration of collimated 45 MeV protons by collisionless shocks driven in low-density, large-scale gradient plasmas by a 10ˆ{20} W/cmˆ2, 1 m laser," *arXiv*, pp. 1–16, 2017. 83

[242] Y.-H. Chen, M. H. Helle, A. Ting, D. F. Gordon, M. N. Polyanskiy, I. Pogorelsky, M. Babzien, and Z. Najmudin, "Observation of monoenergetic protons from a near-critical gas target tailored by a hydrodynamic shock," in *Proc. of SPIE* (K. W. D. Ledingham, K. Spohr, P. McKenna, P. R. Bolton, E. Esarey, C. B. Schroeder, and F. J. Grüner, eds.), vol. 9514, p. 95140C, may 2015. 83

[243] M. N. Polyanskiy, "Personal Communication," 2017. 84

[244] W. H. Richardson, "Bayesian-Based Iterative Method of Image Restoration," *Journal of the Optical Society of America*, vol. 62, no. I, pp. 55–59, 1972. 90

[245] L. B. Lucy, "An iterative technique for the rectification of observed distributions," *The Astronomical Journal*, vol. 79, no. 6, p. 745, 1974. 90

[246] L. A. Shepp and Y. Vardi, "Maximum Likelihood Reconstruction for Emission Tomography," *IEEE Transactions on Medical Imaging*, vol. 1, no. 2, pp. 113–122, 1982. 90

[247] F. van den Bosch, L. Ferrarese, W. Jaffe, H. C. Ford, and R. W. O'Connell, "Hubble Space Telescope photometry of the central regions of Virgo Cluster elliptical galaxies. 1: Observations, discussion, and conclusions," *The Astronomical Journal*, vol. 108, no. 5, pp. 1567–1578, 1994. 90

[248] M. Karovska, W. Hack, J. Raymond, and E. Guinan, "First Hubble Space Telescope Observations of Mira Ab Wind-Accreting Binary System," *The Astronomical Journal*, vol. 482, pp. L175–L178, 1997. 90

[249] N. Dey, L. Blanc-Feraud, C. Zimmer, P. Roux, Z. Kam, J. C. Olivo-Marin, and J. Zerubia, "Richardson-Lucy algorithm with total variation regularization for 3D confocal microscope deconvolution," *Microscopy Research and Technique*, vol. 69, no. 4, pp. 260–266, 2006. 90

[250] M. Ingaramo, A. G. York, E. Hoogendoorn, M. Postma, H. Shroff, and G. H. Patterson, "Richardson-Lucy deconvolution as a general tool for combining images with complementary strengths," *ChemPhysChem*, vol. 15, no. 4, pp. 794–800, 2014. 90

[251] A. Henig, S. Steinke, M. Schnuerer, T. Sokollik, R. Hoerlein, D. Kiefer, D. Jung, J. Schreiber, B. M. Hegelich, X. Q. Yan, J. Meyer-Ter-Vehn, T. Tajima, P. V. Nickles, W. Sandner, and D. Habs, "Radiation-pressure acceleration of ion beams driven by circularly polarized laser pulses," *Physical Review Letters*, vol. 103, no. 24, pp. 3–6, 2009. 100, 101, 149

[252] O. Klimo, J. Psikal, J. Limpouch, and V. T. Tikhonchuk, "Monoenergetic ion beams from ultrathin foils irradiated by ultrahigh-contrast circularly polarized laser pulses," *Physical Review Special Topics - Accelerators and Beams*, vol. 11, no. 3, pp. 1–14, 2008. 120

[253] N. P. Dover, *Exploring novel regimes for ion acceleration driven by intense laser radiation.* PhD thesis, 2013. 127

[254] K. G. Estabrook and W. L. Kruer, "Theory and simulation of one-dimensional Raman backward and forward scattering," *Physics of Fluids*, vol. 26, no. 7, pp. 1892–1903, 1983. 132

[255] S. Steinke, P. Hilz, M. Schnürer, G. Priebe, J. Bränzel, F. Abicht, D. Kiefer, C. Kreuzer, T. Ostermayr, J. Schreiber, A. A. Andreev, T. P. Yu, A. Pukhov, and W. Sandner, "Stable laser-ion acceleration in the light sail regime," *Physical Review Special Topics - Accelerators and Beams*, vol. 16, no. 1, pp. 1–5, 2013. 149

[256] P. Velarde, D. García-Senz, E. Bravo, F. Ogando, A. Relaño, C. García, and E. Oliva, "Interaction of supernova remnants: From the circumstellar medium to the terrestrial laboratory," *Physics of Plasmas*, vol. 13, no. 9, 2006. 157

[257] P. Hartigan, A. Frank, J. M. Foster, B. H. Wilde, M. Douglas, P. A. Rosen, R. F. Coker, and B. E. Blue, "Fluid dynamics of stellar jets in real time: third epoch hubble space telescope images of HH 1, HH 34, and HH 47," *The Astrophysical Journal*, vol. 736, no. 1, p. 29, 2011. 157

[258] D. D. Ryutov, R. P. Drake, J. Kane, E. Liang, B. A. Remington, and W. M. Wood-Vasey, "Similarity criteria for the laboratory simulation of supernova hydrodynamics," *The Astrophysical Journal*, vol. 518, no. 2, pp. 821–832, 1999. 157

[259] P. Woodward and P. Colella, "The numerical simulation of two-dimensional fluid flow with strong shocks," *Journal of Computational Physics*, vol. 54, no. 1, pp. 115–173, 1984. 157

[260] I. I. Glass and L. E. Heuckroth, "Head-On Collision of Spherical Shock Waves," *Physics of Fluids*, vol. 2, no. 5, p. 542, 1959. 157

[261] R. Smith, J. Lazarus, M. Hohenberger, A. Marocchino, J. Robinson, J. Chittenden, A. Moore, E. Gumbrell, and M. Dunne, "High resolution imaging of colliding blast waves in cluster media," *Plasma Physics and Controlled Fusion*, vol. 49, no. 12 B, pp. B117–B124, 2007. 157

[262] F. Suzuki-Vidal, T. Clayson, C. Stehle, G. F. Swadling, J. M. Foster, J. Skidmore, P. Graham, G. C. Burdiak, S. V. Lebedev, U. Chaulagain, R. L. Singh, E. Gumbrell, S. Patankar, C. Spindloe, J. Larour, M. Kozlova, R. Rodriguez, J. M. Gil, G. Espinosa, P. Velarde, and C. Danson, "Counter-propagating radiative shock experiments on the Orion laser," *Physical Review Letters*, vol. 119, p. 055001, 2017. 157

[263] R. C. Elton, D. M. Billings, C. K. Manka, H. R. Griem, J. Grun, and B. H. Ripin, "Spectroscopic diagnostics in a colliding-blast-wave experiment," *Physical Review E*, vol. 49, no. 2, 1994. 157

[264] M. H. Helle, D. F. Gordon, D. Kaganovich, Y. Chen, J. P. Palastro, and A. Ting, "Laser-Accelerated Ions from a Shock-Compressed Gas Foil," *Physical Review Letters*, vol. 117, no. 16, pp. 1–5, 2016. 158

[265] R. Courant and K. O. Friedrichs, *Supersonic flow and shock waves*. Waverly Press, 1948. 158, 159

[266] G. F. Kinney and K. J. Graham, *Explosive Shocks in Air*. New York: Springer-Verlag, 1985. 158

[267] R. P. Drake, "Radiative shocks in astrophysics and the laboratory," *Astrophysics and Space Science*, vol. 298, no. 1-2, pp. 49–59, 2005. 159

[268] L. Yin, B. J. Albright, B. M. Hegelich, and J. C. Fernández, "GeV laser ion acceleration from ultrathin targets: The laser break-out afterburner," *Laser and Particle Beams*, vol. 24, no. 02, pp. 291–298, 2006. 173

[269] L. Yin, B. J. Albright, B. M. Hegelich, K. J. Bowers, K. A. Flippo, T. J. Kwan, and J. C. Fernández, "Monoenergetic and GeV ion acceleration from the laser breakout afterburner using ultrathin targets," *Physics of Plasmas*, vol. 14, no. 5, 2007. 173

[270] S. Buffechoux, J. Psikal, M. Nakatsutsumi, L. Romagnani, A. Andreev, K. Zeil, M. Amin, P. Antici, T. Burris-Mog, A. Compant-La-Fontaine, E. D'Humières, S. Fourmaux, S. Gaillard, F. Gobet, F. Hannachi, S. Kraft, A. Mancic, C. Plaisir, G. Sarri, M. Tarisien, T. Toncian, U. Schramm, M. Tampo, P. Audebert, O. Willi, T. E. Cowan, H. Pépin, V. Tikhonchuk, M. Borghesi, and J. Fuchs, "Hot electrons transverse refluxing in ultraintense laser-solid interactions," *Physical Review Letters*, vol. 105, no. 1, pp. 1–5, 2010. 176

[271] I. V. Pogorelsky, M. Babzien, M. N. Polyanskiy, and W. D. Kimura, "Mid-IR lasers for energy frontier plasma accelerators and colliders," *AIP Conference Proceedings*, vol. 1812, pp. 1–10, 2017. 182

[272] I. V. Pogorelsky, "Personal Communication," 2017. 182

[273] A. A. Sahai, F. S. Tsung, A. R. Tableman, W. B. Mori, and T. C. Katsouleas, "Relativistically induced transparency acceleration of light ions by an ultrashort laser pulse interacting with a heavy-ion-plasma density gradient," *Physical Review E - Statistical, Nonlinear, and Soft Matter Physics*, vol. 88, no. 4, pp. 1–10, 2013. 184

[274] A. A. Sahai, "Motion of the plasma critical layer during relativistic-electron laser interaction with immobile and comoving ion plasma for ion acceleration," *Physics of Plasmas*, vol. 21, no. 5, 2014. 184

[275] T. Grismayer and P. Mora, "Influence of a finite initial ion density gradient on plasma expansion into a vacuum," *Physics of Plasmas*, vol. 13, no. 3, 2006. 190

[276] E. Boella, F. Fiúza, A. S. Novo, R. Fonseca, and L. O. Silva, "Numerical optimization study of shock wave acceleration," *arXiv*, 2017. 190